Exploring new frontiers beyond the Standard Model through Particle and Astro physics

A thesis submitted in partial fulfilment of
the requirements for the degree of

Doctor of Philosophy

by

Debashis Pachhar
Roll No: 20330020

Under the guidance of

Prof. Srubabati Goswami
Physical Research Laboratory
Ahmedabad 380009, Gujarat, India

Department of Physics
Indian Institute of Technology, Gandhinagar
November 2025

Dedicated to,

My parents, Ma'am and my friends without whose endless support, I could not achieve this.

DECLARATION

I hereby declare that this PhD thesis titled **Exploring new frontiers beyond the Standard Model through Particle and Astro physics** is carried out by me to fulfil the requirement of PhD degree at *Theoretical Physics Division* of Physical Research Laboratory (PRL) under the supervision of Prof. Srubabati Goswami. All information and facts provided in this thesis are correct to the best of my knowledge. I also declare that wherever I have borrowed any ideas or results of someone else, I have properly cited to the original sources. No part of this thesis has formed the basis for award of any other degree in any university or institution.

Date:
Place: Ahmedabad, Gujarat

Debashis Pachhar
Theoretical Physics Division
Physical Research Laboratory
Ahmedabad, Gujarat, India

CERTIFICATE

It is certified that the work contained in the thesis titled

Exploring new frontiers beyond the Standard Model through Particle and Astro physics,

by **Debashis Pachhar** (Roll no: **20330020**), has been carried out under my supervision, and this work has not been submitted elsewhere for a degree.

I have read this dissertation, and in my opinion, it is fully adequate in scope and quality as a dissertation for the degree of Doctor of Philosophy.

Date:
Place: Ahmedabad, Gujarat

Prof. Srubabati Goswami
PhD Supervisor
Theoretical Physics Division
Physical Research Laboratory
Ahmedabad, Gujarat, India

Acknowledgements

There are moments in life when words feel inadequate, where gratitude runs so deep that no language can truly encapsulate its depth. As I reach the culmination of my PhD journey, I find myself overwhelmed with emotions—gratitude, nostalgia, and an immense sense of indebtedness to those who have shaped this path.

I wish to express my deepest and most heartfelt gratitude to my PhD supervisor, Prof. Srubabati Goswami, whose exceptional vision, profound expertise, and unwavering guidance have been instrumental in shaping the trajectory of my research. Her mentorship has provided me with the intellectual foundation and analytical rigour essential for conducting high-precision scientific investigations. Throughout this journey, her patience, encouragement, and steadfast support have not only inspired me but have also served as a constant source of motivation. I am truly indebted to her for her invaluable advice, constructive criticism, and for nurturing my scientific curiosity, which has profoundly influenced my academic growth and professional aspirations. Her ability to install confidence in her students, coupled with her dedication to fostering a culture of excellence, has left an indelible mark on my scholarly endeavours.

I am equally grateful to my collaborator, Prof. P.S. Bhupal Dev, whose insightful perspectives, technical expertise, and collaborative spirit have been invaluable throughout the course of my research. Working alongside Prof. Dev has not only broadened my scientific horizons but has also instilled in me a deep appreciation for the power of collaboration in advancing scientific discovery.

I am also sincerely grateful to my DSC members— Prof. Namit Mahajan, Prof. Kinsuk Acharyya and Dr. Satyajit Seth for their invaluable feedback, thought-provoking discussions, and constructive criticism during the DSC seminars. Their insightful observations and rigorous evaluations have significantly enriched my research, enabling me to approach complex problems from diverse and broader perspectives. Their intellectual engagement and encouragement have not only refined my scientific approach but have also strengthened my ability to articulate and defend my findings with clarity and precision. Their collective wisdom and unwavering support have been instrumental in shaping the quality and depth of my research.

Furthermore, I extend my heartfelt appreciation to Dr. Ketan Patel, Dr. Navinder Singh, Prof. Partha Konar, Dr. Naveen Chauhan, and Prof. Varun Sheel for their invaluable teachings, stimulating discussions, and insightful guidance throughout my coursework and research projects. Their profound knowledge, dedication to academic excellence, and mentorship have played a crucial role in deepening my understanding and broadening my scientific perspective. A special acknowledgment is due to Dr. Bhushit Vaishnav, Head of PRL Academic Services, whose unwavering assistance and steadfast support, from my very first day at PRL, have been truly indispensable. His guidance has helped me navigate various academic and administrative aspects with confidence and ease. I am also deeply grateful to Prof. Bijaya Kumar Sahoo, Academic chair, PRL for his readiness to offer help and support whenever needed.

I want to express my deepest gratitude to all the faculty members of the THEPH group including newly joined Dr. Paramita Dutta, Dr. Udit Khanna, and Dr. Jacky Kumar for giving

their constructive inputs during seminars and academic discussions. A special thanks to Dr. Paramita Dutta whose warm affection and fun banter often lifted my spirits during my most tiring days. My sincere appreciation also goes to our incredible office staff members — Divya, Hintal, Rikin and Purvi —for their tireless assistance in managing countless administrative tasks and ensuring smooth operations.

A PhD journey is not merely defined by research and academic rigour, but by the friendships, the shared laughter, the moments of despair, and the unwavering support of those who walk this path alongside me. As I sit down to express my gratitude, I am overwhelmed by the sheer number of people who have touched my life during this time. Some have stayed by my side, some have drifted away, but every single one of them has left an imprint on my heart. The very first name that comes to my mind whenever I think of a friend is Arup (Chakraborty). Although we are literally from the north and south of this world—or, in our case, our state, West Bengal—there is truly no one else whose opinion I care about more than his. He has been my confidant, my harshest critic, and my greatest well-wisher. He was always there whenever I needed him, but more importantly, he was there even when I didn't need him—often inserting himself into my life like an overly attached sidekick. No matter where life takes us, his place in my story is irreplaceable. Lobby-B has been my second home, and Dharmendra, Guru Bhai, and Kamran, you have been my closest companions. You have witnessed my growth, my struggles, and my triumphs, standing by me through both personal and professional challenges. Among the countless moments we have shared, our travels together remain the most precious—long road trips, deep conversations, and sleepless nights beneath the unfamiliar skies. Those are the memories I would never trade for anything in this world. And then there is Wafikul, my brother in spirit, whose unwavering support and friendship has guided me through the highs and lows, the failures and the successes. I will always cherish your appreciation for my cooking—even on those occasions when I added a little too much salt. Above all, your biriyani remains my absolute favourite, a dish I will never forget. It would be a crime not to mention Malika, Akanksha, Trinesh, Arup Maity, Aditya, Chandrima, Mansi, and Sanjay, — you all have made this PhD journey infinitely more enjoyable. The laughter, the shared frustrations, the random deep conversations at odd hours—these are the things that have kept me sane. A heartfelt thank you to my senior, Supriya da, for being my go-to person, whether it was for discussions on physics or a last-minute cooking space. Your kindness and patience have made all the difference. I must specially mention Chandrima Sen - you arrived as a postdoc but quickly claimed the roles of my best friend, gossip partner, and partner-in-crime. Our friendship - built on daily chats, mutual appreciation for good food and roaming Durga Puja pandals in Ahmedabad - is easily one of the unexpected gifts PRL gave me. Shukla ji, your timely advice and humour have been a lifesaver, making the toughest days just a little easier to bear. And then, there were the golden moments—the escape from research into the world of volleyball and football. Bharathi Bhai, Supriya da, and Shukla ji, those evenings of friendly banter, fierce-yet-meaningless rivalries, and pure joy will always remain some of my fondest memories. I would like to sincerely thank Tanmay da, Sidhhartha da, Amit Bhai, Atif Bhai, Pravin Bhai, Ramanuj da, and Sudipto da for embracing me like your younger brother and always guiding me with care and wisdom. Your unwavering support and gentle corrections have kept me on the right path, and I am truly grateful for the bond we share. To Monika di and Meghna di, thank you for welcoming me with such warmth and embracing my presence like true elder sisters. I will stand beside you through every season, quietly choosing you, always, as family. I would also like to sincerely thank Chayan Da, who was not just an exceptional research collaborator but also a wonderful human being with the rare gift of connecting effortlessly with everyone. This journey would not have been the same without the amazing juniors Achintyaa, Namit, Shuvendu, Bhavya, Tamanna, Hemanth, Dibyani, Sandip, Gupta, Rahul, Indrajit, Samarpan,

Aishwarya, Anantshree ... You have made this journey a whole lot more fun, and for that, I am truly grateful.

To my sister and our parents, I extend my deepest gratitude for their unwavering love, endless encouragement, tireless support, and countless sacrifices. Their prayers have been my rock, giving me the strength to overcome every challenge along this journey. It's because of their hard work, dedication, and prayers that I am here today, writing my doctoral thesis.

Last but not least, I wish to express my deepest affection and appreciation to Mitu, whom I have been truly fortunate to know and love. I am truly overwhelmed by the magic you bring into my world, and I am eternally grateful for your unwavering support, understanding, and the profound happiness that you have given me.

As I reflect on this transformative chapter of my life, I am filled with immense gratitude for the people who have walked this path with me. Their encouragement, support, and belief in me have made this journey not just an academic endeavor but a deeply enriching and fulfilling experience. I will forever be indebted to each of them for shaping not just my research but also the person I have become. From the depths of my heart, thank you all—for everything.

Date:
Place:

Debahis Pachhar
Roll No.: 20330020

Abstract

The Standard Model (SM) has been remarkably successful in explaining the short distance physics probed so far and the discovery of the Higgs boson at the Large Hadron Collider completes the particle content of the SM. Despite of its extreme success, there are observational evidences including neutrino oscillation, dark matter, matter-antimatter asymmetry in the universe which remain unexplained within the SM and necessitate the extension of the SM. These extensions generally follow two approaches: i) extend the particle content of the SM, ii) enlarge the symmetry group of the SM which eventually implies the extension of the particle content. These additional degrees of freedom in Beyond Standard Model (BSM) scenarios can significantly impact observables across particle physics, astrophysics, and cosmology.

Although the framework of three-flavor neutrino oscillation is well-established, results from the short-baseline experiments, such as the *Liquid Scintillator Neutrino Detector* (*LSND*) and *MiniBooster Neutrino Experiment (MiniBooNE)*, hint at the potential existence of an additional light neutrino state characterized by a mass-squared difference (Δm_s^2) of approximately $1\,\mathrm{eV}^2$. The new neutrino state is devoid of all SM interactions, commonly referred to as a "*sterile*" state. In addition, a sterile neutrino with a mass-squared difference of 10^{-2} eV^2 has been proposed to improve the tension between the results obtained from the *Tokai to Kamioka (T2K)* and the *NuMI Off-axis ν_e Appearance (NOνA)* experiments. Further, the non-observation of the predicted upturn in the solar neutrino spectra below 8 MeV can be explained by postulating an extra light sterile neutrino state with a mass-squared difference around $10^{-5}\,\mathrm{eV}^2$. The hypothesis of an additional light sterile neutrino state introduces four distinct mass spectra depending on the sign of the mass-squared difference (two with $\Delta m_s^2 > 0$ and two with $\Delta m_s^2 < 0$). We have examined their implications for the mass-related observables such as the sum of neutrino masses (Σ) from cosmology, effective mass of electron neutrino (m_β) from nuclear β decay and effective Majorana mass (m_{ee}) from neutrinoless double beta decay ($0\nu\beta\beta$). The predictions are analysed with the current experimental limit including the bound on Σ from cosmology, the measurements

of m_β from *KATRIN* experiment and *KamLAND-Zen* limits on m_{ee}. Additionally, the potential impact of future experiments such as *Project 8* and *nEXO* is also discussed. The results highlight that the cosmological data and laboratory experiments provide complementary constraints on sterile neutrino mass spectra. While current measurements already exclude significant parameter space, the complete picture will emerge from next-generation experiments like *Project 8* and *nEXO*, which will reach to the precision needed to conclusively test these scenarios across the full range of possible sterile neutrino masses.

Leptoquarks can couple with both quarks and leptons and $0\nu\beta\beta$ is a rare process which involves both sectors. Therefore, we have performed a comprehensive analysis of $0\nu\beta\beta$ and its interplay with low-energy flavor observables in a radiative neutrino mass model with scalar leptoquarks $S_1(\overline{3},1,1/3)$ and $\widetilde{R}_2(3,2,1/6)$. The parameter region consistent with constraints from neutrino mass and mixing, collider searches, as well as measurements of several flavor observables, such as charged lepton flavor violation and rare (semi)leptonic kaon and B-meson decays, including the recent anomalies in $R_{D^{(*)}}$ and $B \to K\nu\overline{\nu}$ observables is carved out from the global analysis of these observables. It is found out that the most stringent constraint on the parameter space comes from $\mu \to e$ conversion in nuclei and $K^+ \to \pi^+\nu\overline{\nu}$ decay. It is also pointed out that there is a serious tension between the muon and electron $(g-2)$ anomalies in this singlet-doublet leptoquark model. Taking benchmark values from the combined allowed regions, the implications for $0\nu\beta\beta$ are studied including both the canonical light neutrino and the leptoquark contributions. It turns out for normal ordering of neutrino masses, the leptoquark contribution removes the cancellation region that occurs for the canonical case. The effective mass in the presence of leptoquarks can lie in the desert region between the standard normal and inverted ordering cases, and this can be probed in future ton-scale experiments like *LEGEND-1000* and *nEXO*.

Grand unified theories (GUT) are motivated from the gauge coupling unification at the high scale and they provide a framework where the quarks and leptons are embedded in the same multiples. It also naturally accommodates leptoquarks in its scalar representations. We then discuss the role of heavy scalar fields in mediating neutrinoless double beta decay $(0\nu\beta\beta)$ within the $SU(5)$ GUT framework. We have considered the canonical $SU(5)$ extended by a triplet scalar field Δ belonging to the

15-dimensional representation of $SU(5)$. This generates Majorana neutrino mass at tree level via type-II seesaw mechanism and also radiatively at one loop via a pair of scalar leptoquarks. $0\nu\beta\beta$ is induced by the Majorana neutrinos as well as by the leptoquarks. However, in the minimal setup, the leptoquarks inducing $0\nu\beta\beta$ also induce proton decay, and the constraint coming from proton decay suppresses the $0\nu\beta\beta$ rate well below the observable level. In order to evade this, an $SU(5) \times \mathcal{Z}_3$ model is constructed in which the diquark interactions of the S_3 leptoquark is forbidden, which automatically satisfies the proton decay constraint. The mixing between the pair of leptoquarks S_3 and $\tilde{R}_2$ necessary for inducing $0\nu\beta\beta$ now occurs through Δ. However, to achieve small neutrino mass, the scalar mass M_Δ is required to be around 10^{16} GeV which again yields a low rate for the scalar-induced $0\nu\beta\beta$. Moreover, in the parameter space consistent with the viable fermion mass spectra, the light-neutrino-induced effective mass for $0\nu\beta\beta$ disfavours the inverted ordering from the current *KamLAND-Zen* limit. Finally, we introduce an additional **15**-plet containing a second triplet scalar Δ_2, decoupled from matter multiplets, which can enhance the scalar-induced $0\nu\beta\beta$ rate beyond the canonical light neutrino exchange contribution. In this case, we find that the cancellations between standard and non-standard contributions to $0\nu\beta\beta$ allow the inverted mass ordering in certain parameter regions. Furthermore, it is also shown that future $0\nu\beta\beta$ decay experiments can be used as a sensitive probe of the new scalar mass M_{Δ_2} across a broad range, from LHC-accessible sub-TeV scales up to $M_{\Delta_2} \sim 10^{10}$ GeV.

We also analysed a scenario where ultralight axion like particles (ALPs) mediate a macroscopic force with long-range monopole-dipole interactions between the Earth and the Sun, if the Earth is treated as a polarized source. It is found that approximately 10^{39} electrons within the Earth become spin-polarised antiparallel to the Earth's rotation axis under the influence of the geomagnetic field. These electrons, in a polarized state, can interact with the unpolarized nucleons in the Sun, giving rise to a monopole-dipole potential between the Sun-Earth system. This phenomenon ultimately influences the trajectories of light and celestial bodies, resulting in observable effects such as gravitational light bending, Shapiro time delay, and perihelion precession of planets. We investigate two scenarios for constraining the monopole-dipole coupling strength. In the first scenario, we establish a constraint on the monopole-dipole strength based on a single astrophysical observation treat-

ing the Earth as a source of polarized electrons. The perihelion precession of Earth provides the most stringent upper limit on the monopole-dipole coupling strength as $g_S g_P \lesssim 1.75 \times 10^{-13}$ for the ALP of mass $m_a \lesssim 1.35 \times 10^{-18}$ eV. In the second scenario, constraints on monopole-monopole coupling strength g_S $\left(\lesssim 3.51 \times 10^{-25}\right)$ arises from the perihelion precession of the planet Mars, while the limit on dipole-dipole coupling strength g_P $\left(\lesssim 1.6 \times 10^{-13}\right)$ is taken from the measurement of the tip of the red giant branch in ω Centauri using Gaia DR2 data. Together, they yield a hybrid constraint on the monopole-dipole coupling strength as $g_S g_P \lesssim 5.61 \times 10^{-38}$. We obtained a hybrid bound which is three orders of magnitude more stringent than the Eöt-Wash experiment and one order of magnitude stronger than the current hybrid $(\mathrm{Lab})^{\mathrm{N}}_{\mathrm{S}} \times (\mathrm{Astro})^{\mathrm{e}}_{\mathrm{P}}$ limit.

Keywords— Beyond Standard Model, sterile neutrino, mass observables leptoquarks, neutrinoless double beta decay, flavor observables, grand unified theory, axion like particles, monopole-dipole potential, perihelion precesion, light bending, Shapiro time delay.

Publications

Published Articles[1]:

(1) Srubabati Goswami, **Debashis Pachhar** and Supriya Pan," *Constraining the mass-spectra in the presence of a light sterile neutrino from absolute mass-related observables*",
arXiv: 2405.04176 [hep-ph]; Phys. Rev. D 110 (2024) 1, 015028

(2) P.S. Bhupal Dev, Srubabati Goswami, Chayan Majumdar and **Debashis Pachhar**,"*Neutrinoless double beta decay from scalar leptoquarks: interplay with neutrino mass and flavor physics*",
arXiv: 2407.04670 [hep-ph]; JHEP 01, (2025) 004

(3) Tanmay Kumar Poddar and **Debashis Pachhar**, "*Constraints on monopole-dipole potential from tests of gravity*",
arXiv:2302.03882 [hep-ph]; Phys. Rev. D. 108 (2023) 10, 103024.

Communicated Article(s):

(1) P.S. Bhupal Dev, Srubabati Goswami, **Debashis Pachhar**, and Saurabh K. Shukla , *"Scalar-induced Neutrinoless double beta decay in SU(5)"*
arXiv: 2507.16606 [hep-ph]; Under Review

Conference Proceeding(s):

(1) **Debashis Pachhar**. *Light sterile neutrino and mass-related observables*; Under review.

[1]The authors are listed alphabetically following the convention in Theoretical High Energy Physics.

Contents

List of Figures

List of Tables

1

Introduction

Humans have always been captivated by the mysteries of nature and driven by a natural desire to unravel its workings at the smallest possible scales. In pursuit of this, it has been unveiled that there are four fundamental forces governing the universe: gravity, weak, strong and electromagnetism. Particle physics, a discipline dedicated to study the elementary constituents of matter and their interactions, helps to have a better understanding of the fundamental particles and their interactions. The elegance of this field stems from its ability to demonstrate how underlying symmetries predict the existence of particles, their properties, and their dynamics.

The Standard Model (SM) of particle physics is a very successful mathematical framework which describes three of the four fundamental forces (excluding gravity) within a theoretical framework. It can accurately describe most of the observed phenomena at low energies and some of the predictions have also been verified in high energy colliders, consolidating the SM on a firm footing. Despite its remarkable success, the SM can not be considered as a complete theory of nature. It fails to account for the key observational phenomena including neutrino oscillations, matter-antimatter asymmetry, and dark matter which necessitate the exploration of theoretical frameworks beyond-the-SM (BSM) — either through the introduction of new degrees of freedom (such as undiscovered particles) or extending the symmetry group of the SM. These extensions aim to reconcile theory with experimental

evidence while preserving the empirically validated predictions of the SM. Beyond purely phenomenological motivations, the study of "*New Physics*" (NP) beyond the SM is also driven by profound theoretical puzzles which the SM can not explain. These include: the hierarchy problem, the strong CP problem, non-inclusion of gravity etc. BSM constructions may provide solutions to these long-standing issues or, at the very least, offer a pathway towards a more fundamental framework.

In the following sections, a brief review of the SM is presented, followed by a discussion of its key theoretical and observational shortcomings. Motivated by these limitations, a plethora of BSM frameworks have been proposed over the past decades. The proposed extensions primarily follow two different approaches: (a) extending the SM with new particles and (b) extending the gauge group to larger symmetry groups e.g. $SU(3)_c \otimes SU(2)_L \otimes SU(2)_R \otimes U(1)_{B-L}$, SU(5), SO(10), etc., which are valid at the high energy scale. The SM is considered to be the low-energy realisation of these fundamental theories and can naturally serves as an "*effective field theory (EFT)*" at lower energies. In this chapter, we have also discussed the preliminary description of the EFT framework.

1.1 Review of the Standard Model

The SM is a renormalisable quantum field theory (QFT) which is invariant under the $SU(3)_c \otimes SU(2)_L \otimes U(1)_{\mathcal{Y}}$ gauge group and Poincaré group [1–3]. The SM consist of different irreducible representation (*irreps*) of the Poincaré group : spin-0, spin-$\frac{1}{2}$ and spin-1 i.e. scalars, fermions and gauge bosons which are characterised by their mass and spin/helicity (projection of spin in the momentum direction). The representations of these fields under $SU(3)_c$ and $SU(2)_L$, along with their hypercharges under $U(1)_{\mathcal{Y}}$, are systematically presented in Tab. 1.1. The hypercharge convention is followed the Gell-Mann-Nishijima relation $Q_{em} = T_{3L} + \mathcal{Y}$, where Q_{em} is the electrical charge, T_{3L} is the third component of the weak isospin and $\mathcal{Y}$ is the hypercharge of the particles.

Table 1.1: The content of the SM together with their quantum number under $SU(3)_c \otimes SU(2)_L \otimes U(1)_\mathcal{Y}$, Baryon Number (B), Lepton Number (L). Here, $a\,\epsilon\,\{1,2,3\}$ represents the colour quantum numbers and $i\,\epsilon\,\{1,2\}$ stands for the weak isospin quantum numbers.

	Fields	Symbol	SM Charges	B	L
Spin - 0	Higgs Boson	$H = \begin{pmatrix} H^+ \\ H^0 \end{pmatrix}$	$(1,2,\frac{1}{2})$	0	0
Spin - $\frac{1}{2}$	Quarks	$Q^i = \begin{pmatrix} u_L^a \\ d_L^a \end{pmatrix}, \begin{pmatrix} c_L^a \\ s_L^a \end{pmatrix}, \begin{pmatrix} t_L^a \\ b_L^a \end{pmatrix}$	$(3,2,\frac{1}{6})$	$\frac{1}{3}$	0
		u_R^a, c_R^a, t_R^a	$(3,1,\frac{2}{3})$	$\frac{1}{3}$	0
		d_R^a, s_R^a, b_R^a	$(3,1,-\frac{1}{3})$	$\frac{1}{3}$	0
	Leptons	$L^i = \begin{pmatrix} \nu_{eL} \\ e_L \end{pmatrix}, \begin{pmatrix} \nu_{\mu L} \\ \mu_L \end{pmatrix}, \begin{pmatrix} \nu_{\tau L} \\ \tau_L \end{pmatrix}$	$(1,2,-\frac{1}{2})$	0	1
		e_R, μ_R, τ_R	$(1,1,1)$	0	1
Spin - 1	Gluons	G	$(8,1,0)$	0	0
	W Bosons	W	$(1,3,0)$	0	0
	B Bosons	B	$(1,1,0)$	0	0

Having specified the field content and their representations under the gauge group, the SM Lagrangian can be written as,

$$\begin{aligned}
\mathcal{L}_{SM} \;=\; & -\frac{1}{4}B_{\mu\nu}B^{\mu\nu} - \frac{1}{4}W^a_{\mu\nu}W^{\mu\nu}_a - \frac{1}{4}G^a_{\mu\nu}G^{\mu\nu}_a \\
& + i\,\overline{Q}^i_L \not{D} Q^i_L + i\,\overline{u}^i_R \not{D} u^i_R + i\,\overline{L}^i_L \not{D} L^i_L + i\,\overline{\ell}^i_R \not{D} \ell^i_R \\
& - Y^u_{ij}\overline{Q}^i_L \widetilde{H} u^j_R - Y^d_{ij}\overline{Q}^i_L\, H\, d^j_R - Y^\ell_{ij}\overline{L}^i_L H \ell^j_R + \text{h.c.} \\
& + \left|D_\mu H\right|^2 + \mu^2 \left|H\right|^2 - \lambda \left|H\right|^4 . \qquad (1.1)
\end{aligned}$$

In the above equation, the colour indices are suppressed and $i, j = 1,2,3$ are the fermion generation index, $\not{D} = \gamma^\mu D_\mu$, and $\widetilde{H} = i\sigma_2 H^*$, where σ_2 is the second Pauli Matrix. Y^f denotes the Yukawa couplings, μ is the Higgs mass parameter and λ is Higgs self-coupling. All the couplings are dimensionless except μ which has a mass dimension 1. These parameters of the SM are not calculable rather they are fixed by the experiments. The interaction between

the matter field and the gauge bosons are encoded in the gauge covariant derivative, given as:

$$D_\mu \;=\; \partial_\mu + i\, g_s G^a_\mu \lambda_a + i\, g_w W^i_\mu T_i + i\, g' \mathcal{Y} B_\mu, \tag{1.2}$$

where g', g_w and g_s are the gauge couplings of the $U(1)_\mathcal{Y}, SU(2)_L$ and $SU(3)_c$ gauge groups, λ_a $(a = 1 \to 8)$ are the $SU(3)_c$ generators, T_i $(i = 1 \to 3)$ are the $SU(2)_L$ generators and the matrix representation of these generators depend on the fermion or boson representations. The covariant field tensors in Eq. (1.1) is defined as:

$$\mathcal{F}^a_{\mu\nu} \;=\; \partial_\mu F^a_\nu - \partial_\nu F^a_\mu + i\, g_G f^{abc}_G F^b_\mu F^c_\nu, \tag{1.3}$$

where g_G is the gauge coupling and f^{abc}_G are structure constant corresponding to the gauge group $G \in \{SU(3), SU(2)\}$. The value of $f^{abc}_G = 0$ for the non-abelian $U(1)_\mathcal{Y}$ group. In the Higgs sector, if certain conditions $\left(\mu^2, \lambda > 0\right)$ are satisfied, the Higgs field develops a non-trivial vaccum expectation value (*vev*)

$$\langle H \rangle \;=\; \frac{1}{\sqrt{2}} \begin{pmatrix} 0 \\ v \end{pmatrix}, \tag{1.4}$$

where $v = \sqrt{\mu^2/\lambda} \simeq 246$ GeV[1]. Therefore, the vaccum state spontaneously breaks the $SU(3)_c \otimes SU(2)_L \otimes U(1)_\mathcal{Y} \to\; SU(3)_c \otimes U(1)_{em}$. This phenomena is referred as the Brout-Englert-Higgs (BEH) mechanism [5–7] or more commonly known as Higgs mechanism. After the electro-weak symmetry breaking (EWSB), three gauge bosons $\left(W^\pm, Z^0\right)$ emerge as massive whereas the gluons and a linear combination of W and B remains massless and is identified as the photon (γ). In the broken symmetry phase, the physical gauge fields can be expressed as,

$$W^{\mp\,\mu} = \frac{1}{\sqrt{2}} \left(W^\mu_1 \pm i W^\mu_2\right) \qquad \text{with mass} \qquad m_W = \frac{1}{2} g_w v,$$

[1]The value of the Higgs vev (v) is fixed from the precise experimental measurement of the Fermi's decay constant, G_F from muon decay and using the relation $v = (2G_F)^{-1/2}$, where $G_F = 1.1663787(6) \times 10^{-5}\,\text{GeV}^{-2}$ [4]

$$Z^\mu = \frac{1}{\sqrt{g_w^2 + g'^2}} \left(g_w W_3^\mu - g' B^\mu\right) \quad \text{with mass} \quad m_Z = \frac{1}{2}\sqrt{g_w^2 + g'^2}\, v,$$
$$A^\mu = \frac{1}{\sqrt{g^2 + g'^2}} \left(g_w W_3^\mu + g' B^\mu\right) \quad \text{with mass} \quad m_A = 0. \tag{1.5}$$

Additionally, after the EWSB, the fermions get masses from the Yukawa interactions as:

$$-\mathcal{L}_{\text{mass}} = \overline{u}_L^i m_{ij}^u u_R^j + \overline{d}_L^i m_{ij}^d d_R^j + \overline{\ell}_L^i m_{ij}^\ell \ell_R^j + \text{h.c.} \tag{1.6}$$

where $m_{ij}^f = Y_{ij}^f \langle H \rangle$ for $f = u, d, e$. The neutrinos remain massless in the SM as ν_R field is absent[2]. The charged fermion mass matrices in general could be complex non-diagonal matrices and can be diagonalised by the following transformations,

$$u_L \to \mathcal{U}_L^u\, u_L, \qquad d_L \to \mathcal{U}_L^d\, d_L, \qquad e_L \to \mathcal{U}_L^e\, e_L, \tag{1.7}$$
$$u_R \to \mathcal{U}_R^u\, u_R, \qquad d_R \to \mathcal{U}_R^d\, d_R, \qquad e_R \to \mathcal{U}_R^e\, e_R. \tag{1.8}$$

Applying the above mentioned transformations, Eq. (1.6) can be rewritten in terms of diagonal mass matrices as:

$$-\mathcal{L}_{mass} = \overline{u}_L^i m_{ij}^{u\ diag} u_R^j + \overline{d}_L^i m_{ij}^{d\ diag} d_R^j + \overline{\ell}_L^i m_{ij}^{\ell\ diag} \ell_R^j + \text{h.c.}, \tag{1.9}$$

where,

$$\begin{aligned} m^{u\ diag} = \text{Diag}\left(m_u, m_c, m_t\right) &= \mathcal{U}_L^{u\,\dagger}\, m^u\, \mathcal{U}_R^u, \\ m^{d\ diag} = \text{Diag}\left(m_d, m_s, m_b\right) &= \mathcal{U}_L^{d\,\dagger}\, m^d\, \mathcal{U}_R^d, \\ m^{\ell\ diag} = \text{Diag}\left(m_e, m_\mu, m_\tau\right) &= \mathcal{U}_L^{\ell\,\dagger}\, m^\ell\, \mathcal{U}_R^\ell, \end{aligned} \tag{1.10}$$

In the quark sector[3], applying the above transformations, the charge current (cc) interaction Lagrangian leads to interaction between the inter generational up and down type quarks via the Cabbibo-Kobayashi-Maskawa (CKM) mixing

[2]Historically, it was observed that only left handed neutrinos and right handed antineutrinos are involved in weak interaction.

[3]Since the neutrinos are massless, it is always possible to choose the charged lepton in their mass basis.

matrix

$$\begin{aligned}\mathcal{L}^{q}_{cc} &\supset -\frac{g_w}{\sqrt{2}}\,\overline{u}^{j}_{L}\,\mathcal{U}^{u*}_{L\,ij}\,\gamma^{\mu}\,\mathcal{U}^{d}_{L\,ik}\,d^{k}_{R\,ik}\,{W_{\mu}}^{+} + \text{h.c.},\\ &\supset -\frac{g_w}{\sqrt{2}}\,\overline{u}^{j}_{L}\,\left(V_{CKM}\right)_{jk}\,\gamma^{\mu}\,d^{k}_{R\,ik}\,{W_{\mu}}^{+} + \text{h.c.},\end{aligned} \tag{1.11}$$

where,

$$V_{CKM} = \mathcal{U}^{u\dagger}_{L}\,\mathcal{U}^{d}_{L}. \tag{1.12}$$

The CKM matrix is a 3×3 complex unitary matrix which describes the transformation of down type quarks from weak interaction basis to mass basis when the up type quarks are considered in the mass basis. It is fully parameterised by four independent physical parameters. In the standard parametrisation adopted by the Particle Data Group, these are expressed as three real mixing angles $(\theta'_{12}, \theta'_{23}, \theta'_{13})$ and one CP-violating phase (δ'_{CP}). The non-trivial structure of this matrix arises from the misalignment between the quark mass bases, leading to flavour-changing charged currents in weak interactions. This flavour violation has been experimentally confirmed through numerous observations of meson and baryon decay processes, with precision measurements constraining all matrix elements to the percent level or better.

As proposed by Kobayashi and Maskawa [8], a profound consequence of the CKM mechanism lies in its capacity to induce CP violation through the complex phase in the quark sector which is needed to explain the observed asymmetry in *K*- and *B*- meson systems. Notably, in the SM, the flavour-changing neutral currents (FCNCs) remain forbidden at the tree level and are generated only via higher order loop corrections which naturally suppresses their amplitudes. This is commonly known as the Glashow-Iliopoulos-Maiani (GIM) mechanism [9].

Apart from the assumed gauge symmetries, the construction of the SM exhibits several accidental global symmetries, emerging from its field content and renormalizable structure.

- The accidental symmetries include exact baryon number conservation through a global $U(1)_B$ symmetry, where each quark carries baryon number $B_q = 1/3$ while leptons have $B_\ell = 0$ (see Tab. 1.1). This symmetry is preserved at the classical level but experiences anomalous breaking in quantum processes through sphaleron transitions, though the combination $B - L$ remains conserved.

- In the lepton sector, three separate global $U(1)_{L_e} \otimes U(1)_{L_\mu} \otimes U(1)_{L_\tau}$ symmetries enforce the individual lepton flavour conservation, prohibiting neutrino oscillations and lepton flavor violating processes like $\mu \to e\gamma$, $\mu \to 3e$ decays, $\mu \to e$ conversion. These symmetries also guarantee flavour-universal couplings between leptons and gauge bosons. The collective conservation leads to an overall lepton number $U(1)_L$ symmetry, which like baryon number, is only violated by quantum anomalies in sphaleron processes.

Interestingly, violation of such symmetries have important consequences and might also hint towards the possible BSM extensions which will be discussed in the subsequent chapters.

1.2 Limitations of the SM

Despite its extremely accurate predictions, the SM consists of various observational and theoretical caveats. While the theoretical shortcomings might be accepted as an anthropogenic principle, but the observational caveats need an serious attention and warrant a theory beyond the SM.

1.2.1 Observational Shortcomings

The incompleteness of the SM becomes undeniable when confronted with three major observational phenomena which are discussed in the following.

Neutrino oscillations

The first clear evidence for the BSM physics emerged from the measured discrepancy between predicted and observed solar and atmospheric neutrino fluxes. Initial measurements by the Homestake experiment in 1968 [10] revealed a striking solar electron neutrino deficit of approximately one third solar ν_e arriving on the Earth as compared to the predicted value by the Standard Solar Model [11]. This is commonly referred to as "*Solar neutrino Problem*" which was subsequently confirmed by multiple independent experiments [10, 12–17]. This anomalous result compelled the particle physics community to consider more radical explanations. The solution came through the neutrino oscillation hypothesis, a phenomenon where neutrino flavours can converted among each others. This phenomena was first proposed by Bruno Pontecorvo [18, 19] and later formalised by Maki, Nakagawa, and Sakata [20].

In the neutrino oscillation framework, the flavour eigenstates of neutrinos are considered as a linear superposition of the propagating eigenstates (mass eigenstates),

$$|\nu_\alpha\rangle = U_{\alpha\, i}\, |\nu_i\rangle, \tag{1.13}$$

where α and i represent the indices for flavour eigenstate and mass eigenstate, respectively. U is an unitary matrix which connects both the eigenstates and characterises the neutrino flavour mixings, is called the PMNS matrix. The evolution of the flavour eigenstates in time t can be expressed as,

$$|\nu_\alpha(t)\rangle \quad = \sum U^*_{\alpha i} e^{-\ i\ E_i t} |\nu_i\rangle. \tag{1.14}$$

The oscillation probability of $\nu_\alpha \rightarrow \nu_\beta$ for the N generation of neutrinos is given by,

$$\begin{aligned} P_{\alpha\beta} &= \delta_{\alpha\beta} - 4\sum_{i<j} \mathrm{Re}(U_{\alpha i} U^*_{\beta i} U^*_{\alpha j} U_{\beta j}) \sin^2[1.27\Delta m^2_{ij} L/E] \\ &+ 2\sum_{i<j} \mathrm{Im}(U_{\alpha i} U^*_{\beta i} U^*_{\alpha j} U_{\beta j}) \sin[2(1.27\Delta m^2_{ij} L/E)], \end{aligned} \tag{1.15}$$

Table 1.2: 3σ ranges and best fit values of three neutrino oscillation parameters [21]. Here, $\Delta m^2_{\rm sol} \equiv m^2_2 - m^2_1$ and $\Delta m^2_{\rm atm} \equiv m^2_3 - m^2_1$ for NO and $m^2_3 - m^2_2$ for IO.

Parameters	Normal Ordering		Inverted Ordering	
	3σ range	Best Fit	3σ range	Best Fit
$\sin^2\theta_{12}$	$0.270 : 0.341$	0.303	$0.270 : 0.341$	0.303
θ_{12}	$31.31^\circ : 35.74^\circ$	33.41°	$31.31^\circ : 35.74^\circ$	33.41°
$\sin^2\theta_{13}$	$0.0202 : 0.0239$	0.0220	$0.0202 : 0.0239$	0.0220
θ_{13}	$8.19^\circ - 8.89^\circ$	8.54°	$8.23^\circ : 8.90^\circ$	8.57°
$\sin^2\theta_{23}$	$0.406 : 0.620$	0.572	$0.412 : 0.623$	0.578
θ_{23}	$39.6^\circ : 51.9^\circ$	49.1°	$39.9^\circ : 52.1^\circ$	49.5°
δ_{13}	197°	$108^\circ : 404^\circ$	286°	$192^\circ : 360^\circ$
$\Delta m^2_{\rm sol}/10^{-5}{\rm eV}^2$	$6.82 : 8.03$	7.41	$6.82 : 8.03$	7.41
$\Delta m^2_{\rm atm}/10^{-3}{\rm eV}^2$	$2.428 : 2.597$	2.511	$(-2.581 : -2.408)$	-2.498

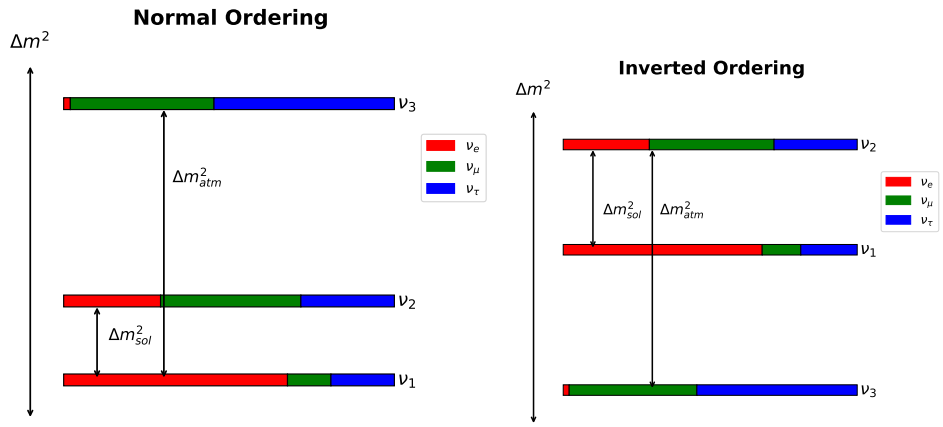

Figure 1.1: Figure representing Normal and Inverted mass ordering of neutrinos. The red, green, and blue colour represents the electron, muon and taun neutrino flavour content in each mass eigenstates.

where $i, j \in \{1, 2, \cdots N\}$, E is the energy of the neutrinos and L is the distance travelled by the neutrinos in vaccum. As per our current understanding, there are three flavours of neutrinos which can oscillate into each other. The three flavour neutrino oscillation framework is completely described by two mass-squared differences ($\Delta m^2_{\rm sol}, \Delta m^2_{\rm atm}$), three mixing angles ($\theta_{12}$, θ_{23}, θ_{13}) and a Dirac CP phase (δ_{13}). The values of these parameters are extracted by analysing the neutrino oscillation data from various solar, atmospheric, accelerator, and reactor experiments. The current best fit values and 3σ ranges of the parameters are given in Tab. 1.2.

Although the three flavour framework is well understood, there are still

some unknowns in this framework. These include:

- **Octant of θ_{23}:** From Tab. 1.2, it is realised that θ_{23} could lie in either the lower ($\theta_{23} < 45^\circ$) or higher ($\theta_{23} > 45^\circ$) octant whereas the other angles are in the first octant.

- **Mass ordering:** Observing the solar neutrinos, it is established that $\Delta m^2_{\rm sol} \equiv m_2^2 - m_1^2 > 0$, but the sign of $\Delta m^2_{\rm atm}$ is still unknown. Depending on the sign of $\Delta m^2_{\rm atm}$, the ordering of neutrino masses can be of two types [given in Fig. 1.1],

  - Normal Ordering (NO): In NO, $\Delta m^2_{\rm atm} \equiv m_3^2 - m_1^2 > 0$. The mass eigenstates are ordered in this scenario as $m_1 < m_2 < m_3$, and the mass relations can be expressed as,

$$m_{\rm lightest} = m_1, \quad m_2 = \sqrt{m_1^2 + \Delta m^2_{\rm sol}}, \quad m_3 = \sqrt{m_1^2 + \Delta m^2_{\rm atm}}. \tag{1.16}$$

  - Inverted Ordering (IO): In this case, the mass ordering is $m_3 < m_1 < m_2$ and $\Delta m^2_{\rm atm} \equiv m_3^2 - m_2^2 < 0$. In this ordering, the mass relations are written as[4],

$$m_{\rm lightest} = m_3, \quad m_2 = \sqrt{m_3^2 + \Delta m^2_{\rm atm}}, \quad m_1 = \sqrt{m_3^2 + \Delta m^2_{\rm atm} - \Delta m^2_{\rm sol}}. \tag{1.17}$$

    Apart from NO and IO, there might be a scenario where $m_1 \approx m_2 \approx m_3$. This scenario is generally referred to as quasi degenerate (QD) spectrum. In this scenario, the value of the lightest mass is greater than $\sqrt{\Delta m^2_{\rm atm}}$.

- Precise value of δ_{13} : It is seen from Tab. 1.2 that the current global fits from the oscillation experiments does not provide precise value for the Dirac CP phase (δ_{13}) in the leptonic sector. Precise value of δ_{13} would be important to understand the amount of CP violation in the leptonic

[4] It is to be noted that, in Eq. 1.17, $\Delta m^2_{\rm atm}$ represent only the magnitude of the mass-squared difference and the sign is properly absorbed in the relation.

which have implications in generating the matter-antimatter asymmetry in the universe.

Neutrino oscillation experiments are also not able to provide information about the following questions:

- **Dirac vs Majorana:** As neutrinos are the only neutral fermions in the SM, it can be either Dirac or Majorana particles. If the neutrinos are distinct from their CP conjugate states, they are called Dirac particles. In contrast, if neutrinos are their own antiparticles, they are considered as Majorana particles. In the Majorana scenario, the PMNS matrix is extended by two Majorana phases which remain unmeasured in the oscillation experiments.
- **Absolute mass scale:** Oscillation experiments only measure Δm^2_{ij}, leaving no clue about the absolute mass scale of the neutrinos. This implies that the lightest neutrino mass (m_{lightest}) remains unconstrained in the oscillation experiments .

Within the SM framework, the absence of right-handed neutrino fields prevents conventional Dirac type mass generation via the Higgs mechanism. The Majorana mass term using the left handed lepton doublets is also forbidden by the SM gauge symmetry. Therefore, neutrinos are strictly mass less in the SM. Extension of the SM is required to account for the neutrino mass, regardless of whether it is Dirac or Majorana. The Majorana mass term would violate the lepton number by two units leading to interesting phenomenological consequences that will be discussed in the subsequent sections.

Matter-Antimatter Asymmetry

Astrophysical and cosmological observations provide compelling evidence that the Universe exhibits a fundamental matter-antimatter asymmetry. This asymmetry is quantitatively described by the baryon asymmetry parameter

(BAU):

$$Y_{\Delta B} \equiv \frac{n_b - n_{\bar{b}}}{s} = \frac{n_B}{s}, \tag{1.18}$$

where n_b, $n_{\bar{b}}$, represent the number densities of baryons and anti-baryons respectively and s denotes the co-moving entropy density. Remarkably, two independent methods - Big Bang Nucleosynthesis (BBN) predictions of light element abundances and precision measurements of the Cosmic Microwave Background (CMB) power spectrum converge on the same value of $Y_{\Delta B} = (8.75 \pm 0.23) \times 10^{-11}$, establishing this as one of the most robust parameters in cosmology [22, 23].

A primordial matter excess cannot explain this asymmetry, as cosmological inflation would have diluted any initial imbalance to negligible levels. The required initial condition - approximately one extra quark per billion quark-antiquark pairs - would represent an implausible fine-tuning. Instead, the leading theoretical framework posits that the BAU emerged dynamically through baryogenesis. Sakharov's seminal 1967 work [24] established three necessary conditions for this process:

1. Baryon number violation.
2. C and CP symmetry violation.
3. Departure from the thermal equilibrium.

While the SM technically satisfies all three conditions [25], the CP violation is insufficient by several orders of magnitude, and the Higgs boson's mass precludes a sufficiently strong electroweak phase transition to maintain the necessary non-equilibrium conditions [26, 27]. These shortcomings necessitate physics beyond the Standard Model with (a) enhanced CP violation sources (b) stronger first-order phase transitions (c) additional out of equilibrium processes.

Intriguingly, neutrino mass models provide a promising pathway to generate excess baryons through a process called leptogenesis [28]. In leptogenesis, out of equilibrium decay of heavy degrees of freedom generates an asymme-

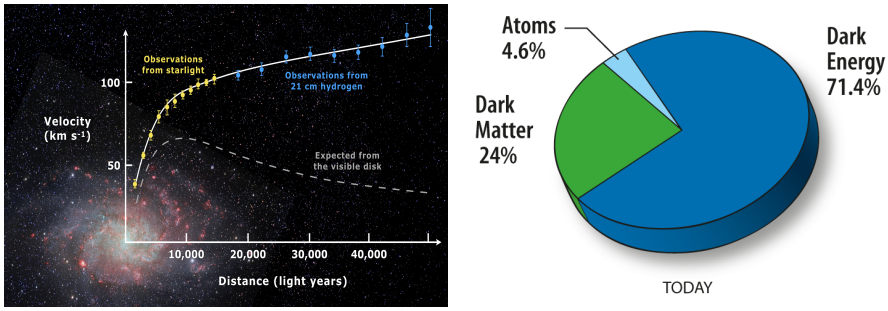

Figure 1.2: **left:** Rotation curve of the Messier 33 spiral galaxy from the galaxy center (yellow and blue points), and theoretical prediction from the distribution of visible matter (gray dashed line). courtesy: wikipedia. **right:** Total energy budget of the universe. Courtesy: https://wmap.gsfc.nasa.gov/universe/uni-matter.html

try in the leptonic sector that could then be converted to the observed baryon asymmetry through electroweak sphaleron processes, offering an elegant solution to one of the most profound puzzles in cosmology.

Dark Matter and Dark Energy

Astronomical observations across multiple wavelengths and cosmological surveys have provided overwhelming evidence that the dominant matter component of the Universe is non-luminous dark matter (DM). This conclusion stems from several independent observational evidences which include: anomalous rotation curves of spiral galaxies [29], velocity dispersions in galaxy clusters, gravitational lensing effects [30] (both strong and weak) and precise measurements of CMB anisotropies [31].

The most recent Planck satellite data, combined with baryon acoustic oscillation measurements, estimate the total energy density of the universe as [31]:

$$\Omega_{\rm b} = 0.0498 \pm 0.0001\,, \quad \Omega_{\rm CDM} = 0.2673 \pm 0.0026\,, \quad \Omega_{\Lambda} = 0.6847 \pm 0.0072, \tag{1.19}$$

where Ω_b, $\Omega_{\rm CDM}$ and Ω_{Λ} correspond to normal baryonic matter, cold dark matter and dark energy densities respectively. The values indicates that ordinary baryonic matter constitutes 5% of all the energy budget whereas dark matter and dark energy accounts for approximately 95%.

Despite this observational evidence, the fundamental nature of DM remains elusive and SM contains no particle candidate that simultaneously satisfies all observational characteristics (stability, lack of electromagnetic interactions, and appropriate abundance) of the DM. This has motivated extensive theoretical exploration of possible extensions to the Standard Model that could incorporate suitable DM candidates, ranging from weakly interacting massive particles (WIMPs) to axions and sterile neutrinos. The identification of the particle nature of DM remains one of the most pressing challenges in modern particle astrophysics.

These empirical shortcomings demonstrate that while the SM provides an excellent description of known particle interactions, it necessarily represents only part of a more fundamental theory of nature.

1.2.2 Flavour Anomalies

Precision measurements of low-energy flavour observables have revealed a growing number of experimental discrepancies with the SM predictions. These anomalies involve violations of lepton flavour universality (LFU) in decays with leptonic final states. While some systematic uncertainties—particularly in hadronic matrix elements—require further refinement, the collective pattern of deviations suggests potential NP in the lepton sector. Below we discuss the most significant anomalies:

1. **Anomalous Magnetic Moments** The magnetic dipole moment of a charged particle characterises the effect of a magnetic field on the charge particle. For a particle with Spin ($\boldsymbol{S}$), the magnetic moment is given as

$$\boldsymbol{\mu_\ell} \;=\; g_\ell \frac{e}{2m_\ell} \boldsymbol{S}, \tag{1.20}$$

where g_ℓ is called the "*Landé g*" factor, and denotes the "*coupling strength*" of the lepton to a magnetic field. From the Dirac equation, Landé g factor comes as $g_\ell = 2$ at the leading order and the quantum corrections breaks

this equality.

In QED, the interaction Lagrangian of a charged lepton with an external photon (quanta of EM field) can be described as

$$-\mathcal{L}_{int} \;=\; e\,\overline{\ell}\,\Gamma^{\mu}\,\ell\,A_{\mu}, \tag{1.21}$$

where

$$\begin{aligned}\Gamma^{\mu} \;=\; \Big[&\left\{F_1^V\left(q^2\right)+F_1^A\left(q^2\right)\gamma_5\right\}\gamma^{\mu}+\tfrac{i}{2m_\ell}\sigma^{\mu\nu}\,q_\nu\left\{F_2^V\left(q^2\right)+F_2^A\left(q^2\right)\gamma_5\right\}\\ &+q^{\mu}\left\{F_3^V\left(q^2\right)+F_3^A\left(q^2\right)\gamma_5\right\}+F_4^A\left(q^2\right)\gamma_5\,q^{\mu}\,\not{q}\Big].\end{aligned} \tag{1.22}$$

Using,

$$\overline{\ell}\,\Gamma^{\mu}\,\ell\,q_{\mu}=0 \qquad \text{(Ward Identity)}\,, \tag{1.23}$$

$$\overline{\ell}\,\gamma_5\,\not{q}\,\ell=2m_\ell\,\overline{\ell}\,\gamma_5\,\ell \tag{1.24}$$

it is very easy to rewrite Eq. (1.22) as,

$$\begin{aligned}\Gamma^{\mu} \;=\; &\Big[\gamma^{\mu}F_1^V\left(q^2\right)+\frac{i}{2m_\ell}\sigma^{\mu\nu}q_\nu\left\{F_2^V\left(q^2\right)+F_2^A\left(q^2\right)\gamma_5\right\}\\ &+F_4^A\left(q^2\right)\gamma_5\left(2m_\ell\gamma^{\mu}-q^{\mu}\,q^2\right)\Big].\end{aligned} \tag{1.25}$$

Here q is the photon's momentum and $F_{1,2,3,4}$ are the electromagnetic form factors. For the general Lagrangian, given in Eq. (1.21), the Landé g factor is given as

$$g_\ell \;=\; 2\Big[F_1(0)+F_2(0)\Big]. \tag{1.26}$$

At the leading order (tree level),

$$F_1(0) \;=\; 1\,, \quad F_{2,3,4}(0)=0. \tag{1.27}$$

Higher order correction to $F_1(0)$ modify the coupling to photon and give the energy scale dependence of the electric charge e. Therefore, the correction to g_ℓ can come only from higher order correction to $F_2(0)$. The

other form factor $F_3(0)$ give contribution to electric dipole moment (d_ℓ) and $F_4(0)$ contribute the "*anapole moment*" which is relevant for the short distance virtual photon exchanges.

The anomalous magnetic moment defined as,

$$a_\ell \;=\; \frac{g_\ell - 2}{2} = F_2(0), \tag{1.28}$$

which is commonly referred to as $(g-2)_\ell$. In the SM, the next to leading order (NLO) QED correction was calculated by Swinger in 1948 [32], resulting in $a_\ell = \alpha_e/2\pi$, where $\alpha_e = e^2/4\pi$ is the electro-magnetic fine structure constant.

The anomalous magnetic moment of the muon stands as a benchmark precision observable in particle physics, with its theoretical prediction requiring the calculation of quantum corrections across multiple sectors. Generally, the quantum corrections to a_ℓ can be divided into three categories. Out of these, the dominant QED contributions, dependent only on the muon mass and fine-structure constant α_e, have been computed up to 5-loop accuracy. Next, electroweak corrections are known up to 2-loop precision, while the third correction comes from hadronic effects. These effects are the largest sources of uncertainty and can be separated into mainly two classes: (i) hadronic vacuum polarisation (HVP), and (ii) hadronic light-by-light (HLbL) scattering. In the SM, the prediction of the anomalous magnetic moment is defined as

$$a_\ell^{\rm SM} = a_\ell^{\rm tree} + a_\ell^{\rm QED} + a_\ell^{\rm Weak} + a_\ell^{\rm strong}, \quad \text{with} \quad a_\ell^{\rm strong} = a_\ell^{\rm HVP} + a_\ell^{\rm HLbL}, \tag{1.29}$$

where the error is dominated by the leading-order HVP calculation. The deficit between the experimental value with the SM prediction is defined as

$$\Delta a_\ell \;=\; a_\ell^{\rm exp} - a_\ell^{\rm SM}. \tag{1.30}$$

- **Muon** $(g-2)_\mu$: For muon $(g-2)$, the old Brookhaven National Laboratory (BNL) experiment reported a 3.7σ discrepancy with re-

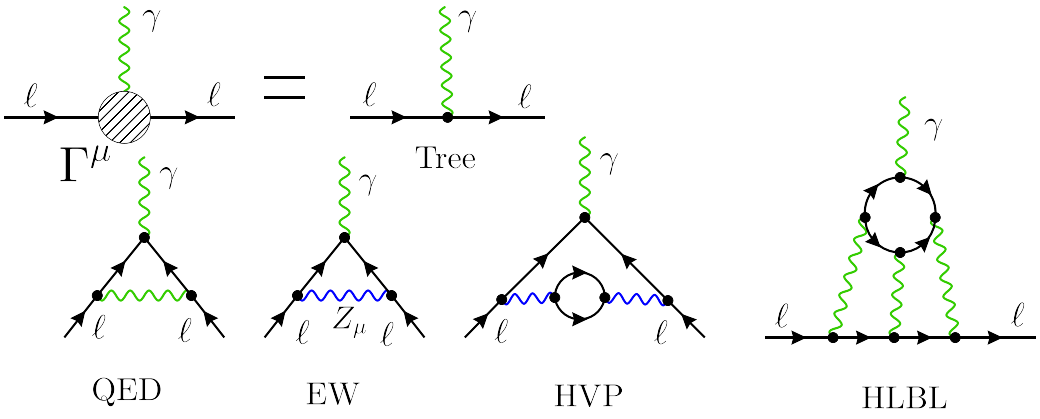

Figure 1.3: Feynman diagrams of the SM corrections to the muon magnetic moment. In the second row, from left to right, it shows the first order QED and weak correction, hadronic vacuum-polarisation correction and the light-by-light hadronic correction.

spect to the SM prediction [33].The BNL result was recently confirmed by the Fermilab Muon $g-2$ collaboration [34], which increased the discrepancy to 5σ level, if one uses the 2020 world average of the SM prediction [35]. However, the BMW lattice result [36] disagrees with the world average [35]. Other lattice calculations now seem to agree with the BMW result at least in the "*intermediate distance regime*" [37] and in this thesis, we have used the BMW result, which gives a 1.5σ deviation from the experimental result: $\Delta a_\mu = (1.07 \pm 0.70) \times 10^{-9}$ [38].

However, recently the *Muon* $g-2$ *Theory Initiative* has updated the SM prediction of a_μ and quoted the value of $\Delta a_\mu = (0.38 \pm 0.63) \times 10^{-9}$ which implies that there is no such tension between the experimental value and the SM prediction [39].

- **Electron** $(g-2)_e$: The situation for electron $(g-2)$ is no better. Although the experimental value of a_e has been measured very precisely [40], the SM prediction [41] relies on the measurement of the fine-structure constant, and currently there is $> 5\sigma$ discrepancy between the results derived using two different measurements based on Rb [42] and Cs [43] atoms. In this thesis both Rb and Cs results are used for analysis: $\Delta a_e(\text{Rb}) = (4.4 \pm 3.0) \times 10^{-13}$ [42] and $\Delta a_e(\text{Cs}) = (-8.8 \pm 3.6) \times 10^{-13}$ [43].

2. **Flavour Changing Charge Current B-Decays:** A number of anomalous measurements have been surfaced with the flavour changing charged current (FCCC) $b \to c\ell\nu_\ell$ decays. In the SM, this transition occurs at the tree level via W_μ boson and can be used to test the universality of the coupling of the leptons to the W_μ gauge bosons. Deviations with respect to the SM can be defined in terms of R_D, R_D^* ratios which is defined as

$$R_{D^{(*)}} = \frac{Br\left(B \to D^{(*)}\tau\overline{\nu}_\tau\right)}{Br\left(B \to D^{(*)}\ell\overline{\nu}_\ell\right)}, \tag{1.31}$$

with $\ell = \mu, e$. The ratio is defined to cancel the uncertainty in the hadronic matrix element. Although several experiments like BaBar [44], Belle I and II [45, 46] and LHCb have measured these ratios, only LHCb has published their result [47]. The average of all these results have been calculated by Heavy Flavour Averaging Group (HFLAV) and compared with the precise result of the SM. According to the most recent update, the world average of the experimental data is [48]

$$R_D = 0.342 \pm 0.026\,, \quad R_{D^*} = 0.287 \pm 0.012, \tag{1.32}$$

and the current SM prediction is [48]

$$R_D^{\text{SM}} = 0.298 \pm 0.004\,, \quad R_{D^*}^{\text{SM}} = 0.254 \pm 0.005\,. \tag{1.33}$$

Therefore, the current result is 3.3σ away from the SM prediction.

3. $B^+ \to K^+\nu\nu$ **Transitions:** Another observable that has taken some attention lately, is related to the flavour changing neutral current (FCNC) related to $b \to s\nu\nu$ transition in $B^+ \to K^+\nu\nu$ decay. In the SM, this decay can happen through either penguin, or box or tree level double-charged current diagram. The SM prediction of this process is [49]

$$Br\left(B^+ \to K^+\nu\nu\right)\Big|_{SM} = (5.58 \pm 0.37) \times 10^{-6} \tag{1.34}$$

Belle-II recently reported the first observation of $B^+ \to K^+\nu\nu$ de-

cay [50]. Using the weighted average of BaBar, Belle and Belle-II data, ref. [49] quoted an experimental value for Branching ratio is $Br\left(B^+ \to K^+ \nu\nu\right)\Big|_{exp} = (1.3 \pm 0.4) \times 10^{-5}$. Therefore the observed branching ratio is 2.7σ above the standard model prediction.

1.2.3 Theoretical Shortcomings

The SM contains a total of 19 free parameters which include 3 gauge couplings (g', g_w, g_s) corresponding to the $U(1)_\mathcal{Y}$, $SU(2)_L$ and $SU(3)_c$ symmetry groups, 2 parameters characterizing the Higgs potential (v and the quartic coupling λ), 10 parameters in the quark sector (6 quark masses, 3 CKM mixing angles, and 1 CP-violating phase), and 3 charged lepton masses and θ_{QCD} which parametrises the amount of CP violation in strong interactions. These parameters are not calculable in the SM, rather fixed by the experiment. Such models with large number of arbitrary free parameters are theoretically ugly. Apart from this, other theoretical shortcomings include:

1. **Quantum theory of gravity :** As mentioned, the SM describes three fundamental forces of nature at short distance scales, naturally it excludes gravity which described classically by Einstein's General Relativity at macroscopic scales but approximately 10^{39} times weaker than the electromagnetic force at atomic scales. This large disparity allows particle physicists to safely neglect the gravitational contributions when studying elementary processes. However, things change near the Planck scale ($\Lambda_{pl} \sim 10^{19}$ GeV, corresponding to a distance of $r \sim 10^{-34}$ m), where the quantum gravitational effects become significant. While the SM was not designed as a fundamental theory of all interactions, the unavoidable convergence of quantum mechanics and general relativity at these extreme energies necessitates a more complete framework. The search for a consistent quantum theory of gravity that reconciles the quantum field theoretical structure of the SM with the geometric description of spacetime remains one of the most profound challenges in theoretical physics. String theory and loop quantum gravity representing two prominent ap-

proaches to this unification problem.

2. **Strong CP problem :** The Quantum chromo dynamics (QCD) sector of the SM introduces an additional fundamental parameter, θ_{QCD}, which represents a potential source of CP violation in the strong interaction sector. This parameter appears in the CP-odd topological term $\mathcal{L}_\theta = \theta_{QCD} \frac{g_s^2}{32\pi^2} G^a_{\mu\nu} \tilde{G}^{\mu\nu}_a$, where $G^a_{\mu\nu}$ denotes the QCD field strength tensor and $\tilde{G}^{\mu\nu}_a = \frac{1}{2}\epsilon_{\mu\nu\rho\sigma} G^{\rho\sigma}$ is its dual. This term is often omitted from the classical Lagrangian due to its total derivative nature, but it has a non-trivial physical consequences in the quantum theory when quark masses are non-zero. This term induces an electric dipole moment (EDM) of neutron and the experimental constraints on the neutron EDM, $|d_n| < 1.8 \times 10^{-26}$ e-cm (90% CL), impose an unnatural stringent limit on the strong CP phase: $\left|\theta_{QCD}\right| \lesssim 10^{-10}$. This presents a profound theoretical puzzle, as the vanishing θ_{QCD} does not correspond to any enhanced symmetry of the theory (CP remains broken by the weak sector even when $\theta_{QCD} = 0$). Following 't Hooft's naturalness criterion [51], such extreme fine-tuning of a dimensionless parameter is technically unnatural, suggesting either an unknown symmetry mechanism (such as the Peccei-Quinn mechanism leading to axion solutions [52–58]) or a deeper theoretical principle remains to be discovered. The strong CP problem thus stands as one of the most significant open questions in particle physics, connecting fundamental symmetries, non-perturbative QCD effects, and potential NP beyond the SM.

3. **Hierarchy problem :** The interactions in the SM are characterised by two fundamental energy scales: the QCD confinement scale $\Lambda_{QCD} \sim \mathcal{O}$ (100) MeV and the electroweak scale $\Lambda_{EW} \sim \mathcal{O}(100)$ GeV. In principle, the SM symmetry could remain valid up to the Planck scale (Λ_{Pl}), where quantum gravitational effects are needed to be included. This large energy gap of about seventeen orders of magnitude poses a theoretical challenge known as the "*desert problem*". More importantly, without a protective symmetry mechanism, the SM scale (Λ_{EW}) becomes highly sensitive to higher scales through large quantum corrections and there is no mecha-

nism in the SM by which it can be stabilised.

For instance, the masses of the SM fermions and gauge bosons are protected by the chiral symmetry and gauge symmetry respectively. However, the Higgs mass term $H^\dagger H$ are invariant under gauge and global symmetries of the SM and suffers from severe quadratic sensitivity to ultraviolet (UV) physics. At leading order, the Higgs mass squared M_H^2 equals the bare parameter μ^2 in the potential. However, considering one-loop corrections, it is found that [59, 60]

$$\Delta M_H^2\big|_{\text{1-loop}} = \frac{\Lambda_{\text{UV}}^2}{16\pi^2}\left[6\lambda + \frac{9}{4}g_w^2 + \frac{3}{4}g'^2 - 6y_t^2 + \cdots\right], \tag{1.35}$$

where Λ_{UV} represents the UV cut-off scale up to which the SM is valid. The presence of this quadratic divergence signals that the Higgs mass is sensitive to UV physics beyond the SM. More specifically, the quadratic divergence effectively represents the finite threshold corrections [59]. Therefore, if one takes $\Lambda_{\text{UV}} \sim M_{Pl}$, it implies corrections 32 orders of magnitude larger compared to the physical Higgs mass scale ($M_H \sim 125$ GeV). Thus, the observed Higgs mass requires an fine cancellation between the bare Higgs mass and the radiative corrections at a level of fine-tuning that is considered unnatural. Furthermore, such cancellation would need to occur at every order in the perturbation theory, implying that the entire mass spectrum of the SM would be sensitive to the cutoff scale [61].

4. **Flavour puzzle :** The SM fermions are organised into three generations without any theoretical justification. This three generation family structure is manifested via the Yukawa coupling matrices, Y_f in flavour space, which parameterise both fermion masses and mixing patterns. The observed fermion masses shows a large hierarchy, ranging from the electron ($\sim$ 0.5 MeV) to the top quark ($\sim$ 100 GeV), with no underlying principle that can explain this disparity. Moreover, the cancellation of the gauge anomalies occur independently within each generation, implying the mathematical consistency of the SM with any number of fermion fam-

ilies. All these suggest that the observed three-generation structure may be an accidental feature rather than a fundamental requirement of the theory. Thus, the origin of fermion families, their specific number, and peculiar patterns of their masses and mixings remain one of the most intriguing unanswered questions in particle physics. They may be potentially pointing towards new symmetries or dynamics beyond the SM framework. Recently in Ref [62–65], the authors have tried to explain the fermion mass hierarchies by employing various gauge symmetries which establish that the NP scale should be at least higher than 10^3 TeV to incorporate the hierarchies without affecting other low-energy observables.

While the theoretical limitations challenge the foundational principles of the SM, they do not diminish its remarkable phenomenological success. The SM still remains an exceptionally effective framework for describing particle interactions, providing a self-consistent mathematical parametrisation of observed phenomena. From a purely empirical perspective, one might adopt a view that Nature simply "*is as it is*" with its unexplained features.

1.3 Going beyond the SM

Motivated by the shortcomings of the SM, a large number of extensions are proposed. In general, there are two approaches adopted to go beyond the SM :

1. **Extending the particle content:** In this approach, the SM is extended with new particles which become useful in addressing the SM shortcomings. Among these extensions, seesaw models are the most popular having extended the SM with fermion singlets, scalar triplets, and fermion triplets etc.

2. **Extending the gauge group:** In this approach, the symmetry group of the SM is enlarged leading to frameworks such as left-right symmetric

models ($SU(3)_c \times SU(2)_L \times SU(2)_R \times U(1)_{B-L}$) and grand unified theories (GUTs) such as $SU(5)$, $SO(10)$, E_6 etc. Apart from addressing the SM anomalies, GUT models also provide an attractive framework for the unified interactions.

All the NP effects appear in energy scales higher than the electroweak scale, but their effects can be taken into account by adding higher dimensional and non-renormalisable operators in the SM Lagrangian. This procedure is commonly known as the "*Effective Field Theory*" approach.

1.3.1 Effective field theory

As discussed above, the shortcomings of the SM has fuelled the search for NP in terms of new particles between EW scale to Planck scale. However, despite tireless efforts, there is no unique UV complete theory which can successfully explain all low-energy phenomena. Yet, we can parametrise the effects of NP with the help of EFT framework which has been a cornerstone of particle physics as it provides a powerful framework to make predictions without requiring complete knowledge of the underlying high-energy theories. If we accept the presence of NP at a certain energy scale between EW scale and Planck scale, the SM Lagrangian can be extended via higher dimensional non-renormalisable operators composed of the SM fields. Schematically, the Lagrangian is written as,

$$\mathcal{L}_{\text{eff}} \;=\; \mathcal{L}_{\text{SM}} + \sum_{n\geq 1} \frac{C_{ij}}{\Lambda_{\text{NP}}^{n}} \mathcal{O}_{ij}^{d=4+n} \tag{1.36}$$

where $\mathcal{O}_{ij}^{d=4+n}$ represent gauge and Lorentz-invariant effective operators of mass dimension $d > 4$ composed of SM fields, and C_{ij} are the corresponding dimensionless Wilson coefficients. The inverse powers of Λ_{NP} provide the suppression for these non-renormalizable operators, with the exponent $n = d - 4$ ensuring proper dimensionality. This EFT is referred to as SM Effective Field Theory (SMEFT). In this formulation, once the new heavy degrees of freedom from the UV complete theory is "*integrated out*", all the NP effects are

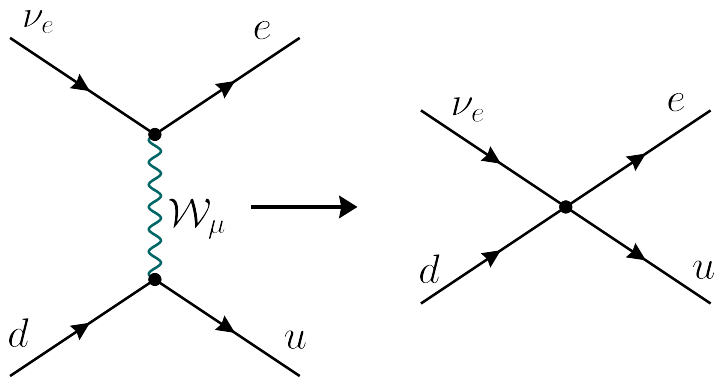

Figure 1.4: Comparison of β decay descriptions in the Standard Model and Fermi theory. **(Left Panel:)** Elementary weak interaction process $\nu_e + d \rightarrow e^- + u$, mediated by a virtual W_μ boson. **(Right Panel:)** Low-energy effective four-fermion interaction in Fermi theory, valid for momentum transfers $q^2 << M_W^2$, where M_W is the W_μ boson mass.

encoded in the Wilson coefficients. This can also be understood as follows: if we work at some typical momentum scale, p which is much smaller than the NP scale ($\Lambda_{\rm NP}$), we can expand the fundamental amplitudes in powers of $p^2/\Lambda_{\rm NP}^2$. In doing so, the heavy propagators are effectively removed from the amplitude calculations, reducing to effective contact interactions.

A canonical example of the EFT is the derivation of Fermi theory of β decay as a low energy limit of the full electroweak theory. In Fig. 1.4, we have presented the Feynman diagram of nuclear β decay both in full theory and Fermi theory. By comparing the full theory and effective theory, one obtains the Fermi constant G_F in terms of fundamental parameters: $G_F/\sqrt{2} = g_w^2/(8M_W^2)$, where g_w is the weak coupling. Hence, this procedure effectively shows that the EFT provides a simplified description valid at energies $p << M_W$, by integrating out the heavy W-boson with all W-boson effects encoded in G_F.

Since, the Wilson coefficients are serving as effective coupling constants in the EFT framework, they are subject to quantum corrections and consequently evolve under renormalisation group (RG) flow, analogous to gauge and Yukawa couplings in the renormalizable SM. The standard procedure for studying NP effects involves first computing the Wilson coefficients at the NP scale by matching the full UV theory to the effective Lagrangian. These

coefficients are then evolved down to the observable scale (e.g., $\mu_{\text{obs}} \sim M_W$) using RG equations, during which the effect of operator mixing can also be important. If the observable scale lies below M_W, additional matching to the low energy EFT (LEFT) is required, where the Higgs, weak gauge bosons, and top quark are integrated out. Crucially, the matching conditions between the SMEFT and LEFT, and the anomalous dimension matrices governing their RG evolutions have been computed up to next-to-leading order (NLO) precision in Refs. [66–71], ensuring robust theoretical control over these transitions. This systematic approach enables consistent connections between high-scale UV completions and low-energy observables, even in the presence of non-trivial operator mixing or threshold effects.

1.3.2 Implication of BSM in Astrophysics

In general, the SM extensions introduce particles with different masses and different interaction strengths. Typically, these BSM models are probed via two approaches: (i) directly producing the new particles in high energy colliders such as LHC (ii) indirect detection via precession measurements of low-energy phenomena. When the new particles have feeble interactions with the SM particles, detecting them in any laboratory experiments becomes challenging. In such cases, the extreme conditions in cosmological and astrophysical environments offer a natural laboratory to test the BSM frameworks. For instance, in many BSM theories, a fifth force can be generated by the exchange of new force carriers. The strength of these forces must be weak otherwise could have detected by now and the range of the fifth force can range from millimetre scale to astronomical scale. The range is inversely proportional to the mass of the force carrier particle, so smaller masses mediate long range interactions. For sufficiently light mediator (range $\simeq \mathcal{O}$(astronomical unit)), the new force can modify the gravitational potential between the large astrophysical objects and can have effect on the trajectory of light and trajectory of planets which are measured very precisely up to an accuracy of 10^{-5}. Therefore, by analysing

these effects, constraints on the fifth-force couplings can be derived.

1.4 Thesis Overview

This thesis examines several SM extensions, analysing their implications for various particle physics experiments, cosmological and astrophysical observations to constrain their parameter spaces. The study combines multiple probes to test these NP scenarios systematically.

The thesis is organised as follows:

In chapter 2, we have reviewed various models that naturally incorporate the small neutrino masses. Among these, special focus is given to the fundamental aspects of seesaw mechanisms and radiative mass generation scenarios. This chapter also outlines the implication of these mass models in terms of neutrinoless double beta decay ($0\nu\beta\beta$) and lepton flavor violating decays (LFVs). As the oscillation experiments provide no information on the absolute mass scale of the neutrinos, we give an overview of the "*mass observables*" which include: the sum of the light neutrino masses (Σ) from cosmology, the effective mass of the electron neutrino from nuclear β decay (m_β), and the effective Majorana mass (m_{ee}) from $0\nu\beta\beta$, and discuss their potential to provide insight into the neutrino mass spectra.

In chapter 3, the implication of a light sterile neutrino for the mass observables is investigated. The inclusion of a new sterile state in the three flavour framework leads to four distinct mass spectra, classified according to the magnitude and sign of its mass-squared difference relative to the active neutrino states. The presence of a sterile state can affect the thermal history of the early universe. We discuss the effect of sterile neutrino on the sum of neutrino masses which is tightly from cosmological probes e.g. cosmic microwave background (CMB) anisotropy and large scale structure (LSS). The presence of an extra light neutrino can also affect the spectrum of electrons emitted from the nuclear β decay. We study the effect of mass-spectra on m_β and use the current

experimental limit of *KATRIN* and future sensitivity of *Project 8*, to validate or discard them. We also studied the $0\nu\beta\beta$ in the presence of a sterile neutrino. We have analysed m_{ee} for all mass spectra and discuss their implications on current and future experiments. The correlations between the different mass observables are also analysed in detail in this chapter.

In chapter 4, we consider a BSM framework where the SM is augmented with a pair of scalar leptoquarks (LQs) i.e. $S_1\,(3,1,1/3)$ and $\tilde{R}_2\,(3,2,1/6)$. The LQs are motivated as a possible explanation for the observation of the lepton flavour universality violations (LFUV). Since LQs simultaneously couple to both quark and lepton fields, they inherently carry both baryon and lepton numbers. We discuss that if the LQs mix with each other via the SM Higgs, it introduces lepton number violation, which also enables the generation of Majorana-type neutrino masses through one-loop radiative corrections. As the violation of the lepton number provides a natural theoretical basis for investigating $0\nu\beta\beta$, we discuss the contributions of the LQ-mediated diagrams to the $0\nu\beta\beta$ amplitude. We also discuss the constraints coming from low-energy flavour observables like charge lepton flavour violating (cLFV) decays ($\mu \to e$ conversion, $\ell_\alpha \to \ell_\beta\gamma$, $\ell_\alpha \to \ell_\beta\ell_\gamma\ell_\delta$), neutrino magnetic moment and rare meson decays ($B \to D\ell\overline{\nu}_\ell$, $B \to K\ell^+\ell^-$) decays. We then show that this framework inherits tension between the muon and electron's magnetic moments. Although the LQs are proposed to explain the anomalies in LFU ratios ($R_D, R_{D^*}, R_K, R_{K^*}$), they remain phenomenologically viable even in scenarios where LFU is preserved.

In chapter 5, we have extended our previous work by considering the LQs originated from grand unified theories, especially $SU(5)$ GUT which is a compelling and elegant framework for unifying the fundamental forces of the SM. Followed by a general description of the $SU(5)$ model, we discuss the effect of $SU(5)$ scalars on the $0\nu\beta\beta$ process. It is found that the effect is extremely small coming out as a consequence of proton decay. We then construct a particular $SU(5) \otimes \mathcal{Z}_3$ scenario where the proton decay constraint can be alleviated. In this setup, the fermion masses arise from considering the tree and one-loop

corrections of the Yukawa couplings. This poses an important constraint on the framework. It is shown that a significant enhancement in the $0\nu\beta\beta$ rate can be achieved by extending the scalar sector with an additional scalar $SU(5)$ irrep ($\widehat{\mathbf{15}}_{\mathrm{H}}$), with $\mathcal{Z}_3 = 1$ charge. By optimizing Yukawa couplings and minimizing LQ masses within experimental limits, a conservative constraint on the scalar mass is derived. This study demonstrates that while minimal $SU(5)$ frameworks face severe phenomenological constraints, extended symmetry structures with carefully chosen scalar sectors can enhance the $0\nu\beta\beta$ rate without conflicting with proton stability and satisfying fermion mass spectra.

In chapter 6, we consider astrophysical observations as a probe to the BSM physics. We have explored a scenario where ultralight axion-like-particles (ALPs) can mediate a long-range monopole-dipole force if they couple to nucleons as scalars and electrons as pseudo-scalars. This force can theoretically act between the Earth and the Sun if the Earth is considered as polarised object. The presence of the monopole-dipole force can induce an extra potential between the Earth and the Sun system and thereby can affect the perihelion precession of the Earth, gravitational light bending and the Shapiro time delay measurements. But the interaction strength of the monopole-dipole force is limited by the measurement uncertainties of the mentioned observables. In this chapter, we present elaborated calculations of the perihelion shift, light bending and Shapiro time delay and after the calculation, it is found that the perihelion precession provides the stringent limit on the ALPs parameter space.

In chapter 7, the thesis is concluded by summarising the key results and outlining some directions for future research.

2

Neutrino mass models and mass observables

Neutrino oscillation phenomena provided the first evidence of BSM physics. It establishes that the neutrinos change their flavour during propagation, and this flavour conversion requires non-zero masses and mixings of neutrinos [18–20]. Additionally, neutrino oscillations indicate the violation of lepton flavour symmetry and consequently, SM extensions that accommodate the neutrino masses and mixings, also allow lepton flavour violating decays like $\mu \to e$ conversion, $\ell_\alpha \to \ell_\beta \gamma$, $\ell_\alpha \to \ell_\beta \ell_\gamma \ell_\delta$ decays etc. As discussed in section 1.2.1 that despite the rigorous experimental efforts in determining the oscillation parameters, there are some open questions in the context of the three flavour neutrino oscillation framework. In addition, neutrino oscillation probabilities depend on the mass-squared differences of the neutrinos; they provide no information about the absolute mass scale of neutrinos. Another intriguing question that is not answered by neutrino oscillation phenomena is related to the nature of the neutrinos. Being the only neutral fermion in the SM, the neutrinos can be described as either a Dirac or Majorana particles.

This chapter mainly focuses on the Majorana mass generation of the neutrinos and discusses models like the seesaw paradigm or radiative mass mechanism where they can be naturally generated. In the end, we briefly discuss the mass related observables that can probe the absolute mass scale of the neutrinos.

The rest of the chapter is as follows: Section 2.1 discusses the Dirac and Majorana masses of the neutrinos and subsequently, we have discussed about

the Weinberg operator in section 2.2. Section 2.3 and section 2.4 lists out some of the tree level and one-loop UV completions of Weinberg operator, respectively. In section 2.5, we discuss the neutrino mass generation by higher dimensional operator whereas, section 2.6 discusses neutrino mass generation in GUT framework. At last, in section 2.7, we list out some of the implications of neutrino masses.

2.1 Dirac vs Majorana

The neutrinos in the SM are represented as Weyl fermions i.e. two component spinors. Since, the SM respect the CPT (charge conjugation, Parity and Time reversal) symmetry, then it must contain the CPT conjugate state of the neutrino field. For a left chiral[1] neutrino field with momentum p and helicity $\pm\frac{1}{2}$, the CPT conjugate state can be describes as,

$$CPT\ |\nu\,(\boldsymbol{p}, \pm 1/2)\rangle_L \;\; = \;\; |\overline{\nu}\,(\boldsymbol{p}, \mp 1/2)\rangle_R\ , \tag{2.1}$$

where $|\overline{\nu}\,(\boldsymbol{p}, \mp 1/2)\rangle_R$ describes an right chiral antineutrino with same momentum with opposite helicity. Neutrinos are neutral particles, but they carry lepton number : ν and $\overline{\nu}$ have opposite lepton number. If the lepton number symmetry is exact, then the neutrinos and anti-neutrinos are different particles and are called "*Dirac*" neutrinos. If the lepton number symmetry is violated, the neutrinos can be their own antiparticles. They are called "*Majorana*" neutrinos.

Majorana neutrinos are described by two degrees of freedom ν_L whereas for the Dirac neutrinos two more degrees of freedom in the form of right chiral Weyl fermions (ν_R) are needed to be included in the SM. The RH neutrino fields do not participate in the gauge interaction; they can only be present in the mass term and hence they are called gauge singlet neutrinos or more popularly "*sterile neutrinos*" as they do not interact via strong, weak or electro-

[1] In this thesis, we will use chirality and handedness inter changeably. Most of the times right handed will referred to right chiral and left handed will correspond to lefty chiral unless and otherwise specified.

magnetic interactions. Using ν_L and ν_R, a Dirac mass term for the neutrinos can be written by constructing a Yukawa interaction term between the right handed neutrino, Lepton doublet and the SM Higgs doublet,

$$-\mathcal{L} \supset Y_\nu \overline{\nu}_R \widetilde{H}^\dagger L_L + \text{h.c.}, \tag{2.2}$$

in analogy with the charged fermion masses in the SM. After the EWSB, the mass term for the leptons becomes,

$$-\mathcal{L}^{\text{Dirac}}_{\text{mass}} = \overline{\ell}_{\alpha R}\, m_\ell^{\alpha\beta}\, \ell_{\beta L} + \overline{\nu}_{\alpha R}\, m_D^{\alpha\beta}\, \nu_{\beta L} + \text{h.c.}, \tag{2.3}$$

where $m_\ell^{\alpha\beta}$ is the mass matrix corresponding to the charge lepton and $m_D^{\alpha\beta}$ denote the Dirac mass matrix, given as $m_D = Y_\nu v/\sqrt{2}$. The four component Dirac neutrinos are defined as, $\nu_{\text{Dirac}} = \nu_L + \nu_R$, wich satisfies the Dirac equation. Similar to the quark sector, both the charged lepton mass matrix and neutrino mass matrix can be diagonalised by the bi-unitary transformations,

$$m_\ell^{\text{diag}} = V_R^\ell\, m_\ell\, V_L^{\ell\dagger}, \qquad m_\nu^{\text{diag}} = V_R^\nu\, m_D\, V_L^{\nu\dagger}. \tag{2.4}$$

The transformation matrices connect the interaction basis to the mass basis which are given by,

$$\ell_{L,R}^{\text{mass}} = V_{L,R}^\ell\, \ell_{L,R}, \qquad \nu_{L,R}^{\text{mass}} = V_{L,R}^\nu\, \nu_{L,R}. \tag{2.5}$$

While the ad-hoc extension can successfully account for the neutrino oscillation phenomena, but it requires extremely small Yukawa couplings ($Y_\nu \lesssim 10^{-12}$) to maintain consistency with experimental constraints on the absolute neutrino mass scale ($m_\nu \lesssim 0.1$ eV). The situation thus raises a naturalness problem regarding the fundamental origin of such hierarchy between the neutrino Yukawa couplings with the other charged fermion Yukawa couplings. The problem of naturalness becomes more evident by applying the 't Hooft naturalness criterion which states "*A physical parameter $\alpha_i(\mu)$ may be naturally small at energy scale μ if setting $\alpha_i(\mu) = 0$ would enhance the symmetry of the system*". In case of Dirac neutrinos, the $m_D \to 0$ limit does not exhibit any new symmetry

in the system.

In the mass basis, the charged current interaction between the leptons and neutrinos is modified as,

$$\begin{aligned} -\mathcal{L}_{\rm cc} &= \overline{\ell}_L^{\,\rm mass}\, V_L^{\ell\dagger}\, V_L^{\nu}\, \gamma^\mu\, \nu_L^{\rm mass}\, \mathcal{W}_\mu + \text{h.c.} \\ &= \overline{\ell}_L^{\,\rm mass}\, \mathcal{U}_{PMNS}\, \gamma^\mu\, \nu_L^{\rm mass}\, \mathcal{W}_\mu + \text{h.c.}, \end{aligned} \tag{2.6}$$

where $\mathcal{U}_{\rm PMNS}$ is referred to as the PMNS matrix named after Pontecorvo-Maki-Nakagawa-Sakata. If one chooses to work with a weak basis where the charged lepton Yukawa couplings are diagonal, then $V_L^\ell = \mathbf{1}$ and $\mathcal{U}_{\rm PMNS} = V_L^\nu$. Therefore, the PMNS matrix characterizes the mixings between the neutrino flavour and mass states.

Unlike the Dirac mass term, using only one type of chiral field (either left or right), one can construct the Majorana mass term for the neutrinos,

$$-\mathcal{L}_{\rm mass}^{\rm Majorana} = \frac{1}{2}\overline{\nu_L^c}\, m_M\, \nu_L + \text{h.c.}\,, \tag{2.7}$$

From Eq. (2.7), it is easily realised that the field ν_L should not contain any gauge or global charge, as the mass term would violate such charge conservation. Lepton number which is an accidental symmetry in the SM, can be violated in BSM scenarios. In these scenarios, a four component Majorana spinor can be defined as $\nu_M = \nu_L + \nu_L^C$, where $\nu_L^C = C\gamma_0\nu_L^*$. This implies that $\nu_M = \nu_M^C$, and it is commonly referred to as "*Majorana condition*". Additionally, it is very easy to check that $\overline{\nu}_L^C\, m_M\, \nu_L = \overline{\nu}_L^C\, m_M^T\, \nu_L$ i.e. m_M is in general a complex symmetric matrix, which can be diagonalised by a unitary matrix, U_ν such that

$$U_\nu^T\, m_M\, U_\nu = m_M^{\rm diag}. \tag{2.8}$$

Similarly to the Dirac neutrino case $\mathcal{U}_{\rm PMNS} = U_\nu$ in the mass basis of the charged lepton.

In general, for the N neutrino flavours, the parametrisation of the PMNS

mixing matrix requires N^2 independent parameters with $N(N-1)/2$ angles and $N(N+1/2)$ phases. Among these $(N-1)$ no of phases can be absorbed by N neutrino fields if the neutrinos are Dirac or they can be considered as Majorana phases for Majorana neutrinos. Another N number of phases can also be rotated away in the charged lepton sector. In total $2N-1$ number of phases can be absorbed in the fields of the Lagrangian. The remaining number of physical phases are $(N-1)(N-2)/2$. Therefore, for the three generations of neutrinos, the PMNS matrix can be parametrised by 3 real angles $(\theta_{12}, \theta_{13}, \theta_{23})$, 1 Dirac CP phase (δ_{13}) and 2 Majorana phases $(\alpha, \beta$ iff the neutrinos are Majorana) and given by

$$\mathcal{U}_{\rm PMNS} = \begin{pmatrix} c_{12}c_{13} & s_{12}c_{13} & s_{13}e^{-i\delta_{13}} \\ -s_{12}c_{23} - c_{12}s_{23}s_{13}e^{-i\delta_{13}} & c_{12}c_{23} - s_{12}s_{23}s_{13}e^{-i\delta_{13}} & s_{23}c_{13} \\ s_{12}s_{23} - c_{12}c_{23}s_{13}e^{-i\delta_{13}} & -s_{23}c_{12} - s_{12}c_{23}s_{13}e^{-i\delta_{13}} & c_{23}c_{13} \end{pmatrix} \begin{pmatrix} 1 & 0 & 0 \\ 0 & e^{i\alpha} & 0 \\ 0 & 0 & e^{i\beta} \end{pmatrix}, \tag{2.9}$$

where $c_{ij} = \cos\theta_{ij}$ and $s_{ij} = \sin\theta_{ij}$.

The most general Lagrangian in the presence of right-handed gauge singlet neutrino field can be written as,

$$\begin{aligned} -\mathcal{L}^{D+M} &= \overline{\nu}_R\, m_D\, \nu_L + \frac{1}{2}\overline{\nu}_R^C\, m_R\, \nu_R + \text{h.c.}, \\ &= \frac{1}{2}\overline{\nu}_R\, m_D\, \nu_L + \frac{1}{2}\overline{\nu}_L^C\, m_D^T\, \nu_R^C + \frac{1}{2}\overline{\nu}_R^C\, m_R\, \nu_R + \text{h.c.}, \\ &= \frac{1}{2}\overline{N}^C\, \mathcal{M}_\nu\, N, \end{aligned} \tag{2.10}$$

where m_D and m_N are called "*Dirac mass*" and "*Majorana mass*" matrix, respectively, and they are in general complex matrices. In Eq. (2.10), we have used the relation $\overline{\nu}_R\, m_D\, \nu_L = \overline{\nu}_L^C\, m_D^T\, \nu_R^C$ which can be shown using the charge conjugation relations. In this case, the neutrino mass matrix can be written in

$N \equiv \begin{pmatrix} \nu_L \\ \nu_R^C \end{pmatrix}$ basis as,

$$\mathcal{M}_\nu = \begin{pmatrix} 0 & m_D^T \\ m_D & m_R \end{pmatrix}. \tag{2.11}$$

The neutrino masses are obtained by diagonalising the $\mathcal{M}_\nu$ mass matrix. For one generation of active and sterile neutrinos, m_D and m_R are just numbers and the eigenvalues of Eq. (2.11) can be written as,

$$m_{1,2} = \frac{1}{2}\left(m_R \pm \sqrt{m_R^2 + 4m_D^2}\right). \tag{2.12}$$

Depending on the choices of m_D, m_R, there can be several possibilities:

- $m_R = 0$, $m_D \neq 0$: $m_{1,2}$ are degenerate and the neutrinos are Dirac particles.
- $m_R \neq 0$, $m_D \neq 0$, and $\frac{m_D}{m_R} << 1$: This condition implies $m_1 = -\frac{m_D^2}{m_R}$, and $m_2 = m_R$. Therefore, in this case, higher mass scale of right-handed neutrinos implies smaller masses of active neutrinos. This mechanism can naturally explain the smallness of active neutrino masses compared to the other charged fermions and is called "*seesaw mechanism* ".

It is to be noted that for more than one generation of neutrinos, the seesaw relations can be generalised as,

$$m^{\text{light}} = -m_D\, m_R^{-1}\, m_D^T, \tag{2.13}$$

$$m^{\text{heavy}} = m_R, \tag{2.14}$$

which will be discussed in the following section.

2.2 Weinberg Operator

Whether the neutrinos are Dirac or Majorana is still an open question, how-

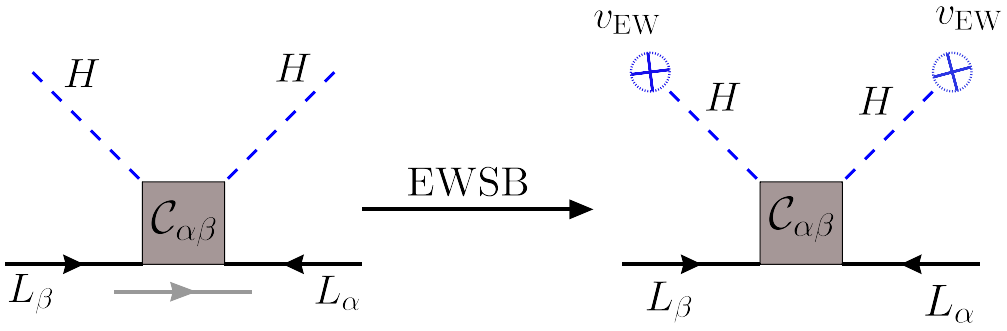

Figure 2.1: Dimension 5 Weinberg operator before and after EWSB. Here α, β are flavour indices.

ever, neutrinos as Majorana fermions have gained a lot of attention for two main reasons: (i) without any additional protective symmetry, small Dirac masses are not technically natural, and (ii) the Majorana neutrinos have richer phenomenology due to the lepton number violation which also allows a pathway to explain the matter-antimatter asymmetry in the universe.

The easiest way to generate a Majorana mass in the SM is by adding a unique dimension 5 operator which violates the lepton number by two units. The operator is called the Weinberg operator and is written as [72],

$$\mathcal{O}_5 \;=\; \frac{\mathcal{C}_{\alpha\beta}}{\Lambda}\,\overline{L_\alpha^C}\,L_\beta\,\widetilde{H^*}\,\widetilde{H}^\dagger + \text{h.c.}, \tag{2.15}$$

with $\mathcal{C}_{\alpha\beta}$ is the model dependent Wilson coefficient which is symmetric under the flavour indices α, β and Λ is the scale of new physics. After the EWSB, the neutrino masses emerge as,

$$m_{\alpha\beta} = \frac{\mathcal{C}_{\alpha\beta}\,v^2}{\Lambda}\,. \tag{2.16}$$

A diagrammatic illustration of the neutrino mass generation by the Weinberg operator is given in Fig. 2.1. The smallness of neutrino mass $(\sim 0.01\,\text{eV})$ is attributed to the high scale of Λ $(\sim 10^{15}\,\text{GeV})$ for $\mathcal{O}(1)$ value of $\mathcal{C}_{\alpha\beta}$, spoiling their testability in current high energy colliders. However, the NP scale can be lowered if the Wilson coefficient is small in the UV theory. There are three possible ways to realise this suppression: (i) generating the neutrino masses

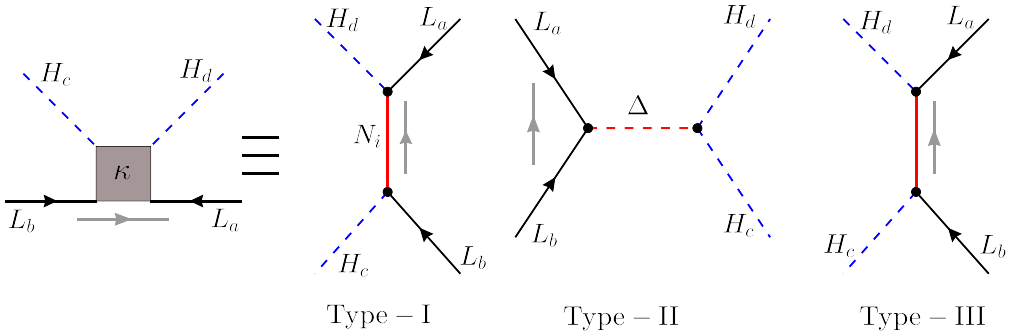

Figure 2.2: Ultraviolet completion of the Weinberg operator at tree level. Here, red solid and dashed lines are corresponding to new fermions and scalars. Here a, b, c, d denote the SU(2) index.

through loop corrections, in which $\mathcal{C}_{\alpha\beta} \propto \frac{1}{(16\pi^2)^n}$, n being number of loops; (ii) forbidding the dimension 5 operator and generating neutrino masses by higher dimensional operators; (iii) the Wilson coefficient $(\mathcal{C}_{\alpha\beta})$ can be small either due to small couplings or due to some nearly conserved symmetries[2]. In the subsequent sections, we briefly review some of these UV theories.

2.3 Tree-level models

The simplest way to open any higher dimensional operator is to consider a UV theory at the tree level. By utilizing the properties of the Pauli matrices, it is easy to show that there are three ways to express the Weinberg operator:

1. $\left(\overline{L}_\alpha^C \widetilde{H}^*\right)\left(\widetilde{H}^\dagger L_\beta\right)$: It corresponds to a scenario where L, H fields form a singlet and the two singlet pairs in the parentheses are connected by a singlet fermion in the UV theory. This simplest scenario is known as the "*Type-I*" seesaw mechanism [77–80]. This situation is depicted in the first diagram at the right hand side of Fig. 2.2.

2. $\left(\overline{L}_\alpha^C \boldsymbol{\sigma} L_\beta\right)\left(\widetilde{H}^\dagger \boldsymbol{\sigma} \widetilde{H^*}\right)$: Here, both L fields and both H fields form a triplet and the two triplet pairs are connected by a heavy triplet scalar field in the UV complete model. This alternative is referred to as the "*Type-II*"

[2]The example for the formal is R-parity violating supersymmetry [73], and inverse [74] or the linear [75, 76] seesaw are examples of the latter.

seesaw mechanism [81–84] and shown in the middle diagram of Fig. 2.2.

3. $\left(\overline{L}_\alpha^C \boldsymbol{\sigma} \widetilde{H^*}\right)\left(\widetilde{H}^\dagger \boldsymbol{\sigma} L_\beta\right)$: This case is called the "*Type-III*" seesaw mechanism and shown in the right most diagram of Fig. 2.2. In this case, L_L, H fields form a triplet and a heavy triplet fermion field connects them in the UV complete model [85].

Beyond the three possibilities mentioned above, there is fourth way to construct a gauge invariant operator as, $\left(\overline{L}_a^C \epsilon_{ab} L_b\right)\left(H_c^T \epsilon_{cd} H_d\right)$, where $a, b, c, d \in SU(2)$ indices. In this case, both L fields and both H fields forms a singlet, but this operator do not contribute to the neutrino mass generation.

2.3.1 Type-I seesaw

Type-I seesaw is the simplest extension of the SM that incorporates the neutrino mass. In this scenario, right handed gauge singlet fermion is added to the SM. The Lagrangian of type-I seesaw is written as,

$$\mathcal{L}_{\text{type-I}} = \mathcal{L}_{\text{SM}} + \mathcal{L}_{\nu_R}, \tag{2.17}$$

where,

$$\mathcal{L}_{\nu_R} = i\overline{\nu}_R \partial\!\!\!/ \nu_R - \overline{\nu}_R \widetilde{H} Y_\nu L - \frac{1}{2}\overline{\nu}_R^C m_R \nu_R + \text{h.c.}. \tag{2.18}$$

To describe the neutrino oscillation data, at least two generation of ν_R must be added. However, as ν_R are SM gauge singlet, any arbitrary generation can be added without violating the gauge invariance or anomaly cancellations. For 3 generations of active neutrinos and N generations sterile neutrinos, the neutrino mass matrix is given in $\begin{pmatrix}\nu_L & \nu_R^C\end{pmatrix}^T$ as,

$$\mathcal{M}_\nu = \begin{pmatrix} 0 & m_D^T \\ m_D & m_R \end{pmatrix}, \tag{2.19}$$

where $m_D = \frac{1}{\sqrt{2}} Y_\nu v$ is $N \times 3$ matrix and m_R is $N \times N$ symmetric matrix and $\mathcal{M}_\nu$ is $(3+N) \times (3+N)$ symmetric matrix. The mass matrix in Eq. (2.19) can be diagonalised by a unitary matrix U_L^ν as,

$$U_L^{\nu T}\, \mathcal{M}_\nu\, U_L^\nu \;=\; \mathcal{M}_\nu^{\rm diag}, \tag{2.20}$$

where $\mathcal{M}_\nu^{\rm diag} = \text{diag}\ (m_1, m_2, m_3, M_1, M_2, \cdots m_N)$ with m_i's being the mass eigenvalues of light neutrinos and M_i's are the same for heavy neutrinos. Following a two step diagonalisation process, the matrix, U_L^ν can be expressed up to the first order of $m_D\, m_R^{-1}$ as [86],

$$\begin{aligned} U_L^\nu \;&=\; W \cdot T = \begin{pmatrix} U_L & V \\ S & U_H \end{pmatrix}, \\ &=\; \begin{bmatrix} \left(1 + \mathcal{O}\left(m_D^2\, m_R^{-2}\right)\right) U_\nu & m_D\, m_R^{-1}\, U_R \\ -\left(\frac{m_D}{m_R}\right)^\dagger U_\nu & \left(1 + \mathcal{O}\left(m_D^2\, m_R^{-2}\right)\right) U_R \end{bmatrix}. \end{aligned} \tag{2.21}$$

Here in the first step, W matrix block diagonalises the neutrino mass matrix as,

$$W^T \begin{pmatrix} 0 & m_D^T \\ m_D & m_R \end{pmatrix} W \;=\; \begin{pmatrix} m_{\rm light} & 0 \\ 0 & m_{\rm heavy} \end{pmatrix}. \tag{2.22}$$

In the seesaw limit, $m_D << m_R$, the light and heavy neutrino mass matrices can be approximated as,

$$m_{\rm light} \;\approx\; -m_D^T\, m_R^{-1}\, m_D\,, \tag{2.23}$$

$$m_{\rm heavy} \;\approx\; m_R, \tag{2.24}$$

and in the second step, the matrix $T = \begin{pmatrix} U_\nu & 0 \\ 0 & U_R \end{pmatrix}$ diagonalises the block diagonal matrix. Here U_ν and U_R diagonalises $m_{\rm light}$ and $m_{\rm heavy}$ respectively. The seesaw relation is realised from Eq. (2.23) that larger the right-handed fermion mass, smaller the active neutrino mass.

2.3.2 Type-II seesaw

In type-II seesaw, a scalar triplet $\Delta : (1,3,1)$ is added to the SM. In the adjoint representation, the triplet scalar can be represented as,

$$\Delta \;=\; \frac{\sigma^i \Delta_i}{\sqrt{2}} = \begin{pmatrix} \Delta^+/\sqrt{2} & \Delta^{++} \\ \Delta^0 & -\Delta^+/\sqrt{2} \end{pmatrix}, \tag{2.25}$$

and the relevant terms of the type-II seesaw Lagrangian is written as,

$$\mathcal{L}_{\text{type}-\text{II}} \;=\; \mathcal{L}_{\text{SM}} - Y_\Delta^{\alpha\beta} \left(\overline{L}_\alpha^C (i\sigma_2)\Delta\, L_\beta\right) - \left(\mu_\Delta\, H^T (i\sigma_2)\Delta^\dagger\, H\right). \tag{2.26}$$

In this scenario, lepton number violation arises either via the Yukawa interaction term or via the scalar interaction term depending on whether the scalar triplet, Δ is assigned with lepton number or not. If $L\ (\Delta) = 0$, then Y_Δ term violates lepton number and if $L\ (\Delta) = -2$, then μ_Δ term violates lepton number by two units. During the EWSB, the triplet scalar develops an induced vev, v_Δ as,

$$v_\Delta \;=\; \frac{\mu_\Delta\, v^2}{\sqrt{2}\, M_\Delta^2}, \tag{2.27}$$

where μ_Δ is the tri-linear scalar coupling, v is the Higgs vev and M_Δ is the mass of the triplet scalar. The light neutrino mass matrix is given as,

$$m_{\text{light}} \;=\; \frac{1}{\sqrt{2}} Y_\Delta\, v_\Delta = \frac{Y_\Delta \mu_\Delta\, v^2}{2M_\Delta^2}. \tag{2.28}$$

The seesaw relation is manifested here in Eq. (2.28), as the mass of the scalar triplet gets higher, the neutrino masses become smaller. For $\mu_\Delta \sim M_\Delta$, $Y_\Delta \sim \mathcal{O}(1)$, and $m_{\text{light}} \sim 0.01\,\text{eV}$, the mass of the triplet scalar must be $M_\Delta \sim 10^{15}$ GeV. which makes these new scalar particles practically inaccessible to the current and future colliders. However, a TeV scale realisation is also possible if lepton number is explicitly violated at a low energy scale, satisfying $\mu_\Delta \ll v \ll M_\Delta$ [87]. Under this assumption, light neutrino masses of $\mathcal{O}(0.01\text{ eV})$ can be generated by choosing the parameters as $\mu_\Delta \sim \mathcal{O}(1\,\text{eV})$, $M_\Delta \sim \mathcal{O}(1\text{ TeV})$,

and Yukawa coupling $Y_\Delta \sim \mathcal{O}(1)$.

2.3.3 Type-III seesaw

Type-III seesaw scenario is analogous to type-I seesaw, except that a fermion triplet with zero hypercharge is added to the SM instead of a singlet fermion. The relevant terms in the Lagrangian can be written as,

$$\mathcal{L}_{\text{type-III}} = \mathcal{L}_{\text{SM}} + \mathcal{L}_{\Sigma_R}, \tag{2.29}$$

where,

$$\mathcal{L}_{\Sigma_R} = i\overline{\Sigma}_R \not{D} \Sigma_R - \widetilde{H}^\dagger \overline{\Sigma}_R Y_\Sigma L - \frac{1}{2}\overline{\Sigma}_R^C m_\Sigma \Sigma_R + \text{h.c.}. \tag{2.30}$$

Similarly to the triplet scalar, the triplet fermion can be also represented as,

$$\Sigma_R = \frac{\sigma^i \Sigma_R^i}{\sqrt{2}} = \begin{pmatrix} \Sigma_R^0/\sqrt{2} & \Sigma_R^+ \\ \Sigma_R^- & -\Sigma_R^0/\sqrt{2} \end{pmatrix}, \tag{2.31}$$

Once the Higgs field develops a vev, the neutrino mass matrix can be written as,

$$\mathcal{M}_\nu = \begin{pmatrix} 0 & m_D^T \\ m_D & m_\Sigma \end{pmatrix}, \tag{2.32}$$

where $m_D = \frac{Y_\Sigma v}{\sqrt{2}}$ and in the seesaw limit, the neutrino masses are given as,

$$m_{\text{light}} = -m_D^T m_\Sigma^{-1} m_D\,, \tag{2.33}$$

$$m_{\text{heavy}} = m_\Sigma \tag{2.34}$$

The key difference between the type-I and type-III seesaw lies in the extra gauge interactions of the triplet fermion which makes the type-III seesaw phenomenologically interesting. Apart from neutral leptons, the charge lepton mass matrix also gets modified in this framework.

2.3.4 TeV scale seesaw

In the minimal type-I and III seesaw scenarios, the lepton number violating scale coincide with the seesaw scale which is high ($\Lambda \sim 10^{15}$ GeV) and the small neutrino masses are the consequence of this high scale suppression. However, the two scales can be decoupled from each other by adding more singlet fermions in these minimal frameworks. In these non-minimal scenarios, the SM is extended with m right-handed neutrinos (ν_R) and n gauge singlet fermions (ν_S). Here, ν_R and ν_S are assigned lepton numbers with $L = +1$ and $L = -1$, respectively. The most general Lagrangian can be written as,

$$-\mathcal{L} \supset \overline{L} Y_\nu \widetilde{H} \nu_R + \overline{L} Y_S \widetilde{H} \nu_S + \overline{\nu}_R^C m_{RS} \nu_S + \frac{1}{2} \overline{\nu}_S^C \mu_S \nu_S + \frac{1}{2} \overline{\nu}_R^C m_N \nu_R + \text{h.c.}, \tag{2.35}$$

where Y_ν and Y_S are the Yukawa coupling matrices; m_N and μ_s are Majorana mass matrix for right handed and gauge singlet neutrinos. After the EWSB, the neutrino mass matrix can be defined as,

$$-\mathcal{L}_{\text{mass}} = \frac{1}{2} \begin{pmatrix} \overline{\nu}_L & \overline{\nu}_R^C & \overline{\nu}_S^C \end{pmatrix} \begin{pmatrix} 0 & m_D & m_{LS} \\ m_D^T & m_N & m_{RS} \\ m_{LS}^T & m_{RS}^T & \mu_S \end{pmatrix} \begin{pmatrix} \nu_L^C & \nu_R & \nu_S \end{pmatrix} + \text{h.c.}, \tag{2.36}$$

where m_{LS}, m_N and μ_s introduces the lepton number violation in the theory. One can have different variants of the low-scale seesaw considering different limits and approximations on the mass matrix elements. Two of the popular ones are,

- $m_N = m_{LS} = 0$: In this case, μ_s is the only LNV violating term. For $\mu_s << m_D << m_{RS}$, the light neutrino mass matrix is approximated as,

$$m_{\text{light}} \approx m_D \left(m_{RS}^T\right)^{-1} \mu_s \, m_{RS}^{-1} \, m_D^T, \tag{2.37}$$

  Unlike the canonical seesaw case, here the smallness of neutrino mass is related to the smallness the lepton number violating term μ_S which can

be technically natural as $\mu_s \to 0$ restores the lepton number symmetry in the theory. This mechanism is known as the "*inverse seesaw*" mechanism and was originally proposed in the context of E_6 GUT theories [74].

- $m_N = \mu_S = 0$: In this case, LNV is introduced by m_{LS} term. For $m_{LS} \ll m_D \ll m_{RS}$, the light neutrino mass matrix becomes,

$$m_{\text{light}} \approx m_D \left(m_{RS}^T\right)^{-1} m_{LS}^T + m_{LS}\, m_{RS}^{-1}\, m_D^T\,, \tag{2.38}$$

This is called "*linear seesaw*" mechanism.

2.4 One-loop models

Beyond extending the SM with singlet neutral fermions to reduce the seesaw scale, small neutrino masses can be alternatively generated via higher order loops where each loop will add a suppression factor of $\frac{1}{16\pi^2}$. In these radiative mass models, the Weinberg operator is forbidden at the tree level due to the field content or any imposed symmetry. However, they can be generated through loop corrections. In this section, we only discuss the one-loop realisations while acknowledging that the neutrino mass can also be generated via higher order loops with additional suppression factors [76, 88].

Zee model

In Zee model, the SM is extended with an additional Higgs doublet, Φ and a charged scalar, h^+. Both the Higgs doublet couple to the SM fermions whereas h_+ couples to $L\,L$ with an antisymmetric Yukawa coupling in the flavour space. The relevant Lagrangian can be written as [88],

$$-\mathcal{L} = Y_H\, \overline{\ell}_R\, \widetilde{H} L + Y_\Phi\, \overline{\ell}_R\, \widetilde{\Phi} L + Y_h\, \overline{L}^C\, (i\sigma_2)\, L\, h_+ + \mu_{\text{Zee}}\, \widetilde{H}^\dagger\, \Phi\, h_+^* + \text{h.c.}\,, \tag{2.39}$$

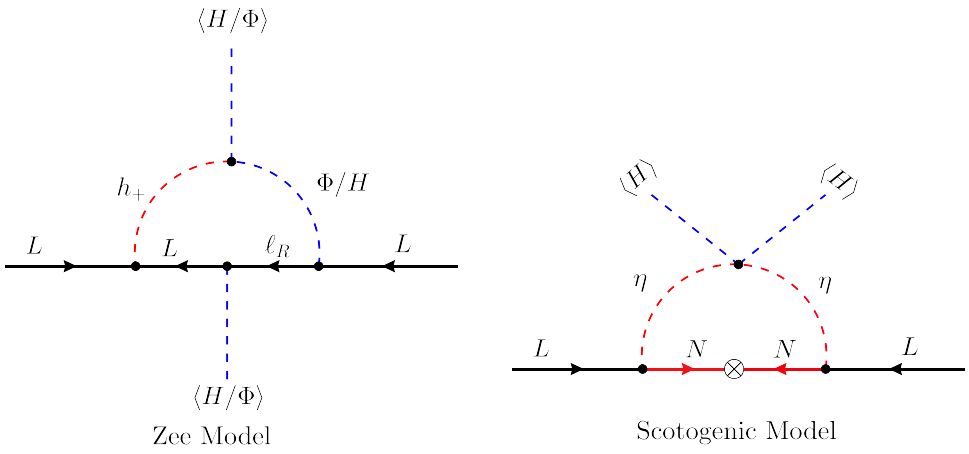

Figure 2.3: Feynman diagrams of one-loop neutrino mass generated in the Zee model [88] and the scotogenic model [76]. Here red color denote new degrees of freedom except the Higgs doublet which is shown in blue color.

The simultaneous presence of the last two terms in Eq. (2.39) breaks the lepton number by two units. The neutrino mass is generated by the one-loop diagram, given in Fig. 2.3 and given as,

$$m_{\text{light}} \;=\; \frac{1}{16\pi^2}\,\mu_{\text{zee}}\,C\,\left(Y_h\,m_\ell\,Y_\eta - Y_\eta^T\,m_\ell\,Y_h\right)\,, \tag{2.40}$$

where $\eta = H, \Phi$ and C contains other information of the one-loop calculations. Note that, for $\left(Y_\eta\right)_{ij} = y_i\,\delta_{ij}$, $\left(m_{\text{light}}\right)_{ij} = 0$ i.e. to obtain the non-zero neutrino masses some of the off-diagonal the Yukawa couplings of Y_Φ or Y_H need to be zero, thereby enabling the LFV process, such as $\mu \to e\gamma$, $\ell_\alpha \to \ell_\beta\ell_\gamma\ell_\delta$, $h \to \tau\mu$ etc.

2.4.1 Scotogenic model

Scotogenic models are one of the popular extensions among the radiative mass models as they connect the origin of neutrino masses to the dark matter particles. The conventional scotogenic model consists of three fermion singlets N_i and one Higgs doublet (η). In this scenario, the SM symmetry group is also extended with a discrete $\mathcal{Z}_2$ symmetry under which all the SM particles are

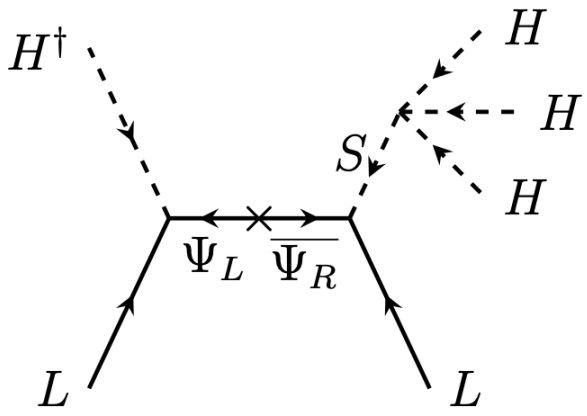

Figure 2.4: Feynman diagram generating neutrino masses in the BNT model [89] which boils down to d=7 operator in the standard model effective field theory.

evenly charged and all new particles have odd charge. The imposed $\mathcal{Z}_2$ symmetry does not allow type-I seesaw by forbidding the $\overline{N}\,\widetilde{H}\,L$ interaction term. The lightest $\mathcal{Z}_2$ odd particle serves as a dark matter candidate and the stability is ensured by the discrete symmetry itself.

The relevant Lagrangian can be written as [76],

$$-\mathcal{L} \;=\; \overline{N} Y_N\, \eta^T\, L + \frac{1}{2}\overline{N}^C\, M_N N + \lambda_5 \left(H^\dagger \eta\right)^2 + \text{h.c.}\,. \tag{2.41}$$

In the above equation, lepton number is violated by the Majorana mass term of N and the λ_5 term. In the small λ_5 limit, the light neutrino mass is computed as,

$$m_{\text{light}} = \frac{1}{16\pi^2}\,\lambda_5\, v^2 \left(Y_N\, M_N^{-1}\, Y_N^T\right)\,. \tag{2.42}$$

The scotogenic models get an extra suppression of $\frac{\lambda_5}{16\pi^2}$ compared to type-I seesaw.

2.5 Higher dimension operators

As mentioned in section 2.2, the NP scale can be lowered by generating the neutrino mass through higher dimensional operators. In this context, in this

section, we discuss two dimension 7 operators that are widely studied in the literature.

2.5.1 Weinberg like operator

Other than the dimension 5 operator, the lowest dimension generating Majorana neutrino mass is the dimension 7 operator. Among these dimension 7 operators, the most studied operator structure is $\mathcal{O}_7^{(1)} = \mathcal{O}_5\ \left(H^\dagger H\right)$. The UV completion of this operator is first postulated in BNT model which was first discussed in Ref. [89] by Babu, Nandi and Tavartkiladze. Here, the SM is extended with a vector like fermion triplet, $\Psi_{L,R}\,(1,3,1)$ and a scalar quadruplet, $S\,(1,3/2,3/2)$. The relevant Lagrangian can be written as,

$$-\mathcal{L} \;=\; \overline{\Psi}_L\, M_\Psi\, \Psi_R + \overline{L}_L^C\, Y_H\, H^\dagger\, \Psi_L + \overline{L}_L\, Y_S\, S^*\Psi_R + \lambda_5\, \left(H^3\, S^*\right) + \text{h.c.}. \tag{2.43}$$

Here, depending on the lepton number assignments to the new fields Ψ and S, there can be three possibilities for lepton number violation:

1. If $L(L) = +1\,,\ L(\Psi) = +1$ and $L(S) = 0$, then Y_H term violates the lepton number by two units.
2. If $L(L) = +1\,,\ L(\Psi) = -1$ and $L(S) = 0$, then Y_S term violates the lepton number by two units [90].
3. In the third case, λ_5 term violates the lepton number if the charge assignment follows, $L(L) = +1\,,\ L(\Psi) = -1$ and $L(S) = -2$.

In this model, the light neutrino mass is generated via $\mathcal{O}_7^{(1)}$ and is given as,

$$m_{\text{light}} \;=\; -\frac{\lambda_5\, v^4}{M_S^2}\left(Y_S M_\Psi^{-1} Y_H^\dagger + Y_H^* M_\Psi^{-1} Y_S^T\right). \tag{2.44}$$

The presence of charged scalar and charged fermion makes this model phenomenologically very active and interesting [90, 91].

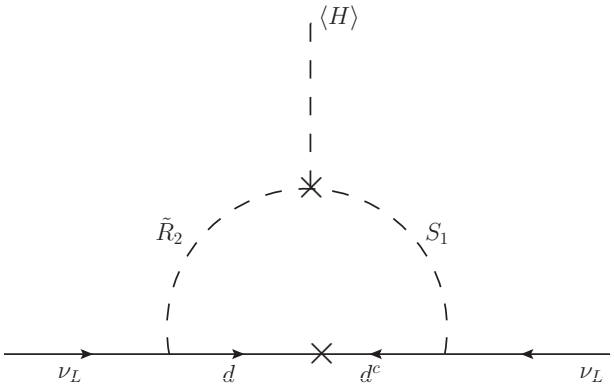

Figure 2.5: Feynman diagram generating neutrino mass in leptoquark model [92, 93] via $\mathcal{O}_7^{(2)}$ operator.

2.5.2 Dimension-7 operator at one loop

Beyond the Weinberg-like operators, interesting seven dimensional operator exists that generates neutrino masses $\mathcal{O}_7^{(2)} = H(LQ)(Ld^C)$ [94–96]. The UV model corresponding to this operator is discussed in Ref. [92, 93]. In this scenario, the SM is augmented by two scalars leptoquarks (LQs), i.e. $S_1(\overline{3}, 1, 1/3)$ and $\widetilde{R}_2(3, 2, 1/6)$ and generate the neutrino mass at the 1-loop level if the LQs mix with each other. The lepton number violation in this model is introduced by the mixing term of the leptoquarks. The neutrino mass generation in this model is depicted in Fig. 2.5. The relevant Lagrangian of the model is ,

$$-\mathcal{L} = Y_1^L \overline{Q}_L^C \epsilon \ell_L S_1 + Y_2 \overline{d}_R \widetilde{R}_2^T \epsilon \ell_L + \kappa H^\dagger \widetilde{R}_2 S_1 + \text{h.c.}, \tag{2.45}$$

and the neutrino mas is given by,

$$m_{\text{light}} = -\frac{3}{32\pi^2} \frac{\kappa v}{m_{\text{LQ}}^2} \left(\widetilde{Y_1^L}^T \mathcal{M}_d Y_2 + Y_2^T \mathcal{M}_d \widetilde{Y_1^L} \right). \tag{2.46}$$

The model will be discussed in detail in the Chapter 4.

2.6 Neutrino masses in GUTs

Among the gauge extensions of the SM, grand unified theories should have a special mention due to its ability to unify all the SM forces at an high energy scale. In the earlier discussions, we have found that to incorporate the light neutrino masses, the natural scale of seesaw is approximately 10^{15} GeV which is very near to the GUT scale. Therefore, the seesaw mechanisms can naturally be embedded in GUT frameworks. In GUT frameworks, the SM gauge group is embedded inside a larger group. $SU(5)$ is the simplest Lie group which contains the SM gauge group as subgroup. In the minimal version of $SU(5)$ framework, all the SM fermions reside in $\overline{5}_F$ and 10_F representations, whereas the Higgs scalar is embedded in both 5_H and 45_H representations which is required to reproduce the observed mass spectrum of the charged fermions. Apart from these, one needs 24_H to break the GUT symmetry at very high scales. With this minimal version of the field contents, $SU(5)$ framework is unable to produce neutrino mass. However, by enlarging the field content or adding other Fermion or Higgs irreducible representations (irreps), it is possible to generate neutrino masses via the above-mentioned neutrino mass mechanisms.

- Type-I seesaw can be embedded in $SU(5)$ GUT by adding singlet fermions into the framework.
- If the scalar sector is extended with **15**-dimensional representation, then the neutrino masses are generated via type-II seesaw at tree level, and also via the $\mathcal{O}_7^{(2)}$ at one loop level.
- Type-III seesaw can be implemented in $SU(5)$ GUT by adding one **24**-dimensional representation that contains the triplet fermion field.

Another well studied GUT framework is $SO(10)$. This framework naturally contains all the SM fermions along with singlet right-handed neutrinos in the 16-dimensional irrep. Consequently, type-I seesaw mechanism is naturally embedded in $SO(10)$ framework. For a detailed discussions of neutrino mass

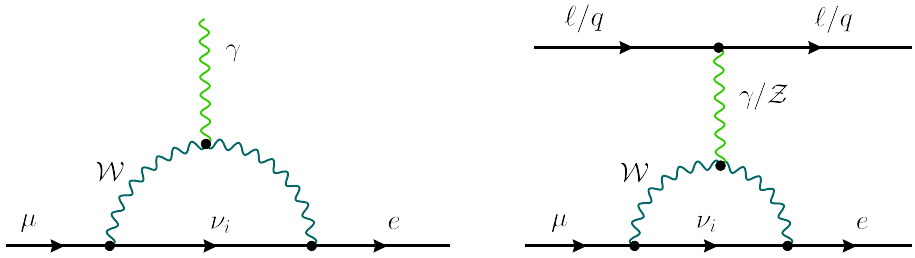

Figure 2.6: LFV decays originating from neutrino masses. The left panel shows $\mu \to e\gamma$ process. In the right panel the $\mathcal{Z}$ boson can either couple to two electrons giving $\mu \to 3e$ or couples to two quarks mediating $\mu \to e$ conversion in a nuclei.

generation in GUTs, the reader is referred to [97].

2.7 Implication of neutrino mass

In the preceding section, we briefly described the neutrino mass models whereas in this section, we will provide the implication of this neutrino masses and mixings on the low energy phenomenology. One straightforward implication of neutrino mass is the neutrino oscillation phenomena that has been discussed in section 1.2.1. Other implications of the neutrino masses include lepton flavour violation (LFV), electric and magnetic dipole moments, and $0\nu\beta\beta$, which are discussed in the subsequent subsections.

2.7.1 Lepton Flavour Violation

Neutrino oscillation already indicates that individual lepton flavour symmetry is not respected in the neutral lepton sector. Now, the question arises whether it is also violated in the charge lepton sector. For the mass models discussed above, LFV decays are one of the consequences of the neutrino masses and mixings and the relevant processes are $\mu \to e\gamma$, $\mu \to 3e$ and $\mu \to e$ conversion in nuclei. The considered processes are forbidden in the SM, but they can be generated at 1-loop if the SM is extended by neutrino masses and mixings, as shown in Fig. 2.6. The current upper bounds on these processes are given as,

$$\begin{aligned}
&\text{BR}\,(\mu\,N \to\ e\,N) < 7\times10^{-13} && \textit{SINDRUM II}\ [98],\\
&\text{BR}\,(\mu \to\ e\,\gamma) < 4.2\times10^{-13} && \textit{MEG II}\ [99],\\
&\text{BR}\,(\mu \to\ 3\,e) < 1.0\times10^{-12} && \textit{SINDRUM}\ [100],\ .
\end{aligned}$$

The light neutrino contribution, shown in Fig. 2.6 is extremely tiny due to the smallness of neutrino mass. However, in various BSM frameworks, these contributions can reach up to the current experimental limit or even surpass them for certain cases. In such cases, these LFV decays can provide stringent limits on the model parameter space. In chapter 4, we have presented the expressions for lepton flavour violating decays and corresponding constraints on parameter spaces imposed by these decays in the context of a specific BSM scenario.

2.7.2 Electromagnetic properties

Neutrinos are electrically neutral fermions and in the SM, they do not have any electromagnetic interaction. However, in some BSM frameworks, electromagnetic properties of neutrinos are generated when they effectively couple to photons via loop diagrams. The most general electromagnetic interaction vertex of the neutrinos can be written as [101, 102]

$$\mathcal{L}_{\text{int}} \;=\; -\overline{\nu}\,\Gamma^{\mu}_{(\nu)}\,\nu\,A_{\mu}\,, \tag{2.47}$$

where $\Gamma^{\mu}_{(\nu)}$ following Eq. (1.22) can be written as,

$$\begin{aligned}
\Gamma^{\mu}_{(\nu)} \;=\; i\,e\Big[&\gamma^{\mu}\left\{F_1^V(q^2)+F_1^A(q^2)\gamma_5\right\}+\frac{i}{2\,m_\nu}\sigma^{\mu\nu}\,q_\nu\left\{F_2^V(q^2)+F_2^A(q^2)\,\gamma_5\right\}\\
&+q^{\mu}\left\{F_3^V(q^2)+F_3^A(q^2)\,\gamma_5\right\}+F_4^A\left(q^2\right)\,\gamma_5\,q^{\mu}\,\not{q}\Big]\,,
\end{aligned} \tag{2.48}$$

where q is the momentum of the outgoing photon, $F_1^V, F_1^A, F_2^V, F_2^A$ are the electric charge, anapole, magnetic dipole and electric dipole form factors, respectively. The physical importance of these form factors can be understood when they are simplified in non-relativistic (NR) limits. For instance, if we consider

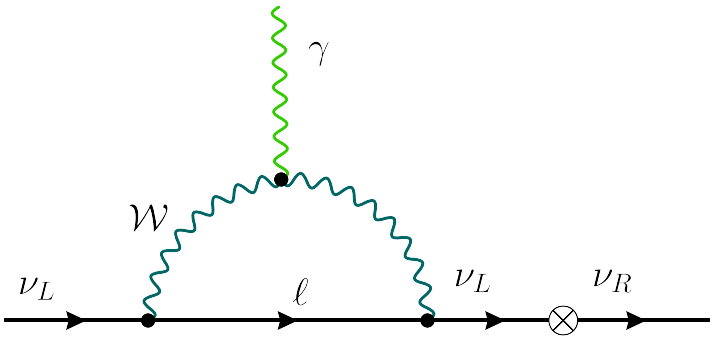

Figure 2.7: Feynman diagram contributing to magnetic and electric dipole moments in the SM that is extended with only the Dirac mass term.

only the F_2^V term in Eq. (2.48) for the interaction with photon field

$$\frac{ie\,F_2^V}{2m_\nu}\overline{u}(p')\,\sigma^{\mu\nu}\,u(p)\,q_\nu\epsilon_\mu \;=\; \frac{ie\,F_2^V}{4m_\nu}\overline{u}(p')\,\sigma^{\mu\nu}\,u(p)\,\left(q_\nu\epsilon_\mu-\epsilon_\nu\,q_\mu\right). \quad (2.49)$$

The equivalent interaction of Eq. (2.49) in position space can be written,

$$\frac{e\,F_2^V}{4m_\nu}\,\overline{\nu}\sigma^{\mu\nu}\,\nu\,F_{\mu\nu} \xrightarrow{\text{NR Limit}} \frac{e\,F_2^V}{2m_\nu}\,\boldsymbol{S}\cdot\boldsymbol{B}. \quad (2.50)$$

Comparing Eq. (2.50) with the classical interaction Hamiltonian, the magnetic dipole moment (MDM) is given as,

$$\mu_\nu \;=\; \frac{e\,F_2^V}{2m_\nu}. \quad (2.51)$$

Similarly, for the F_2^A term interaction is given as,

$$\begin{aligned}
&\frac{ie\,F_2^A}{2m_\nu}\overline{u}(p')\,\sigma^{\mu\nu}\,\gamma_5\,u(p)\,q_\nu\epsilon_\mu \\
=&\frac{e\,F_2^A}{4m_\nu}\overline{u}(p')\,\sigma^{\mu\nu}\gamma_5\,u(p)\,F_{\mu\nu} \\
=&\frac{ie\,F_2^A}{8m_\nu}\overline{u}(p')\,\epsilon^{\mu\nu\alpha\beta}\sigma_{\alpha\beta}\,u(p)\,F_{\mu\nu}, && \text{as}\;\; \sigma_{\mu\nu}\gamma_5=-\frac{i}{2}\epsilon^{\mu\nu\alpha\beta}\sigma_{\alpha\beta} \\
=&\frac{ie\,F_2^A}{4\,m_\nu}\overline{u}(p')\,\sigma_{\alpha\beta}\,u(p)\,\tilde{F}^{\alpha\beta}, && \tilde{F}^{\alpha\beta}=\frac{1}{2}\epsilon^{\mu\nu\alpha\beta}F_{\mu\nu}.
\end{aligned} \quad (2.52)$$

Eq. (2.52) is similar to Eq. (2.49), except the field strength tensor is replaced by its dual tensor. The component of the dual tensor can be obtained by substituting $\boldsymbol{E}\to\boldsymbol{B}$ and $\boldsymbol{B}\to-\boldsymbol{E}$ to the field strength tensor. Therefore, in

the NR limit the interaction Hamiltonian will be,

$$\langle H \rangle \;=\; -i\frac{e\,F_2^A}{2m_\nu}\,\boldsymbol{S}.\boldsymbol{E}\,, \tag{2.53}$$

which by comparing to the classical Hamiltonian, the electric dipole moment (EDM) is identified as,

$$d_\nu \;=\; -i\frac{e\,F_2^A}{2m_\nu}\,. \tag{2.54}$$

In the minimal extension of the SM, where it is added with the Dirac mass term, the $\overline{\nu}_\alpha\,\Gamma^\mu\,\nu_{\alpha'}\,\mathcal{A}_\mu$ effective interaction vertex is given in Fig. 2.7 and calculated as [97],

$$\Gamma_\mu \;\approx\; -\frac{eG_F}{4\sqrt{2}\,\pi^2}\,\left(m_\alpha P_L + m_{\alpha'} P_R\right)\,\sigma_{\mu\nu}q^\nu\,\left(U_{\ell\alpha}\,U^*_{\ell\alpha'}\,f\left(m_\ell^2/M_W^2\right)\right)\,, \tag{2.55}$$

where U_{ij} is the ij^{th} element of the PMNS matrix, m_α is the mass of α^{th} flavour neutrino, and $f(r)$ is the loop function and defined as,

$$f(r) \;\simeq\; -\frac{3}{2} + \frac{3}{4}\,r + \cdots \tag{2.56}$$

Therefore, comparing Eq. (2.55) with Eq. (2.48), MDM and EDM are identified as,

$$\mu_{\alpha\alpha'} = \left(m_\alpha + m_{\alpha'}\right)\,K\,, \qquad\qquad d_{\alpha\alpha'} = -i\left(m_\alpha - m_{\alpha'}\right)\,K, \tag{2.57}$$

where $K = \frac{eG_F}{8\sqrt{2}\,\pi^2}\,\left(U_{\ell\alpha}\,U^*_{\ell\alpha'}\,f\left(m_\ell^2/M_W^2\right)\right)$. For diagonal elements i.e. $\alpha = \alpha'$, above equations are simplified as,

$$\begin{aligned} \mu_\nu &\simeq \frac{3eG_F}{8\sqrt{2}\pi^2}\,m_\alpha, \qquad\qquad & d_\nu = 0\,, \\ &\simeq 3\times 10^{-20}\mu_B\,\left(\frac{m_\alpha}{0.1\text{ eV}}\right). \end{aligned} \tag{2.58}$$

Note that, for Majorana neutrinos, the MDM and EDM interaction can be

written as,

$$\overline{\nu}^C_\alpha \, \sigma^{\mu\nu} \left(F_2^V + F_2^A \, \gamma_5 \right) \, \nu_{\alpha'} \, q_\nu \, \mathcal{A}_\mu = -\overline{\nu}^C_{\alpha'} \, \sigma^{\mu\nu} \left(F_2^V + F_2^A \, \gamma_5 \right) \, \nu_\alpha \, q_\nu \, \mathcal{A}_\mu. \quad (2.59)$$

From Eq. (2.59), it is clearly seen that for $\alpha = \alpha'$, $F_2^{A,V} = 0$. Therefore, the diagonal matrix elements of μ_ν and d_ν vanish for Majorana neutrinos; only the off-diagonal are non-vanishing, called transition moments.

Stringent limits on the neutrino MDM come from the brightness measurement of the tip of the red giant branch in ω-Centauri globular cluster using Gaia DR2 data. Ref. [103] quotes this limit as $\mu_\nu < 1.2 \times 10^{-12} \, \mu_B$, where $\mu_B = \frac{e}{2 m_e}$ is the Bohr magneton. As far as the neutrino EDM is concerned, no experimental limit exists yet, but several theoretical and indirect bounds have been obtained. The most stringent limit on electron and muon neutrino EDM is quoted as $d_{\nu_e, \nu_\mu} < 10^{-21} e$-cm [104] whereas, for the tau neutrino, $d_{\nu_\tau} < 10^{-17} e$-cm [105].

2.7.3 Mass related observables

Neutrino oscillation experiments provide no information about the absolute mass scale of neutrinos. The information on absolute mass scale of neutrinos are provided by the mass-related observables such as,

- Sum of neutrino masses (Σ) from cosmological observations.
- Effective electron neutrino mass (m_β) measured in nuclear beta decay experiments and
- Effective Majorana mass (m_{ee}) probed in neutrinoless double beta decay searches.

Standard neutrino cosmology

Neutrinos in the early universe were produced through frequent interactions in the hot, dense plasma that existed shortly after the Big Bang. They are

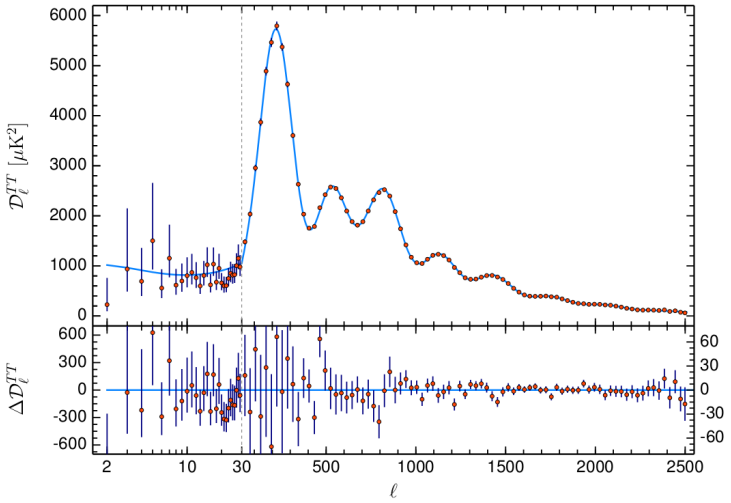

Figure 2.8: CMB spectrum [31].

the lightest fermions in the SM and interact only through the weak interaction. This weakly interacting nature allows them to travel long distances unaffected. This unique property makes them an important probes of large-scale cosmic evolution. In the early universe at temperatures ($T >> 1$ MeV), neutrinos maintained thermal equilibrium with the primordial plasma, as their interaction rate $\Gamma(T) \sim G_F^2\, T_\nu^5$ exceeded the Hubble expansion rate $H(T)$ [106, 107]. As the universe cooled to $T \approx 1$ MeV or below, neutrino interactions became insufficient to maintain the equilibrium and $\Gamma(T) << H(T)$, leading to their decoupling of the neutrinos from the thermal plasma. Initially the neutrinos were relativistic, preserving the standard Fermi-Dirac distribution, but at least two neutrino mass states have become non-relativistic in the current epoch. During their relativistic phase, neutrinos contributed significantly to the universe's radiation density, given as,

$$\rho_\nu \;=\; N_{\text{eff}} \left(\frac{7\pi^2\, T_\nu^4}{120} \right), \tag{2.60}$$

where N_{eff} represents the effective number of relativistic degrees of freedom beyond photons, and T_ν denotes the neutrino decoupling temperature. The SM predicts $N_{\text{eff}} \approx 3$ (precisely $N_{\text{eff}}^{SM} = 3.0440 \pm 0.0002$ [108, 109]) for three neutrino flavours.

This radiation density directly influences the cosmic expansion rate:

$$H^2 = \frac{8\pi G}{3}(\rho_\gamma + \rho_\nu)\,. \tag{2.61}$$

Eq. (2.61) reveals that $N_{\rm eff}$ directly affects the Hubble parameter, which has direct observable consequences for Big Bang nucleosynthesis (BBN). Precise measurements of BBN products, particularly the neutron-to-proton ratio and Helium-4 mass fraction, provide stringent constraints on $N_{\rm eff}$ as [110],

$$N_{\rm eff} = 2.88 \pm 0.28, \quad (68\%\text{CL}) \tag{2.62}$$

which limits the neutrino species to be nearly three. At later epoch, when neutrinos become non-relativistic they contribute to the matter energy density as,

$$\Omega_\nu = \frac{\rho_{\nu,0}}{\rho_{c,0}} = \frac{g_i}{(2\pi)^3\,\rho_{c,0}} \sum_{i=species} \int m_i\, d^3p\, f_\nu(p), \tag{2.63}$$

where m_i is the mass of neutrinos, $f_\nu(p)$ is the momentum distribution of neutrinos and is given by the Fermi-Dirac distribution function and $\rho_{c,0}$ is the critical energy density of the universe at the present epoch and is given by,

$$\begin{aligned}\rho_{c,0} &= \frac{3H_0^2}{8\pi G} \\ &= 1.05 \times 10^4\,\text{eV/cm}^3.\end{aligned} \tag{2.64}$$

Eq. (2.64) assumes the value of the present Hubble parameter as $H_0 = 100\,h$ Km/sec/Mpc and the Newton constant as $G = 10^{-38}\text{GeV}^{-2}$. Using these, Eq. (2.63) can be simplified as

$$\begin{aligned}\Omega_\nu h^2 &= \frac{8\pi G h^2}{3H_0^2}\,\frac{g_i \sum m_\nu}{2\pi^2} \int dp\, p^2\, \frac{1}{e^{p/T}+1} \\ &= \frac{8\pi G h^2}{3H_0^2}\,\frac{\sum m_\nu\, 3\,\zeta(3) T_{\nu,0}^3}{2\pi^2}\,.\end{aligned} \tag{2.65}$$

Applying the values from above and $T_{\nu,0} = \left(\frac{4}{11}\right)^{1/4} T_{\gamma,0} = 1.95$ K, the neu-

trino energy density can be written as

$$\Omega_\nu\, h^2 \;=\; \frac{\sum m_\nu}{94.1\,\mathrm{eV}}. \tag{2.66}$$

Cosmological observations constrain $\Omega_\nu\, h^2$, and consequently, the sum of the neutrino masses ($\sum m_\nu$).

The primary anisotropies of the Cosmic Microwave Background (CMB) represent temperature and polarisation fluctuations imprinted at the surface of last scattering. The angular correlation between directions $\hat{n}$ and $\hat{n'}$ is given by:

$$\left\langle \frac{\Delta T(\hat{n})}{T} \frac{\Delta T(\hat{n'})}{T} \right\rangle \;=\; \sum_{l=0}^{\infty} \frac{2l+1}{4\pi}\, C_l^{TT}\, \mathcal{P}_l\left(\hat{n}\cdot\hat{n'}\right), \tag{2.67}$$

where the coefficients C_l^{TT} of the Legendre polynomial $\mathcal{P}_l\left(\hat{n}\cdot\hat{n'}\right)$ encode information about primordial anisotropies. In the early universe, the opposite effects of gravity and radiation pressure in the photon-baryon fluid generated acoustic oscillations that became *"frozen"* into the CMB spectrum at the photon decoupling, manifesting as characteristic peaks in the power spectrum (see Fig. 2.8). The height of the first acoustic peak is particularly sensitive to the redshift of matter-radiation equality [111]:

$$z_{eq} \;=\; \frac{\omega_b + \omega_c}{(1 + 0.2271\, N_{\mathrm{eff}})\,\omega_\gamma}, \tag{2.68}$$

making the CMB spectrum an independent probe of N_{eff}.

Large-scale matter clustering provides another powerful constraint on neutrino properties, described by the two-point correlation function in the matter densities:

$$\left\langle \delta_m\left(\boldsymbol{k}, z\right) \delta_m\left(\boldsymbol{k'}, z\right)\right\rangle \;=\; P_m\left(k, z\right) \delta^{(3)}\left(\boldsymbol{k} - \boldsymbol{k'}\right), \tag{2.69}$$

where $\delta_m(\boldsymbol{k}, z)$ represents Fourier-transformed matter density perturbations and $P_m(k, z)$ the matter power spectrum at redshift, z_{eq} which denotes the matter-radiation equality. In other words, the matter power spectrum is sensi-

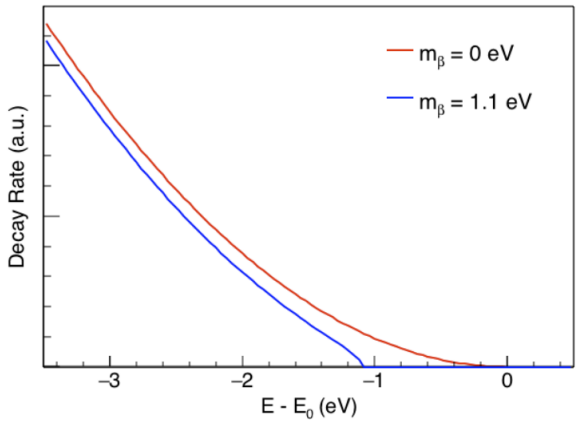

Figure 2.9: Tritium decay endpoint spectrum for different m_β having the same extrapolated endpoint energy [112].

tive to z_{eq} which in turn carries information about N_{eff}. Additionally, massive neutrinos become non-relativistic after the neutrino decoupling, have large thermal velocities that suppress clustering below the free-streaming scale, leading to characteristic damping in the matter power spectrum at small scales.

Current constraints from combined CMB and large-scale structure data yield:

$$N_{\text{eff}} = 2.99^{+0.34}_{-0.33} \quad (95\%\,\text{CL})\,, \tag{2.70}$$

$$\sum m_\nu < 0.12\,\text{eV}, \tag{2.71}$$

assuming three degenerate neutrino mass states within a ΛCDM framework extended with N_{eff} and $\sum m_\nu$ as free parameters.

Kinetic mass from nuclear β decay

Nuclear β decay provides a model-independent probe of absolute neutrino mass. In nuclear β decay, the available energy from the mass difference between the decaying nucleus and the daughter nucleus is distributed among the electron, neutrino, and daughter nucleus according to quantum mechanical phase space. A non-zero neutrino mass manifests as a spectral distortion near the endpoint where the electron's kinetic energy approaches its maxi-

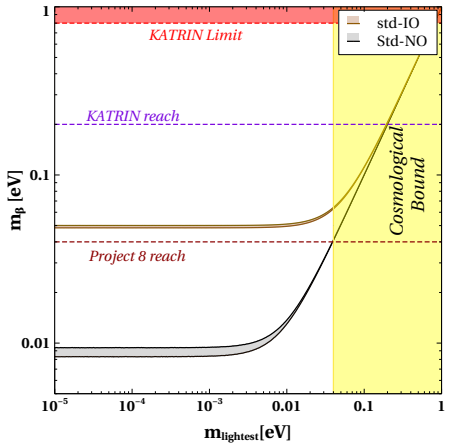

Figure 2.10: m_β is plotted for NO (grey) and IO (brown) scenario against the lightest neutrino mass. Current limit (future sensitivity) of *KATRIN* is shown by red (purple) dashed line whereas the reach of proposed *Project 8* experiment is highlighted in brown dashed line.

mum value. The sensitivity to neutrino mass is enhanced by selecting isotopes with minimal Q-values. Prime candidates include: ^3H, ^{163}Ho, ^{187}Re, ^{135}Cs, and ^{115}In. The current best limit on the effective neutrino mass from β decay comes from *KATRIN* experiment which used ^3H as the decaying nucleus. For tritium decay ($^3H \rightarrow {}^3He^+ + e^- + \nu_e$), the differential electron energy spectrum accounting for neutrino mass eigenstates is [112, 113]:

$$\begin{aligned}\frac{d\Gamma}{dE} &= \frac{G_F^2|V_{ud}|^2}{2\pi^3}(G_V^2+3G_A^2)F(Z,\beta)\beta(E+m_e)^2(E_0-E) \\ &\times \sum_{i=1}^{3}|U_{ei}|^2\sqrt{(E_0-E)^2-m_i^2}\,\Theta\,(E_0-E-m_i),\end{aligned} \tag{2.72}$$

where G_F is the Fermi constant, V_{ud} is (1,1) element of the CKM matrix, $F(Z,\beta)$ the Fermi function and $E(\beta)$ is the energy (velocity) of the emitted electron. E_0 is the "*endpoint energy*" of the electron corresponding to zero neutrino mass. The step function $\Theta(E_0-E-m_i)$ enforces the energy conservation. If the energy resolution exceeds neutrino mass splitting, the spectrum can be characterised by an effective electron-weighted mass,

$$m_\beta = \sqrt{\sum_{i=1}^{3}|U_{ei}|^2 m_i^2}. \tag{2.73}$$

All the information of neutrino mass is encoded near the end point energy of the spectrum where the differential energy of the electron spectrum can be modeled as [114],

$$\frac{dN}{d\epsilon} \approx 3rt\epsilon^2 \left(1 - \frac{m_\beta^2}{2\epsilon^2}\right), \tag{2.74}$$

where $\epsilon = E_0 - E$, r is the rate into the last 1 eV of the spectrum with $m_\beta = 0$, and t is the observation time. An example of the endpoint spectrum distortion due to a finite neutrino mass is shown in Fig 2.9. The current stringent limit on the effective neutrino mass using this method is obtained from the *KATRIN* experiment, with $m_\beta \leq 0.8$ eV mass at 90% CL from the tritium β decay with a future sensitivity upto $m_\beta \leq 0.2$ eV. The *Project 8* collaboration is developing a novel approach using Cyclotron Radiation Emission Spectroscopy (CRES) to measure electrons from β decay. By Utilizing atomic tritium source the projected sensitivity can go up to $m_\beta \leq 0.04$ eV at (90% CL) [112]. This next-generation experiment aims to improve upon current neutrino mass limits by an order of magnitude compared to existing technologies. Fig. 2.10 shows that the future sensitivity of the *KATRIN* experiment can probe the lightest neutrino mass up to $m_{\text{lightest}} \approx 0.1$ eV but will not be able to distinguish between the NO and IO ordering whereas the *Project 8* experiment can completely probe the IO scenario of neutrinos and for the NO case, it can probe the lightest neutrino mass upto 0.02 eV, considering the standard three neutrino flavour scenario.

Effective Majorana mass from $0\nu\beta\beta$

Cosmological observations and tritium decay measurements are sensitive to the absolute mass scale of neutrinos but not to their nature. If the neutrinos are Majorana type, then it validates lepton number violation in the theory, which is believed to be an accidental symmetry in the SM. The violation of lepton number can be probed through a very rare process called $0\nu\beta\beta$ and it also provides information about the neutrino mass scale. The $0\nu\beta\beta$ unambiguously proves the Majorana nature of the neutrinos [115]. In the minimal extension

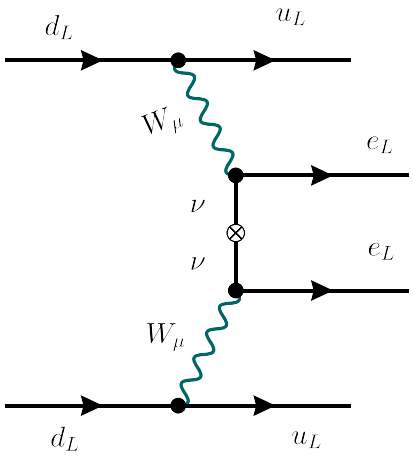

Figure 2.11: The standard mechanism of $0\nu\beta\beta$ in the SM extended with Majorana mass of neutrinos. Note that the neutrino mass insertion is represented by a cross in the ν propagator.

of the SM, where neutrinos turn out to be Majorana, $0\nu\beta\beta$ can occur through the Feynman diagram given in Fig 2.11. $0\nu\beta\beta$ experiments such as *KamLAND-Zen* [116], *GERDA* [117], *CUPID* [118], *CUORE* [119], *LEGEND* [120], *EXO-200* [121], *nEXO* [122] measures the half-life of the decaying isotope, which can be expressed as,

$$T_{1/2} = \frac{m_e^2}{G_{0\nu} |\mathcal{M}_{0\nu}|^2 m_{ee}^2}, \tag{2.75}$$

where m_e is electron mass, $G_{0\nu}$ denotes the leptonic phase space factor (PSF) and $\mathcal{M}_{0\nu}$ is the nuclear transition matrix element (NME) of the decay and m_{ee} (also popularly known as m_{ee}) is the effective Majorana mass which can be expressed as,

$$m_{ee} = \sum_i U_{ei}^2 m_i, \tag{2.76}$$

where i runs over the light neutrino species.

So far, the decay has not been observed by any of the experiment, only an upper limit exists. Upper limits on $m_{ee} \leq (36 - 156)$ meV and $(79 - 180)$ meV are reported by the *KamLAND-Zen* and *GERDA* experiments respectively. However, the major uncertainty in the m_{ee} measure comes from the nuclear ma-

Table 2.1: 3σ ranges of different combinations of oscillation parameters relevant to understanding the effective Majorana mass in the standard three-flavour scenario.

Param.	$\sqrt{r}$	$\sqrt{r}\, s^2_{12}$	$\sqrt{r}\, \cos 2\theta_{12}$	t^2_{13}	$\sqrt{r}\, t^2_{13}$
Max	0.18	0.0614	0.0828	0.0246	0.00443
Min	0.16	0.0432	0.0509	0.0204	0.00326

trix elements calculations. In the standard three-flavour framework Eq. (2.76) can be expressed as

$$m^{\rm std}_{ee} \;=\; m_1\, c^2_{12}\, c^2_{13} + m_2\, s^2_{12}\, c^2_{13}\, e^{i\alpha} + m_3\, s^2_{13}\, e^{i\beta}. \tag{2.77}$$

Unlike neutrino oscillation experiments, the effective Majorana mass is sensitive to the Majorana phases of the neutrinos. In addition, the effective Majorana mass is also sensitive to the mass orderings. In Fig. 2.12 grey and light brown regions display the effective Majorana mass governing $0\nu\beta\beta$ as a function of the lowest mass in the standard three-flavour framework for NO and IO respectively. In these figures, the oscillation parameters are varied over their 3σ ranges as tabulated in the Tab. 1.2, and Majorana phases (α, β) are varied between $(0 : \pi)$.

The following observations can be made from Fig. 2.12 for the NO case $(m_1 < m_2 < m_3)$:

- For $m_{\rm lightest}(m_1) << \sqrt{\Delta m^2_{\rm sol}} << \sqrt{\Delta m^2_{\rm atm}}$, $m_2 \approx \sqrt{\Delta m^2_{\rm sol}} \approx 0.01\,$eV and $m_3 \approx \sqrt{\Delta m^2_{\rm atm}} \approx 0.05\,$eV. The effective Majorana mass can be approximated as

$$\mathbf{m}^{\rm std-NO}_{ee} \;=\; \sqrt{\Delta m^2_{\rm atm}} c^2_{13} \left(\sqrt{r}\, s^2_{12}\, e^{i\,\alpha} + t^2_{13}\, e^{i\beta} \right), \tag{2.78}$$

  where $r = \frac{\Delta m^2_{\rm sol}}{\Delta m^2_{\rm atm}}$. Complete cancellation is possible if $\sqrt{r}\, s^2_{12} = t^2_{13}$. In Tab. 2.1, we enlist different combinations of parameters appearing in the expression of $\mathbf{m}^{\rm std-NO}_{ee}$. As can be seen from the Tab. 2.1, the maximum value of t^2_{13} is much less than $\sqrt{r}\, s^2_{12}$, so complete cancellation is not pos-

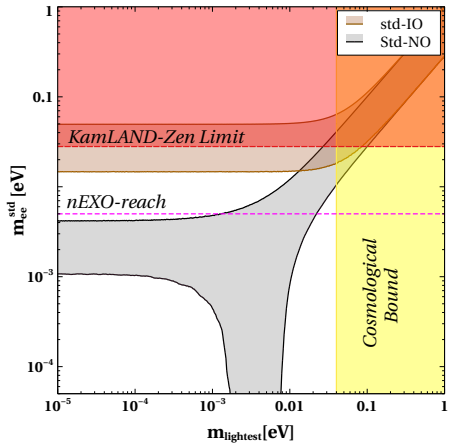

Figure 2.12: $m_{ee}^{\rm std}$ is plotted for NO (grey) and IO (light brown) scenario against the lightest neutrino mass with neutrino mixing parameters varied over their 3σ ranges.

sible in this region. For $\alpha = \beta = 0$, we get the highest value of $\mathbf{m}_{ee}^{\rm std-NO}$, while the lowest value is obtained for $\alpha = 0\,,\ \beta = \pi$ or $\alpha = \pi\,,\ \beta = 0$. In this region, the effective mass satisfies $0.001\,\text{eV} \lesssim \left|\mathbf{m}_{\rm ee}^{\rm std-NO}\right| \lesssim 0.004\,\text{eV}$.

- For $m_{\rm lightest} \approx \sqrt{\Delta m^2_{\rm sol}}$, $\mathbf{m}_{ee}^{\rm std-NO}$ can be expressed as

$$\mathbf{m}_{ee}^{\rm std-NO} \;=\; \sqrt{\Delta m^2_{\rm atm}}\, c^2_{13} \left(\sqrt{r} c^2_{12} + \sqrt{r}\, s^2_{12}\, e^{i\,\alpha} + t^2_{13}\, e^{i\,\beta}\right). \qquad (2.79)$$

  The effective mass attains minimum value for $\alpha = \beta = \pi$ and complete cancellation occurs when $\sqrt{r}\,\cos 2\theta_{12} = t^2_{13}$ From Tab. 2.1, it can be inferred that complete cancellation is not possible in this region, which is also observed in Fig. 2.12.

- It can also be seen that the value of m_{ee}^{std} is very small in a region $0.002\,\text{eV} \lesssim \mathrm{m}_{\rm lightest} \lesssim 0.007\,\text{eV}$. This region is commonly referred to as the cancellation region. To provide a numerical estimate, considering the mixing parameters equal to their best fit values and $m_{\rm lightest} = 0.005\,\text{eV}$, the value of the effective Majorana mass turns out to be $m_{ee}^{std} \approx 10^{-4}$ for the Majorana phases $\alpha = \beta = \pi$.

Similarly, for the Inverted ($m_3 < m_1 < m_2$) mass ordering of neutrinos:

- In the limit $m_3 \approx 0$, $m_1 \approx m_2 \approx \sqrt{\Delta m^2_{\rm atm}}$ and the effective mass can be

expressed as,

$$\mathbf{m}_{ee}^{\text{std}-\text{IO}} \;=\; \sqrt{\Delta m^2_{\text{atm}}}\, c^2_{13} \left(c^2_{12} + s^2_{12}\, e^{i\,\alpha} \right). \tag{2.80}$$

In this region, $\mathbf{m}_{ee}^{\text{std}-\text{IO}}$ is bounded from below and above by minimum and maximum values as,

$$\begin{aligned} \left|\mathbf{m}_{ee}^{\text{std}-\text{IO}}\right|_{\text{min}} &= \sqrt{\Delta m^2_{\text{atm}}}\, c^2_{13}\,.\cos 2\theta_{12} = 0.02\,\text{eV} \\ \left|\mathbf{m}_{ee}^{\text{std}-\text{IO}}\right|_{\text{max}} &= \sqrt{\Delta m^2_{\text{atm}}}\, c^2_{13} = 0.05\,\text{eV}\,. \end{aligned} \tag{2.81}$$

In addition to the hierarchical mass orderings (normal and inverted), neutrinos may exhibit a degenerate mass spectrum characterised by ($m_1 \approx m_2 \approx m_3 \gtrsim 0.05\,\text{eV}$). In Fig. 2.12, this region corresponds to $m_{\text{lightest}} \gtrsim \sqrt{\Delta m^2_{\text{atm}}} \gtrsim 0.05$ eV (for both mass orderings), where m_1 , m_2 , m_3 are approximately equal. The effective mass for the quasi degenerate spectrum can be expressed as

$$\mathbf{m}_{ee}^{\text{QD}} \;=\; m_0\, c^2_{13} \left(c^2_{12} + s^2_{12}\, e^{i\alpha} + t^2_{13}\, e^{i\,\beta} \right). \tag{2.82}$$

In this region, cancellation between the different terms in Eq. (2.82) is not possible, as $t^2_{13} \approx 0.02, s^2_{12} \approx 0.3$ will not be able to cancel out $c^2_{12} \approx 0.7$ as can also be seen from the Fig. 2.12. This region is in serious tension with the cosmological observations because, for three degenerate neutrinos, the bound on $m_{\text{lightest}} < 0.04$ eV considering $\sum m_\nu < 0.12$ eV (cf. Eq. (2.70)).

3

Sterile Neutrino and Mass Observables

3.1 Overview

The three-flavour neutrino oscillation (3ν) framework has been firmly established through solar, atmospheric, reactor, and accelerator neutrino oscillation experiments. The observations in these experiments can be explained by neutrino oscillations governed by two mass-squared differences $\Delta m^2_{\text{sol}} \sim 7.5 \times 10^{-5}$ eV^2 (solar), $\Delta m^2_{\text{atm}} \sim 2.5 \times 10^{-3}$ eV^2 (atmospheric), three mixing angles $(\theta_{12}, \theta_{13}, \theta_{23})$ and one Dirac CP phase. However, certain experimental observations remain inconsistent with this 3ν framework. Among these, one of the most intriguing results is the observed excess of electron (anti)neutrino events reported in pure muon (anti)neutrino beams by the *Liquid Scintillator Neutrino Detector (LSND)* [123], followed by similar observations at *MiniBooster Neutrino Experiment (MiniBooNE)* [124].

The *LSND* experiment at Los Alamos National Laboratory searched for $\overline{\nu_\mu} \to \overline{\nu_e}$ oscillations with a detector placed at 30 m from $\overline{\nu}_\mu$ source with energy $20 - 50$ MeV. The *LSND* collaboration reported a significant ν_e event excess of 87.9 ± 22.4 (stat) ± 6.0 (sys), consistent with two-neutrino oscillations, which is shown in the left panel of Fig. 3.1 as a function of reconstructed L/E_ν. This anomalous result was interpreted as a potential indication for oscillations in the presence of an extra neutrino state without any SM interaction, a sterile neutrino [125]. The best-fit parameters for the sterile neutrino oscillation is $\Delta m^2 = 1.2\,\text{eV}^2$ and $\sin^2 2\theta_{\mu e} = 0.003$ [123]. The anomalous re-

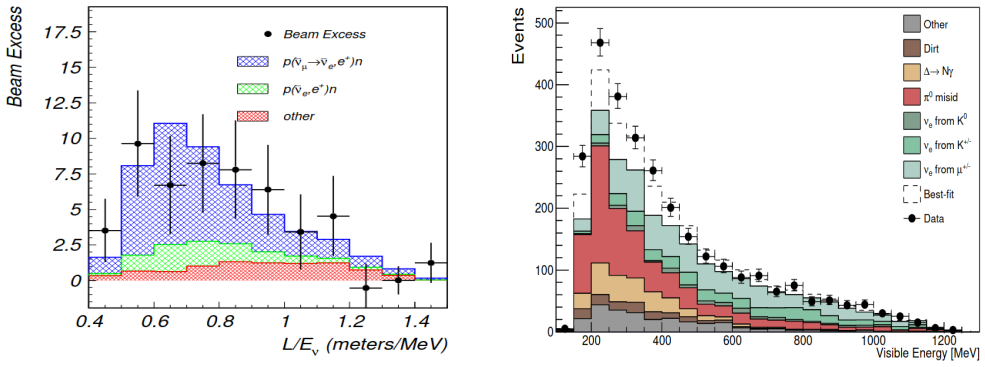

Figure 3.1: (Left Panel:) The *LSND* anomalous events as a function of L/E_ν [123]. The blue shaded region is for a best fit two-neutrino oscillation fit of $\sin^2 2\theta = 0.003$ and $\Delta m^2 = 1.2\,\text{eV}^2$. (Right Panel:) The final *MiniBooNE* results corresponding to 18.75×10^{20} Proton On Target (POT) in neutrino mode for the reconstructed visible energy [124].

sult of *LSND* prompted verification of the sterile neutrino hypothesis in many other experiments. Few experiments probing the appearance channel $P_{\mu e}$ did not observe any excess, e.g., *KARMEN* [126] ruled out sterile neutrino with mass-squared difference $\Delta m_s > 4$ eV^2, whereas, *NOMAD* [127], *ICARUS* [128] ruled out $\Delta m_s > 10$ eV^2, but couldn't rule out the best-fit of LSND. In the follow-up experiment to LSND, *Booster Neutrino Beamline (BNB)* at Fermilab, provided with a $\sim$ 99.5% pure muon neutrino beam with a mean energy of $\sim$ 600 MeV, and the *MiniBooNE* detector was designed maintaining a similar L/E ratio to *LSND* ($L/E \approx 0.4 - 1.0$ m/MeV) while operating at a longer baseline of 540 m and higher peak energy $\sim$700 MeV. *MiniBooNE* collaboration also reported an excess in the $\overline{\nu}_\mu \to \overline{\nu}_e$ channels [129, 130]. This excess can be explained by the inclusion of a sterile neutrino with Δm_s of the order $\sim 1.3\,\text{eV}^2$ [130]. However, this $3+1$ framework including a sterile neutrino of mass $\sim$ 1 eV suffers from a tension between the appearance and the disappearance datasets [131]. The tension originates from the fact that the allowed region of sterile neutrino parameter space obtained from appearance channels in *LSND* and *MiniBooNE* lacks support from the disappearance channel experiments like *MINOS/MINOS+* [132, 133], *Super-Kamiokande* [134], *MicroBooNE* [135], *NOvA* [136], *IceCube Deep-Core* [137]. Moreover, reactor-based electron disappearance experiments such as *Bugey-3* [138] and *Daya-Bay* [139] also did not provide any evidence in favour of a sterile neutrino. Additionally,

MicroBooNE experiment, an upgrade of *MiniBooNE*, using its advanced liquid argon time projection chamber technology with better particle identification and background rejection, reported no excess in electron-like events after three years of data collection [140–142] and showed compatibility with the 3ν scenario within 1σ confidence [143]. Interestingly, it is found that the electron disappearance data from *MicroBooNE* indicates sterile neutrino oscillations with the highest significance of 2.4σ (using the Feldman-Cousins approach) coming from the Wire-Cell analysis, with preferred parameters $\sin^2(2\theta_{14}) = 0.35^{+0.19}_{-0.16}$ and $\Delta m^2_{41} = 1.25^{+0.74}_{-0.39}\text{eV}^2$ [144]. A joint analysis of *MiniBooNE* and *MicroBooNE* data showed preference for the 3+1 neutrino model over the no oscillation hypothesis [145]. Upcoming detectors such as *TRISTAN* [146] at the *KATRIN*, *SBN* [147] at Fermilab, *JSNS2* [148] at *J-PARC*, along with a complete analysis of data in *MicroBooNE* experiment, are expected to shed more light on the existence of an eV-scale sterile neutrino.

Another notable challenge to the standard 3ν framework emerged from the observed discrepancies in electron neutrino flux during the calibration of gallium-based experiments. Radiochemical detectors including *GALLEX* [149], *SAGE* [150], and *BEST* [151] were originally designed to measure solar neutrino flux through the following reaction:

$$\nu_e + {}^{71}Ga \rightarrow {}^{71}Ge + e^-. \tag{3.1}$$

In this process, the produced radioactive ^{71}Ge atoms are chemically extracted and counted to determine the incident neutrino flux. During the calibration of the detectors using artificial ^{51}Cr and ^{37}Ar neutrino sources with precisely known neutrino energy, the detectors observed a deficit of electron neutrinos compared to the theoretical predictions at a combined significance of 4.5σ. This anomaly, known as the "*gallium anomaly*", could be explained by introducing an additional light neutrino state with $\Delta m^2 \sim 1\,\text{eV}^2$ [125]. These results have been interpreted as evidence for oscillations in the presence of a sterile neutrino with $\Delta m^2 \sim 1\text{eV}^2$, suggesting an extension of the standard 3ν framework.

There are also motivations for considering sterile neutrinos with mass-

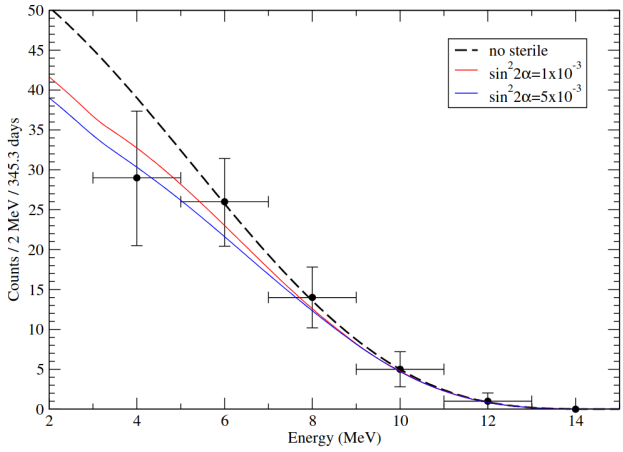

Figure 3.2: The figure shows the prediction for $B-$ neutrino spectrum at Borexino [153] versus the experimental data [152].

squared differences much below the $1\,\mathrm{eV}^2$, coming from other sectors of neutrino experiments. Three flavour neutrino oscillation framework with the solar matter effect predicts an upturn in the survival probability P_{ee} in the $1-7$ MeV energy range. However, measurements of the solar neutrino spectrum in Super Kamiokande-III [14] with a lower threshold and Borexino [152] have not seen this upturn below 8 MeV. Motivated by this, in [153], a sterile neutrino with a mass-squared difference (Δm_s^2) of $\sim 10^{-5}\,\mathrm{eV}^2$ has been proposed to explain the absence of the expected upturn in solar neutrino survival probability below 8 MeV. The situation is depicted in Fig. 3.2 where it is shown that the Borexino data can be explained with the inclusion of a sterile neutrino with mass-squared difference $\Delta m_s^2 \sim 10^{-5}\,\mathrm{eV}^2$ and $\sin^2\alpha \simeq 10^{-3}$ compared to the no sterile neutrino scenario.

Tokai to Kamioka (T2K) [154–157] in Japan and *NuMI Off-Axis ν_e Appearance* ($NO\nu A$) [158–160] in United States are two major accelerator neutrino experiments, operating at baseline of 295 km and 810 km respectively setup to precisely measure the neutrino oscillation parameters. These experiments have a good sensitivity towards currently unknown parameters: mass orderings and Dirac CP phase (δ_{CP}). The analysis of *T2K* and $NO\nu A$ data suggests different best fit region in $\sin^2\theta_{23} - \delta_{CP}$ space for normal mass-ordering. The major tension is *T2K* prefers $\delta_{CP} = 3\pi/2$ for the NO scenario, which is disfavoured by $NO\nu A$ at 2σ. Although for IO, they both prefer $3\pi/2$, the global analy-

sis of the neutrino oscillation data, as well as the joint analysis of these two experiments, slightly prefers the NO at $2-3\sigma$. It has been shown that the tension between *NOνA* and *T2K* data could be partially alleviated by introducing a sterile neutrino with $\Delta m_s^2 \sim (10^{-4} : 10^{-2})$ eV^2 [161]. The potential of sterile neutrinos would not only introduce a new fundamental particle species but might also imply novel interactions beyond the SM framework. Recent studies have explored the implications of sub-eV sterile neutrinos in future experiments, particularly in the context of long-baseline atmospheric neutrino measurements [162–165].

In this chapter, the impact of an ultralight sterile neutrino with Δm_s^2 in the range $(10^{-4} : 10^{-2})$ eV^2 is examined in relation to mass-related observables such as sum of neutrino masses (Σ), effective electron mass (m_β) and effective Majorana mass (m_{ee}). Such investigations in the context of an eV-scale sterile neutrino have been explored in [166]. Here, along with the sub-eV scale sterile neutrino, we also present the results for an eV-scale sterile neutrino with the current constraints on the mixing parameters. We consider the 3+1 picture with a single sterile neutrino added to the three sequential SM neutrinos. In this case, there can be four mass possible spectra, two each with $\Delta m_s^2 > 0$ and $\Delta m_s^2 < 0$. We explore the implications of the cosmological constraint on the sum of light neutrino masses for these spectra. We also discuss the constraints on the possible mass spectra in the light of *KATRIN* results on m_β and *KamLAND-Zen* results on m_{ee}. Additionally, we examine the implications of the future measurements by proposed experiments *Project8*, *nEXO*.

The rest of the chapter is as follows: Section 3.2 gives a brief overview of the neutrino mass and mixing scenarios in the 3+1 framework. In section 3.3, 3.4 and 3.5, we discuss the implications of the various mass spectra in cosmology. nuclear β decay and $0\nu\beta\beta$. Section 3.6 presents an analysis on the correlation among Σ, m_β and m_{ee}. Finally, we summarise all the findings in section 3.7.

3.2 The 3+1 neutrino flavour framework

In the $3+1$ framework, the presence of a sterile neutrino introduces several new parameters: an additional mass-squared difference $(\Delta m^2_s \equiv m^2_4 - m^2_1)$, three new mixing angles $(\theta_{14}\,,\,\theta_{24}\,,\theta_{34})$, two new Dirac CP-violating phases $(\delta_{14}\,,\,\delta_{24})$, and one extra Majorana phase (γ). The neutrino mass matrix in the flavour basis can then be expressed as,

$$\mathcal{M}^s_\nu \;=\; U\, M^{\rm diag}_\nu\, U^T, \quad \text{where} \quad M^{\rm diag}_\nu = \text{diag}\,(\mathrm{m}_1, \mathrm{m}_2, \mathrm{m}_3, \mathrm{m}_4)\,. \tag{3.2}$$

The mixing matrix U can be parameterised as,

$$\begin{aligned} U \;&=\; R_{34}(\theta_{34})\,\widetilde{R}_{24}(\theta_{24},\delta_{24})\,\widetilde{R}_{14}(\theta_{14},\theta_{14})\,R_{23}(\theta_{23})\,\widetilde{R}_{13}(\theta_{13},\delta_{13})\,R_{12}(\theta_{12})\,P \\ &=\; \begin{pmatrix} U_{e1} & U_{e2} & U_{e3} & U_{e4} \\ U_{\mu 1} & U_{\mu 2} & U_{\mu 3} & U_{\mu 4} \\ U_{\tau 1} & U_{\tau 2} & U_{\tau 3} & U_{\tau 4} \\ U_{s1} & U_{s2} & U_{s3} & U_{s4} \end{pmatrix}, \end{aligned} \tag{3.3}$$

where R_{ij}'s are the standard rotational matrices in the i,j generational space. For instance

$$R_{34}(\theta_{34}) \;=\; \begin{pmatrix} 1 & 0 & 0 & 0 \\ 0 & 1 & 0 & 0 \\ 0 & 0 & c_{34} & s_{34} \\ 0 & 0 & -s_{34} & c_{34} \end{pmatrix}, \quad \widetilde{R}_{14}(\theta_{14},\delta_{14}) = \begin{pmatrix} c_{14} & 0 & 0 & s_{14}\,e^{-i\,\delta_{14}} \\ 0 & 1 & 0 & 0 \\ 0 & 0 & 1 & 0 \\ -s_{14}\,e^{i\,\delta_{14}} & 0 & 0 & c_{14} \end{pmatrix}.$$

Here, $c_{ij}(s_{ij})$ stands for $\cos\theta_{ij}\,(\sin\theta_{ij})$ and P is the diagonal matrix containing the Majorana phases, defined as $P = \text{diag}\left(1,\, e^{i\frac{\alpha}{2}},\, e^{i\left(\frac{\beta}{2}+\delta_{13}\right)},\, e^{i\left(\frac{\gamma}{2}+\delta_{14}\right)}\right)$.

In this 3+1 framework, the sign and the magnitude of Δm^2_s lead to different mass spectra.

1. **SNO-NO** $(\Delta m^2_s > 0\,,\, \Delta m^2_{\rm atm} > 0\,)$**:**

   In this scenario, mass orderings are different for $\Delta m^2_s > \Delta m^2_{\rm atm}$ and $\Delta m^2_s < \Delta m^2_{\rm atm}$ which is depicted in Fig. 3.3. The left panel corresponds to

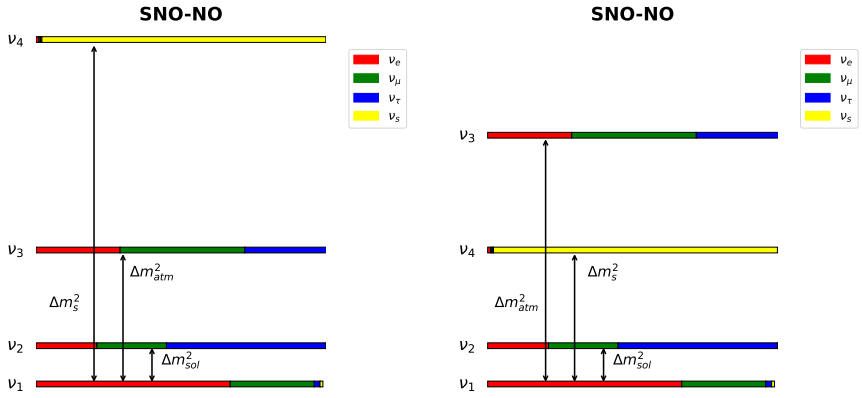

Figure 3.3: SNO-NO mass spectra with the inclusion of a sterile neutrino. Here $\nu_1, \nu_2, \nu_3, \nu_4$ are the mass eigenstates and red, green, blue, and yellow are the proportions of ν_e, ν_μ, ν_τ and ν_s in the respective mass states. When $\Delta m^2_s > \Delta m^2_{\text{atm}}$, the spectrum follows the left side figure, and right side figure depicts the $\Delta m^2_s < \Delta m^2_{\text{atm}}$ scenario.

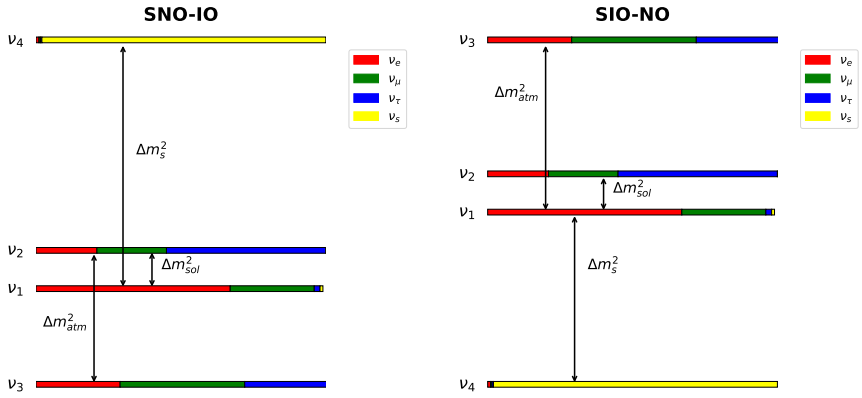

Figure 3.4: SIO-NO mass spectra with the inclusion of a sterile neutrino. Here $\nu_1, \nu_2, \nu_3, \nu_4$ are the mass eigenstates and red, green, blue, and yellow are the proportions of ν_e, ν_μ, ν_τ and ν_s in the respective mass states. The spectra is same for both $\Delta m^2_s > \Delta m^2_{\text{atm}}$ and $\Delta m^2_s < \Delta m^2_{\text{atm}}$ cases.

$\Delta m^2_s > \Delta m^2_{\text{atm}}$ and the mass ordering is $m_1 < m_2 < m_3 < m_4$. Whereas for $\Delta m^2_s < \Delta m^2_{\text{atm}}$, the ordering is $m_1 < m_2 < m_4 < m_3$ and shown in the right panel. In both cases, the mass relations are expressed as

$$\begin{aligned} m_{\text{lightest}} = m_1, \qquad & m_2 = \sqrt{m_1^2 + \Delta m^2_{\text{sol}}} \\ m_3 = \sqrt{m_1^2 + \Delta m^2_{\text{atm}}}, \qquad & m_4 = \sqrt{m_1^2 + \Delta m^2_s}. \end{aligned} \tag{3.4}$$

2. **SNO-IO** $(\Delta m^2_s > 0\,,\, \Delta m^2_{\text{atm}} < 0\,)$ **:**

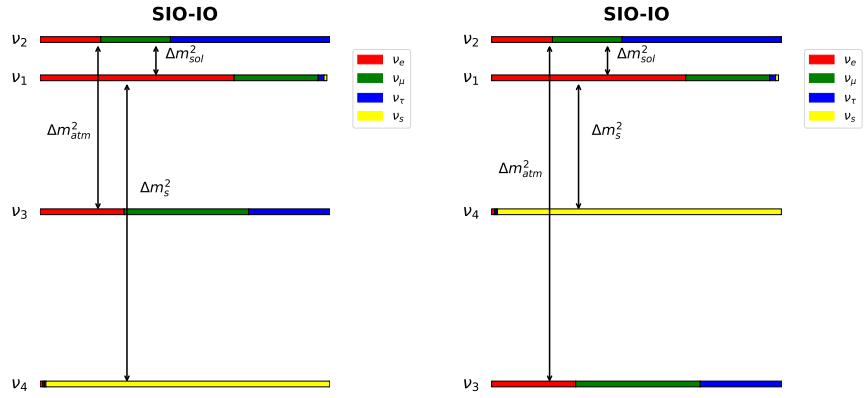

Figure 3.5: SIO-IO mass spectra with the inclusion of a sterile neutrino. Here $\nu_1, \nu_2, \nu_3, \nu_4$ are the mass eigenstates and red, green, blue, and yellow are the proportions of ν_e, ν_μ, ν_τ and ν_s in the respective mass states. The spectra is same for both $\Delta m^2_s > \Delta m^2_{\text{atm}}$ and $\Delta m^2_s < \Delta m^2_{\text{atm}}$ cases.

In this case, the ordering of neutrino mass eigenstates is the same for both $\Delta m^2_s > \Delta m^2_{\text{atm}}$ and $\Delta m^2_s < \Delta m^2_{\text{atm}}$ and delineated in the left panel of Fig. 3.4. The mass spectrum becomes $m_3 < m_1 < m_2 < m_4$ and is expressed as,

$$\begin{aligned} m_{\text{lightest}} = m_3, \qquad m_2 &= \sqrt{m_3^2 + \Delta m^2_{\text{atm}}} \\ m_1 = \sqrt{m_3^2 + \Delta m^2_{\text{atm}} + \Delta m^2_{\text{sol}}}, \qquad m_4 &= \sqrt{m_3^2 + \Delta m^2_{\text{atm}} - \Delta m^2_{\text{sol}} + \Delta m^2_s}. \end{aligned} \tag{3.5}$$

3. **SIO-NO** $(\Delta m^2_s < 0\,,\, \Delta m^2_{\text{atm}} > 0\,)$ **:**
   The mass ordering in this scenario is defined as $m_4 < m_1 < m_2 < m_3$, and it is the same for both the Δm^2_s ranges. The mass relations can be written as,

$$\begin{aligned} m_{\text{lightest}} = m_4, \qquad m_2 &= \sqrt{m_4^2 + \Delta m^2_s + \Delta m^2_{\text{sol}}} \\ m_1 = \sqrt{m_4^2 + \Delta m^2_s}, \qquad m_3 &= \sqrt{m_4^2 + \Delta m^2_s + \Delta m^2_{\text{atm}}}. \end{aligned} \tag{3.6}$$

4. **SIO-IO** $(\Delta m^2_s < 0\,,\, \Delta m^2_{\text{atm}} < 0\,)$ **:**

   - For $\Delta m^2_s > \Delta m^2_{\text{atm}}$, the mass ordering is $m_4 < m_3 < m_1 < m_2$ and the

mass relations are defined as :

$$\begin{aligned} m_{\text{lightest}} = m_4, \qquad & m_2 = \sqrt{m_4^2 + \Delta m_s^2 + \Delta m_{\text{sol}}^2} \\ m_1 = \sqrt{m_4^2 + \Delta m_s^2}, \qquad & m_3 = \sqrt{m_4^2 + \Delta m_s^2 + \Delta m_{\text{sol}}^2 - \Delta m_{\text{atm}}^2} \end{aligned} \tag{3.7}$$

- For $\Delta m_s^2 < \Delta m_{\text{atm}}^2$, the mass ordering is $m_3 < m_4 < m_1 < m_2$ and the mass relations can be expressed as :

$$\begin{aligned} m_{\text{lightest}} = m_3, \qquad & m_2 = \sqrt{m_3^2 + \Delta m_{\text{atm}}^2} \\ m_1 = \sqrt{m_3^2 + \Delta m_{\text{atm}}^2 - \Delta m_{\text{sol}}^2}, \qquad & m_4 = \sqrt{m_3^2 + \Delta m_{\text{atm}}^2 - \Delta m_{\text{sol}}^2 - \Delta m_s^2}. \end{aligned} \tag{3.8}$$

3.3 Sterile neutrino and cosmology

Light sterile neutrinos can have a significant impact on the evolution of the universe, and using cosmological observations, the presence of sterile neutrinos can be investigated. As discussed in the previous chapter, neutrinos affect cosmology by contributing to the effective relativistic degree of freedom (N_{eff}) when they are relativistic and the matter energy density when they become non-relativistic. Similarly, if the added sterile neutrinos are massless, they contribute to the light relativistic degrees of freedom in the early universe, quantified as N_{eff}, which is directly constrained from CMB and LSS data. The effective relativistic degrees of freedom, $N_{\text{eff}}^{\text{SM}} = 3.0440^{+0.0002}_{-0.0002}$ [108, 109, 167], predicted by the SM, assuming three degenerate light active neutrinos, can increase when the sterile neutrino contribution is added [1].

In presence of the light degree of freedom, i.e., sterile neutrino, the change in the N_{eff} can be written as [172]

$$\Delta N_{\text{eff}} = N_{\text{eff}} - N_{\text{eff}}^{\text{SM}} = \frac{\frac{1}{\pi^2}\int dp\, p^3 f(p)}{\frac{7}{8}\frac{\pi^2}{15}\, T_\nu^{id\,4}}, \tag{3.9}$$

[1] However, N_{eff} can be decreased in certain scenarios like very low-reheating in sterile neutrinos [168, 169] or self-interacting sterile neutrinos [170, 171]

with $f(p)$ is momentum distribution of the sterile neutrino between $p \rightarrow p + dp$ and $T_\nu^{id} = \left(\frac{4}{11}\right)^{1/3} T_\gamma$ is the instantaneous decoupling temperature of active neutrinos. If a sterile neutrino state exhibits large mixing with the active neutrino flavours $(\nu_e, \nu_\mu, \nu_\tau)$, a thermal population of light sterile neutrinos can be produced prior to the neutrino decoupling. This production mechanism is driven by a combination of active-sterile oscillations and collisional interactions (elastic/inelastic scattering) with the SM plasma in the early universe. In other words, initially, the neutrino ensemble solely consists of active states. As the universe cools, the oscillation frequency $\omega_{osc} \sim \Delta m^2/2E$ (where Δm^2 is the mass-squared splitting and E is the neutrino energy) becomes comparable to, and eventually exceeds, the Hubble expansion rate $H(T)$. This allows for coherent active-sterile flavour transitions and populates the early universe with sterile neutrinos. The deficiency in the active flavour states can be compensated by the collisions (including elastic scatterings, annihilation, and production) of neutrino states with the thermal plasma. If the sterile neutrinos thermalise with the active neutrinos in the early universe, which may happen if the mixing angle is large enough, then the temperature of the sterile neutrinos will be the same as the active neutrinos, and so will the distribution function $f(p)$. In this scenario, Eq. (3.9) can be approximated as $\Delta N_{\rm eff} \approx 1$, which is heavily disfavoured by BBN and CMB data. Therefore, a completely thermalised sterile neutrino possesses serious tension with cosmology. But, tuning the mixings of the active-sterile states, these catastrophes can be avoided. There are cases where it may happen that the sterile state follows the same distribution (generally Fermi-Dirac) as the active neutrinos, but they have a different temperature (T_s) from the active neutrinos. In this case,

$$\Delta N_{\rm eff} \;=\; \left(\frac{T_s}{T_\nu^{id}}\right)^4 . \tag{3.10}$$

Therefore, current cosmological limit on $\Delta N_{\rm eff}$ can accommodate thermally distributed sterile neutrinos with $\frac{T_s}{T_\nu^{id}} \leq 0.8$ [172]. This implies a sterile neutrino with temperature, $T_s \lesssim 0.8$ MeV, is allowed by the cosmological data.

There is another popular way to accommodate sterile neutrino with cosmo-

logical scenario, called the non-thermal production of sterile neutrino [173]. If the mixing angle between active and sterile neutrino is very small, then the non-resonant production of the sterile neutrinos in the early universe is very suppressed. Once the universe cools, active-sterile oscillation becomes dominant and sterile neutrinos are produced. In this case, the temperature of the sterile neutrino is the same as the active one, but the momentum distribution is multiplied by the overall constant factor equal to $\Delta N_{\rm eff}$. Hence in this case, $f(p)$ is described as

$$f_s(p) \;=\; \frac{\Delta N_{\rm eff}}{e^{p/T_\nu}+1}. \tag{3.11}$$

To summarise the discussion, the sterile neutrino, when relativistic, contributes to the total radiation content of the universe. If they are thermalised with the active neutrinos, then $\Delta N_{\rm eff} \approx 1$, which is disfavoured, but for non-thermal sterile neutrinos, there is still hope in the cosmological datasets.

Apart from contributing to $N_{\rm eff}$, sterile neutrinos contribute to the matter energy density as they become non-relativistic later in time. At such point in the evolution, its contribution to the energy density can be parametrised as an effective mass [172]

$$\Omega_s\, h^2 \;=\; \frac{h^2\, m_s}{\pi^2\, \rho_{cr,0}} \int dp\, p^2\, f_s(p), \tag{3.12}$$

where $\rho_{cr,0} = \frac{3H_0^2}{8\pi G}$, is the critical energy density in present time, m_s is the sterile neutrino physical mass. For the thermalised sterile neutrino with T_s Eq. (3.12) can be written as

$$\begin{aligned}
\Omega_s\, h^2 \;&=\; \frac{8\pi G\, h^2}{3H_0^2}\, \frac{g_i\, m_s}{2\pi^2} \int dp\, p^2\, \frac{1}{e^{p/T_s}+1} \\
&=\; \frac{m_s}{94.1\text{eV}} \left(\frac{T_{s,0}}{T_{\nu,0}}\right)^3 \\
&=\; \frac{m_s\, \Delta N_{\rm eff}{}^{3/4}}{94.1\text{eV}} = \frac{m_s^{\rm eff}}{94.1\,\text{eV}}.
\end{aligned} \tag{3.13}$$

In case of non-thermal sterile neutrino Eq. (3.12) can be written as

$$\begin{aligned}\Omega_s\, h^2 &= \frac{8\pi G\, h^2}{3H_0^2}\,\frac{g_i\, m_s}{2\pi^2}\int dp\; p^2\,\frac{\Delta N_{\rm eff}}{e^{p/T_s}+1}\\ &= \frac{m_s\,\Delta N_{\rm eff}}{94.1{\rm eV}} = \frac{m_s^{\rm eff}}{94.1\,{\rm eV}}.\end{aligned} \tag{3.14}$$

Therefore, for massive sterile neutrinos, cosmological observations can be affected due to it's contribution to $N_{\rm eff}$ and $m_s^{\rm eff}$. The effective sterile neutrino mass is different from its physical mass (m_s) but can be related as $m_s^{\rm eff} = \Delta N_{\rm eff}^{3/4}\, m_s$ if the neutrinos are thermalised with active neutrinos and $m_s^{\rm eff} = \Delta N_{\rm eff}\, m_s$ for the partially thermalised sterile neutrinos where $\Delta N_{\rm eff} = N_{\rm eff} - N_{\rm eff}^{\rm SM}$.

When PLANK 2018 data is fitted with standard $\Lambda_{\rm CDM}$ cosmological model, it tends to disfavour the presence of extra light relativistic degrees of freedom [31]. However, with the inclusion of more parameters with the standard $\Lambda_{\rm CDM}$ cosmological model and fitting more data from different cosmological observations, the cosmological constraints can be relaxed. For example, in a recent analysis, the Plank + BAO + Hubble parameter measurement [174] + Supernova Ia [175] data fitted with a 10 parameter cosmological model (*10-PCM*) i.e $\Lambda_{CDM} + N_{\rm eff} + m^s_{\rm eff} + w_0 + n_{run}$, gives the constraints on $N_{\rm eff}$ and Σ as follows [176],

$$N_{\rm eff} = 3.11^{+0.37}_{-0.36},\;\; \Sigma m_\nu = 0.16\,{\rm eV}\,, \tag{3.15}$$

where ω_0 is the equation of state parameter of the dark energy and n_{run} is the running of the scalar spectral index, a parameter related to the initial conditions of the universe.

In this analysis, sterile neutrinos are considered to be produced through non-thermally in the early universe. Hence, for this analysis Σm_ν is defined as [177]

$$\sum m_\nu \equiv \Sigma = m_1 + m_2 + m_3 + \Delta N_{\rm eff}\, m_4, \tag{3.16}$$

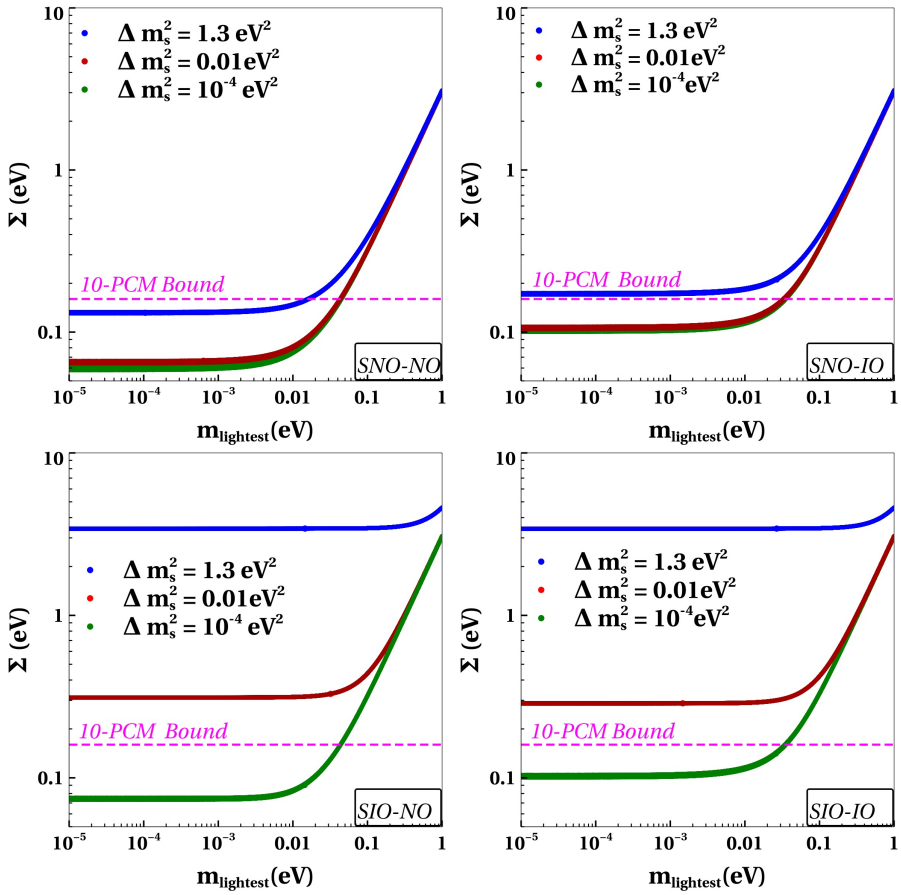

Figure 3.6: The variation total effective mass Σ with the lightest neutrino mass m_{lightest} in different scenarios SNO-NO (top-left), SNO-IO (top-right), SIO-NO (bottom-left), and SIO-IO (bottom-right). The green, red, and blue colours correspond to $\Delta m_s^2 = 10^{-4}\,\text{eV}^2, 0.01\,\text{eV}^2, 1.3\,\text{eV}^2$, respectively. The magenta dashed line corresponds to the 10 parameter cosmological (*10-PCM*) model.

The variation in Σm_ν is plotted as a function of the lightest neutrino mass for different mass schemes in a 3+1 scenario, as shown in Fig. 3.6. The value $N_{\text{eff}} = 3.11$, derived from Eq. (3.15), is adopted for this analysis. Cosmological limit of $\Sigma = 0.16\,\text{eV}$ from *10-PCM* model is indicated by the pink dashed line.

The important features observed from Fig. (3.6) are as follows,

- The *10-PCM* model disfavour $\Delta m_s^2 = 1.3\,\text{eV}^2$ above $m_{\text{lightest}} > 0.01\,\text{eV}$ and $\Delta m_s^2 = 10^{-4}\,\text{eV}^2$, $0.01\,\text{eV}^2$ above $m_{\text{lightest}} > 0.04\,\text{eV}$.
- For SNO-IO, $\Delta m_s^2 = 1.3\ \text{eV}^2$ is disfavoured by the *10-PCM* model for the entire range of m_{lightest}. The lower values of Δm_s^2 are still allowed up to $m_{\text{lightest}} \sim 0.04\,\text{eV}$.

Table 3.1: The table summarises the status of four mass spectra for three different Δm_s^2 in the light of different cosmological models. The limits correspond to the value of $m_{\rm lightest}$ up to which the scenario is allowed.

Mass ordering ($m_{\rm lightest}$)	$\Delta m_s^2 = 10^{-4}\,{\rm eV}^2$	$\Delta m_s^2 = 0.01\,{\rm eV}^2$	$\Delta m_s^2 = 1.3\,{\rm eV}^2$
	Limit *10-PCM*	Limit *10-PCM*	Limit *10-PCM*
SNO-NO (m_1)	< 0.04	< 0.04	< 0.01
SNO-IO (m_3)	< 0.03	< 0.03	Disallowed
SIO-NO (m_4)	< 0.04	Disallowed	Disallowed
SIO-IO (m_3/m_4)	< 0.04	Disallowed	Disallowed

- For SIO-NO and SIO-IO, the *10-PCM* model disfavours $\Delta m_s^2 = 0.01\,{\rm eV}^2$ and $1.3\,{\rm eV}^2$ for the entire range of $m_{\rm lightest}$ but $\Delta m_s^2 = 10^{-4}\,{\rm eV}^2$ is still allowed up to $m_{\rm lightest} \sim 0.03\,{\rm eV}$.

The above discussion is summarised in Tab. 3.1.

So far, the discussion deals with the impact of the sterile neutrino on cosmological observation, and sterile neutrinos are considered to be partially thermalised with the plasma. In order to do so, the active to sterile oscillation probability needs to be small. Thus, in order not to fully thermalise the sterile neutrino prior to BBN via non-resonant collisional processes, the sterile neutrino parameters must satisfy

$$\frac{\Delta m_{\alpha s}^2}{1\,{\rm eV}^2}\,\sin^4 2\theta_{\alpha s} \;\lesssim\; 10^{-5}\,(\Delta N_{\rm eff})^2\,, \tag{3.17}$$

where $\sin^2 2\theta_{\alpha s} = 4\,|U_{\alpha 4}|^2\,|U_{s4}|^2$. For Δm_{41}^2, $|U_{\alpha 4}| = \sin\theta_{14}$ and $|U_{s4}| \approx 1$. Using $N_{\rm eff}$ given in Eq. (3.15), the limits on the active-sterile mixing angle turned out to be $\sin^2\theta_{14} \leq 10^{-3}$ for $\Delta m_{41}^2 = 1.3\,{\rm eV}^2$, $\sin^2\theta_{14} \leq 10^{-2}$ for $\Delta m_{41}^2 = 0.01\,{\rm eV}^2$ and $\sin^2\theta_{14} \leq 0.1$ for $\Delta m_{41}^2 = 10^{-4}\,{\rm eV}^2$. Although cosmology imposes stringent bounds on sterile neutrino mixing angles ($\theta_{\alpha 4}$), these constraints can be evaded in specific scenarios:

- In cosmological scenarios with low reheating temperature ($T_{RH} \lesssim 10$ MeV), the production of sterile neutrinos is significantly suppressed due to incomplete thermalisation processes [169]. The reheating temperature refers to the temperature at which the universe transitions to ra-

diation domination phase from the inflation-dominated expansion. For $T_{RH} \sim \mathcal{O}(1)$ MeV, even the SM active neutrinos have barely enough time to interact with the plasma prior to their decoupling, preventing them from achieving full thermal equilibrium. This suppressed thermalisation of active neutrinos consequently reduces the production rate of sterile neutrinos through active-sterile mixing, as the process relies on the availability of thermalised active states. This mechanism allows for larger values of Δm^2 and $\sin^2\theta$ in the sterile neutrino parameter space, while maintaining a value of N_{eff} consistent with the SM prediction. Such extended parameter ranges may provide viable explanations for various neutrino anomalies while remaining compatible with cosmological constraints. The specific realisation of this scenario depends crucially on the detailed dynamics of the reheating process and subsequent thermalisation history [168, 178–180].

- Models with neutrino self interaction, non-standard interaction or secret interactions [171, 181–184] mediated by new gauge bosons or scalars provide an elegant way to suppress the sterile neutrino production in the early universe to evade the cosmological constraints. The new interactions of the sterile neutrinos generate a matter potential which in turn suppresses the production rate [182, 183]. Additionally, after neutrino decoupling, the same interactions can drive sterile neutrinos into kinetic equilibrium with active neutrinos via scattering, leading to the partial or full equipartition between the active and sterile states. More details on this can be found in Refs. [170, 185–187].

Disregarding cosmological limits, the most stringent bound on the sterile neutrino parameter space ($\sin^2 2\theta_{\mu e}$, Δm^2_{41}) is obtained from dedicated short-baseline experiments *MINOS/MINOS*$^+$ via ν_μ disappearance measurements [188]. In Ref. [139], 90% exclusion limits on the sterile neutrino parameter space is given after comparing *MINOS, MINOS*$^+$*, Daya-Bay and Bugey-3* data and the exclusion contours are given in Fig. 3.7. In Tab. 3.2, the extracted limit on $\sin^2\theta_{14}$ from the exclusion contours are given for reference and in the

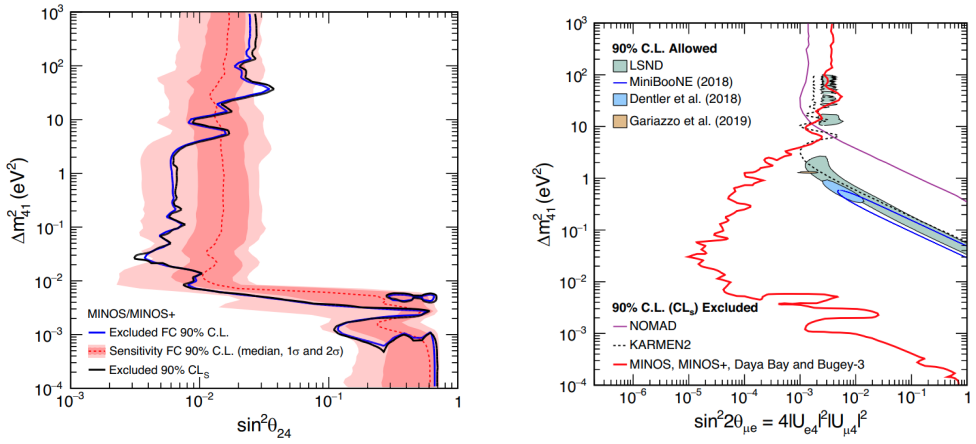

Figure 3.7: This figure presents the 90% confidence level exclusion contours obtained using both the Feldman-Cousins and CLs statistical methods from *MINOS/MINOS+* data [139]. The excluded regions (at right of each curve) represent parameter space ruled out at 90% CL using the CLs approach.

Table 3.2: Allowed values of the sterile neutrino parameters Δm^2_s, $\sin^2\theta_{14}$ in the 3+1 scenario for three different mass squared differences ($\Delta m^2_s = 10^{-4}\,\mathrm{eV}^2$, $0.01\,\mathrm{eV}^2$ and $1.3\,\mathrm{eV}^2$) are given. The value of the $\sin^2\theta_{14}$ is chosen to be consistent with *MINOS* , *MINOS*$^+$, *Daya-Bay* and *Bugey-3* data [133, 139]

Parameters	Case I	Case II	Case III
Δm^2_s	$10^{-4}\,\mathrm{eV}^2$	$10^{-2}\,\mathrm{eV}^2$	$1.3\,\mathrm{eV}^2$
$\sin^2\theta_{14}$	$0.1 \;:\; 0.2$	$5\times10^{-4} \;:\; 5\times10^{-3}$	$0.001 \;:\; 0.01$

forthcoming sections these values will be used.

3.4 Sterile neutrino and Tritium β decay

As discussed earlier, a direct and model-independent constraint on the neutrino mass can be derived through the experimental analysis of the electron energy spectrum resulting from beta decay in atomic nuclei. In presence of the sterile neutrino, the effective electron mass, m_β, can be written as,

$$\begin{aligned} m_\beta &= \sqrt{|U_{e1}|^2 m_1^2 + |U_{e2}|^2 m_2^2 + |U_{e3}|^2 m_3^2 + |U_{e4}|^2 m_4^2} \\ &= \sqrt{c_{12}^2 c_{13}^2 c_{14}^2 m_1^2 + s_{12}^2 c_{13}^2 c_{14}^2 m_2^2 + s_{13}^2 c_{14}^2 m_3^2 + s_{14}^2 m_4^2}. \end{aligned} \tag{3.18}$$

The effective electron neutrino mass m_β is plotted in Fig. 3.8 as a function of the lightest neutrino mass, with all parameters in Eq. (3.18) varied within

Table 3.3: 3σ ranges of different combinations of oscillation parameters relevant to understanding kinematic mass (m_β) in the 3+1 scenario.

$\lvert U_{e2}\rvert^2\Delta m^2_{\rm sol}$	$(1-\lvert U_{e2}\rvert^2)$ $\times\Delta m^2_{\rm sol}$	$\lvert U_{e3}\rvert^2\Delta m^2_{\rm atm}$	$\lvert U_{e4}\rvert^2\,\Delta m^2_s$		
			$\Delta m^2_s\,(10^{-4}\text{eV}^2)$	$\Delta m^2_s\,(0.01\text{eV}^2)$	$\Delta m^2_s\,(1.3\text{eV}^2)$
$(1.77 : 2.65)$ $\times 10^{-5}$	$(4.57 : 5.95)$ $\times 10^{-5}$	$(4.86 : 6.24)$ $\times 10^{-5}$	$(1:2)\times 10^{-5}$	$(0.5 : 5)\times$ 10^{-5}	$(0.13 : 1.3)\times$ 10^{-2}

their experimentally allowed ranges, and $\sin^2\theta_{14}$ varied as specified in Tab. 3.2. The projected sensitivities of the *KATRIN* experiment (0.2 eV) and the future *Project 8* experiment (40 meV) are indicated by a cyan dashed line and a black dash-dotted line, respectively. In Tab. 3.3, the necessary values are provided to explain the characteristics of Fig. 3.8. In the following subsections, we describe the features of Fig. 3.8 for different mass spectra.

3.4.1 SNO-NO

For SNO-NO scenario, using Eq. (3.4), Eq. (3.18) can be approximated as

$$m_\beta^{\rm SNO-NO} \;=\; \sqrt{m^2_{\rm lightest} + \lvert U_{e2}\rvert^2\,\Delta m^2_{\rm sol} + \lvert U_{e3}\rvert^2\,\Delta m^2_{\rm atm} + \lvert U_{e4}\rvert^2\,\Delta m^2_s}. \tag{3.19}$$

- For $m_{\rm lightest} < \sqrt{\Delta m^2_{\rm sol}} < \sqrt{\Delta m^2_{\rm atm}}$, it is seen from Tab. 3.3 that the second, third and the fourth term in Eq. (3.19) varies in the similar range for $\Delta m^2_s = 10^{-4}\,\text{eV}^2$ and $\Delta m^2_s = 0.01\,\text{eV}^2$. Hence $m_\beta^{\rm SNO-NO}$ varies as $(0.009 : 0.01)$ and $(0.008 : 0.011)\,\text{eV}$. In the case of $\Delta m^2_s = 1.3\,\text{eV}^2$, $m_\beta^{\rm SNO-NO} \approx \lvert U_{e4}\rvert\sqrt{\Delta m^2_s}$ and varies between $(0.036 : 0.114)\,\text{eV}$.
- For $\sqrt{\Delta m^2_{\rm sol}} < m_{\rm lightest} < \sqrt{\Delta m^2_{\rm atm}} < \sqrt{\Delta m^2_s}$, $m_\beta^{\rm SNO-NO} \approx m_{\rm lightest}$ for $\Delta m^2_s = 10^{-4}\,\text{eV}^2$ and $\Delta m^2_s = 0.01\,\text{eV}^2$. Whereas $\lvert U_{e4}\rvert^2\,\Delta m^2_s$ still dominates in this region for $\Delta m^2_s = 1.3\,\text{eV}^2$.
- For $\sqrt{\Delta m^2_{\rm atm}} << \lvert U_{e4}\rvert\sqrt{\Delta m^2_s} << m_{\rm lightest}$, $m_\beta^{\rm SNO-NO}$ is completely determined by the value of $m_{\rm lightest}$.

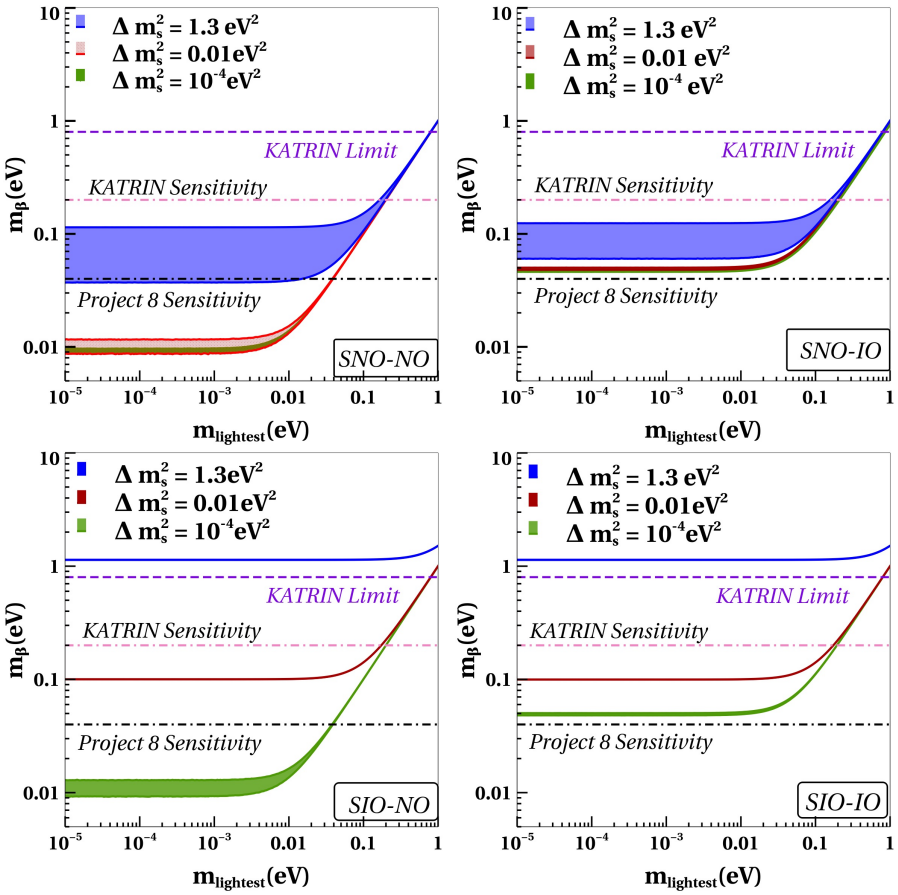

Figure 3.8: Kinematic mass m_β from tritium β decay in different scenarios of SNO-NO (top-left), SNO-IO (top-right), SIO-NO (bottom-left), and SIO-IO (bottom-right) for $\Delta m_s^2 = 10^{-4}\,\text{eV}^2$ (green), $\Delta m_s^2 = 0.01\,\text{eV}^2$ (red) and $\Delta m_s^2 = 1.3\,\text{eV}^2$ (blue).

3.4.2 SNO-IO

For the SNO-IO scenario, m_β can be approximated as

$$\begin{aligned} m_\beta^{\text{SNO-IO}} &= \sqrt{m_{\text{lightest}}^2 + \Delta m_{\text{atm}}^2\,(1-|U_{e3}|^2) + \Delta m_{\text{sol}}^2\,(|U_{e1}|^2 - |U_{e4}|^2) + |U_{e4}|^2\,\Delta m_s^2} \\ &\approx \sqrt{m_{\text{lightest}}^2 + \Delta m_{\text{atm}}^2 + |U_{e4}|^2\,\Delta m_s^2}. \end{aligned} \tag{3.20}$$

- For $m_{\text{lightest}} << \Delta m_{\text{sol}}^2 < \Delta m_{\text{atm}}^2$, $m_\beta^{\text{SNO-IO}} \approx \sqrt{\Delta m_{\text{atm}}^2} \approx 0.05\,\text{eV}$ for $\Delta m_s^2 = 10^{-4}\,\text{eV}^2$ and $0.01\,\text{eV}^2$ as $|U_{e4}|^2$ is very small. For $\Delta m_s^2 = 1.3\,\text{eV}^2$, the value of $m_\beta^{\text{SNO-IO}} \approx \sqrt{\Delta m_{\text{atm}}^2 + |U_{e4}|^2\,\Delta m_s^2}$. Thus, the value of m_β for $\Delta m_s^2 = 1.3\,\text{eV}^2$ is greater than the $\sqrt{\Delta m_{\text{atm}}^2}$ till $m_2 \approx 0.1\,\text{eV}$.
- $0.1 << m_{\text{lightest}}$, $m_\beta^{\text{SNO-IO}} \approx m_{\text{lightest}}$ for the values of Δm_s^2. Hence, for higher m_{lightest}, the behaviour of m_β is fully characterised by m_{lightest}.

3.4.3 SIO-NO

$$m_\beta^{\mathrm{SIO-NO}} = \sqrt{m_{\mathrm{lightest}}^2 + \Delta m_s^2 + |U_{e2}|^2\,\Delta m_{\mathrm{sol}}^2 + |U_{e3}|^2\,\Delta m_{\mathrm{atm}}^2}. \quad (3.21)$$

- For $m_{\mathrm{lightest}} << \sqrt{\Delta m_{\mathrm{sol}}^2} << \sqrt{\Delta m_{\mathrm{atm}}^2}$, $m_\beta^{\mathrm{SIO-NO}} \approx \sqrt{\Delta m_s^2}$ for $\Delta m_s^2 = 0.01\,\mathrm{eV}^2$ and $1.3\,\mathrm{eV}^2$. For $\Delta m_s^2 = 10^{-4}\,\mathrm{eV}^2$, second and third term vary $\sim 10^{-5}$, so we get a small variation due to that.
- For $\sqrt{\Delta m_s^2} << m_{\mathrm{lightest}}$, $m_\beta^{\mathrm{SIO-NO}} \approx m_{\mathrm{lightest}}$, and the value value of $m_\beta^{\mathrm{SIO-NO}}$ depend on m_{lightest} only.

3.4.4 SIO-IO

- For $\Delta m_s^2 > \Delta m_{\mathrm{atm}}^2$, $m_\beta^{\mathrm{SIO-IO}}$ can be written as

$$m_\beta^{\mathrm{SIO-IO}} = \sqrt{m_{\mathrm{lightest}}^2 + \Delta m_s^2}. \quad (3.22)$$

  In this case, the conclusions are similar to SIO-NO for $\Delta m_s^2 = 0.01\,\mathrm{eV}^2$ and $1.3\,\mathrm{eV}^2$.

- For $\Delta m_s^2 < \Delta m_{\mathrm{atm}}^2$, m_{ee}^{SIO-IO} can be expressed as

$$m_\beta^{\mathrm{SIO-IO}} = \sqrt{m_{\mathrm{lightest}}^2 + \Delta m_{\mathrm{atm}}^2}. \quad (3.23)$$

  In this case, for lower $m_{\mathrm{lightest}}\,(< \sqrt{\Delta m_{\mathrm{atm}}^2})$ region , $m_\beta^{\mathrm{SIO-IO}} \approx \sqrt{\Delta m_{\mathrm{atm}}^2} \approx 0.05\,\mathrm{eV}$. For higher values of $m_{\mathrm{lightest}}\,(> \sqrt{\Delta m_{\mathrm{atm}}^2})$, the value of $m_\beta^{\mathrm{SNO-IO}}$ is proportional to m_{lightest}, which leads to a straight line behaviour in the figures.

In summary, *KATRIN*'s future sensitivity allows to probe m_β only above $m_{\mathrm{lightest}} \sim 0.2$ eV for SNO-NO, SNO-IO for all values of Δm_s^2. In case of SIO-NO, SIO-IO *KATRIN* will be able to probe the entire spectrum of m_{lightest} for $\Delta m_s^2 = 1.3$ eV^2, and above $m_{\mathrm{lightest}} \sim 0.02$ eV for $\Delta m_s^2 = 10^{-4}, 0.01$ eV^2. Moreover, in future, the proposed sensitivity of *Project 8* allows to probe m_β

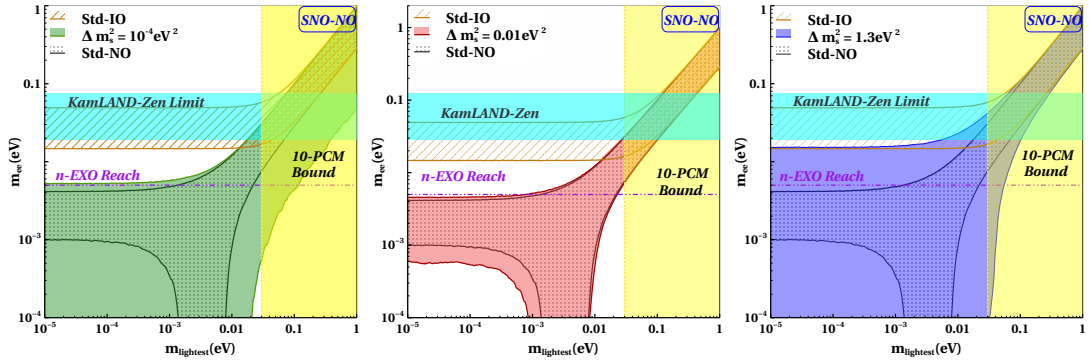

Figure 3.9: m_{ee} is plotted for SNO-NO (green) scenario against the lightest neutrino mass with the mass squared difference (Δm_s^2) = 10^{-4}eV^2 (green), 0.01 eV^2 (red), and 1.3 eV^2(blue) along with standard three flavour NO (black curve) and IO (brown).

only above $m_{\text{lightest}} \sim 0.03$ eV for SNO-NO and SIO-NO of $\Delta m_s^2 = 10^{-4}\,\text{eV}^2$. However, *Project 8* might be able to probe SNO-IO, SIO-NO, and SIO-IO for $\Delta m_s^2 = 0.01\,\text{eV}^2$ and $1.3\,\text{eV}^2$ in the entire range of m_{lightest}.

3.5 Sterile neutrino and $0\nu\beta\beta$

In this section, the behaviour of m_{ee} is studied in the context of various mass orderings in the presence of a light sterile neutrino. The plots in Figs. 3.9, 3.10, 3.11, 3.12 are generated by allowing all the oscillation parameters to vary in their 3σ range as mentioned in Tab. 1.2, and the sterile parameters are varied according to the Tab. 3.2.

3.5.1 SNO-NO

The effective Majorana mass in this scenario can be approximated as

$$m_{ee}^{\text{SNO-NO}} \;=\; c_{14}^2 \left| \mathbf{m}_{ee}^{\text{std-NO}} + t_{14}^2\, m_4\, e^{i\gamma} \right| , \tag{3.24}$$

where $\mathbf{m}_{ee}^{\text{std-NO}}$ is the standard three flavour effective mass for normal ordering. In Fig. 3.9, $m_{ee}^{\text{SNO-NO}}$ as a function of the lightest neutrino mass ($m_{\text{lightest}} = m_1$) for the three mass squared differences is plotted. To explain the behaviour of $m_{ee}^{\text{SNO-NO}}$ in Fig. 3.9, different limits of m_{lightest} is considered.

Table 3.4: 3σ ranges of different combinations of oscillation parameters relevant to understanding the effective Majorana mass for SNO-NO in the 3+1 framework.

Regions	$\mathbf{m}_{ee}^{\text{std}-\text{NO}}$ (eV)	$\lvert m_4\, t_{14}^2 \rvert$ (eV)		
		$\Delta m_s^2 = 10^{-4}\,\text{eV}^2$	$\Delta m_s^2 = 0.01\,\text{eV}^2$	$\Delta m_s^2 = 1.3\,\text{eV}^2$
$m_1 \approx 0$	0.001 : 0.004	0.001 : 0.002	5×10^{-5} : 10^{-4}	0.001 : 0.01
$m_1 \approx \sqrt{\Delta m^2_{\text{sol}}}$	0.0018 : 0.018	0.0014 : 0.003	5×10^{-5} : 10^{-4}	0.001 : 0.01
$m_1 \approx 0.1$	0.02 : 0.1	0.01 : 0.02	5×10^{-4} : 10^{-3}	0.001 : 0.01

The values of different terms in Eq. (3.24) are mentioned for various limits of m_1 in the Tab. 3.4, where the maximum value of $m_{ee}^{\text{SNO}-\text{NO}}$ corresponds to $\gamma = 0$ and the minimum is for $\gamma = \pi$. The important points are as follows:

- For $m_1 << \sqrt{\Delta m^2_{\text{sol}}} << \sqrt{\Delta m^2_{\text{atm}}} << \sqrt{\Delta m_s^2}$, it is seen from Tab. 3.4 that for $\Delta m_s^2 = 10^{-4}, 1.3$ eV^2 complete cancellation is possible between $\mathbf{m}_{ee}^{\text{std}-\text{NO}}$ and $m_4\, t_{14}^2$ for $\gamma = \pi$.
- For $m_1 \approx \sqrt{\Delta m^2_{\text{sol}}}$, complete cancellations continue to occur for $\Delta m_s^2 = 10^{-4}, 1.3$ eV^2.
- At higher values of $m_1 \approx 0.1$ eV, complete cancellation happens only for $\Delta m_s^2 = 10^{-4}$ eV^2 as seen from third row.
- In the 3+1 scenario quasi-degenerate (QD) condition will arise when $m_1 \approx m_2 \approx m_3 \approx m_4$. *KamLAND-Zen* and *nEXO*[2] both can probe a fraction of the QD region for $\Delta m_s^2 = 10^{-4}$ eV^2 and the entire region for $\Delta m_s^2 = 0.01$ eV^2. However, cosmological bounds ($m_1 > 0.03$ eV) reject the QD region for both values of Δm_s^2.

3.5.2 SNO-IO

The effective Majorana mass from double beta decay can be expressed as

$$m_{ee}^{\text{SNO}-\text{IO}} \;=\; c_{14}^2 \left| \mathbf{m}_{ee}^{\text{std}-\text{IO}} + t_{14}^2 m_4\, e^{i\gamma} \right| . \tag{3.25}$$

[2]While the work was published, *nEXO* was considered as a promising future $0\nu\beta\beta$ experiment but now the plan for this experiment has been shut down. However, the limit corresponding to *nEXO* remains valid for other ton-scale experiments having sensitivities up to 10^{28} years half-lives.

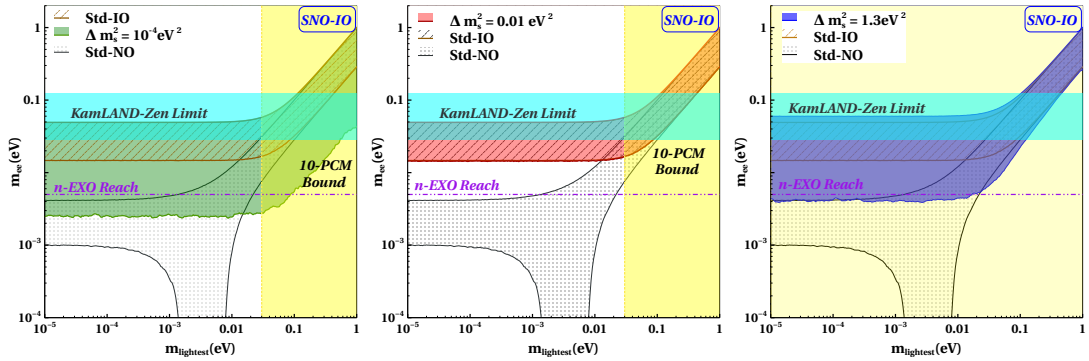

Figure 3.10: m_{ee} is plotted for SNO-IO scenario against the lightest neutrino mass with the mass squared difference (Δm_s^2) = 10^{-4}eV^2 (green), 0.01 eV^2 (red), 1.3 eV^2 (blue) along with standard three flavour Normal Ordering (black curve) and Inverted Ordering (brown-hatched) .

Table 3.5: The 3σ ranges of different combinations of oscillation parameters relevant to understanding the effective Majorana mass for SNO-IO in the 3+1 framework.

Regions	$\mathbf{m}_{ee}^{\text{std}-\text{IO}}$ (eV)	$m_4\, t_{14}^2$ (eV)		
		$\Delta m_s^2 = 10^{-4}\,\text{eV}^2$	$\Delta m_s^2 = 0.01\,\text{eV}^2$	$\Delta m_s^2 = 1.3\,\text{eV}^2$
$m_3 \approx 0$	0.02 : 0.05	0.005 : 0.01	5×10^{-5} : 5×10^{-4}	0.001 : 0.01
$m_3 \approx 0.1$	0.03 : 0.1	0.01 : 0.025	7.5×10^{-5} : 7.5×10^{-4}	0.001 : 0.01

$m_{ee}^{\text{SNO}-\text{IO}}$ as a function of the lightest neutrino mass (m_3) for the three mass squared differences is plotted in the Fig. 3.10. The values of the terms in Eq. (3.25) are enlisted in the Tab. 3.5. The notable points in the SNO-IO case are as follows,

- It is evident from Tab. 3.5, that the minimum value of $\mathbf{m}_{ee}^{\text{std}-\text{IO}}$ is always greater than the maximum value of $m_4\, t_{14}^2$ for all the three mass squared differences. Hence, complete cancellation is not possible for the entire range of m_{lightest}.
- The value of $m_4\, t_{14}^2$ for $\Delta m_s^2 = 0.01\,\text{eV}^2$ is very small compared to $\mathbf{m}_{ee}^{\text{std}-\text{IO}}$. Therefore, $m_{ee}^{\text{SNO}-\text{IO}}$ is approximately equal to $\mathbf{m}_{ee}^{\text{std}-\text{IO}}$, which is visible from the middle panel of Fig. 3.10.
- For $\Delta m_s^2 = 10^{-4}\,\text{eV}^2$ and $1.3\,\text{eV}^2$, the minimum value of $m_{ee}^{\text{SNO}-\text{IO}} \approx 0.01\,\text{eV}$ is attained for $\gamma = \pi$ which can be probed partially in the future experiment, *nEXO*.
- The QD region is occurred at $m_3 > \mathcal{O}(0.1)$ eV for $\Delta m_s^2 = 10^{-4}$, 0.01

Table 3.6: The 3σ ranges of different combinations of oscillation parameters relevant to understanding the effective Majorana mass for SIO-NO in the 3+1 framework.

Regions	$\sqrt{\Delta m_s^2}\cos 2\theta_{12}$ (eV)			$\sqrt{\Delta m^2_{\rm atm}}\, t^2_{13}$ (eV)	$m_4\, t^2_{14}$ (eV)		
	$\Delta m_s^2 = 10^{-4}\text{eV}^2$	$\Delta m_s^2 = 0.01\text{eV}^2$	$\Delta m_s^2 = 1.3\text{eV}^2$		$\Delta m_s^2 = 10^{-4}\text{eV}^2$	$\Delta m_s^2 = 0.01\text{eV}^2$	$\Delta m_s^2 = 1.3\text{eV}^2$
$m_4 \approx 0$	0.003	0.03	0.33	0.001	0	0	0
$m_4 \approx 0.01$	0.003	0.03	0.33	0.001	1×10^{-3} : 2×10^{-3}	5×10^{-5} : 5×10^{-4}	$(10^{-5} : 10^{-4})$

eV^2. Although the QD region is disfavoured by cosmology for both the Δm_s^2 values, *KamLAND-Zen* and *nEXO* can probe this region partially for $\Delta m_s^2 = 10^{-4}$ eV^2 and completely for $\Delta m_s^2 = 0.01$ eV^2.

3.5.3 SIO-NO

In this case, the effective Majorana mass is expressed as,

$$
\begin{aligned}
m_{ee}^{\rm SIO-NO} &\approx c_{14}^2\left(\sqrt{m_4^2+\Delta m_s^2}\left(c_{12}^2+s_{12}^2\,e^{i\alpha}\right)+m_4\,t_{14}^2\,e^{i\,\gamma}\right) \qquad \left[\text{for } \Delta m_s^2 > \Delta m^2_{\rm atm}\right] \\
m_{ee}^{\rm SIO-NO} &\approx c_{14}^2\left(c_{13}^2\left(\sqrt{m_4^2+\Delta m_s^2}\left(c_{12}^2+s_{12}^2\,e^{i\alpha}\right)+\sqrt{m_4^2+\Delta m^2_{\rm atm}}\,s_{13}^2\,e^{i\beta}\right)+m_4\,t_{14}^2\,e^{i\,\gamma}\right) \\
&\qquad\qquad \left[\text{for } \Delta m_s^2 < \Delta m^2_{\rm atm}\right]. \qquad (3.26)
\end{aligned}
$$

In the previous equations, the mass relations mentioned in Eq. (3.6) are used. In Fig. 3.11, m_{ee} as a function of $m_{\rm lightest}$ (m_4) is shown in three panels corresponding to different values of Δm_s^2. Useful values for Eq. (3.26) is given in Tab. 3.6.

- For the region where the lightest mass is negligible, Eq. (3.6) will be,

$$
\begin{aligned}
&m_4 \approx 0, \quad m_2 \approx m_1 \approx m_3 \approx \sqrt{\Delta m_s^2} && \left[\text{for } \Delta m_s^2 > \Delta m^2_{\rm atm}\right] \\
&m_4 \approx 0, \quad m_1 \approx m_2 \approx \sqrt{\Delta m_s^2},\ m_3 \approx \sqrt{\Delta m^2_{\rm atm}} && \left[\text{for } \Delta m_s^2 < \Delta m^2_{\rm atm}\right]. \qquad (3.27)
\end{aligned}
$$

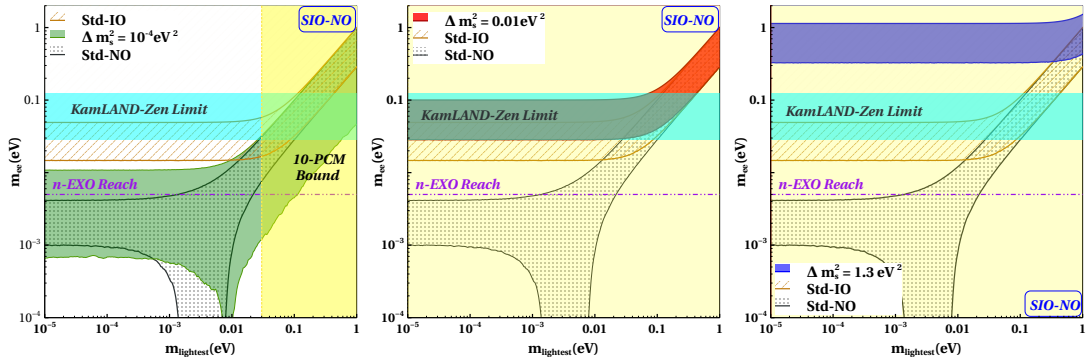

Figure 3.11: m_{ee} is plotted for SIO-NO (green) scenario against the lightest neutrino mass with the mass squared difference $(\Delta m_s^2) = (10^{-4}\,\text{eV}^2, 0.01\,\text{eV}^2, 1.3\,\text{eV}^2)$ along with standard three flavour Normal Ordering (black-curve) and Inverted Ordering (brown hatched).

Therefore, the effective Majorana mass can be approximated as

$$\begin{aligned} m_{ee}^{\text{SIO}-\text{NO}} &= \sqrt{\Delta m_s^2}\left(c_{12}^2 + s_{12}^2\, e^{i\alpha}\right) && \left[\text{for } \Delta m_s^2 > \Delta m_{\text{atm}}^2\right] \\ m_{ee}^{\text{SIO}-\text{NO}} &= c_{13}^2\, c_{14}^2\left(\sqrt{\Delta m_s^2}\left(c_{12}^2 + s_{12}^2\, e^{i\alpha}\right) + \sqrt{\Delta m_{\text{atm}}^2}\, t_{13}^2\, e^{i\beta}\right) && \left[\text{for } \Delta m_s^2 < \Delta m_{\text{atm}}^2\right]. \end{aligned} \tag{3.28}$$

In the first case, complete cancellation can happen for $\alpha = \pi$ and $c_{12}^2 = s_{12}^2$. But, since θ_{12} is less than 45°, this cannot happen, as shown in Fig. 3.11 for $\Delta m_s = 10^{-4}$ eV^2. In the second case, complete cancellation occurs for $\alpha = \beta = \pi$ and

$$\sqrt{\Delta m_s^2}\,\cos 2\theta_{12} = \sqrt{\Delta m_{\text{atm}}^2}\, t_{13}^2\,. \tag{3.29}$$

This condition is not satisfied for $\Delta m_s^2 = 1.3,\, 0.01$ eV^2 as can be seen from Tab. 1.2 and Tab. 3.6. The value of $m_{ee}^{\text{SIO}-\text{NO}}$ varies between $(0.3 : 1)$ eV and $(0.001 : 0.01)$ eV for $\Delta m_s^2 = 1.3, 10^{-4}$ eV^2 respectively, as seen in from Fig. 3.11.

- Around $m_4 \approx 0.01$ eV, in case of $\Delta m_s^2 = 0.01\,\text{eV}^2$ and $1.3\,\text{eV}^2$, the sterile contribution is negligible compared to other terms as the value of θ_{14} is small and thus no cancellation occurs. But due to large θ_{14} for $\Delta m_s^2 = 10^{-4}$, the value of $m_4\, t_{14}^2$ varies between $(0.001 : 0.002)$ which allows us to have a narrow cancellation region for $\alpha = \beta = \gamma = \pi$.

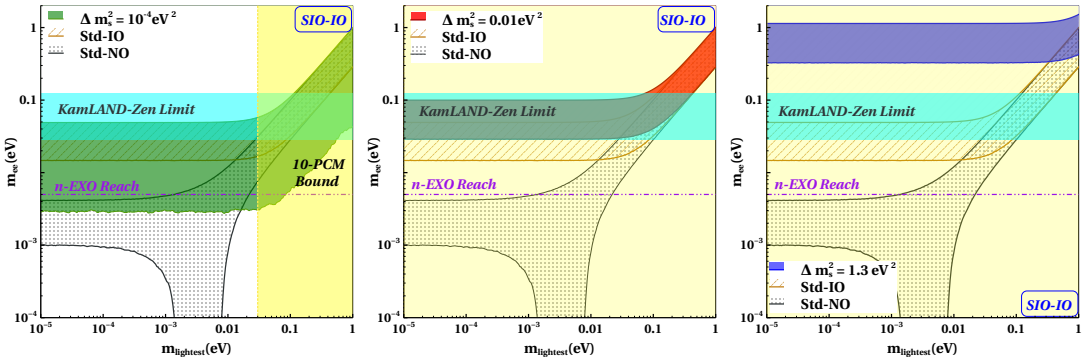

Figure 3.12: m_{ee} is plotted for SIO-IO (green) scenario against the lightest neutrino mass with the mass squared difference (Δm_s^2) = (10^{-4} eV^2, 0.01 eV^2, 1.3 eV^2) along with standard three flavour Normal Ordering (black curve) and Inverted Ordering (brown-hatched) .

- It is to be noted that the *KamLAND-Zen* experiment disallows the entire parameter space of $m_{ee}^{\text{SIO}-\text{NO}}$ for $\Delta m_s^2 = 1.3\,\text{eV}^2$. For $\Delta m_s^2 = 0.01$ eV^2, a part of the parameter space gets disfavoured for all values of m_{lightest}, whereas for $\Delta m_s^2 = 10^{-4}$ eV^2 regions with higher values of $m_{\text{lightest}} (> 0.3\,\text{eV})$ are disfavoured. For 10^{-4} eV^2, the allowed region of $m_{ee}^{\text{SIO}-\text{NO}}$ can be partially probed by *nEXO* experiment.

3.5.4 SIO-IO

In three panels of Fig. 3.12, Majorana mass m_{ee} in SIO-IO scenario is plotted against $m_{\text{lightest}} = m_4$.

- For $\Delta m_s^2 > \Delta m_{\text{atm}}^2$, m_{ee} is exactly similar to the SIO-NO scenario ($\Delta m_s^2 > \Delta m_{\text{atm}}^2$). Thus, the results and the conclusions remain identical.
- For $\Delta m_s^2 < \Delta m_{\text{atm}}^2$, the value of m_{ee} in a region where m_{lightest} is small, can be approximated as

$$\left(m_{ee}^{\text{SIO}-\text{IO}}\right)_{\Delta m_s^2 < \Delta m_{\text{atm}}^2} = \sqrt{\Delta m_{\text{atm}}^2}\, c_{14}^2 \left(c_{12}^2 + s_{12}^2\, e^{i\alpha} + t_{14}^2\, e^{i\gamma}\right). \tag{3.30}$$

Here, complete cancellation requires $\alpha = \gamma = \pi$ and

$$\cos 2\theta_{12} = t_{14}^2\,. \tag{3.31}$$

In this region, complete cancellation is not possible as Eq. (3.31) is not satisfied for the allowed range of mixing angle θ_{14} given in Tab. 3.2.

- When $m_{\text{lightest}} > \sqrt{\Delta m^2_{\text{atm}}}$, $m_1 \approx m_2 \approx m_3 \approx m_4 \approx m_0$ and the value of m_{ee} can be written as

$$\left(m_{ee}^{\text{SIO}-\text{IO}}\right)_{\Delta m^2_s < \Delta m^2_{\text{atm}}} = m_0\, c_{14}^2 \left(c_{12}^2 + s_{12}^2\, e^{i\alpha} + t_{14}^2\, e^{i\gamma}\right) . \tag{3.32}$$

  In this region, cancellation is also not possible, and m_{ee} is proportional to the value of the lightest mass.

- It can be seen from Fig. 3.12, higher values of m_{ee} are disfavoured by *KamLAND-Zen* for all values of m_{lightest} and *nEXO* can rule out an even greater part of the parameter space in the absence of any signal.

In summary, it is realised that all the mass spectra depending on the sterile neutrino mass and mixings have distinct signatures in $0\nu\beta\beta$ experiment. The existing experimental constraints on m_{ee} have already excluded certain regions of the parameter space, unless complete decoupling of the sterile sector from active neutrinos, which assumes $\theta_{14} = 0$, a scenario considered highly improbable. Future ton-scale experiments will play a crucial role in determining the neutrino mass ordering, whether within the standard three-flavour framework or in an extended 3+1 flavour scenario. These next-generation searches are expected to provide significantly improved sensitivity, enabling a more definitive probe of the allowed parameter space for both three flavour and 3+1 flavour scenarios.

3.6 Correlation between mass observables

In the earlier sections, independent constraints on mass variables from cosmology, single β decay, and $0\nu\beta\beta$ are discussed. In this section, the correlations among mass observables are studied. This type of correlation study was first done in ref. [189]. The correlation of m_β against Σ (left), m_{ee} against Σ (middle), and m_{ee} against m_β (right) for all the mass spectra is plotted from Fig. 3.13 to

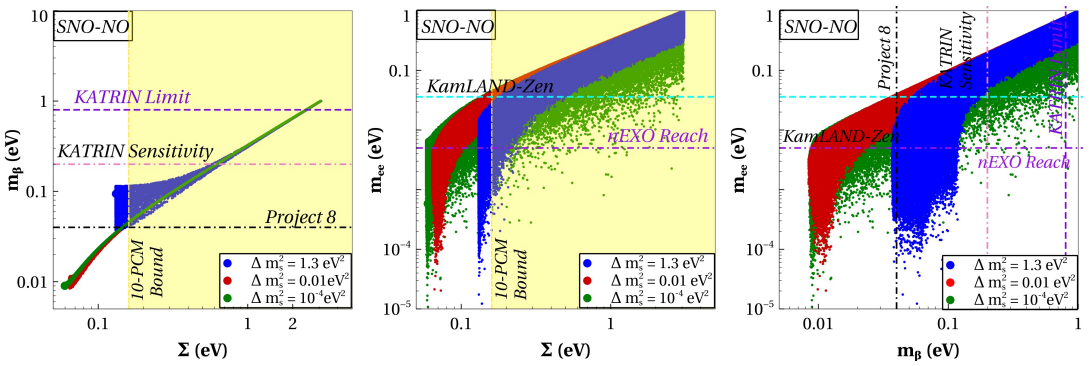

Figure 3.13: Correlations of m_β against and Σ(left) , m_{ee} against Σ (middle) and m_{ee} against m_β (right) for SNO-NO is plotted here. The green, blue, and red regions describe the values for $\Delta m_s^2 = 10^{-4}\,\text{eV}^2$, $0.01\,\text{eV}^2$, and $1.3\,\text{eV}^2$ respectively. The yellow-shaded region corresponds to the exclusion regions by Eq. (3.15).

Fig. 3.16. The yellow-shaded region corresponds to cosmologically excluded regions mentioned in Eq. (3.15). The other horizontal and vertical lines are the current experimental limits (*KamLAND-Zen* [Cyan]) and future sensitivity (*KATRIN* [Pink], *Project 8* [Black], *nEXO* [Magenta]) with their respective colours mentioned in brackets. Blue, red, and green regions in the plots of Fig. 3.13-3.16 correspond to $\Delta m_s^2 = 1.3$, 0.01, 10^{-4} eV^2 respectively. For each value of Δm_s^2, the mixing angles and mass squared differences are varied within the 3σ range mentioned in Tab. 1.2 and Tab. 3.2. The lightest neutrino mass and the Majorana phases are varied over $(10^{-5} : 1)$ eV and $(0 : \pi)$ respectively. The nature of the plots can be understood from the plots of Σ, m_β, m_{ee} presented earlier. For instance, the left-most panel is the correlation plot in the $m_\beta - \Sigma$ plane. From Fig. 3.6 and Fig. 3.8 it is seen that for SNO-NO and $\Delta m_s^2 = 1.3$ eV^2, Σ is in the range $\sim (0.3 : 3)$ eV while m_β is in the range $\sim (0.04 : 1)$ eV. This is reflected in the blue shaded regions in the figure (3.13). For the m_{ee} plots (middle and the right panels) the widths are due to the Majorana phases and correspond to the ranges obtained in Fig. 3.9. Similarly, for other mass spectra, the nature of the plots can also be explained by looking at the figures. Below, the correlations among the different observables is discussed:

1. **SNO-NO**

   The correlation plots for SNO-NO are shown in Fig. 3.13.

   - From the left panel, it is seen that the cosmological mass bound dis-

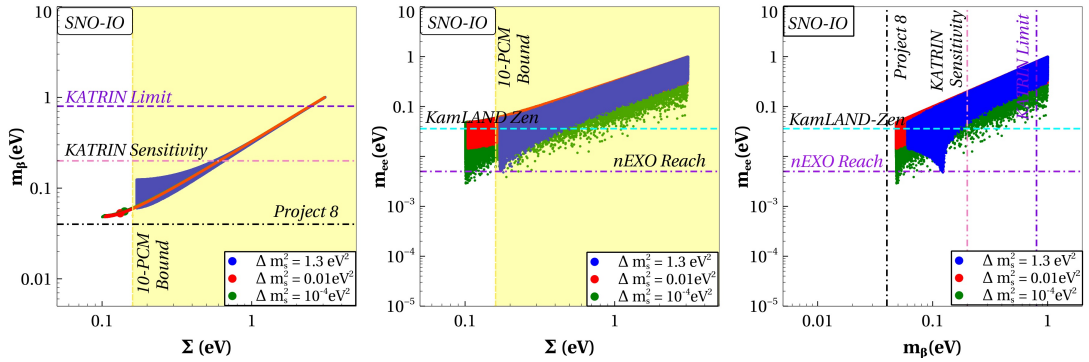

Figure 3.14: Correlations of m_β against and Σ(left) , m_{ee} against Σ (middle) and m_{ee} against m_β (right) for SNO-IO is plotted here. The green, blue, and red regions describe the values for $\Delta m_s^2 = 10^{-4}\,\text{eV}^2$, $0.01\,\text{eV}^2$, and $1.3\,\text{eV}^2$, respectively. The yellow-shaded region corresponds to the exclusion regions by Eq. (3.15).

favours a large parameter space for all three mass-squared differences. The allowed region from cosmology will not be sensitive to *KATRIN*'s projected limit, but the proposed *Project 8* experiment can probe the parameter space for $\Delta m_s^2 = 1.3\,\text{eV}^2$.

- From the middle panel, it is observed that some part of the parameter space disfavoured by the cosmological bound is also disfavoured by *KamLAND-Zen*. In the region allowed by cosmology, m_β can be very low. Therefore, *KamLAND-Zen* can probe a very small part of it, and the projected sensitivity *nEXO* experiment can only probe some parts of these regions for all the mass-squared differences.
- From the right panel, it can be noted that the proposed experiments *nEXO* and Project-8 together can rule out almost the entire parameter space for $\Delta m_s^2 = 1.3\ \text{eV}^2$ in the absence of any signal. However, in the case of $\Delta m_s^2 = 0.01, 10^{-4}\ \text{eV}^2$, only parts of the parameter space can be probed by the upcoming above-cited experiments.

2. **SNO-IO**

Fig. 3.14 shows the correlation plots for SNO-IO.

- From the left panel, it is visible that $\Delta m_s^2 = 1.3\,\text{eV}^2$ is ruled out by stringent cosmological limit. But for $\Delta m_s^2 = 10^{-4}\,\text{eV}^2$ and $0.01\,\text{eV}^2$ small parts of parameter space are allowed by cosmology and *KATRIN*'s projected sensitivity. These allowed regions can be com-

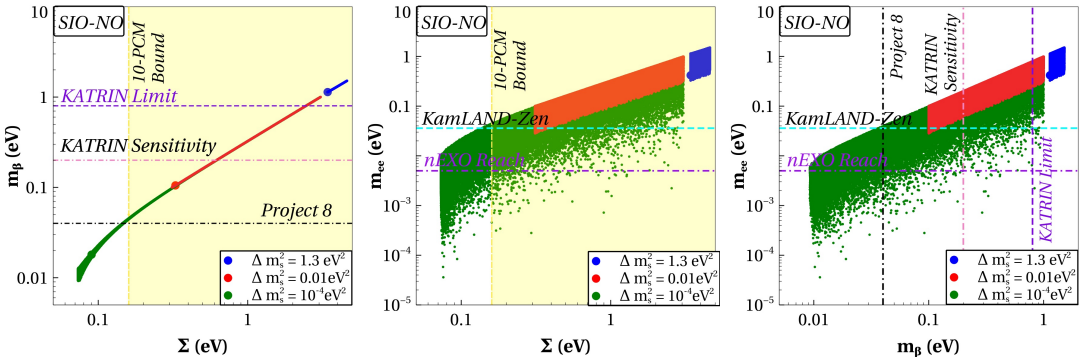

Figure 3.15: Correlations of m_β against and Σ(left) , m_{ee} against Σ (middle) and m_{ee} against m_β (right) for SNO-IO is plotted here. The green, blue, and red regions describe the values for $\Delta m_s^2 = 10^{-4}\,\mathrm{eV}^2$, $0.01\,\mathrm{eV}^2$, and $1.3\,\mathrm{eV}^2$, respectively. The yellow-shaded regions correspond to the exclusion regions by Eq. (3.15).

pletely probed in the proposed *Project 8* experiment.

- It can be noted from the middle panel that *KamLAND-Zen* and cosmology rule out a large part of the parameter space for all the mass-squared differences. For $\Delta m_s^2 = 0.01,\ 10^{-4}\,\mathrm{eV}^2$, the region allowed by cosmology and *KamLAND-Zen* can be probed in future experiment *nEXO*.
- From the right panel, it is observed that *Project 8* and *nEXO* experiments together can probe the entire parameter space for $\Delta m_s^2 = 10^{-4}$, 0.01 and $1.3\,\mathrm{eV}^2$.

3. **SIO-NO**

In Fig. 3.15, correlations between the mass variables for the SIO-NO scenario are plotted.

- The left and middle panels show that the cosmological *10-PCM* model disfavour the whole parameter space for $\Delta m_s^2 = 0.01, 1.3\,\mathrm{eV}^2$, however with the given cosmological limit only a part of $\Delta m_s^2 = 10^{-4}\,\mathrm{eV}^2$ is preferred.
- From the left panel, it is visible that the current *KATRIN* bound complementarily disfavour a common parameter space which is also ruled out by *10-PCM* model (e.g. $\Delta m_s^2 = 1.3\,\mathrm{eV}^2$). It seems that *KATRIN* future sensitivity can't probe the regions allowed by the *10-PCM* model. Only proposed *Project 8* can probe a little allowed

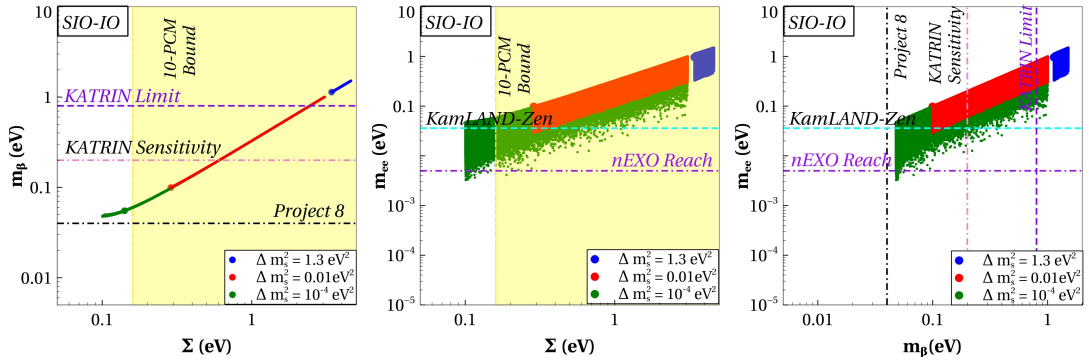

Figure 3.16: Correlations of m_β against and Σ(left) , m_{ee} against Σ (middle) and m_{ee} against m_β (right) are plotted here. The green, blue, black, and red regions describe SNO-NO, SNO-IO, SIO-NO & SIO-IO, respectively. The shaded regions correspond to the exclusion regions of the respective x-axis labels.

regions for $10^{-4}\,\text{eV}^2$.

- The middle panel depicts that the cosmology ruled out the favored regions of *KamLAND-Zen* limit for $\Delta m_s^2 = 0.01\,\text{eV}^2$. Some parameter space for $\Delta m_s^2 = 10^{-4}\,\text{eV}^2$ is still allowed by cosmology and as well as by the *nEXO* reach.
- It is to be noted from the right panel that the future experiments *nEXO* and *Project 8* can together probe the entirety of the parameter space for $\Delta m_s^2 = 1.3,\ 0.01\ \text{eV}^2$, and a fraction of the regions for $\Delta m_s^2 = 10^{-4}\ \text{eV}^2$.

4. **SIO-IO**

The correlations among the mass variables for the SIO-IO scenario are plotted in Fig. 3.16.

- From the left panel, we understand that the SIO-IO scenario is similar to the SIO-NO scenario. The only difference is that *Project 8* will be able to probe the entire cosmologically allowed regions of $\Delta m_s^2 = 10^{-4}\ \text{eV}^2$.
- The middle panel portrays similar observations to that of SIO-NO, apart from the fact that now future experiment *nEXO* can cover almost the total parameter space for all Δm_s^2 values considered by us.
- From the right panel, it can be seen that the proposed experiments *Project 8* and *nEXO* can together cover the entire parameter space for

all the values of Δm_s^2.

3.7 Summary and Discussion

The existence of an additional neutrino state with a mass-squared difference of $\mathcal{O}(\text{ eV})$ has been suggested as an explanation to the anomalous results obtained from short-baseline neutrino oscillation experiments such as *LSND* and *MiniBooNE*, as well as radiochemical experiments including *GALLEX*, *SAGE*, and *BEST*. Furthermore, the discrepancy between the measurements reported by the *T2K* and *NOνA* collaborations has been found to be alleviated through the introduction of a sterile neutrino with a mass-squared difference of $\sim 10^{-2}\,\text{eV}^2$. Additionally, the observed suppression of low-energy solar neutrino events below 8 MeV has been interpreted as a possible signature of an ultralight sterile neutrino. Consequently, sterile neutrinos spanning a broad range of mass-squared differences ($\Delta m_s^2 = m_4^2 - m_1^2$) have been extensively considered in theoretical and phenomenological studies. The addition of a sterile neutrino state leads to four distinct mass spectra, which are categorised based on the sign of the atmospheric mass-squared difference (Δm^2_{atm}) and the sterile mass-squared difference (Δm_s^2): (i) SNO-NO ($\Delta m_s^2 > 0\,,\, \Delta m^2_{\text{atm}} > 0$), (ii) SNO-IO ($\Delta m_s^2 > 0\,,\, \Delta m^2_{\text{atm}} < 0$), (iii) SIO-NO ($\Delta m_s^2 < 0\,,\, \Delta m^2_{\text{atm}} > 0$), and (iv) SIO-IO ($\Delta m_s^2 < 0\,,\, \Delta m^2_{\text{atm}} < 0$), where NO (normal ordering) and IO (inverted ordering) refer to the sign of Δm^2_{31}, while SNO (sterile normal ordering) and SIO (sterile inverted ordering) denote the sign of Δm^2_{41}. The schematic representations of these mass spectra are provided in Fig. 3.3, Fig. 3.4, and Fig. 3.5. The implications of these mass spectra are investigated in the context of cosmological constraints on the sum of neutrino masses, as well as their signatures in beta decay and $(0\nu\beta\beta)$ experiments. Each mass spectra is examined for consistency with existing experimental bounds and future sensitivities, thereby providing a comprehensive assessment of the viability of sterile neutrinos across different mass scales. The interplay between oscillation data, cosmological observations, and direct mass measurements is critically analysed to identify allowed parameter regions and potential experimental signatures.

- The SIO scenarios of $\Delta m_s^2 = 1.3\,\mathrm{eV}^2$ are found to be in conflict with the cosmological bound on the sum of neutrino masses. The specific cosmological bounds depend on the chosen data sets and the cosmological models used for fitting. Here a cosmological model with 10 parameter cosmological model (*10-PCM*) is considered which provides the limit on the total mass of the light neutrino species as $\Sigma < 0.16\,\mathrm{eV}$. It is observed that SIO-NO and SIO-IO is completely ruled out by cosmology. Furthermore, these scenarios have been independently disfavoured by experimental results from the *KATRIN* collaboration, which provides stringent limits on the effective electron neutrino mass ($m_\beta \leq 0.8$ eV), and from the *KamLAND-Zen* experiment, which constrains the effective Majorana mass parameter (m_{ee}). It must be emphasised that the exclusion of SIO-NO and SIO-IO for $\Delta m_s^2 = 1.3\,\mathrm{eV}^2$ is not solely based on cosmological arguments but is additionally supported by the direct laboratory measurements. In contrast, the SNO-NO and SNO-IO scenarios will remain phenomenologically viable with current bounds from *KATRIN* and *KamLAND-Zen* for $m_{\mathrm{lightest}} < 0.1\,\mathrm{eV}$, but the proposed *Project 8* experiment, with its projected sensitivity to $m_\beta \leq 0.04$ eV, is expected to probe these remaining parameter spaces, potentially either confirming their viability or ruling them out through improved precision measurements.

- It is often believed that sterile neutrinos with a mass-squared difference smaller than $1.3\ \mathrm{eV}^2$ can be allowed by cosmology. In this study, it turned out that for $\Delta m_s^2 = 0.01\,\mathrm{eV}^2$, SIO-NO and SIO-IO mass spectra are disfavoured from cosmology. It is also noted that projected sensitivity from *KATRIN* experiments will not be able to probe the mass spectra, but SNO-IO, SIO-NO, and SIO-IO scenarios can be probed completely with *Project 8*'s proposed sensitivity. In the case of neutrinoless double decay measurements, *KamLAND-Zen* experiment ruled out most of the parameter space of SIO-NO and SIO-IO scenario for $\Delta m_s^2 = 0.01\,\mathrm{eV}^2$, and the next generation experiment *nEXO* will be able to probe the parameter space completely. Moreover, *nEXO* will also be able to probe the SNO-IO scenario completely for $\Delta m_s^2 = 0.01\,\mathrm{eV}^2$.

- It is seen from Fig. 3.6 that all mass spectra for $\Delta m_s^2 = 10^{-4}\,\mathrm{eV}^2$ i.e. sterile neutrino with very small mass-squared difference is allowed up to $m_{\text{lightest}} \approx \mathcal{O}(0.01\,\mathrm{eV})$ from cosmology. In the case of direct mass measurement, *KATRIN*'s projected limit can probe the mass spectra up to $m_{\text{lightest}} \approx 0.2\,\mathrm{eV}$ whereas *Project 8* will be able to probe SNO-IO, SIO-IO scenarios completely and SNO-NO, SIO-NO scenarios up to $m_{\text{lightest}} \approx 0.04\,\mathrm{eV}$. We also find that neither *KamLAND-Zen* nor *nEXO* can completely probe the mass spectra, but they rule out some parameter space for SNO-IO, SIO-NO and SIO-IO scenarios.

In conclusion, in the presence of a light sterile state, mass-related observables can provide constraints on the possible spectra and can disfavour some of these depending on the mass of the sterile state.

This page is intentionally left blank.

4

LeptoQuarks and Neutrinoless double beta decay

4.1 Overview

In section 2.5, it is extensively described that a natural way to lower the NP scale to the experimental reach is by invoking higher-dimensional operators beyond the dimension five Weinberg operator. Similarly, for radiative neutrino mass models [88, 190, 191], the tree-level Lagrangian does not generate the operator $\mathcal{O}_5$, and non-zero neutrino mass is only induced at loop level, which automatically comes with a loop suppression factor.

A prime example of such radiative neutrino mass generation with dimension-7 operator with TeV-scale new physics involves leptoquarks [191], which are theoretically well-motivated BSM particles that emerge naturally in extensions of the SM such as technicolor and composite models [192] or models that unify quarks and leptons [193, 194]; see Ref. [195] for a review on leptoquarks. Here, we consider one such model with two scalar leptoquarks $S_1(\bar{3},1,1/3)$ and $\widetilde{R}_2(3,2,1/6)$ [92, 93], where the charges are given under the SM gauge group $SU(3)_c \otimes SU(2)_L \otimes U(1)_\mathcal{Y}$. This model is known to generate neutrino mass at one-loop level via a dimension-7 operator of the type $\mathcal{O}_7^{(2)} = H(LQ)(Ld^C)$[1]. The leptoquarks with lepton number violating (LNV) and lepton flavour violating (LFV) interactions also contribute to a va-

[1]The same one-loop mechanism is also realised in R-parity violating supersymmetric models [196], where the $S_1^{1/3}$ and $\widetilde{R}_2^{-1/3}$ components are identified as the down-type squarks $\widetilde{d}^C$ and $\widetilde{d}$, respectively.

riety of low-energy rare processes, namely the LNV process like $0\nu\beta\beta$ [197], LFV processes [198–200] like $\mu \to e\gamma$, $\mu \to e$ conversion in nuclei as well as $\ell \to \ell' gg$ decay, and semileptonic K and B-meson decays [201–208]. In fact, the recent hints of lepton flavour universality violation (LFUV) in charged-current semileptonic B-meson decays, defined by the ratio of branching ratios (BRs), $R_{D^{(*)}} = \frac{\text{BR}(\overline{B}\to D^{(*)}\tau\overline{\nu})}{\text{BR}(\overline{B}\to D^{(*)}\ell\overline{\nu})}$ with $\ell = e, \mu$, by *BaBar* [44], *LHCb* [47], *Belle* [45] and *Belle-II* [46], and the muon $(g-2)$ anomaly [33, 34, 209], have led to a deluge of papers invoking the S_1 leptoquark as a possible explanation of both anomalies [210–215] (see Ref. [216] for a recent review). Note that another combination of scalar LQs such as $S_3(\overline{3}, 3, 1/3)$ and $\widetilde{R}_2(3, 2, 1/6)$ leptoquarks also works for neutrino mass generation [95] and gives additional contribution to $0\nu\beta\beta$ [197]; however S_3 cannot explain the $R_{D^{(*)}}$ anomaly [217], and therefore, we choose to work with the $(S_1, \widetilde{R}_2)$ combination.

In this chapter, we perform a detailed study of the $0\nu\beta\beta$ predictions in presence of the scalar leptoquarks S_1 and $\widetilde{R}_2$. Going beyond earlier works on the study of $0\nu\beta\beta$ in leptoquark models [197, 218–223], we analyse the interplay of $0\nu\beta\beta$ with neutrino mass and flavour observables, including the $R_{D^{(*)}}$ and $(g-2)$ anomalies. For $0\nu\beta\beta$, we include two types of long-range contributions via light-neutrino exchange mechanism. One is mediated via two standard model $V-A$ vertices, the other via one standard model and one leptoquark vertex. There can be either constructive or destructive interference between these contributions, depending on the signs of the leptoquark Yukawa couplings involved. This leads to interesting correlations between the $0\nu\beta\beta$ and other low-energy flavour observables, which we study in detail for the first time. In particular, we impose the latest LHC constraints on the leptoquark masses, as well as the low-energy LFV and LFUV constraints on their Yukawa couplings, including the recently updated $R_{K^{(*)}}$ results from *LHCb* [224, 225] and $B^+ \to K^+\nu\overline{\nu}$ results from *Belle-II* [50]. We then perform a multi-dimensional scan over all the relevant leptoquark couplings and find some non-trivial (anti)correlations between them. We identify the parameter space that could simultaneously address the $R_{D^{(*)}}$ anomaly [44–47], as well as the electron [42, 43] and muon [34] $(g-2)$ anomalies, while satisfying all

other flavour constraints. It turns out that the $\mu \to e$ conversion in nuclei is the most constraining flavour observable in the parameter space of our interest. However, it still allows the leptoquark contribution to the $0\nu\beta\beta$ process to dominate over the canonical light neutrino contribution, for both normal and inverted orderings for some values of the parameter space. We find that for our chosen benchmark scenario, the current *KamLAND-Zen* limit already excludes leptoquark masses below 3.3 TeV and 6.6 TeV for normal ordering (NO) and inverted ordering (IO), respectively when the lightest neutrino have zero mass. The future $0\nu\beta\beta$ experiments like *nEXO* can probe leptoquark masses up to $\mathcal{O}(10)$ TeV, beyond the reach of HL-LHC.

It should be mentioned here that earlier attempts were made to simultaneously explain the neutral-current B-decay anomalies, most notably the $R_{K^{(*)}}$ anomaly, along with the $R_{D^{(*)}}$ and muon $(g-2)$ anomalies within the leptoquark model under consideration (or its extensions) [211–213, 226, 227]; however, since the $R_{K^{(*)}}$ anomaly has now disappeared [224, 225], it gives an additional constraint on the leptoquark couplings, as it can be seen later. In the same vein, in this chapter, a hypothetical situation is considered where the current $R_{D^{(*)}}$ anomaly disappears, and analysed its implications for the allowed model parameter space.

The chapter is organised as follows: In Section 4.2 we briefly describe the leptoquark model under consideration. Section 4.3 discusses how neutrino mass is generated at one-loop level in this model. In section 4.4, we present the $0\nu\beta\beta$ analysis in this model. In section 4.5, we discuss the leptoquark contributions to various flavour observables, including charge lepton flavour violating (cLFV) decays, lepton $(g-2)$, neutrino electric and magnetic dipole moment and semileptonic B and K-meson decays. Section 4.6 presents our numerical analysis and results. In section 4.7, we conclude with a summary and outlook.

4.2 The LeptoQuark Model

The considered leptoquark model consists of the SM particle content augmented with two scalar leptoquarks

$$S_1(\bar{3},1,1/3) \equiv S_1^{1/3}, \qquad \widetilde{R}_2(3,2,1/6) \equiv \begin{pmatrix} \widetilde{R}_2^{+2/3} \\ \widetilde{R}_2^{-1/3} \end{pmatrix}, \tag{4.1}$$

where the leptoquark states are also expanded into its components of $SU(2)_L$ group, with the superscripts denoting the electric charges. The corresponding Yukawa interaction terms are given by the Lagrangian

$$\begin{aligned} -\mathcal{L}_{\rm LQ} \;&\supset\; Y_1^L \overline{Q}_L^C \epsilon \ell_L S_1 + Y_1^R \overline{u}_R^C e_R S_1 + Y_2 \overline{d}_R \widetilde{R}_2^T \epsilon \ell_L + \text{h.c.} \\ &=\; Y_1^L\, \overline{u}_L^C\, e_L\, S_1 - Y_1^L\, \overline{d}_L^C\, \nu_L\, S_1 + Y_1^R\, \overline{u}_R^C\, e_R\, S_1 + Y_2\, \overline{d}_R\, \widetilde{R}_2^{2/3}\, e_L - Y_2\, \overline{d}_R\, \widetilde{R}_2^{-1/3}\, \nu_L + \text{h.c.} \end{aligned} \tag{4.2}$$

Here the flavour indices are suppressed and $Y_1^{L,R}$ and Y_2 are in general 3×3 complex matrices describing the Yukawa interactions of the leptoquarks S_1 and $\widetilde{R}_2$, respectively.

The scalar potential involving the leptoquarks is given by

$$\begin{aligned} \mathcal{V}_{\rm LQ} \;=\; & m_1^2 S_1^\dagger S_1 + m_2^2 \widetilde{R}_2^\dagger \widetilde{R}_2 + \alpha_1 \left(H^\dagger H\right)\left(S_1^\dagger S_1\right) + \alpha_2 \left(H^\dagger H\right)\left(\widetilde{R}_2^\dagger \widetilde{R}_2\right) \\ & + \alpha_2' \left(H^\dagger \widetilde{R}_2\right)\left(\widetilde{R}_2^\dagger H\right) + \left(\kappa H^\dagger \widetilde{R}_2 S_1 + \text{h.c.}\right), \end{aligned} \tag{4.3}$$

where α_1, α_2 and α_2' are real dimensionless couplings describing the strength of quartic scalar interactions between the leptoquarks and the SM Higgs doublet. In Eq. (4.3) the trilinear coupling κ is in general complex with mass dimension one and plays a crucial role in the phenomenology of this model. It results in the mixing between the singlet ($S_1^{1/3}$) and the electromagnetic charge $1/3$ component of the doublet ($\widetilde{R}_2^{1/3}$) leptoquark after the electroweak symmetry breaking.

Note that in Eq. (4.2) and Eq. (4.3) terms that preserve baryon number,

is considered as the baryon number violating terms lead to the presence of the diquark coupling terms with S_1, as well as the quartic term of the form $S_1^2 \widetilde{R}_2^\dagger H$. The presence of such terms can lead to fast proton decay [228], which provide a stringent limit on the leptoquark masses, $m_{\rm LQ} \gtrsim 10^{10}$ GeV and there is no way to test these models in collider experiments and other low energy observables. In this work, Baryon number conservation is assumed to get rid of these baryon number violating terms. To conserve baryon number throughout the framework, Baryon number $B = -1/3$ is assigned to S_1 and $B = +1/3$ to $\widetilde{R}_2$ which ensures the absence of the B-violating terms in the Lagrangian at the renormalizable level.

In leptoquark models, a generalised fermion number can be defined as $F = 3B + L$, where B and L denote the baryon and lepton numbers, respectively [195]. This quantity is conserved in addition to the conservation of baryon number. Within the SM framework, $L = 1, B = 0$ is assigned to all SM leptons, while quarks are characterised by $L = 0, B = 1/3$. The conservation of F provides a useful symmetry for classifying allowed interactions in leptoquark scenarios [195]. In this singlet (S_1) - doublet $(\tilde{R}_2)$ leptoquark scenario, it is easy to notice from Eq. (4.2) that S_1 carries $L = -1, B = -1/3$, while $\widetilde{R}_2$ carries $L = -1, B = 1/3$ and for the SM Higgs doublet, $B = L = 0$. Therefore, for S_1 the F number is -2 while for $\widetilde{R}_2$ it is 0. Note that in Eq. (4.2) the simultaneous presence of the Yukawa couplings Y_1^L and Y_2, in association with the trilinear scalar coupling κ in Eq. (4.3), violates lepton number in the model[2] which serves an explanation to two of the puzzles in the SM i.e. the generation of the neutrino mass and its fundamental nature.

The mass matrix involving S_1 and $\widetilde{R}_2^{*1/3}$ is given by

$$\mathcal{M}^2_{1/3} = \begin{pmatrix} m^2_{S_1} & \frac{1}{\sqrt{2}}\kappa v \\ \frac{1}{\sqrt{2}}\kappa v & m^2_{\widetilde{R}_2} \end{pmatrix}, \tag{4.4}$$

where $m^2_{S_1} = m_1^2 + \frac{1}{2}\alpha_1 v^2$ and $m^2_{\widetilde{R}_2} = m_2^2 + \frac{1}{2}(\alpha_2 + \alpha_2')\, v^2$, with $v =$

[2]Under the assumption that the scalar sector only comprises the SM Higgs and scalar leptoquarks, this is one of the only two possibilities to break lepton number in the scalar sector [229, 230], the other one being the combination of $\widetilde{R}_2(3,2,1/6)$ and $S_3(\bar{3},3,1/3)$.

$(\sqrt{2}G_F)^{-1/2} \simeq 246$ GeV, G_F being the Fermi constant. The 2×2 matrix (4.4) can be diagonalised by a 2×2 rotational matrix parameterised by one mixing angle ($\theta_{\rm LQ}$). It can be shown that

$$\tan 2\theta_{\rm LQ} \;=\; \frac{\sqrt{2}\kappa\, v}{m^2_{\widetilde{R}_2} - m^2_{S_1}}\,. \tag{4.5}$$

The physical mass eigenstates are

$$\begin{aligned} X_1^{1/3} &= \cos\theta_{\rm LQ} S_1^{1/3} - \sin\theta_{\rm LQ}\widetilde{R}_2^{*\,1/3}, \\ X_2^{1/3} &= \sin\theta_{\rm LQ} S_1^{1/3} + \cos\theta_{\rm LQ}\widetilde{R}_2^{*\,1/3}, \end{aligned} \tag{4.6}$$

and the corresponding mass eigenvalues are

$$m^2_{X_1,X_2} \;=\; \frac{1}{2}\left[m^2_{S_1} + m^2_{\widetilde{R}_2} \mp \sqrt{\left(m^2_{S_1} - m^2_{\widetilde{R}_2}\right)^2 + 2\kappa^2 v^2}\right]. \tag{4.7}$$

As for the charge 2/3 component of the $\widetilde{R}_2$ leptoquark, its mass is simply given by

$$m^2_{\widetilde{R}_2^{2/3}} \;=\; m_2^2 + \frac{1}{2}\alpha_2 v^2\,. \tag{4.8}$$

The current LHC constraints on the leptoquark masses are of order $\mathcal{O}(1\text{ TeV})$[3], depending on the Yukawa couplings [231–240]. This requires to go to the decoupling limit with $m_1, m_2 \gg v$. In this case, all three physical mass eigenstates $X_{1,2}, \widetilde{R}_2^{2/3}$ are quasi-degenerate.

4.3 Neutrino Mass Generation

With a single leptoquark it is not possible to generate Majorana mass for light neutrinos. Therefore, two scalar leptoquarks are needed in this model, which will run in the loop for radiative neutrino mass generation. The singlet-doublet

[3]For the scalar leptoquark scenario, the ATLAS collaboration has set stringent lower limits on the LQ mass by analysing the decay channel to a τ lepton and a b quark. They have excluded masses below 1.28 (1.53) TeV for a Yukawa coupling of 1.0 (2.5) [231].

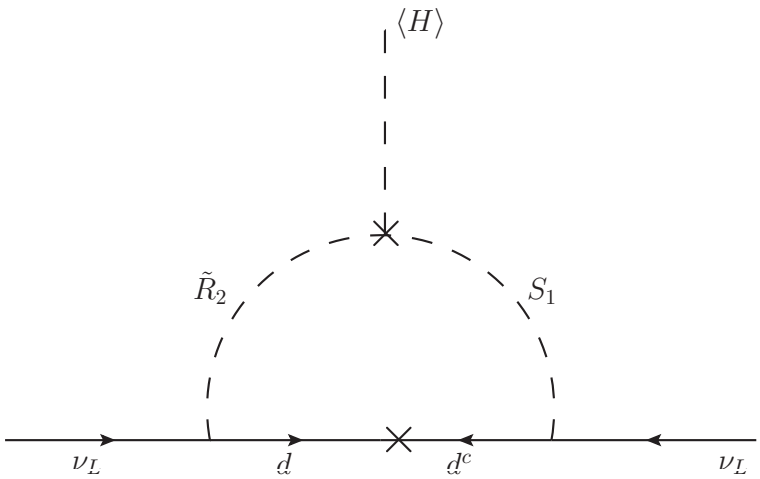

Figure 4.1: Radiatve Majorana mass generation for active neutrinos via the mixing of singlet-doublet scalar leptoquarks.

leptoquark mixing, parameterised by $\theta_{\rm LQ}$ in Eq. (4.5), which depends on the trilinear coupling κ, is crucial for this purpose, as noted earlier [229, 230]; see Fig. 4.1. In this singlet-doublet scenario, $\widetilde{R}_2^{1/3}$ and $S_1^{1/3}$ together can generate one-loop Majorana mass for active neutrinos, given by [92, 93]

$$\mathcal{M}_\nu \;=\; \frac{3\sin 2\theta_{\rm LQ}}{32\pi^2}\ln\left(\frac{m^2_{X_1}}{m^2_{X_2}}\right)\left(\widetilde{Y_1^L}^T\mathcal{M}_d Y_2 + Y_2^T\mathcal{M}_d\widetilde{Y_1^L}\right). \tag{4.9}$$

For large values of leptoquark masses i.e $m^2_{S_1} \approx m^2_{\widetilde{R}_2} \approx m^2_{\rm LQ}$ Eq. (4.9) can be approximated as

$$m_\nu \;=\; 0.01\,{\rm eV}\left(\frac{\kappa}{m_{\rm LQ}}\right)\left(\frac{m_q}{m_b}\right)\left(\frac{1\,{\rm TeV}}{m_{\rm LQ}}\right)\left(\frac{y_1^L y_2}{10^{-6}}\right), \tag{4.10}$$

where y_1^L and y_2 are typical values of the elements of $\widetilde{Y_1^L}$ (or Y_1^L) and Y_2, respectively. Here $\widetilde{Y_1^L} = V_{CKM}\cdot Y_1^L$ (V_{CKM} being the CKM quark mixing matrix) as the up-type quarks are considered in their mass basis and $\mathcal{M}_d$ is the diagonal mass matrix for down-type quarks. The diagonal mass matrix $\mathcal{M}_\nu^{\rm diag}$ (with eigenvalues m_{ν_i}, where $i = 1,2,3$) can be obtained for light neutrinos by diagonalizing $\mathcal{M}_\nu$ with the usual PMNS mixing matrix $\mathcal{U}_{\rm PMNS}$ which is parameterised by three mixing angles $\theta_{12}, \theta_{13}, \theta_{23}$ and three phases i.e., one Dirac phase ($\delta_{\rm CP}$) and two Majorana phases (α, β).

4.4 Leptoquark contribution to $0\nu\beta\beta$

With Majorana neutrinos, as discussed earlier, $0\nu\beta\beta$ can occur in this model, mediated by long-range $W_L - W_L$ contribution to $0\nu\beta\beta$, as shown in Fig. 2.12. In the presence of S_1 and $\widetilde{R}_2$ leptoquarks, new long-range mechanisms contribute to the $0\nu\beta\beta$ mediated by $W_L - S_1$ exchange, as shown in Figs. 4.2(a) and (b), as well as from the mixing between $S_1^{1/3}$ and $\widetilde{R}_2^{1/3}$, as shown in Figs. 4.2(c) and (d) [197]. These new contributions are referred to as non-standard contributions. Diagram (a) is purely dependent on Y_1^L while diagram (c) arises from the combination of both Y_1^L and Y_2 couplings, whereas (b) and (d) arise from the combination of Y_1^L, Y_1^R and Y_1^R, Y_2 couplings, respectively [cf. Eq. (4.2)].

The most general LEFT Lagrangian for long-range mechanisms can be written as [241–243][for details, see Appendix. B],

$$-\mathcal{L}_{\text{eff}} \supset \frac{G_F}{\sqrt{2}}\left[j^{\mu}_{V-A} J_{V-A,\mu} + \sum_{\alpha,\beta} \epsilon^{\beta}_{\alpha}\, j_{\beta}\, J_{\alpha} + \text{h.c..}\right], \tag{4.11}$$

where the leptonic and hadronic currents in the second term are defined as $j_\beta = \bar{e}\mathcal{O}_\beta \nu_e^C$ and $J_\alpha = \bar{u}\mathcal{O}_\alpha d$. The Greek indices β can be $V+A$, $S+P$, $T+T_5$, and α can be $V \mp A$, $S \mp P$, $T \mp T_5$ where V, A, S, P, T, T_5 correspond to vector, axial-vector, scalar, pseudo-scalar, tensor, and axial-tensor respectively. In Eq. (4.11), the standard canonical long range mechanism (first term) is separated from the non-standard contributions, with the $\epsilon^{\beta}_{\alpha}$ being the corresponding Wilson coefficients of the non-standard operators.

For the standard $W_L - W_L$ mediation channel, the leptonic and hadronic currents are both connected via the SM gauge boson W_L, and two electrons of the same helicity ($e_L e_L$) are emitted, as shown in Fig. 2.12. In case of standard $0\nu\beta\beta$ mechanism, the half-life of the decay is written as [cf. Eq. (B.28)]

$$\left(T^{0\nu}_{1/2}\right)^{-1}_{\text{std}} = g_A^4 G_{01} \left|\mathcal{M}^{(3)}_{\nu}\right|^2 \frac{\left|m^{\text{std}}_{ee}\right|^2}{m_e^2}, \tag{4.12}$$

where $g_A = 1.27$ is the axial coupling, G_{01} is the phase space integral and $M^{(3)}_{\nu}$ is the NME for the standard light neutrino exchange mechanism, m_e

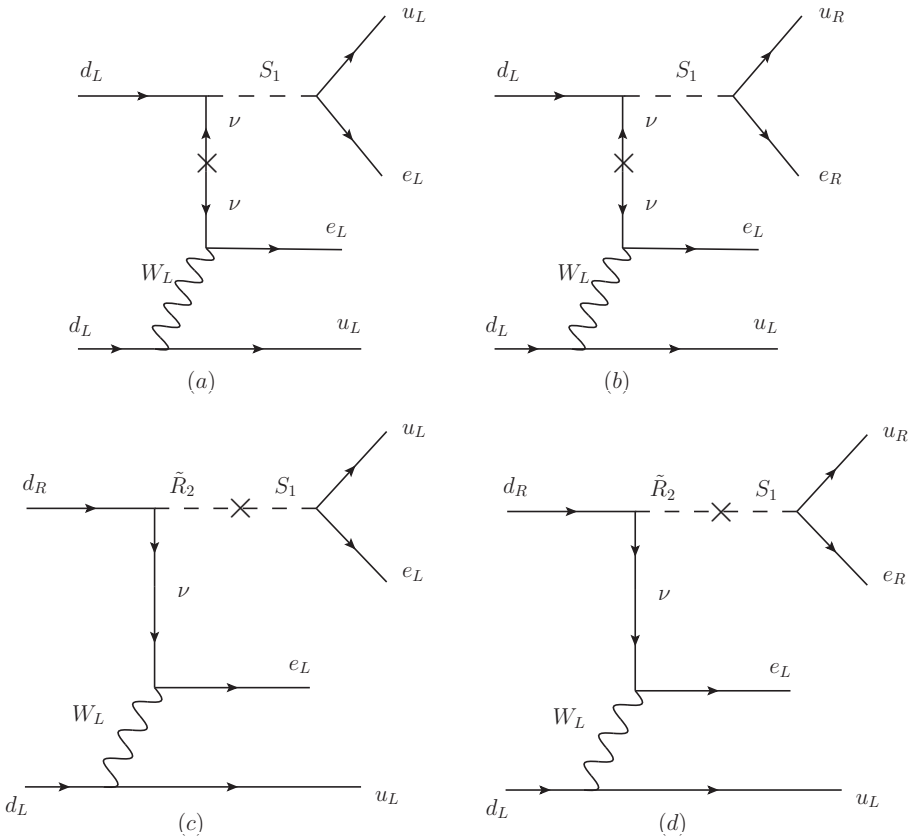

Figure 4.2: Feynman diagrams for different contributions to the $0\nu\beta\beta$ process in the leptoquark model. The top panel shows the purely S_1-mediated diagrams. The bottom panel shows the diagrams mediated by $S_1 - \tilde{R}_2$ mixing. Diagram (a) is purely dependent on Y_1^L while diagram (c) arises from the combination of both Y_1^L and Y_2 couplings, whereas (b) and (d) arise from the combination of Y_1^L, Y_1^R and Y_1^R, Y_2 couplings, respectively.

is mass of electron and $m_{ee}^{\text{std}} = |\sum_i U_{ei}^2 m_{\nu_i}|$ represents the effective Majorana mass parameter for the canonical case. In the leptoquark-mediated channels, depending on whether the Y_1^L or Y_1^R couplings are involved, either $e_L e_L$ or $e_L e_R$ can be emitted in the final state, as shown in Fig. 4.2 (a-d). It is also seen from these figures that the amplitude of these diagrams are $\mathcal{O}(\epsilon)$, as one of the standard operators in Fig. 2.12 is replaced by the NP operator mediated by leptoquarks. The NP operators and the corresponding Wilson coefficients for $0\nu\beta\beta$ are identified below. They are matched directly to the LEFT scale ($\mu = \mu_{\text{ew}}$) i.e. after integrating out the W boson and the massive leptoquark (X_1, X_2) states.

LNV is introduced by the majorana mass of the neutrinos (shown by the

mass insertion in the middle) in Fig. 2.12 and in diagrams (a)-(b) of Fig. 4.2. Whereas, in diagrams (c)-(d) LNV is introduced through the $S_1 - \tilde{R}_2$ mixing (shown as a cross in the middle of the leptoquark line). It can be seen from the middle panel of Fig. 4.2 that the amplitudes for diagrams (a) and (b) are proportional to the small neutrino mass and inversely proportional to the leptoquark mass squared, which gives an extra suppression relative to the standard mechanism. Hence, the contribution of these diagrams to $0\nu\beta\beta$ can be simply ignored. On the other hand, diagrams (c) and (d), being dependent on the neutrino momentum, give important contribution to $0\nu\beta\beta$ which, depending on the leptoquark masses and couplings, can be dominant over the standard canonical contribution [197].

The NP operator that contributes to the upper half of diagram (c) in Fig. 4.2 is given by,

$$\mathcal{O}^{(c)} = \left(\frac{G_F}{\sqrt{2}}\right)\left[\epsilon^{S+P}_{S+P}\left(\bar{u}P_R d\right)\left(\bar{e}P_R \nu_e^C\right) + \epsilon^{T+T_5}_{T+T_5}\left(\bar{u}\sigma^{\alpha\beta}P_R d\right)\left(\bar{e}\sigma_{\alpha\beta}P_R \nu_e^C\right)\right], \tag{4.13}$$

where the dimensionless parameters ϵ^{S+P}_{S+P} and $\epsilon^{T+T_5}_{T+T_5}$ at the LEFT scale are given by

$$\epsilon^{S+P}_{S+P} = \frac{\cos\theta_{\rm LQ}\sin\theta_{\rm LQ}}{\sqrt{2}\,G_F}\left(Y_2^*\right)_{11}\left(Y_1^{L\,*}\right)_{11}\left(\frac{1}{m^2_{X_1}} - \frac{1}{m^2_{X_2}}\right), \tag{4.14}$$

$$\epsilon^{T+T_5}_{T+T_5} = -\frac{1}{4}\,\epsilon^{S+P}_{S+P}, \tag{4.15}$$

corresponding to the $S+P$ and $T+T_5$ contributions, respectively.

Eq. (4.14) can be recast using Eq. (4.7) in the $m_{S_1} = m_{\tilde{R}_2} = m_{\rm LQ}$ limit,

$$\epsilon^{S+P}_{S+P} \simeq \frac{\kappa\, v^3}{m^4_{\rm LQ}}\left(Y_2^*\right)_{11}\left(Y_1^{L\,*}\right)_{11}. \tag{4.16}$$

Similarly, the effective NP operator that generates diagram (d) in Fig. 4.2 is

given by

$$\mathcal{O}^{(d)} = \left(\frac{G_F}{\sqrt{2}}\right) \epsilon^{V+A}_{V+A} \left(\bar{u}\gamma_\alpha P_R d\right) \left(\bar{e}\gamma^\alpha P_R \nu_e^C\right), \tag{4.17}$$

where the $V+A$ term is given by

$$\epsilon^{V+A}_{V+A} = -\frac{\cos\theta_{\rm LQ}\sin\theta_{\rm LQ}}{\sqrt{2}\,G_F} \left(Y_2^*\right)_{11} \left(Y_1^R\right)^*_{11} \left(\frac{1}{m^2_{X_1}} - \frac{1}{m^2_{X_2}}\right), \tag{4.18}$$

which can also be recast into a form similar to Eq. (4.16).

After identifying the relevant LEFT operators and their Wilson coefficients, the half-life of the $0\nu\beta\beta$ decaying nucleus can be calculated using the master formula outlined in [244][see Eq. (B.26)],

$$\left(T^{0\nu}_{1/2}\right)^{-1}_{\rm total} = g_A^4 \sum_k G_{0k} \left|\mathcal{A}_k\left(\{C_i\}\right)\right|^2, \tag{4.19}$$

where G_{0k} denote the atomic phase space factors and $\mathcal{A}_k\left(\{C_i\}\right)$ are the sub-amplitudes which depend on the NMEs, low-energy constants (LECs) and the Wilson coefficients of the relevant operators; see Appendix B for details. Here, we have used νDoBe [222], a python package to calculate the half-life for ^{136}Xe, with the NMEs from the IBM2 model [245]. The running of the Wilson coefficients $\left(\text{especially } \epsilon^{S+P}_{S+P} \text{ and } \epsilon^{T+T_5}_{T+T_5}\right)$ from $\mu = \mu_{\rm ew}$ to $\mu = 2$ GeV is taken care of by the νDoBe package. Note that in νDoBe, the decay-rate formula is expressed in terms of the Wilson coefficients at the chiral symmetry-breaking scale $\mu \sim 2$ GeV, following Ref. [244]. From Eq. (4.19), the effective Majorana mass can be extracted in a form silimar to Eq. (4.12), i.e.

$$\left(T^{0\nu}_{1/2}\right)^{-1}_{\rm total} = g_A^4 G_{01} \left|\mathcal{M}^{(3)}_\nu\right|^2 \frac{\left|m^{\rm eff}_{ee}\right|^2}{m_e^2}. \tag{4.20}$$

where $m^{\rm eff}_{ee} = m^{\rm std}_{ee} + m^{\rm LQ}_{ee}$. The advantage of writing it this way is that when the leptoquark contribution becomes sub-dominant i.e., $m^{\rm LQ}_{ee} << m^{\rm std}_{ee}$, the canonical result $\left(m^{\rm eff}_{ee} \approx m^{\rm std}_{ee}\right)$ is recovered. In other words, the deviation of $m^{\rm eff}_{ee}$ from $m^{\rm std}_{ee}$ gives a measure of the leptoquark contribution, including interference with the SM contribution. The lower limit on the half-life of ^{136}Xe from the

KamLAND-Zen experiment translates to an upper bound on $m_{ee} < (28 - 122)$ meV at 90% CL [116]. The uncertainty band in m_{ee} is taking into account different NME calculations. The next-generation ton-scale experiment *nEXO* will reach a sensitivity of $T^{0\nu}_{1/2} > 1.35 \times 10^{28}$ yrs at 90% CL with 10 years of data taking [122]. This translates into an upper limit on $m_{ee} < (4.7 - 20.7)$ meV. The *LEGEND-1000* experiment using ^{76}Ge isotope will reach a similar design sensitivity of $T^{0\nu}_{1/2} > 1.6 \times 10^{28}$ yrs at 90% CL [120], which translates into an upper limit on $m_{ee} < (9 - 21)$ meV. These information are used for the numerical analysis.

4.5 Leptoquark and Flavour Observables

This section presents the relevant low-energy observables for LFV and LFUV, which constrain the parameter space of the leptoquark models. There are additional constraints, such as those from perturbative unitarity [246] and electroweak T-parameter [247], which however are negligible for the choice of small trilinear coupling κ (assumed in the chapter), and hence, are not shown here.

4.5.1 Charged Lepton Sector

In this section, cLFV processes namely, $\mu \to e$ conversion in nuclei, charged lepton decays like $\ell_\alpha \to \ell_\beta \gamma$, $\ell_\alpha \to \ell_\beta \ell_\gamma \ell_\delta$, and lepton anomalous magnetic moments (a_l) is considered to constrain the model parameter space.

$\mu \to e$ Conversion in Nuclei

In this model, leptoquark can mediate $\mu \to e$ conversion inside nuclei, i.e. $\mu N \to e N$. As the nucleons (proton and neutron) made with quarks, at a fundamental level left diagram of Fig. 4.3 denote the $\mu \to e$ transition inside a nucleus where $\ell_\alpha \equiv \mu$ and $\ell_\beta \equiv e$. As this process occurs at tree level, it

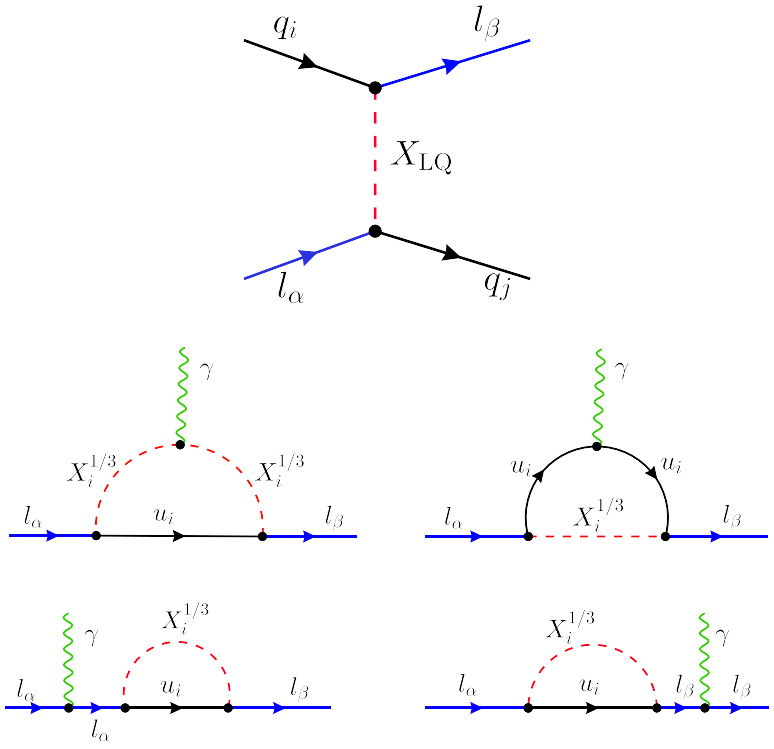

Figure 4.3: Feynman diagrams contributing to (top panel) $\mu \to e$ conversion in nuclei and (middle and lower panel) $\ell_\alpha \to \ell_\beta \gamma$ process. The diagrams contributing to $\ell_\alpha \to \ell_\beta \gamma$ processes also contribute to $(g-2)_\ell$ when $\alpha = \beta$.

provides one of the most stringent constraints among the flavour observables on the Yukawa couplings involving first and second generation leptons. The conversion ratio is denoted as

$$\mathcal{R}|^N_{\mu\to e} \;=\; \frac{\Gamma^N\,(\mu \to\, e)}{\Gamma^N_{\rm capture}}\,, \tag{4.21}$$

where N denotes a particular nucleus and $\Gamma^N_{\rm capture}$ implies the muon capture rate of that nucleus. The low energy effective Lagrangian describing $\mu\, N \to e\, N$ can be written as [248]

$$\begin{aligned}\mathcal{L}_{\bar{q}q\bar{e}\mu} \;\supset\; -\sqrt{2}G_F \sum_{q=u,d,s}\sum_{X,Y=L,R}\Big[C^q_{V_{XY}}\,(\bar{e}\,\gamma^\mu\,P_X\,\mu)\;(\bar{q}\,\gamma_\mu\;P_Y\,q) + C^q_{S_{XY}}\,(\bar{e}\,P_X\,\mu)\;(\bar{q}\,P_Y q)\\ + C^q_{T_{XY}}\,(\bar{e}\,\sigma^{\mu\nu}\,P_X\,\mu)\;(\bar{q}\,\sigma_{\mu\nu}\,P_Y q)\Big] + \text{h.c.}\end{aligned} \tag{4.22}$$

Here, the operators with the gluon field strength tensor are neglected because they are suppressed in this model [249]. The relevant Wilson coefficients in

this framework are given by

$$C^u_{V_{LL}} = \frac{v^2}{2}\left(Y_1^L\right)_{12}\left(Y_1^L\right)^*_{11}\left(\frac{\cos^2\theta_{\rm LQ}}{m^2_{X_1}}+\frac{\sin^2\theta_{\rm LQ}}{m^2_{X_2}}\right), \tag{4.23}$$

$$C^d_{V_{LR}} = -\frac{v^2}{2}\frac{(Y_2)_{12}\,(Y_2)^*_{11}}{m^2_{\widetilde{R}_2^{2/3}}}, \tag{4.24}$$

$$C^u_{V_{RR}} = \frac{v^2}{2}\left(Y_1^R\right)_{12}\left(Y_1^R\right)^*_{11}\left(\frac{\cos^2\theta_{\rm LQ}}{m^2_{X_1}}+\frac{\sin^2\theta_{\rm LQ}}{m^2_{X_2}}\right), \tag{4.25}$$

$$C^u_{S_{LL}} = -\frac{v^2}{4}\left(Y_1^L\right)_{12}\left(Y_1^R\right)^*_{11}\left(\frac{\cos^2\theta_{\rm LQ}}{m^2_{X_1}}+\frac{\sin^2\theta_{\rm LQ}}{m^2_{X_2}}\right), \tag{4.26}$$

$$C^u_{S_{RR}} = -\frac{v^2}{4}\left(Y_1^R\right)_{12}\left(Y_1^L\right)^*_{11}\left(\frac{\cos^2\theta_{\rm LQ}}{m^2_{X_1}}+\frac{\sin^2\theta_{\rm LQ}}{m^2_{X_2}}\right), \tag{4.27}$$

$$C^u_{T_{LL}} = -\frac{1}{4}C^u_{S_{LL}}\,, \qquad C^u_{T_{RR}} = -\frac{1}{4}C^u_{S_{RR}}\,. \tag{4.28}$$

For the coherent conversion process in which the initial and final nucleus are the same, the tensor contribution vanishes and the total conversion ratio can be written as [248]

$$\mathcal{R}|^N_{\mu\to e} = \frac{2\,G_F^2\,m_\mu^5}{\Gamma^N_{\rm capture}}\left|C^p_{SL}\,S^p + C^n_{SL}\,S^n + C^p_{VL}\,V^p + C^n_{VL}\,V^n\right|^2 + L\leftrightarrow, R \tag{4.29}$$

where the S^p, S^n, V^p and V^n are called the overlap integrals whose values along with $\Gamma^N_{\rm capture}$ are given in Tab. (4.1) for two nuclei. The coefficients of the overlap integrals are defined as :

$$C^p_{SL} = \sum_{q=u,d} G_S^{q,p}\,\frac{1}{2}C^q_{S_{LL}} \tag{4.30}$$

$$C^n_{SL} = \sum_{q=u,d} G_S^{q,n}\,\frac{1}{2}C^q_{S_{LL}} \tag{4.31}$$

$$C^p_{VL} = \left[C^u_{V_{LL}} + \frac{1}{2}C^d_{V_{LR}}\right], \tag{4.32}$$

$$C^n_{VL} = \left[\frac{1}{2}C^u_{V_{LL}} + C^d_{V_{LR}}\right], \tag{4.33}$$

and similarly for $L \to R$. The coefficients of the scalar operators are $G_S^{u,p} = G_S^{d,n} = 5.1$ and $G_S^{u,n} = G_S^{d,p} = 4.3$. Currently, the most stringent

Table 4.1: Muon capture rates [252] and overlap integral values [248] relevant for $\mu \to e$ conversion in $^{197}_{79}$Au and $^{27}_{13}$Al.

N	$\Gamma^N_{\text{capture}}$ (MeV)	S^p	S^n	V^p	V^n
$^{197}_{71}$Au	8.7×10^{-15}	0.05023	0.0610	0.08059	0.108
$^{27}_{13}$Al	4.6×10^{-16}	0.0153	0.0163	0.0159	0.0169

limit on $\mu \to e$ conversion comes from the *SINDRUM* experiment using $^{197}_{79}$Au nucleus: $\mathcal{R}|^{\text{Au}}_{\mu\to e} < 7.0 \times 10^{-13}$ [98], whereas in the future, the *Mu2e* experiment at Fermilab [250] and *COMET* experiment at J-PARC [251] are expected to improve the experimental sensitivity down to 10^{-17} level using $^{27}_{13}$Al.

$\ell_\alpha \to \ell_\beta \gamma$

As mentioned in Section 4.2, the interaction of the leptoquarks can be characterised by the generalised fermion number $F = 3B + L$. In this model, two leptoquarks with two different generalised fermion numbers, i.e. $F_{S_1} = -2\,, \quad F_{\widetilde{R}_2} = 0$ is present. The interaction of these leptoquarks with the charged lepton can be written as [253]

$$-\mathcal{L}^{|F|=2} \supset \overline{u}_i^C \left(Y_1^L\right)_{ij} P_L\, e_j\, S_1^{1/3} + \overline{u}_i^C \left(Y_1^R\right)_{ij} P_R\, e_j\, S_1^{1/3} + \text{h.c.}, \tag{4.34}$$

$$-\mathcal{L}^{|F|=0} \supset \overline{d}_i \left(Y_2\right)_{ij} P_L e_j\, \widetilde{R}_2^{2/3} + \text{h.c.} \tag{4.35}$$

Using the interaction Lagrangian, it is easy to construct an effective Lagrangian describing the $\ell_\alpha \to \ell_\beta \gamma$ as

$$-\mathcal{L}_{\text{eff}} = \frac{e}{2}\, \overline{\ell_\beta}\, i\, \sigma^{\mu\nu}\, F_{\mu\nu} \left(\sigma_L^{\alpha\beta}\, P_L + \sigma_R^{\alpha\beta}\, P_R\right) \ell_\alpha + \text{h.c.} \tag{4.36}$$

In the considered model the diagrams contributing to this process are given in the right panel of Fig. 4.3.

The $\ell_\alpha \to \ell_\beta \gamma$ partial decay rate is given by

$$\Gamma\left(\ell_\alpha \to \ell_\beta \gamma\right) = \frac{\alpha_{\text{em}}\, m_\alpha^3}{4} \left(1 - \frac{m_\beta^2}{m_\alpha^2}\right)^3 \left(\left|\sigma_L^{\alpha\beta}\right|^2 + \left|\sigma_R^{\alpha\beta}\right|^2\right). \tag{4.37}$$

Here $\alpha_{\rm em} = \frac{e^2}{4\pi}$ is the fine structure constant, and the $\sigma_L^{\alpha\beta}$ and $\sigma_R^{\alpha\beta}$ can be expressed in the leptoquark mass basis $\left(X_1^{1/3}, X_2^{1/3}\right)$ as

$$\sigma_L^{X_1} = \frac{i\,N_c \cos^2\theta_{\rm LQ}}{16\pi^2 m_{X_1}^2} \sum_{q=u,c,t} \left[\left(Y_1^L\right)_{q\alpha} \left(Y_1^R\right)^*_{q\beta} m_q\, \mathcal{G}(x_{q_1}) + m_\alpha \left(Y_1^R\right)^*_{q\beta} \left(Y_1^R\right)_{q\alpha} \mathcal{F}(x_{q_1}) \right], \tag{4.38}$$

$$\sigma_L^{X_2} = \frac{i\,N_c \sin^2\theta_{\rm LQ}}{16\pi^2 m_{X_2}^2} \sum_{q=u,c,t} \left[\left(Y_1^L\right)_{q\alpha} \left(Y_1^R\right)^*_{q\beta} m_q\, \mathcal{G}(x_{q_2}) + m_\alpha \left(Y_1^R\right)^*_{q\beta} \left(Y_1^R\right)_{q\alpha} \mathcal{F}(x_{q_2}) \right], \tag{4.39}$$

$$\sigma_R^{X_1} = \frac{i\,N_c\, \cos^2\theta_{\rm LQ}}{16\pi^2 m_{X_1}^2} \sum_{q=u,c,t} \left[\left(Y_1^{L*}\right)_{q\beta} \left(Y_1^R\right)_{q\alpha} m_q\, \mathcal{G}(x_{q_1}) + m_\alpha \left(Y_1^L\right)^*_{q\beta} \left(Y_1^L\right)_{q\alpha} \mathcal{F}(x_{q_1}) \right], \tag{4.40}$$

$$\sigma_R^{X_2} = \frac{i\,N_c\, \sin^2\theta_{\rm LQ}}{16\pi^2 m_{X_2}^2} \sum_{q=u,c,t} \left[\left(Y_1^{L*}\right)_{q\beta} \left(Y_1^R\right)_{q\alpha} m_q\, \mathcal{G}(x_{q_2}) + m_\alpha \left(Y_1^{L*}\right)_{q\beta} \left(Y_1^L\right)_{q\alpha} \mathcal{F}(x_{q_2}) \right]. \tag{4.41}$$

Here $x_{q_i} = m_q^2/m_{X_i}^2$, $N_c = 3$ is the number of colours, and the loop functions $\mathcal{F}(x)$ and $\mathcal{G}(x)$ are given as,

$$\mathcal{F}(x) = Q_S f_S(x) - f_F(x)\,, \qquad \mathcal{G}(x) = Q_S\, g_S(x) - g_F(x), \tag{4.42}$$

where Q_S is the electromagnetic charge for the scalar leptoquark and

$$f_S(x) = \frac{x+1}{4(1-x)^2} + \frac{x\,\ln x}{2(1-x)^3}, \tag{4.43}$$

$$f_F(x) = \frac{x^2-5x-2}{12(x-1)^3} + \frac{x\,\ln x}{2(x-1)^4}, \tag{4.44}$$

$$g_S(x) = \frac{1}{x-1} - \frac{\ln x}{(x-1)^2}, \tag{4.45}$$

$$g_F(x) = \frac{x-3}{2(x-1)^2} + \frac{\ln x}{(x-1)^3}. \tag{4.46}$$

For $x \ll 1$, these loop functions can be approximated as

$$f_S(x) \simeq \frac{1}{4}, \quad f_F(x) \simeq \frac{1}{6}, \quad g_S(x) \simeq -\ln(x), \quad g_F(x) \simeq -\ln(x)\,. \tag{4.47}$$

Note that for leptoquark $\widetilde{R}_2^{2/3}$ with $Q_S = 2/3$, we have $\mathcal{F}(x) \sim \frac{2}{3} \times \frac{1}{4} - \frac{1}{6} = 0$ and $\mathcal{G}\,(x) = \frac{1}{3}\ln(x)$.

For all cLFV processes $\ell_\alpha \to \ell_\beta\gamma$, the mass of ℓ_β can be neglected with respect to the mass of ℓ_α and the total σ (for a given $\alpha\beta$ combination) can be written as

$$\sigma_L = \sigma_L^{X_1} + \sigma_L^{X_2}, \qquad \sigma_R = \sigma_R^{X_1} + \sigma_R^{X_2}\,. \tag{4.48}$$

The cLFV decay branching ratios (BRs) can be written as

$$\mathrm{BR}\left(\ell_\alpha \to \ell_\beta\gamma\right) = \frac{\alpha_{\mathrm{em}}\, m_\alpha^3}{4\,\Gamma_\alpha}\left(\left|\sigma_L^{\alpha\beta}\right|^2 + \left|\sigma_R^{\alpha\beta}\right|^2\right)\,. \tag{4.49}$$

Here Γ_α is the total decay width for lepton flavour α, which is 2.996×10^{-19} GeV for μ and 2.267×10^{-12} GeV for τ.

These theoretical predictions for the LFV BRs are to be compared with the current experimental upper limits:

$$\begin{aligned}
&\mathrm{BR}\left(\mu \to e\gamma\right) < 3.1 \times 10^{-13} && \textit{MEG-II}\ [99],\\
&\mathrm{BR}\left(\tau \to \mu\,\gamma\right) < 4.2 \times 10^{-8} && \textit{Belle}\ [254],\\
&\mathrm{BR}\left(\tau \to e\,\gamma\right) < 3.3 \times 10^{-8} && \textit{BaBar}\ [255]\,.
\end{aligned}$$

Belle-II is expected to improve the tau LFV limits by a factor of few [256].

Lepton $g-2$

The same one-loop diagrams that contribute to $\ell_\alpha \to \ell_\beta\gamma$ also give rise to the anomalous magnetic moment of ℓ_α for $\alpha = \beta$. The leptoquark contribution can thus be written as

$$\Delta a_\alpha = i\, m_\alpha\left(\sigma_L^\alpha + \sigma_R^\alpha\right), \tag{4.50}$$

where

$$\begin{aligned}
\sigma_L^\alpha = \frac{i\,N_c m_\alpha}{16\pi^2}\left(\frac{\cos^2\theta_{\mathrm{LQ}}}{m_{X_1}^2} + \frac{\sin^2\theta_{\mathrm{LQ}}}{m_{X_2}^2}\right)\sum_{q=u,c,t}\Bigg[&\mathrm{Re}\left[\left(Y_1^L\right)_{q\alpha}\left(Y_1^R\right)_{q\alpha}^*\right] m_q\,\mathcal{G}(x_q)\\
&+m_\alpha\left(\left|\left(Y_1^R\right)_{q\alpha}\right|^2 + \left|\left(Y_1^L\right)_{q\alpha}\right|^2\right)\mathcal{F}(x_q)\Bigg],
\end{aligned}$$

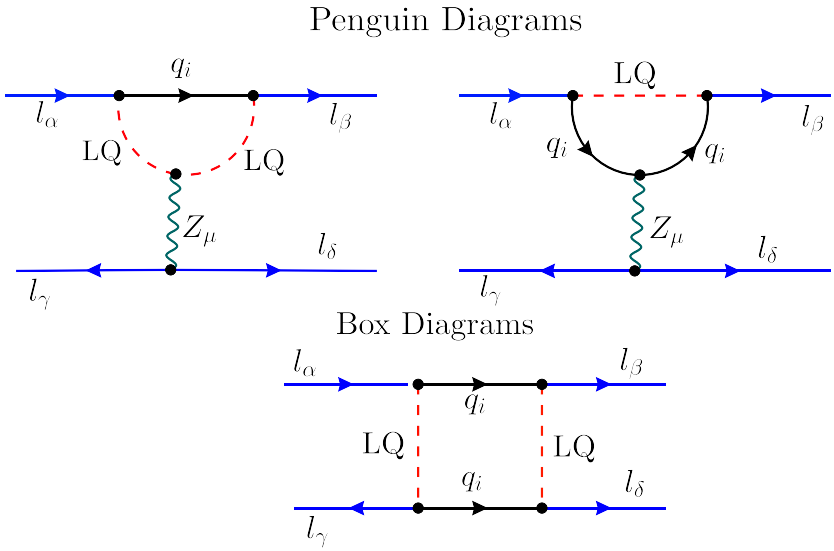

Figure 4.4: Penguin (top panel) and box (bottom panel) feynman diagrams contributing to $l_\alpha \to l_\beta l_\gamma l_\delta$ decays.

$$\sigma_R^\alpha = \frac{i\,N_c m_\alpha}{16\pi^2}\left(\frac{\cos^2\theta_{\rm LQ}}{m^2_{X_1}}+\frac{\sin^2\theta_{\rm LQ}}{m^2_{X_2}}\right)\sum_{q=u,c,t}\left[{\rm Re}\left[\left(Y_1^L\right)^*_{q\alpha}\left(Y_1^R\right)_{q\alpha}\right] m_q\,\mathcal{G}(x_q)\right. \tag{4.51}$$

$$\left. + m_\alpha\left(\left|\left(Y_1^R\right)_{q\alpha}\right|^2+\left|\left(Y_1^L\right)_{q\alpha}\right|^2\right)\mathcal{F}(x_q)\right]. \tag{4.52}$$

For muon $(g-2)$, as mentioned in section. 1.2.2, using the BMW's lattice result, the anomalous magnetic moment deviation is quoted as $\Delta a_\mu = (1.07 \pm 0.70) \times 10^{-9}$ [38] and for electron magnetic moment, $\Delta a_e({\rm Rb}) = (4.4 \pm 3.0) \times 10^{-13}$ [42] and $\Delta a_e({\rm Cs}) = (-8.8 \pm 3.6) \times 10^{-13}$ [43] is used.

$\ell_\alpha \to \ell_\beta \ell_\gamma \ell_\delta$

The four-lepton LFV amplitude is mediated by penguin and box diagrams involving leptoquarks and quarks. The figures are shown in Fig. 4.4. The amplitude typically scales as $y^2/m^2_{\rm LQ}$ for the penguin diagrams and as $y^4/m^2_{\rm LQ}$ for the box diagrams, where y is the relevant leptoquark coupling. As the

Yukawa couplings involved in this processes are small due to the constraints from cLFV processes, the bounds coming from the box diagrams turn out to be subdominant to those from the penguins. However, typically the photon penguin contribution to $\ell_\alpha \to \ell_\beta \ell_\gamma \ell_\delta$ is dominant over the Z penguins. Now, as the leptoquark couples to both left and the right chiral fermions, the dipole contributions are dominant for $\ell_\alpha \to \ell_\beta \ell_\gamma \ell_\delta$. The branching ratio of $\ell_\alpha \to 3\ell_\beta$ decay is found as [257, 258]

$$\frac{BR\left(\ell_\alpha \to 3\,\ell_\beta\right)}{BR\left(\ell_\alpha \to \ \ell_\beta\,\gamma\right)} \ = \ \frac{\alpha_{\rm em}}{3\pi}\left[\ln\left(\frac{m_\alpha}{m_\beta}\right) - \frac{11}{4}\right] . \tag{4.53}$$

This is to be compared with the current limis:

$$\begin{aligned}
&\mathrm{BR}\left(\mu \to\ 3\,e\right) < 1.0 \times 10^{-12} && \textit{SINDRUM}\ [100],\\
&\mathrm{BR}\left(\tau \to\ 3\,\mu\right) < 2.1 \times 10^{-8} && \textit{Belle}\ [259],\\
&\mathrm{BR}\left(\tau \to\ 3\,e\ \right) < 2.7 \times 10^{-8} && \textit{Belle}\ [259]\ .
\end{aligned}$$

We find that the corresponding limits in the leptoquarks are weaker than those from $\mu \to e$ conversion in nuclei. Therefore, we do not further discuss the results for $\ell_\alpha \to 3\,\ell_\beta$ type processes here.

4.5.2 Neutrino electric and magnetic dipole moments

In this leptoquark model, neutrinos can interact with the photon at 1-loop (by just attaching a photon line to Fig. 4.1) which generates magnetic dipole moment (MDM) and electric dipole moment (EDM) for the neutrinos [102, 260–262]. The most general electromagnetic vertex function can be written as [101, 102]

$$\begin{aligned}
\Gamma^\mu \ = \ i\,e\Big[&\gamma^\mu\left\{F_1^V(q^2) + F_1^A(q^2)\gamma_5\right\} + \frac{i}{2\,m_\nu}\sigma^{\mu\nu}\,q_\nu\,\left\{F_2^V(q^2) + F_2^A(q^2)\,\gamma_5\right\}\\
&+q^\mu\,\left\{F_3^V(q^2) + F_3^A(q^2)\,\gamma_5\right\} + F_4^A\left(q^2\right)\,\gamma_5\,q^\mu\,\not{q}\Big] ,
\end{aligned} \tag{4.54}$$

where q is the momentum of the outgoing photon, $F_1^V, F_1^A, F_2^V, F_2^A$ are the electric charge, anapole, magnetic dipole and electric dipole form factors, respec-

tively. The MDM and EDM of the neutrino are then given as,

$$\mu_\nu^{ij} = e\,\frac{F_2^V(0)}{2\,m_\nu}\,, \qquad\qquad d_\nu^{ij} = -i\,e\,\frac{F_2^A(0)}{2\,m_\nu}\,. \tag{4.55}$$

If the neutrinos are majorana, the dipole moments are anti-symmetric which means only the transition elements i.e off-diagonal elements are non-vanishing.

Stringent limits on the neutrino MDM come from the brightness measurement of the tip of the red giant branch in ω-Centauri globular cluster using Gaia DR2 data. Ref. [103] quotes this limit as $\mu_\nu < 1.2 \times 10^{-12}\,\mu_B$, where $\mu_B = \frac{e}{2\,m_e}$ is the Bohr magneton. As far as the neutrino EDM is concerned, no experimental limit exists yet, but several theoretical and indirect bounds have been obtained. The most stringent limit on electron and muon neutrino EDM is quoted as $d_{\nu_e,\nu_\mu} < 10^{-21} e$-cm [104] whereas, for the tau neutrino, $d_{\nu_\tau} < 10^{-17} e$-cm [105].

In this doublet-triplet leptoquark model, there are two 1-loop diagrams, similar to Fig. 4.1, that contribute to MDM and EDM, depending on whether the photon radiates off either from the scalar leptoquark with charge 1/3 or from the down-type quark. If the photon is emitted from the leptoquark, the amplitude can be written as

$$\begin{aligned}\mathcal{M}_a^{ij} \;=\; & i\,e \int \frac{d^4k}{(2\pi)^4} \frac{\left[\overline{u}(q_2)\,P_L\,(\not{k} + m_{d_m})\;P_L\,u(q_1)\;\left(q_1^\mu + q_2^\mu\right)\right]}{\left(k^2 - m_{d_m}^2\right)\left((q_1-k)^2 - m_{X_i}^2\right)\left((q_2-k)^2 - m_{X_i}^2\right)} \\ & \times \sum_{\alpha,\beta,m} \left(\widetilde{Y_1^L}\right)_{m\alpha} (Y_2)_{m\beta}\; U_{j\alpha}\,U_{i\beta}\,,\end{aligned} \tag{4.56}$$

where i, j denote the initial and final neutrino state, k is the loop momentum, q_1, q_2 are the momenta of external neutrinos, m_{d_m} denotes the mass of down-type quark with flavour m, and $(\alpha,\,\beta)$ run over the flavours of neutrinos, i.e. $\{e, \mu, \tau\}$. Similarly, the amplitude of the diagram where the photon is emitted

from the down-quark leg can be written as

$$\mathcal{M}_b^{ij} = ie\int \frac{d^4k}{(2\pi)^4}\frac{[\overline{u}(q_2)\,P_L\,(\not{q}_2-\not{k}+m_{d_m})\,\gamma^\mu\,(\not{q}_1-\not{k}+m_{d_m})\,P_L\,u(q_1)]}{\left(k^2-m_{X_i}^2\right)\left((q_1-k)^2-m_{d_m}^2\right)\left((q_2-k)^2-m_{d_m}^2\right)} \times \sum_{\alpha,\beta,m}\left(\widetilde{Y_1^L}\right)_{m\alpha}(Y_2)_{m\beta}\,U_{j\alpha}\,U_{i\beta}\,. \tag{4.57}$$

Note that the electromagnetic charge of $1/3$ is canceled by the colour factor of 3 in both Eqs. (4.56) and (4.57).

From the total amplitude, $\mathcal{M} = \mathcal{M}_a + \mathcal{M}_b$, the dominant contribution to the MDM can be identified as

$$\mu_\nu^{ij} = \frac{m_b\,m_e}{32\,\pi^2}\sin(2\theta_{\rm LQ})\,L(x_b)\left(\frac{1}{m_{X_1}^2}-\frac{1}{m_{X_2}^2}\right)\mathrm{Im}\left[\sum_{\alpha,\beta}\left(\widetilde{Y_1^L}\right)_{3\alpha}(Y_2)_{3\beta}\left(U_{i\beta}\,U_{j\alpha}^*-U_{i\alpha}^*\,U_{j\beta}\right)\right], \tag{4.58}$$

where, $x_b = m_b^2/m_{\rm LQ}^2$. Note that as MDM depends on the mass of the down-type quark, the dominant contribution comes from the bottom quark. The loop function $L(x)$ is defined as

$$L(x) = \frac{\log x}{(1-x)^2}+\frac{1}{(1-x)}\,. \tag{4.59}$$

Similarly, the dominant contribution to the EDM can be identified as

$$d_\nu^{ij} = -\frac{m_b\,\sin(2\theta_{\rm LQ})}{32\,\pi^2}\,L(x_b)\left(\frac{1}{m_{X_1}^2}-\frac{1}{m_{X_2}^2}\right)\mathrm{Re}\left[\sum_{\alpha,\beta}\left(\widetilde{Y_1^L}\right)_{3\alpha}(Y_2)_{3\beta}\left(U_{i\beta}\,U_{j\alpha}^*-U_{i\alpha}^*\,U_{j\beta}\right)\right]. \tag{4.60}$$

Assuming the Yukawa coupling to be $\mathcal{O}(1)$, both MDM and EDM can be expressed in terms of neutrino masses, as follows:

$$\mu_\nu^{ij} \approx 5\times10^{-20}\,\mu_B\left(\frac{m_\nu}{0.01\,\mathrm{eV}}\right)\left(\frac{\mathrm{TeV}}{m_{\rm LQ}}\right)^2, \quad \left|d_\nu^{ij}\right| \approx 2\times10^{-30}e\text{-cm}\left(\frac{m_\nu}{0.01\,\mathrm{eV}}\right)\left(\frac{\mathrm{TeV}}{m_{\rm LQ}}\right)^2. \tag{4.61}$$

This implies that for TeV-scale LQs, both MDM and EDM of neutrinos are far

below the current experimental limits.

Note that there are no leptoquark contributions to the electron, proton, or neutron EDM in this model, if Yukawa couplings are assumed to be real [263, 264].

4.5.3 Rare Meson Decays

In this section, the leptoquark contributions to the (semi)leptonic rare decays of B and K mesons is discussed. Here, the neutral-current B decays involving $b \to s\ell^+\ell^-$ and charged-current B decays involving $b \to c\ell\overline{\nu}$, in particular the LFUV observables can be parameterised in terms of the ratios of BRs,

$$R_{D^{(*)}} = \frac{\mathrm{BR}(\overline{B} \to D^{(*)}\tau\overline{\nu})}{\mathrm{BR}(\overline{B} \to D^{(*)}\ell\overline{\nu})} \quad \text{with } \ell = e, \mu, \tag{4.62}$$

$$R_K = \frac{\mathrm{BR}(B^+ \to K^+\mu^+\mu^-)}{\mathrm{BR}(B^+ \to K^+e^+e^-)}, \tag{4.63}$$

$$R_{K^*} = \frac{\mathrm{BR}(B^0 \to K^{*0}\mu^+\mu^-)}{\mathrm{BR}(B^0 \to K^{*0}e^+e^-)}, \tag{4.64}$$

which are theoretically clean observables with strongly suppressed hadronic and CKM-angle uncertainties. Other rare decays such as $B \to K\nu\overline{\nu}$, $K^+ \to \pi^+\nu\overline{\nu}$, and the rare kaon decays $K_L \to \mu^\pm e^\mp$ and $K^+ \to \pi^+\mu^\pm e^\mp$ are also considered in this section.

R_K and R_{K^*}

The relevant effective Hamiltonian for the process can be written as

$$\mathcal{H}_{\text{eff}} \;=\; \frac{4\,G_F}{\sqrt{2}}\,\lambda_t^{bs}\left[\sum_{X=9,10}\left(C_X^{\ell\ell}\,\mathcal{O}_X^{\ell\ell} + C_{X'}^{\ell\ell}\,\mathcal{O}_{X'}^{\ell\ell}\right)\right], \tag{4.65}$$

where $\lambda_q^{bs} = V_{qb}\,V_{qs}^*$, $C_{X^{(\prime)}}$ is the Wilson coefficients corresponding to the operator $\mathcal{O}_{X^{(\prime)}}$, defined as

$$\mathcal{O}_9 \;=\; \frac{\alpha_{\text{em}}}{4\pi}\,(\bar{s}\,\gamma^\mu P_L\,b)\,\left(\bar{\ell}\,\gamma_\mu\,\ell\right),$$

$$\begin{aligned}
\mathcal{O}_{10} &= \frac{\alpha_{\rm em}}{4\pi}\,(\bar{s}\,\gamma^\mu P_L\,b)\,\left(\bar{\ell}\,\gamma_\mu\,\gamma_5\,\ell\right)\,, \\
\mathcal{O}_{9'} &= \frac{\alpha_{\rm em}}{4\pi}\,(\bar{s}\,\gamma^\mu P_R\,b)\,\left(\bar{\ell}\,\gamma_\mu\,\ell\right)\,, \\
\mathcal{O}_{10'} &= \frac{\alpha_{\rm em}}{4\pi}\,(\bar{s}\,\gamma^\mu P_R\,b)\,\left(\bar{\ell}\,\gamma_\mu\,\gamma_5\,\ell\right)\,.
\end{aligned} \tag{4.66}$$

At tree level, $\mathcal{O}_{X'}$ operators can be generated by the mediation of $\tilde{R}_2^{2/3}$ and $\mathcal{O}_X$ operators are generated at 1-loop from the EW penguin and box diagrams where S_1 leptoquark is circulating inside the loop [265]. When Y_1^L Yukawa couplings are $\mathcal{O}(1)$, Y_2 needs to be very small to generate a small neutrino mass for TeV scale LQ mass. In this case, the EW penguin and box contributions are greater than the tree-level contribution. At the tree-level, the Wilson coefficients are

$$\delta C_9' = -\delta C_{10}' = \frac{\pi\,v^2}{\alpha_{\rm em}\,V_{tb}\,V_{ts}^*}\,\frac{(Y_2)_{s\ell}\,(Y_2^*)_{b\ell}}{2\,m^2_{\tilde{R}_2}}. \tag{4.67}$$

For the penguin and box diagrams, the NP Wilson coefficients are given by

$$\begin{aligned}
\delta C_{9\ell\ell}^{\rm penguin} &= \frac{v^2}{16\,\lambda_t^{bs}}\sum_{i=1,3}\left(\widetilde{Y_1^L}\right)_{2i}\left(\widetilde{Y_1^L}^*\right)_{3i}\left(\frac{\cos^2\theta}{m^2_{X_1}}+\frac{\sin^2\theta}{m^2_{X_2}}\right)\,, \\
\delta C_{9\ell\ell}^{\rm box} &= \frac{v^2}{64\,\pi\,\alpha_{\rm em}\,\lambda_t^{bs}}\sum_{i=1,3}\sum_{j=u,c,t}\left(\widetilde{Y_1^L}\right)_{2i}\left(\widetilde{Y_1^L}^*\right)_{3i}\left(\left|(Y_1^L)_{j\ell}\right|^2+\left|(Y_1^R)_{j\ell}\right|^2\right) \\
&\qquad\times\left(\frac{\cos^2\theta}{m^2_{X_1}}+\frac{\sin^2\theta}{m^2_{X_2}}\right)\,, \\
\delta C_{10\ell\ell}^{\rm box} &= \frac{v^2}{64\,\pi\,\alpha_{\rm em}\,\lambda_t^{bs}}\sum_{i=1,3}\sum_{j=u,c,t}\left(\widetilde{Y_1^L}\right)_{2i}\left(\widetilde{Y_1^L}^*\right)_{3i}\left(\left|(Y_1^L)_{j\ell}\right|^2-\left|(Y_1^R)_{j\ell}\right|^2\right) \\
&\qquad\times\left(\frac{\cos^2\theta}{m^2_{X_1}}+\frac{\sin^2\theta}{m^2_{X_2}}\right).
\end{aligned} \tag{4.68}$$

The *LHCb* experiment recently presented new measurements of the $R_{K^{(*)}}$ ratios which turned out to be compatible with the SM [224, 225]. From a recent global analysis using all available $b \to s\ell^+\ell^-$ data [266], it was found that the primed operators $\mathcal{O}_9'$ and $\mathcal{O}_{10}'$ (with right chiral quark currents) are loosely constrained

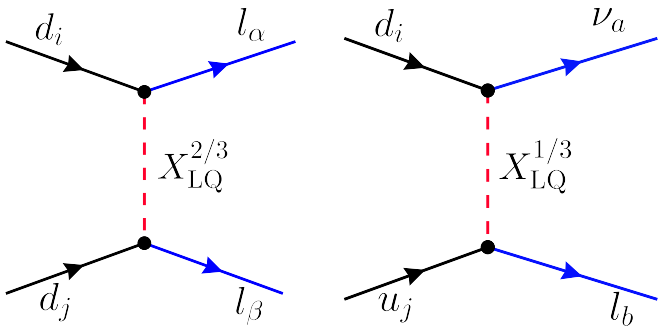

Figure 4.5: Feynman Diagrams contributing to (left) $d_i \to d_j \ell_\alpha \ell_\beta$ transition which contribute to $B \to K\ell\ell$, $K_L \to \mu e$ and $K \to \pi\mu e$ processes, (right) $d_i \to u_j \ell_\alpha \nu_\beta$ which is responsible for $B \to D\ell\nu$ process.

with the best-fit values

$$\begin{aligned} \delta C_9 &= -1.18 \pm 0.19 \qquad \delta C_{10} = 0.23 \pm 0.20 \\ \delta C_{9'} &= 0.06 \pm 0.31 \qquad \delta C_{10'} = -0.05 \pm 0.19 \end{aligned} \tag{4.69}$$

Therefore, $R_{K^{(*)}}$ does not impose any stringent constraint on the considered doublet-triplet leptoquark model parameter space.

R_D and R_{D^*}

Both S_1 and $\widetilde{R}_2$ leptoquarks contribute to $R_{D^{(*)}}$. The effective Hamiltonian can be written as [267]

$$\mathcal{H}_{\rm eff} = \frac{4\,G_F}{\sqrt{2}} V_{cb} \left[(\delta_{\ell\tau} + C_{V_L})\ \mathcal{O}_{V_L} + C_{S_L}\,\mathcal{O}_{S_L} + C_{T_L}\,\mathcal{O}_{T_L} \right], \tag{4.70}$$

where the operators are defined as

$$\mathcal{O}_{V_L} = (\bar{c}\gamma^\mu P_L b)\left(\bar{\ell}\gamma_\mu P_L \nu\right), \tag{4.71}$$

$$\mathcal{O}_{S_L} = (\bar{c} P_L\, b)\left(\bar{\ell}\, P_L\, \nu\right), \tag{4.72}$$

$$\mathcal{O}_{T_L} = (\bar{c}\,\sigma^{\mu\nu}\, P_L\, b)\left(\bar{\ell}\,\sigma_{\mu\nu}\, P_L\, \nu\right), \tag{4.73}$$

and the $\delta_{\ell\tau}$ term denotes the SM-dominant contribution for $b \to c\tau^-\overline{\nu}$. The Wilson coefficients can be found as

$$C_{V_L} = \frac{v^2}{V_{cb}} \frac{\left(Y_1^L\right)^*_{c\ell} \left(\widetilde{Y_1^L}\right)_{b\ell}}{4} \left(\frac{\cos^2\theta_{\rm LQ}}{m^2_{X_1}} + \frac{\sin^2\theta_{\rm LQ}}{m^2_{X_2}}\right), \tag{4.74}$$

$$C_{S_L} = \frac{v^2}{V_{cb}} \frac{\left(Y_1^R\right)^*_{c\ell} \left(\widetilde{Y_1^L}\right)_{b\ell}}{4} \left(\frac{\cos^2\theta_{\rm LQ}}{m^2_{X_1}} + \frac{\sin^2\theta_{\rm LQ}}{m^2_{X_2}}\right), \tag{4.75}$$

$$C_{T_L} = -\frac{C_{S_L}}{4}. \tag{4.76}$$

The Wilson coefficients, mentioned above are extracted at $\mu = \mu_{\rm ew}$. To compare with the experimental observables,they are needed to run them down to $\mu = m_b = 4.18$ GeV using the renormalisation group equations, i.e.

$$C_i(\mu = m_b) = \Omega_N(\mu, \mu_{\rm ew})\, C_i(\mu_{\rm ew}), \tag{4.77}$$

where at the lowest order (leading logarithm), the evolution operator is given by [268–271]

$$\Omega_N(\mu, \mu_{\rm ew}) = \left(\frac{\alpha_s^{(5)}(m_b)}{\alpha_s^{(5)}(m_t)}\right)^{-\gamma_1^J/\beta_1^{(5)}} \tag{4.78}$$

with QCD running β-function, $\beta_1^{(n_f)} = (2n_f - 33)/6$, where n_f is the relevant number of quark flavours at the hadronic scale. The anomalous dimensions for the currents are

$$\gamma_1^V = 0, \qquad \gamma_1^S = 2, \qquad \gamma_1^T = -2/3. \tag{4.79}$$

Note that the vector currents are not affected as a consequence of the Ward Identity, while the scalar and tensor currents renormalise multiplicatively. The ratio of R_D (R_{D^*}) to the SM prediction can be expressed as [48],

$$\begin{aligned} r_D = \frac{R_D}{R_D^{\rm SM}} \approx\ & |1 + C_{V_L}|^2 + 1.01\,|C_{S_L}|^2 + 0.84\,|C_{T_L}|^2 + 1.49\ {\rm Re}\left[(1 + C_{V_L})C^*_{S_L}\right] \\ & + 1.08\ {\rm Re}\left[(1 + C_{V_L})\, C^*_{T_L}\right], \end{aligned} \tag{4.80}$$

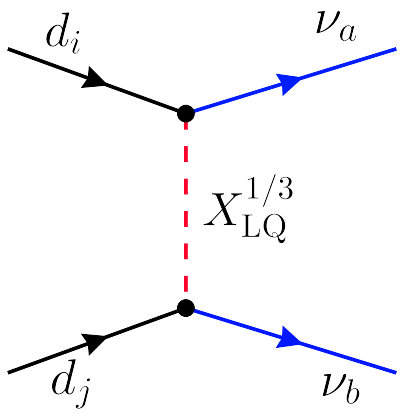

Figure 4.6: Feynman Diagrams contributing to $d_i \to d_j \nu_a \nu_b$ transitions which contribute to $B \to K\nu\nu$ and $K \to \pi\nu\nu$ decays.

$$r_{D^*} = \frac{R_{D^*}}{R_{D^*}^{\rm SM}} \approx |1 + C_{V_L}|^2 + 0.04\,|C_{S_L}|^2 + 16.07\,|C_{T_L}|^2 - 0.11\ {\rm Re}\left[(1 + {\rm C_{V_L}})\,{\rm C_{S_L}^*}\right] - 5.17\ {\rm Re}\left[(1 + {\rm C_{V_L}})\,{\rm C_{T_L}^*}\right] \quad (4.81)$$

Using a recent global fit to the experimental results, Ref. [48] found a 4.3σ deviation from the SM prediction:

$$r_D = 1.186 \pm 0.072, \qquad r_{D^*} = 1.149 \pm 0.04. \quad (4.82)$$

Treating this $R_{D^{(*)}}$ anomaly at the face value, the parameter space which can successfully fit this anomaly will be analysed. Given the volatile situation with flavour anomalies, a hypothetical case is considered in this chapter where this anomaly disappears with more data in the future, i.e. both R_D and R_{D^*} are consistent with the SM predictions.

$B^+ \to K^+ \nu\,\overline{\nu}$

Leptoquarks can also induce rare semi-leptonic B decays like $B^+ \to K^+\nu\overline{\nu}$ and $B^0 \to K^{*0}\nu\overline{\nu}$, governed by $(\overline{q}q\overline{\nu}\nu)$ effective interactions. The SM predictions for these decays are ${\rm BR}\,(B^+ \to K^+\nu\overline{\nu}) = (4.65 \pm 0.62) \times 10^{-6}$ and ${\rm BR}\left(B^0 \to K^{*0}\nu\overline{\nu}\right) = (10.13 \pm 0.92) \times 10^{-6}$ [272]. *Belle-II* recently reported the first observation of $B^+ \to K^+\,\nu\,\overline{\nu}$ decay [50]. Using the weighted average

of *BaBar*, *Belle* and *Belle-II* data, Ref. [49] quoted an experimental value for $\mathrm{BR}\left(B^+ \to K^+ \nu\,\overline{\nu}\right)_{\mathrm{exp}} = (1.3 \pm 0.4) \times 10^{-5}$. As for $B^0 \to K^{*0}\nu\overline{\nu}$, the current experimental upper limit is $\mathrm{BR}\left(B^0 \to K^{*0}\nu\overline{\nu}\right) < 2.7 \times 10^{-5}$ at 90% CL by the *Belle* collaboration [273]. The constraints on new physics (NP) contributions are expressed in terms of the ratios $R^{\nu\nu}_{K^{(*)}}$, defined as

$$R^{\nu\nu}_{K^{(*)}} = \frac{\mathrm{BR}^{\mathrm{SM+NP}}\left(B^{+(0)} \to K^{+(*)}\nu\overline{\nu}\right)}{\mathrm{BR}^{\mathrm{SM}}\left(B^{+(0)} \to K^{+(*)}\nu\overline{\nu}\right)}. \tag{4.83}$$

From the recent *Belle-II* measurement [50], it is found that $R^{\nu\nu}_{K} = (2.8 \pm 0.94)$ and the upper limit [273] $R^{\nu\nu}_{K^*} < 2.7$ is taken from the *Belle* Result.

The relevant effective Hamiltonian governing these decays can be written as

$$\mathcal{H}_{\mathrm{eff}} = \frac{4G_F}{\sqrt{2}} V_{tb}\, V^*_{ts} \left(C^{ij}_L\, \mathcal{O}^{ij}_L + C^{ij}_R \mathcal{O}^{ij}_R\right), \tag{4.84}$$

where the operators are defined as

$$\mathcal{O}^{ij}_L = \frac{\alpha_{\mathrm{em}}}{4\pi}\left(\overline{d}\gamma^\mu P_L s\right)\left(\overline{\nu}_i \gamma_\mu (1-\gamma_5)\nu_j\right), \tag{4.85}$$

$$\mathcal{O}^{ij}_R = \frac{\alpha_{\mathrm{em}}}{4\pi}\left(\overline{d}\gamma^\mu P_R s\right)\left(\overline{\nu}_i \gamma_\mu (1-\gamma_5)\nu_j\right). \tag{4.86}$$

The corresponding Wilson coefficients are given as

$$\begin{aligned} C^{ij}_L &= C_{\mathrm{SM}}\delta^{ij} + \delta C^{ij}_L \\ &= C_{\mathrm{SM}}\delta^{ij} + \frac{\pi\, v^2}{2\,\alpha_{\mathrm{em}}\, V_{tb}\, V^*_{ts}} \left(\frac{\cos^2\theta}{m^2_{X_1}} + \frac{\sin^2\theta}{m^2_{X_2}}\right) \left(\widetilde{Y^L_1}\right)_{2j} \left(\widetilde{Y^L_1}^*\right)_{3i}, \end{aligned} \tag{4.87}$$

$$C^{ij}_R = \delta C^{ij}_R = -\frac{\pi\, v^2}{2\,\alpha_{\mathrm{em}}\, V_{tb}\, V^*_{ts}} \left(\frac{\sin^2\theta}{m^2_{X_1}} + \frac{\cos^2\theta}{m^2_{X_2}}\right) (Y_2)_{2j}\, (Y^*_2)_{3i}. \tag{4.88}$$

As the experiments cannot tag the neutrino flavour, the final neutrino states are summed over all possible flavour combinations while calculating the ratio of branching fractions in Eq. (4.83). The ratios can be expressed as [274, 275]

$$R^{\nu\nu}_K = \frac{1}{3\,|C_{\mathrm{SM}}|^2} \sum_{i,j} \left|C^{ij}_L + C^{ij}_R\right|^2, \tag{4.89}$$

$$R_{K^*}^{\nu\nu} = \frac{1}{3\left|C_{\rm SM}\right|^2}\sum_{i,j}\left|C_L^{ij}+C_R^{ij}\right|^2 - \frac{2}{3\left|C_{\rm SM}\right|^2}(1+\eta)\sum_{i,j}{\rm Re}\left[C_L^{ij}\,C_R^{*ij}\right] \quad (4.90)$$

The numerical value of η was found to be 0.63 ± 0.09 using the Light Cone Sum Rule (LCSR) method [276].

$K^+ \to \pi^+ \nu\,\overline{\nu}$

Apart from B meson decays, leptoquark models are also constrained from the rare K meson decays. One such example is $K^+ \to \pi^+\nu\overline{\nu}$ which gets tree-level contribution from the scalar leptoquarks [49, 201, 277, 278]. The experimentally determined value is ${\rm BR}\left(K^+ \to \pi^+\nu\overline{\nu}\right)_{\rm exp} = \left(10.6^{+4.1}_{-3.5}\times 10^{-11}\right)$ by *NA62* [279] which is consistent with the SM prediction ${\rm BR}\left(K^+ \to \pi^+\nu\overline{\nu}\right)_{\rm SM} = (7.73 \pm 0.61)\times 10^{-11}$ [280]. Thus, there is a very small room for the NP contribution for $K^+ \to \pi^+\,\nu\,\overline{\nu}$ because the SM value is already well inside the range of experimental uncertainty. The BR of $K^+ \to \pi^+\nu\,\overline{\nu}$ can be written as [277, 281]

$${\rm BR}\left(K^+ \to \pi^+\nu\,\overline{\nu}\right) = \kappa_+\frac{(1+\Delta_{\rm em})}{3\,\lambda^{10}}\sum_{i,j=e,\mu,\tau}\left[{\rm Im}^2\left(\lambda_t^{sd}\,X_t^{ij}\right)+{\rm Re}^2\left(\lambda_c^{sd}\,X_c^{ii}+\lambda_t^{sd}\,X_t^{ij}\right)\right], \quad (4.91)$$

where i,j denote the flavours of the emitted neutrinos, $\lambda = 0.225$ is the Wolfenstein parameter of the CKM matrix, $\Delta_{\rm em} = -0.003$, $\kappa_+ = 0.52\times 10^{-10}\left(\frac{\lambda}{0.225}\right)$ and $\lambda_q^{sd} = V_{qs}\,V_{qd}^*$, where q is the quark flavour. The short-distance contribution X is defined as $X_t^{ij} = X_{\rm SM}(x_t)\delta_{ij} + X_{\rm LQ}^{ij}$, where $x_t = m_t^2/m_{\rm LQ}^2$. In the SM, the dominant contribution to the branching ratio comes from the top quark and the corresponding $X_{\rm SM}(x_t) = 1.481 \pm 0.009$ and $X_c \approx 10^{-3}$ is the charm quark contribution [281]. NP contributions in the considered leptoquark model can be written as

$$X_{\rm LQ}^{ij} = -\frac{\sin^2\theta_w\,\pi v^2}{\alpha_{\rm em}}\,\frac{\left(C_L^{ij}+C_R^{ij}\right)}{\lambda_t^{sd}}, \quad (4.92)$$

where θ_w is the weak mixing angle, and

$$C_L^{ij} = \frac{1}{2}\left(\widetilde{Y_1^L}\right)_{2i}\left(\widetilde{Y_1^L}\right)_{1j}\left(\frac{\cos^2\theta_{\rm LQ}}{m^2_{X_1}}+\frac{\sin^2\theta_{\rm LQ}}{m^2_{X_2}}\right), \tag{4.93}$$

$$C_R^{ij} = \frac{1}{2}\left(Y_2\right)_{2i}\left(Y_2\right)_{1j}\left(\frac{\sin^2\theta_{\rm LQ}}{m^2_{X_1}}+\frac{\cos^2\theta_{\rm LQ}}{m^2_{X_2}}\right). \tag{4.94}$$

An analogous decay of the neutral kaon, $K_L \to \pi^0\,\nu\,\overline{\nu}$ might have been considered as well but this has not been observed yet, and there only exists an upper bound on $\mathrm{BR}(K_L \to \pi^0\,\nu\,\overline{\nu})_{\rm exp} < 4.9\times10^{-9}$ from *KOTO* [282]. This is more than two orders of magnitude larger than the SM prediction: $\mathrm{BR}(K_L \to \pi^0\,\nu\,\overline{\nu})_{\rm SM} = (2.94\pm0.15)\times10^{-11}$ [283]. Therefore, this process cannot put any meaningful constraint on the NP scenario at the moment.

$K_L \to \mu^\pm e^\mp$ and $K^+ \to \pi^+\mu^\pm e^\mp$

The effective Hamiltonian for these purely leptonic decays of the pseudoscalar meson $P \to \ell_i\,\ell_j$ and $P \to P'\,\ell_i\,\ell_j$ can be written as,

$$\mathcal{H}_{\rm LEFT} = \sqrt{2}\,G_F \sum_{I\in\{V,S,T\}} C_{I_{XY}}\,\mathcal{O}_{I_{XY}}, \tag{4.95}$$

where $X, Y \in \{L, R\}$. The relevant operator generated at tree level $K_L \to \ell_i^-\,\ell_j^+$ and $K^+ \to \pi^+\,\ell_i^-\,\ell_j^+$ is $\mathcal{O}^{ij21}_{V_{LR}} = \left(\overline{\ell}_i\gamma^\mu\,P_L\,\ell_j\right)\left(\overline{s}\gamma_\mu\,P_R\,d\right)$ and the corresponding Wilson coefficient is denoted as

$$C^{ij}_{V_{LR}} = \frac{1}{2\,G_F\,m^2_{\widetilde{R}_2^{2/3}}}\left(\left(Y_2\right)_{2j}\left(Y_2\right)^*_{1i}+\left(Y_2\right)_{1j}\left(Y_2\right)^*_{2i}\right). \tag{4.96}$$

Here 1, 2 correspond to the first (down) and second (strange) generation quarks. Besides the tree level diagram, one loop box diagrams mediated by S_1 leptoquark also contribute to these processes. The penguin diagrams are not possible in this case because of the absence of flavour-changing neutral current (FCNC) for Z_μ and A_μ. The Wilson coefficients generated from the box

diagrams are

$$
\begin{aligned}
C^{ij}_{V_{LL}} &= \frac{v^2}{64\sqrt{2}\,\pi^2}\sum_{l=1,3}\sum_{m=u,c,t}\left(\widetilde{Y_1^L}\right)_{2l}\left(\widetilde{Y_1^L}^{*}\right)_{3l}\left(Y_1^L\right)_{mi}\left(Y_1^L\right)^{*}_{mj}\left(\frac{\cos^2\theta}{m^2_{X_1}}+\frac{\sin^2\theta}{m^2_{X_2}}\right),\\
C^{ij}_{V_{RL}} &= \frac{v^2}{64\sqrt{2}\,\pi^2}\sum_{l=1,3}\sum_{m=u,c,t}\left(\widetilde{Y_1^L}\right)_{2l}\left(\widetilde{Y_1^L}^{*}\right)_{3l}\left(Y_1^R\right)_{mi}\left(Y_1^R\right)^{*}_{mj}\left(\frac{\cos^2\theta}{m^2_{X_1}}+\frac{\sin^2\theta}{m^2_{X_2}}\right).
\end{aligned}
\tag{4.97}
$$

The branching ratio of $K_L \to \ell_i^- \ell_j^+$ can be computed as [249]

$$
\mathrm{BR}\left(K_L \to \ell_i^- \ell_j^+\right) = \tau_K \frac{f_K^2\, m_K\, m_\ell^2}{128\,\pi\, v^4}\left(1-\frac{m_\ell^2}{m_K^2}\right)^2\left\{\left|C^{ij}_{VA}\right|^2+\left|C^{ij}_{AA}\right|^2\right\}, \tag{4.98}
$$

where m_K is the kaon mass, τ_K is its lifetime, and f_K is the kaon decay constant. The Wilson coefficients in Eq. (4.98) are defined as

$$
\begin{aligned}
C^{ij}_{VA} &= C^{ij}_{V_{LR}} - C^{ij}_{V_{LL}} - C^{ij}_{V_{RL}},\\
C^{ij}_{AA} &= C^{ij}_{V_{LL}} - C^{ij}_{V_{LR}} - C^{ij}_{V_{RL}}.
\end{aligned}
\tag{4.99}
$$

Similarly, the branching ratio for $K^+ \to \pi^+ \ell_i \ell_j$ can be written as [249]

$$
\mathrm{BR}\left(K^+ \to \pi^+ \ell_i \ell_j\right) = a_{VV}\left|C^{ij}_{VV}\right|^2 + a_{AV}\left|C^{ij}_{AV}\right|^2, \tag{4.100}
$$

where $a_{VV} \simeq a_{AV} \simeq 0.157$ are kaon form factors in the limit where the light lepton mass is neglected, and the Wilson coefficients are given as

$$
C^{ij}_{VV} = C^{ij}_{V_{LR}} + C^{ij}_{V_{LL}} + C^{ij}_{V_{RL}}, \qquad C^{ij}_{AV} = C^{ij}_{V_{RL}} - C^{ij}_{V_{LL}} - C^{ij}_{V_{LR}}. \tag{4.101}
$$

These BRs are subjected to stringent experimental limits: $\mathrm{BR}\left(K_L \to \mu^\pm e^\mp\right) < 4.7\times10^{-12}$ [284] and $\mathrm{BR}\left(K^+ \to \pi^+ \mu^+ e^-\right) < 1.3\times10^{-11}$ [285] at 90% CL.

4.6 Numerical Analysis

In this section, considering all the above mentioned constraints, a multidimensional scan over all the leptoquark parameters is performed to carve out the allowed parameter space.

4.6.1 Parametrisation of the Yukawa Coupling Matrix

In the canonical seesaw mechanism, the Yukawa couplings can be expressed in terms of the PMNS mixing matrix elements and light neutrino masses using the Casas-Ibarra (CI) parametrisation [286]. However, in the leptoquark scenario with multiple Yukawa couplings, the standard CI approach does not work. However, a similar approach can be used to parameterise one Yukawa coupling in terms of the other Yukawa couplings, PMNS matrix elements and neutrino masses [287], as follows:

$$Y_2 = \frac{1}{\mathbf{C}_1}\,\mathcal{M}_d^{-1}\left(\widetilde{Y_1^L}^T\right)^{-1} U^*\,\sqrt{\mathcal{M}_\nu^{\text{diag}}}\,\mathbb{R}\,\sqrt{\mathcal{M}_\nu^{\text{diag}}}\,U^\dagger\,, \tag{4.102}$$

where $\mathbf{C}_1 = \frac{3\sin 2\theta_{\text{LQ}}}{32\pi^2}\ln\left(\frac{m^2_{X_1}}{m^2_{X_2}}\right)$ is the prefactor in the neutrino mass matrix [cf. Eq. (4.9)], and $\mathbb{R}$ is an arbitrary 3×3 complex matrix with $\mathbb{R}+\mathbb{R}^T = \mathbb{I}$. Thus, using Eq. (4.102), Y_2 can be determined in terms of Y_1^L, $\mathbb{R}$, neutrino masses and PMNS matrix elements. In general, the complex $\mathbb{R}$ matrix can be parameterised in several ways; one such choice is [287]

$$\mathbb{R} = \begin{pmatrix} \frac{1}{2} & r_1 & r_2 \\ -r_1 & \frac{1}{2} & r_3 \\ -r_2 & -r_3 & \frac{1}{2} \end{pmatrix}.$$

In general, r_1, r_2 and r_3 can be any complex number. For simplicity, an additional assumption assumption is made as follows:

$$r_1 = r_2 = r_3 = r\,, \tag{4.103}$$

which is an unknown parameter in the model. For the numerical analysis, r can be varied within the range $(-10^2 : 10^2)$. For concreteness, a benchmark point is chosen for the leptoquark masses, which satisfies the current LHC constraints [93, 288]:

$$m_1 = m_2 = m_{\rm LQ} = 2.0\,{\rm TeV}, \quad \alpha_1 = \alpha_2 = \alpha_2' = 0.2, \quad \kappa = m_{\rm LQ}/10\,, \quad (4.104)$$

which yields

$$\theta_{\rm LQ} = 0.7420\ {\rm rad}, \quad m_{X_1} = 1.99\,{\rm TeV}, \quad m_{X_2} = 2.011\,{\rm TeV}, \quad m_{\widetilde{R}_2^{2/3}} = 2.00\,{\rm TeV}\,. \quad (4.105)$$

Later, to examine the dependence of the observables on the leptoquark mass, Eq. (4.105) can be relaxed and $m_{\rm LQ}$ is varied from TeV scale GUT scale. It will be shown later, for suitable benchmark values of Yukawa couplings, large values of r will be constrained from $\mu \to$ e conversion and $B \to K^+ \nu\,\overline{\nu}$, and for the benchmark value of $m_{\rm LQ} \approx 2$ TeV chosen here, r cannot be larger than $\mathcal{O}(1)$.

In order to determine the Yukawa matrix Y_2, the following textures for Y_1^L and Y_1^R is taken:

$$Y_1^L = \begin{pmatrix} y_{11}^L & y_{12}^L & y_{13}^L \\ 0 & 0 & y_{23}^L \\ y_{31}^L & y_{32}^L & y_{33}^L \end{pmatrix}, \qquad Y_1^R = \begin{pmatrix} y_{11}^R & y_{12}^R & y_{13}^R \\ 0 & 0 & y_{23}^R \\ y_{31}^R & y_{32}^R & y_{33}^R \end{pmatrix}. \quad (4.106)$$

Here, $y_{21}^L, y_{22}^L, y_{21}^R, y_{22}^R$ is explicitly assumed to be zero to prevent NP contributions to $B \to D\ell\nu$ (with $\ell = e, \mu$), which does not give a good fit to the $b \to c\ell\nu$ observables, as noted in Ref. [289]. With the above textures, the elements of the matrices Y_1^L and Y_1^R are randomly varied between their perturbative limits $\left(-\sqrt{4\pi} : \sqrt{4\pi}\right)$. The oscillation parameters required in Eq. (4.102) are given as inputs in their currently allowed $3\,\sigma$ range [21, 290], assuming NO for concreteness. The Majorana phases are included in U and are varied in the range $(0 : \pi)$ and the lightest neutrino mass is varied over $(10^{-5} : 1)$ eV. The Y_2 ma-

Table 4.2: List of rare meson decay constraints on the Yukawa couplings.

Process	Observable	Yukawa couplings involved
$B \to K l^+ l^-$	$\delta C_9 = -1.18 \pm 0.19$ [266]	$\left\lvert\left(\widetilde{Y_1^L}\right)_{2i}\left(\widetilde{Y_1^L}^*\right)_{3i}\right\rvert \times \left(\frac{2\text{TeV}}{m_{\text{LQ}}}\right)^2 < 10$
	$\delta C_{10} = 0.23 \pm 0.20$ [266]	$\left\lvert\left(\widetilde{Y_1^L}\right)_{2i}\left(\widetilde{Y_1^L}^*\right)_{3i}\left(\lvert(Y_1^L)_{jl}\rvert^2 \pm \lvert(Y_1^R)_{jl}\rvert^2\right)\right\rvert \times \left(\frac{2\text{TeV}}{m_{\text{LQ}}}\right)^2 < 1$
$B^* \to K^* l^+ l^-$	$\delta C_9' = 0.06 \pm 0.31$ [266]	
	$\delta C_{10}' = -0.05 \pm 0.19$ [266]	$\lvert(Y_2)_{2i}(Y_2)_{3i}\rvert \times \left(\frac{2\text{TeV}}{m_{\text{LQ}}}\right)^2 \lesssim 10^{-4}$
$B \to D \ell \overline{\nu_l}$	$r_D = [1.114 - 1.258]$ [48]	$1.189 \lesssim (Y_1^L)_{23}(\widetilde{Y_1^L})_{33} \times \left(\frac{2\text{TeV}}{m_{\text{LQ}}}\right)^2 \lesssim 1.937$
$B^* \to D^* \ell \overline{\nu}$	$r_{D^*} = [1.109 - 1.189]$ [48]	$1.466 \lesssim (Y_1^R)_{23}(\widetilde{Y_1^L})_{33} \times \left(\frac{2\text{TeV}}{m_{\text{LQ}}}\right)^2 \lesssim 2.425$
$B^+ \to K^+ \nu \overline{\nu}$	$R_K^{\nu\nu} = 2.8 \pm 0.92$ [50]	$0.216 \lesssim \left\lvert\left(\widetilde{Y_1^L}\right)_{2i}\left(\widetilde{Y_1^L}\right)_{3i}\right\rvert \times \left(\frac{2\text{TeV}}{m_{\text{LQ}}}\right)^2 \lesssim 0.294$
		$-0.374 \lesssim (Y_2)_{2i}(Y_2)_{3i} \times \left(\frac{2\text{TeV}}{m_{\text{LQ}}}\right)^2 \lesssim -0.217$
$B \to K^* \nu \overline{\nu}$	$R_{K^*}^{\nu\nu} < 2.7$ [273]	$0.375 \lesssim \left\lvert\left(\widetilde{Y_1^L}\right)_{2i}\left(\widetilde{Y_1^L}\right)_{3j}\right\rvert \times \left(\frac{2\text{TeV}}{m_{\text{LQ}}}\right)^2 \lesssim 0.452$
		$0.375 \lesssim \left\lvert(Y_2)_{2i}(Y_2)_{3j}\right\rvert \times \left(\frac{2\text{TeV}}{m_{\text{LQ}}}\right)^2 \lesssim 0.452$
$K^+ \to \pi^+ \nu \overline{\nu}$	$\text{BR}(K^+ \to \pi^+ \nu\nu) = \left(10.6^{+4.1}_{-3.5} \times 10^{-11}\right)$ [279]	$1.0 \times 10^{-3} \lesssim (\widetilde{Y_1^L})_{2i}(\widetilde{Y_1^L})_{1j} \times \left(\frac{2\text{TeV}}{m_{\text{LQ}}}\right)^2 \lesssim 1.6 \times 10^{-3}$
		$1.0 \times 10^{-4} \lesssim (Y_2)_{2i}(Y_2)_{1j} \times \left(\frac{2\text{TeV}}{m_{\text{LQ}}}\right)^2 \lesssim 1.6 \times 10^{-3}$
$K_L \to \mu^\pm e^\mp$	$\text{BR}(K_L \to \mu^\pm e^\mp) < 4.7 \times 10^{-12}$ [284]	$\left\lvert\left(\widetilde{Y_1^L}\right)_{2l}\left(\widetilde{Y_1^L}\right)_{3l}(Y_1^L)_{m1}(Y_1^L)_{m2}\right\rvert \times \left(\frac{2\text{TeV}}{m_{\text{LQ}}}\right)^2 < 0.0354$
		$\lvert(Y_2)_{11}(Y_2)_{22}\rvert \times \left(\frac{2\text{TeV}}{m_{\text{LQ}}}\right)^2 < 7.93 \times 10^{-5}$
		$\lvert(Y_2)_{12}(Y_2)_{21}\rvert \times \left(\frac{2\text{TeV}}{m_{\text{LQ}}}\right)^2 < 7.93 \times 10^{-5}$
$K^+ \to \pi^+ \mu^\pm e^\mp$	$\text{BR}(K^+ \to \pi^+ \mu^\pm e^\mp) < 1.3 \times 10^{-11}$ [285]	$\left\lvert\left(\widetilde{Y_1^L}\right)_{2l}\left(\widetilde{Y_1^L}\right)_{3l}(Y_1^L)_{m1}(Y_1^L)_{m2}\right\rvert \times \left(\frac{2\text{TeV}}{m_{\text{LQ}}}\right)^2 < 0.538$
		$\lvert(Y_2)_{11}(Y_2)_{22}\rvert \times \left(\frac{2\text{TeV}}{m_{\text{LQ}}}\right)^2 < 6.02 \times 10^{-4}$

Table 4.3: Yukawa couplings needed to satisfy 1σ values of lepton $g-2$.

Lepton $g-2$	Experimental value	Yukawa couplings needed
$(g-2)_\mu$	$\Delta a_\mu = (1.07 \pm 0.70) \times 10^{-9}$ [38]	$0.99 \times 10^{-3} \lesssim (Y_1^L)_{32}(Y_1^R)_{32} \times \left(\frac{2\text{TeV}}{m_{\text{LQ}}}\right)^2 \lesssim 4.71 \times 10^{-3}$
$(g-2)_e$	$\Delta a_e(\text{Rb}) = (4.4 \pm 3.0) \times 10^{-13}$ [42]	$0.78 \lesssim (Y_1^L)_{11}(Y_1^R)_{11} \times \left(\frac{2\text{TeV}}{m_{\text{LQ}}}\right)^2 \lesssim 4.13$
		$0.77 \times 10^{-4} \lesssim (Y_1^L)_{31}(Y_1^R)_{31} \times \left(\frac{2\text{TeV}}{m_{\text{LQ}}}\right)^2 \lesssim 4.08 \times 10^{-4}$
	$\Delta a_e(\text{Cs}) = (-8.8 \pm 3.6) \times 10^{-13}$ [43]	$-6.92 \lesssim (Y_1^L)_{11}(Y_1^R)_{11} \times \left(\frac{2\text{TeV}}{m_{\text{LQ}}}\right)^2 \lesssim -2.90$
		$-6.84 \times 10^{-4} \lesssim (Y_1^L)_{31}(Y_1^R)_{31} \times \left(\frac{2\text{TeV}}{m_{\text{LQ}}}\right)^2 \lesssim -2.87 \times 10^{-4}$

trix determined with these input values is subjected to perturbativity bounds and as well as constraints from rare meson decays, cLFV processes and lepton $g-2$, as discussed in Section 4.5, and tabulated in Tabs. 4.2, 4.4 and 4.3, respectively. In Tabs. 4.4 and 4.3, current experimental limits on the observables are given and the corresponding upper bounds on the relevant Yukawa couplings for the benchmark value of the leptoquark mass chosen in Eq. (4.105), assuming these to contribute maximally to that particular observable.

Table 4.4: Constraints on Yukawa couplings put by the corresponding cLFV processes and $0\nu\beta\beta$.

Process	Observable	Limits on Yukawa
$\mu N \to eN$	$\mathcal{R}\vert^{\mathrm{Au}}_{\mu\to e} < 7\times10^{-13}$ [98]	$\left[\vert(Y_1^L)_{12}(Y_1^L)_{11}\vert\,,\vert(Y_1^R)_{12}(Y_1^R)_{11}\vert\right]\times\left(\frac{2\mathrm{TeV}}{m_{\mathrm{LQ}}}\right)^2 < 4.06\times10^{-5}$ $\left[\vert(Y_1^L)_{12}(Y_1^R)_{11}\vert\,,\vert(Y_1^R)_{12}(Y_1^L)_{11}\vert\right]\times\left(\frac{2\mathrm{TeV}}{m_{\mathrm{LQ}}}\right)^2 < 4.21\times10^{-5}$ $\vert(Y_2)_{12}(Y_2)_{11}\vert\times\left(\frac{2\mathrm{TeV}}{m_{\mathrm{LQ}}}\right)^2 < 3.68\times10^{-5}$
$\mu \to e\gamma$	$\mathrm{BR}(\mu\to e\gamma) < 3.1\times10^{-13}$ [99]	$\left[\vert(Y_1^L)_{11}(Y_1^L)_{12}\vert,\vert(Y_1^R)_{11}(Y_1^R)_{12}\vert\right]\times\left(\frac{2\mathrm{TeV}}{m_{\mathrm{LQ}}}\right)^2 < 2.74\times10^{-3}$ $\left[\vert(Y_1^L)_{31}(Y_1^L)_{32}\vert,\vert(Y_1^R)_{31}(Y_1^R)_{32}\vert\right]\times\left(\frac{2\mathrm{TeV}}{m_{\mathrm{LQ}}}\right)^2 < 2.49\times10^{-3}$ $\left[\vert(Y_1^R)_{11}(Y_1^L)_{12}\vert,\vert(Y_1^L)_{11}(Y_1^R)_{12}\vert\right]\times\left(\frac{2\mathrm{TeV}}{m_{\mathrm{LQ}}}\right)^2 < 5.92\times10^{-4}$ $\left[\vert(Y_1^L)_{31}(Y_1^R)_{32}\vert,\vert(Y_1^L)_{32}(Y_1^R)_{31}\vert\right]\times\left(\frac{2\mathrm{TeV}}{m_{\mathrm{LQ}}}\right)^2 < 5.86\times10^{-8}$
$\tau \to \mu\,\gamma$	$\mathrm{BR}(\tau\to\mu\,\gamma) < 4.2\times10^{-8}$ [254]	$\left[\vert(Y_1^L)_{12}(Y_1^R)_{13}\vert,\vert(Y_1^L)_{13}(Y_1^R)_{12}\vert\right]\times\left(\frac{2\mathrm{TeV}}{m_{\mathrm{LQ}}}\right)^2 < 8.7$ $\left[\vert(Y_1^L)_{12}(Y_1^L)_{13}\vert,\vert(Y_1^R)_{12}(Y_1^R)_{13}\vert\right]\times\left(\frac{2\mathrm{TeV}}{m_{\mathrm{LQ}}}\right)^2 < 2.2$ $\left[\vert(Y_1^L)_{32}(Y_1^L)_{33}\vert,\vert(Y_1^R)_{32}(Y_1^R)_{33}\vert\right]\times\left(\frac{2\mathrm{TeV}}{m_{\mathrm{LQ}}}\right)^2 < 2.39$ $\left[\vert(Y_1^L)_{32}(Y_1^R)_{33}\vert,\vert(Y_1^L)_{33}(Y_1^R)_{32}\vert\right]\times\left(\frac{2\mathrm{TeV}}{m_{\mathrm{LQ}}}\right)^2 < 8.60\times10^{-4}$
$\tau \to e\,\gamma$	$\mathrm{BR}(\tau\to e\,\gamma) < 3.3\times10^{-8}$ [255]	$\left[\vert(Y_1^L)_{31}(Y_1^R)_{33}\vert,\vert(Y_1^R)_{31}(Y_1^L)_{33}\vert\right]\times\left(\frac{2\mathrm{TeV}}{m_{\mathrm{LQ}}}\right)^2 < 7.61\times10^{-4}$ $\left[\vert(Y_1^L)_{11}(Y_1^L)_{13}\vert\right]\times\left(\frac{2\mathrm{TeV}}{m_{\mathrm{LQ}}}\right)^2 < 0.5$ $\left[\vert(Y_1^R)_{11}(Y_1^R)_{13}\vert\right]\times\left(\frac{2\mathrm{TeV}}{m_{\mathrm{LQ}}}\right)^2 < 2.11$
$0\nu\beta\beta$	$m_{\beta\beta} < 0.036\,\mathrm{eV}$ [116]	$-0.0005 < (Y_1^L)_{11}(Y_2)_{11}\times\left(\frac{2\mathrm{TeV}}{m_{\mathrm{LQ}}}\right)^2 < 0.0003$ $-0.0006 < (Y_1^R)_{11}(Y_2)_{11}\times\left(\frac{2\mathrm{TeV}}{m_{\mathrm{LQ}}}\right)^2 < 0.0003$

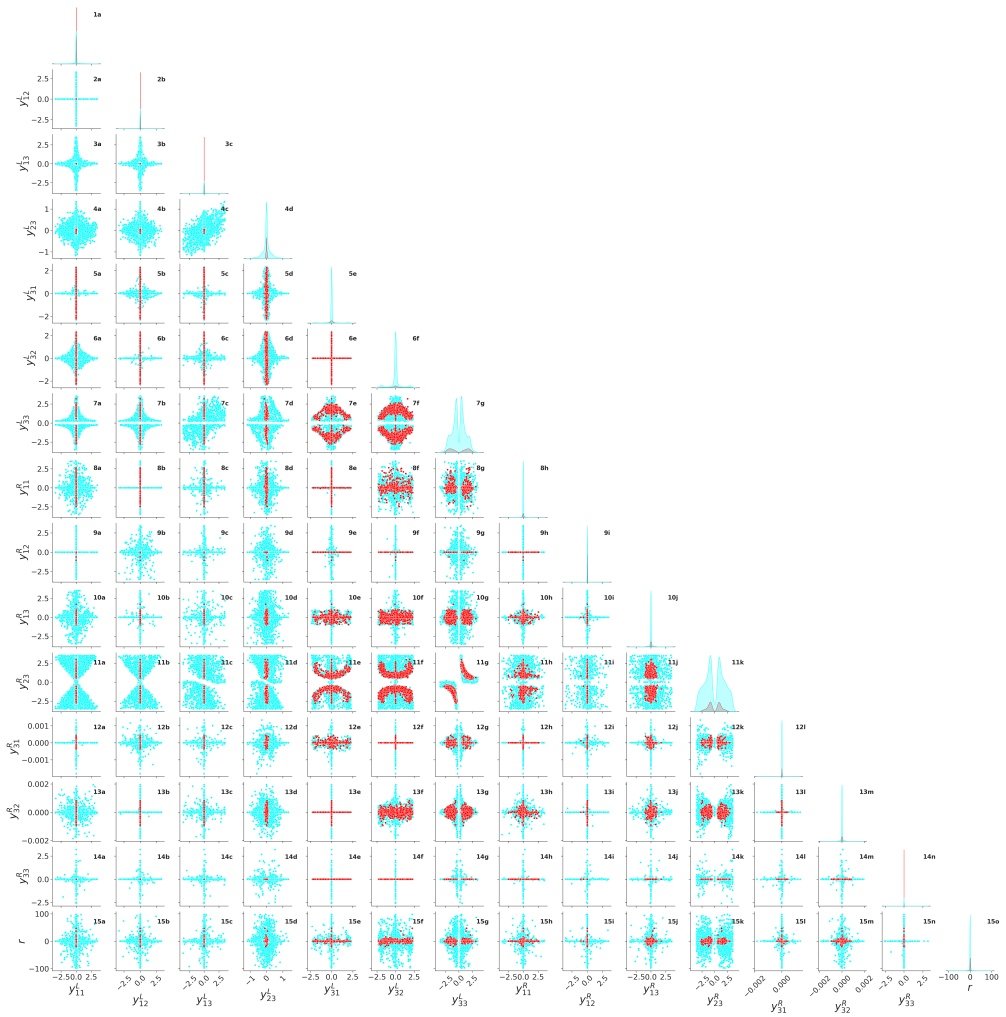

Figure 4.7: Pairwise correlation plot between various Yukawa matrix Y_1^L, Y_1^R elements, as well as the parameter r of the $\mathbb{R}$ matrix, in the presence of R_D, R_D^* anomaly (Case I). The cyan points satisfy the constraints from cLFV decays, LFUV ratios, $B \to K \nu \overline{\nu}$ constraints and generate the correct order of magnitude for neutrino masses and oscillation parameters. Red points survive after putting the constraint from $\mu \to e$ conversion in Au nucleus.

4.6.2 Discussion of the Results

To capture the interplay between the different elements of Yukawa matrices, pairwise correlations between different elements of the Yukawa matrices Y_1^L and Y_1^R, as well as the parameter r appearing in the $\mathbb{R}$ matrix [cf. Eq. (4.103)] is presented in Figs. 4.7 and 4.8. In both figures, the rightmost panel in each row has the same parameter on the x and y axes; hence, these are just the distributions over which a particular parameter is varied. As stated earlier, two different cases for the $R_{D^{(*)}}$ observables is considered in this analysis and

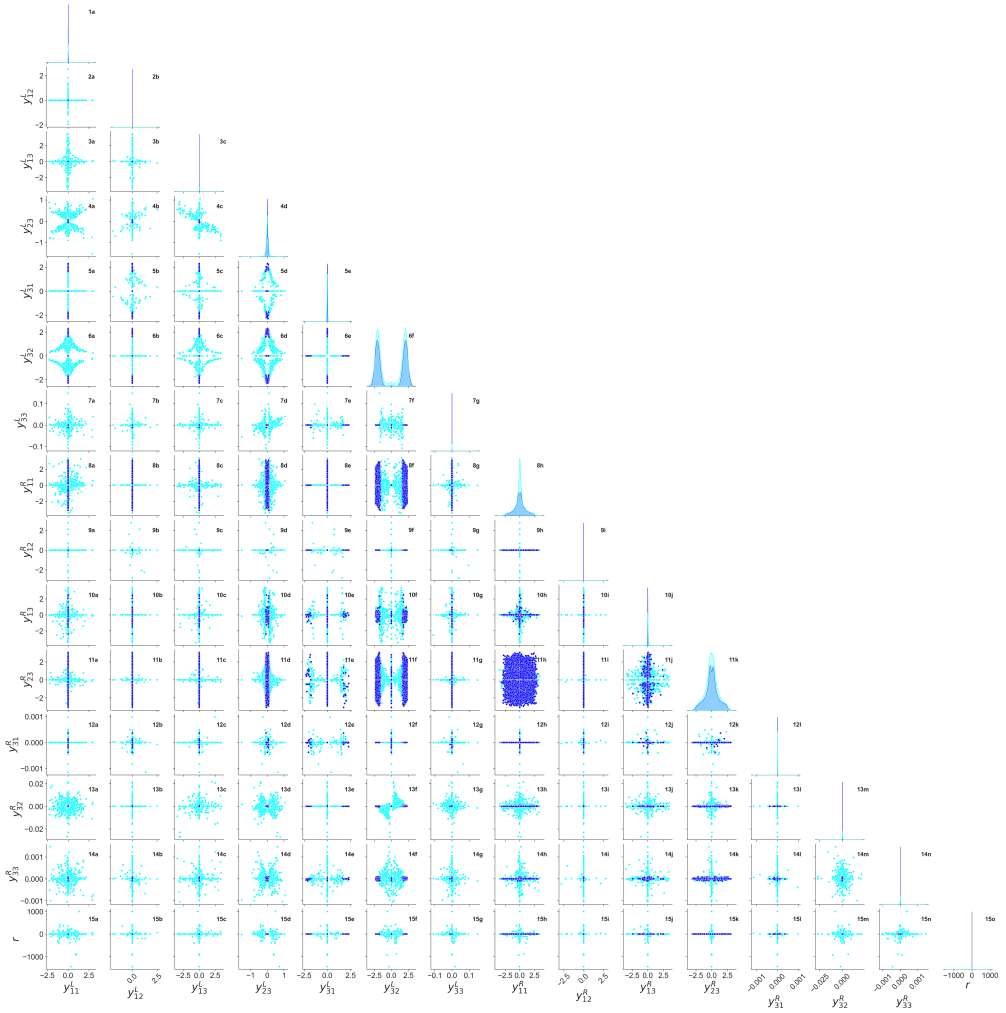

Figure 4.8: Pairwise correlation plot between various Yukawa matrix Y_1^L, Y_1^R elements as well as the parameter r of the $\mathbb{R}$ matrix, in the hypothetical scenario where R_D, R_D^* anomaly is gone (Case II). The cyan points satisfy the constraints from cLFV decays, LFUV ratios in Case II, $B \to K \nu \overline{\nu}$ constraints and generate the correct order of magnitude for neutrino masses and oscillation parameters. Blue points survive after putting the constraint from $\mu \to e$ conversion in Au nucleus.

they are the following:

1. **Case I**: R_D, R_{D^*} are anomalous, i.e the experimental values of R_D, R_{D^*} are not consistent with the SM predictions, which seems to be the current situation [cf. Eq. (4.82)]. Fig. 4.7 refers to this case.

2. **Case II**: This is a hypothetical scenario where the experimental values of R_D, R_{D^*} are consistent with the SM predictions within the 1σ error bars. In this case, $\Delta r_{D^{(*)}} = \left| r_{D^{(*)}} - r_{D^{(*)}}^{\rm SM} \right| < 10^{-3}$ is considered to constrain the parameter space. Fig. 4.8 refers to this case.

In Figs. 4.7 and 4.8, the cyan points produce the correct neutrino mass as well as oscillation parameters assuming NO, satisfy the current constraints from cLFV decays ($\mu \to e\gamma$, $\tau \to \mu\gamma$ and $\tau \to e\gamma$), the rare B and K meson decays listed in section 4.5.3 and also can reproduce the observed value of electron $(g-2)$ (either Cs or Rb-based value). The red points in Fig. 4.7 are obtained after putting the constraint coming from $\mu \to e$ conversion in Gold (Au) nucleus. It is seen from (2a) and (8a) panel of the figure that this process gives the most stringent constraint on the Yukawa couplings as much of the allowed parameter space gets disfavoured after putting $\mu \to e$ conversion constraint. The strongest anti-correlation is seen in panel (11g) which indicates that the dominant contribution to R_D and R_{D^*} comes from C_{S_L} [cf. Eq. (4.76)] which involves y^L_{33} and y^R_{23}. Panel (11g) also implies that $y^L_{33}\, y^R_{23} > 0$, otherwise, the leptoquark contribution will destructively interfere with the SM contribution and Eq. (4.82) will be smaller than one.

Fig. 4.8 shows the correlation between the same Yukawa matrix elements and r, like in Fig. 4.7, but with the assumption that $R_D - R_{D^*}$ are consistent with the SM predictions (Case II). As a result, certain correlations or anti-correlations among the pair of respective Yukawa couplings, observed in the earlier figure, vanish. In panel (11g), now the points near to origin (0,0) are allowed as the $R_D - R_{D^*}$ anomaly is absent in this case. However, the $\mu \to e$ conversion still puts the most stringent constraint in this case also and disfavors a large part of the parameter space. The final surviving points are shown in blue.

In Fig. 4.9, the tension between electron and muon $(g-2)$ anomalies is described for both Case I and II. The left panel is for Case I (with $R_{D^{(*)}}$ being anomalous) and the right panel is for Case II (where $R_{D^{(*)}}$ is consistent with the SM). In both figures, the cyan points satisfy the cLFV decay constraints (excluding the $\mu \to e$ conversion) and rare meson decays, whereas the red (blue) points in Case I (II) also include the $\mu \to e$ conversion bound. The dark (light) coral shaded region correspond to the 1σ (2σ) region of Δa_μ taking the BMW result for the SM prediction. It is seen from the left panel that with

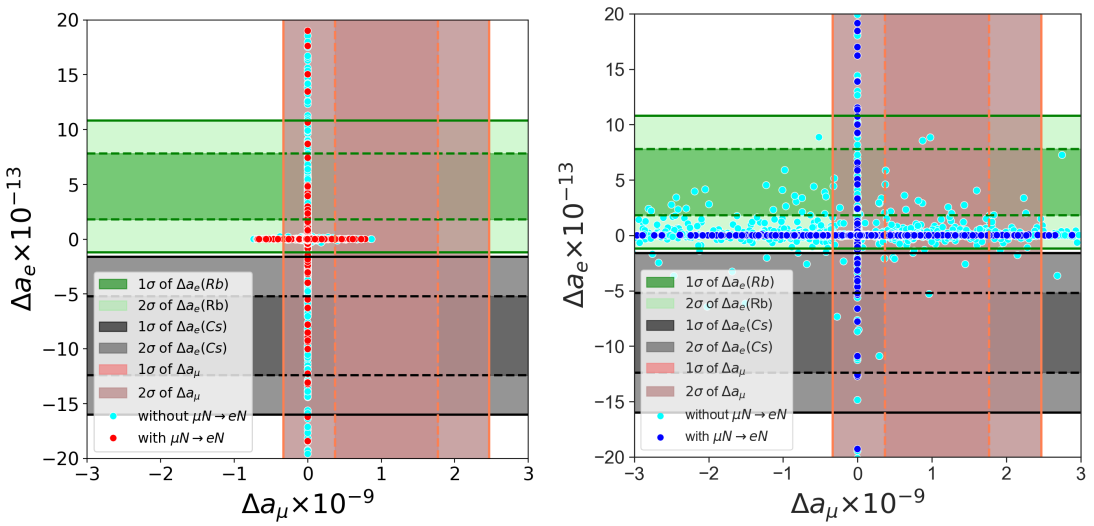

Figure 4.9: **Left Panel:** Plot of Δa_μ *vs* Δa_e in our leptoquark scenario satisfying current experimental limits on R_D-R_{D^*} (Case I). **Right Panel:** Assuming R_D-R_{D^*} is no longer anomalous (Case II). The cyan points satisfy all constraints except $\mu \to e$ conversion, and red (blue) points also satisfy $\mu \to e$ conversion bound for Case I (Case II). The vertical coral shaded bands show the 1σ and 2σ allowed ranges of Δa_μ, whereas the horizontal green (grey) shaded bands show the 1σ and 2σ allowed ranges of Δa_e for Rb (Cs).

R_D, R_{D^*} not consistent with the SM prediction, the allowed points of muon $(g-2)$ can not be arbitrarily large. This occurs because, to satisfy $R_D - R_{D^*}$, y^L_{33} must be at least $\sim \mathcal{O}(0.1)$. This constraint forces y^L_{32} and y^R_{32} to remain small to comply with the $\tau \to \mu\,\gamma$ limit, resulting in very small values of Δa_μ. If the constraints coming from R_D, R_{D^*} are relaxed as in the right panel, then the muon $(g-2)$ can be large as seen from the right panel because the absence of the $R_D - R_{D^*}$ anomaly suggests small values of y^L_{33}. Thus, even with the sizable values of y^L_{23} and y^R_{23}, constraints from $\tau \to \mu\gamma$ can be avoided.

In Fig. 4.9, the dark (light) green shaded region correspond to the 1σ (2σ) range of Δa_e for Rb. The black (grey) shaded region represent the same for the Cs. It is seen from both panels that the cyan points can reach the 1σ range of Δa_e value. However, when $\mu \to e$ conversion constraint is applied, there are points which can still satisfy Δa_e for Rb or Cs. It is seen from both panels that the anomalous Δa_μ and Δa_e results can not be simultaneously satisfied in this leptoquark model. This is due to the constraints coming from cLFV decays especially from $\mu \to e\gamma$ and $B^+ \to K^+ \nu\,\overline{\nu}$. To explain the Δa_μ anomaly

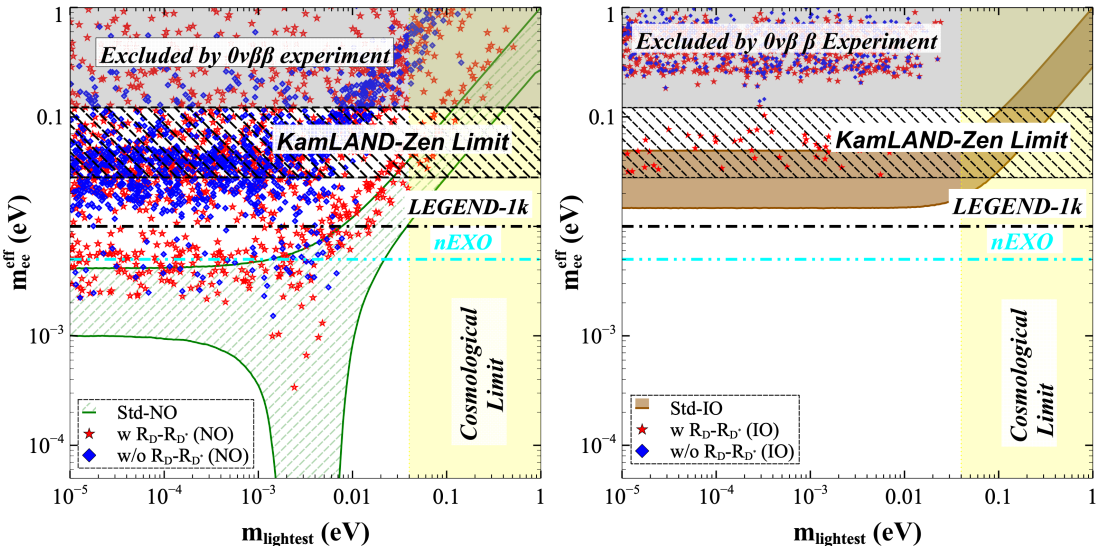

Figure 4.10: Plot of $m_{ee}^{\rm eff}$ as a function of the lightest neutrino mass where active neutrino masses obey NO (left panel) and IO (right panel). The standard NO and IO regions are denoted by lime green hatched and brown shaded regions, respectively. The blue diamonds (red stars) denote the $m_{ee}^{\rm eff}$ contributions in Case I and II, respectively. The magenta hatched horizontal region denotes the current *KamLAND-Zen* upper bound on m_{ee} for different NMEs while the black dashed-dot (cyan dashed-dot-dot) line denotes the future reach of *LEGEND-1000* (*nEXO*) on m_{ee}. The vertical light yellow shaded region represents the excluded range from the cosmological limit on the sum of light neutrino masses.

y_{32}^L and y_{32}^R need to satisfy the relation mentioned in Tab. 4.3. Therefore, the constraints from $\mu \to e\,\gamma$ require both y_{31}^L and y_{31}^R very small, $\mathcal{O}(< 10^{-6})$ and similarly, the constraint from $B \to K^+ \nu\,\overline{\nu}$ requires y_{11}^L to smaller than $\mathcal{O}(0.1)$. Hence, Δa_e is small in this case. On the other hand, for lowest values of y_{32}^L and y_{32}^R i.e when Δa_μ is small, y_{31}^L and y_{31}^R can be large and one can have large Δa_e values. In conclusion, when Δa_μ is small, Δa_e is large, and vice versa, indicating a contrast between the two lepton g-2 values.

4.6.3 Impact of $0\nu\beta\beta$ constraint on the leptoquark parameter space

In this section, the effect of the allowed leptoquark parameter space from the flavour observables and neutrino mass constraints on the $0\nu\beta\beta$ is studied. In Fig. 4.10, $m_{ee}^{\rm eff}$ [cf. Eq. (4.20)] as a function of the lightest neutrino mass for values of Yukawa couplings that are allowed from the combined analysis as presented in Figs. 4.7 and 4.8 is plotted. The oscillation parameters are varied in

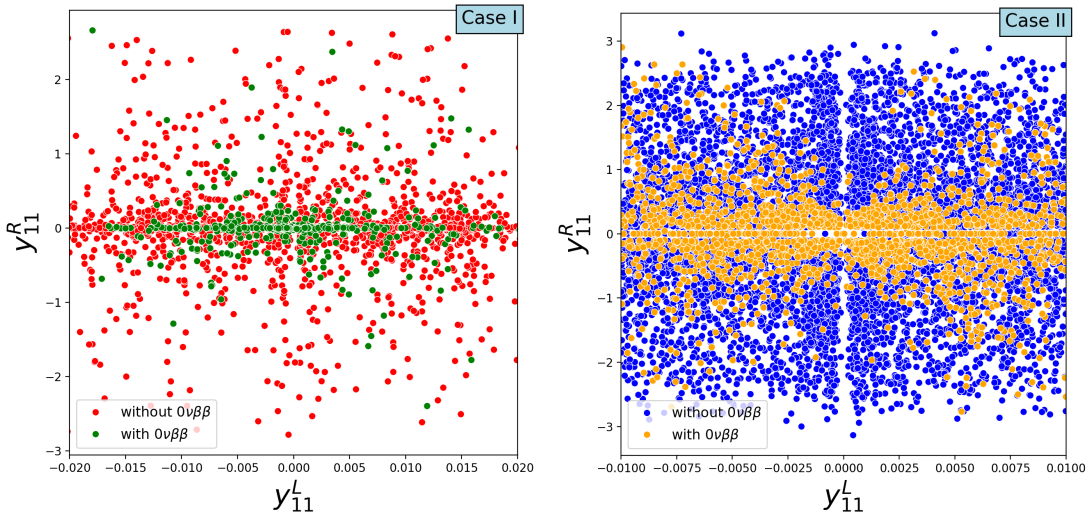

Figure 4.11: **Left Panel:** Plot of $y_{11}^L - y_{11}^R$ with and without the $0\nu\beta\beta$ *(KamLAND-Zen)* constraint on the parameter space for Case I. The red points correspond to the parameter space, indicated in Fig. 4.7 and the green points are the allowed parameter space by the $0\nu\beta\beta$. **Right Panel:** Plot of $y_{11}^L - y_{11}^R$ with and without the $0\nu\beta\beta$ *(KamLAND-Zen)* constraint on the parameter space for Case II. The blue points correspond to the parameter space, indicated in Fig. 4.8 and the orange points denote the parameter space allowed by the $0\nu\beta\beta$.

their allowed 3σ range [290], and the Majorana phases are varied in the range $(0 : \pi)$. In the left (right) panel the red stars [blue diamonds] denote the values of m_{ee}^{eff} after including the leptoquark contributions for NO (IO) for Case I [II]. The standard contribution to m_{ee}^{eff} for NO (IO) is displayed in green (brown) for comparison purposes. Also, the current bound on m_{ee} from *KamLAND-Zen* experiment [116] and the future projections from *LEGEND-1000* [120] and *nEXO* [122] are shown using magenta hatched filled band (with the band representing NME uncertainties), black dashed-dot and cyan dashed-dot-dot lines respectively. The cosmologically disfavoured region is denoted by the yellow vertical band from Planck data [31]. From the left panel, it is seen the cancellation region found in the standard 3-flavour picture is no longer there when leptoquark contributions are added. For some values of parameters, m_{ee}^{eff} can exceed the maximum value of the standard scenario. Most of these regions can be explored in the future ton-scale experiments like *LEGEND-1000* and *nEXO*, as can be seen from the figure. In the scanned region, m_{ee}^{eff} for NO including the leptoquark contribution goes into the standard IO region. In order to distinguish the standard IO region without leptoquarks from NO region with

leptoquarks, just $0\nu\beta\beta$ is not enough, and additional flavour and/or collider observables is needed. This is why the study of $0\nu\beta\beta$ correlations with other observables is so important.

It is found that for certain parameter space, large values of m_{ee}^{eff} is possible which are already ruled out by $0\nu\beta\beta$ experiments. This suggests that $0\nu\beta\beta$ can further constrain the leptoquark parameter space, particularly y_{11}^{L} and y_{11}^{R} (shown in Fig. 4.11), depending on the whether diagram (c) or diagram (d) gives dominant contribution. Similarly for IO (right panel), adding the leptoquark contribution will enhance the value of m_{ee}^{eff} and there are a few points which give very high contributions and are disfavoured by the current *KamLAND-Zen* upper bound on m_{ee}. When $R_D - R_{D^*}$ values are consistent with the SM, the values of y_{33}^{L} are small. Since Y_2 depends on the inverse of Y_1^L, Y_2 becomes large, resulting in larger values of m_{ee}^{eff}. This is also evident from Fig. 4.10, which shows that the values of m_{ee}^{eff} are slightly higher in the scenario without $R_D - R_{D^*}$ anomaly present than in the scenario with $R_D - R_{D^*}$ anomaly. Additionally, the inverted mass ordering for neutrinos is relatively disfavoured (compared to the normal ordering) by $0\nu\beta\beta$ constraints in the vanishing $R_D - R_{D^*}$ scenario.

4.6.4 Effect of Varying Leptoquark Mass

In the previous section, impact of leptoquarks with mass, fixed at 2 TeV on the flavour observables is discussed but in this section effect of a varying leptoquark mass is discussed. To see the effect of varying leptoquark mass, the Yukawa couplings Y_1^L and Y_1^R are fixed to a suitable representative benchmark value and the leptoquark mass is varied to see what is its maximum allowed value that can explain the $R_{D^{(*)}}$ and Δa_ℓ anomalies. It is important to mention here that the following analysis is strictly valid only for the chosen benchmark

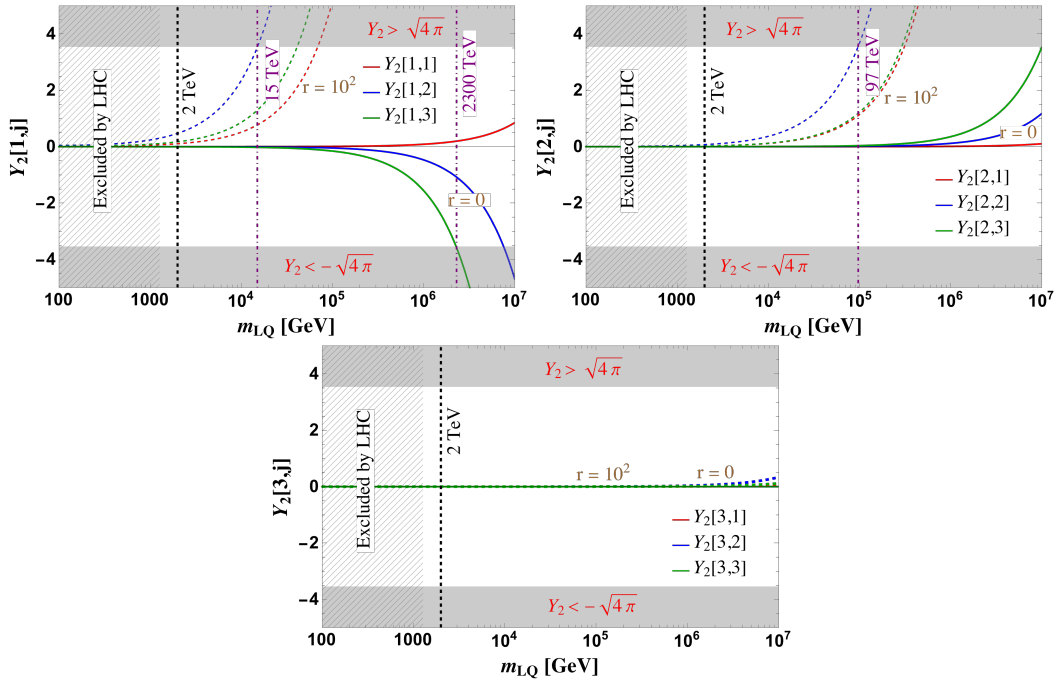

Figure 4.12: Variation of Y_2 elements with leptoquark mass when all the elements of Y_1^L and Y_1^R are fixed as given by Eq. (4.107). The solid (dashed) curves are for $r = 0$ (10^2). The horizontal shaded regions represent the perturbativity limit on the Yukawa couplings. The vertical hatched region is excluded by LHC searches for leptoquarks.

values of the Yukawa couplings:

$$Y_1^L = \begin{pmatrix} -0.02 & 0 & -0.001 \\ 0 & 0 & 0.001 \\ 0 & 1.5 & 0.5 \end{pmatrix}, \qquad Y_1^R = \begin{pmatrix} 1.0 & 0 & 0.01 \\ 0 & 0 & 1.8 \\ 0 & 0.001 & 10^{-4} \end{pmatrix}. \quad (4.107)$$

Once Y_1^L and Y_1^R are fixed to the above values, the Y_2 elements are fully determined from Eq. (4.102), giving the input parameters as discussed in the earlier Section. In determining the value of Y_2, the mass of the lightest neutrino is fixed as (m_{lightest}) 0 eV. The U_{PMNS} parameters are fixed to their best fit values mentioned in Ref. [290] and the Majorana phases are fixed as $\alpha = 0$ and $\beta = 0$. In Fig. 4.12, the variation of the elements of Y_2 as a function of the leptoquark mass is shown for two different values of r. The hatched region on the left corresponds to the collider exclusion limit on m_{LQ} from direct LHC searches [291]. The vertical lines correspond to the different leptoquark masses as depicted in the figure. It is seen that the magnitude of the Y_2 matrix

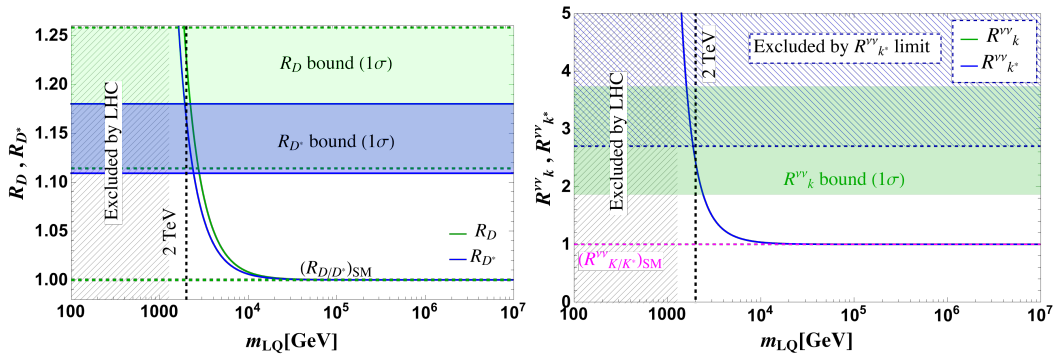

Figure 4.13: **Left Panel:** Variation of R_D (green) and R_{D^*} (blue) as a function of leptoquark mass. The green (light blue) shaded region corresponds to the current experimental values on R_D (R_{D^*}) at 1σ. The green dashed line corresponds to the SM prediction. **Right Panel:** $R_K^{\nu\nu}$ (green) and $R_{K^*}^{\nu\nu}$ (blue) as a function of leptoquark mass for three values of r. The green-shaded region corresponds to the current experimental value on $R_K^{\nu\nu}$ at 1σ, and the light blue-shaded region shows the experimental limit on ($R_{K^*}^{\nu\nu}$).

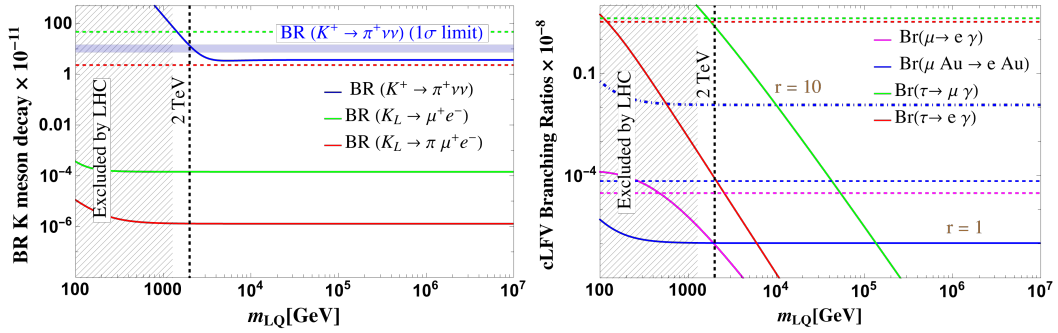

Figure 4.14: **Left Panel:** BR of K meson decays ($K^+ \to \pi^+ \nu\, \overline{\nu}$ (blue, 1σ), $K_L \to \mu^+ e^-$ (green), $K_L \to \pi\mu^+ e^-$ (red)) as a function of leptoquark mass. Blue band denotes the experimental value of $K^+ \to \pi^+ \nu\, \overline{\nu}$. Green and red lines correspond to the current experimental limits on the corresponding BRs. **Right Panel:** BRs of cLFV decays as a function of the leptoquark mass. Magenta, blue, green and brown curves correspond to BRs of $\mu \to e\,\gamma$, $\tau \to \mu\,\gamma$, $\tau \to e\,\gamma$ and $\mu \to e$ conversion ratio respectively, and the horizontal lines denote their experimental limits.

elements increases with increasing leptoquark mass. This is because as $m_{\rm LQ}$ grows, $\mathbf{C}_1 \approx \kappa\, v/m_{\rm LQ}^2$ [cf. Eq. (4.102)]; therefore, the value of Y_2 increase as the LQ mass increases. This can also be understood from Eq. (4.10) that Y_2 must increase as $m_{\rm LQ}$ increases to generate neutrino masses of the $\mathcal{O}(10^{-2})$ eV. As Y_2 is proportional to $\mathbb{R}$ [cf. Eq. (4.102)], it also increases with r for a given value of the leptoquark mass. From this figure, it is found that the elements of Y_2 matrix exceed the perturbativity limit for $m_{\rm LQ} > 15$ TeV for $r = 100$. So, large values of r are not allowed by the perturbativity conditions of the elements of Y_2 matrix.

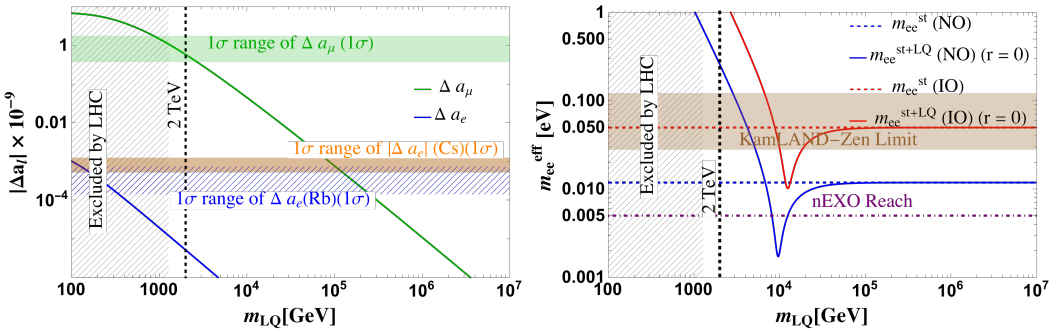

Figure 4.15: **Left Panel:** Variation Δa_μ and $|\Delta a_e|$ as a function of leptoquark mass. Green bands correspond to the 1σ value of Δa_μ whereas, blue (brown) band shows the same for Δa_e (Δa_e) for Rb (Cs) . **Right Panel:** Variation of m_{ee}^{eff} as a function of m_{LQ} for $r = 1$ (allowed by $\mu \to e$ conversion). The solid blue (red) dashed line denotes the standard contribution for NO. The horizontal brown shaded band is the current *KamLAND-Zen* limit at 90% CL including NME uncertainties, and the purple dashed-dot line is the future *nEXO* projection.

Fig. 4.13 shows the variation of R_D, R_{D^*}, $R_K^{\nu\nu}$, $R_{K^*}^{\nu\nu}$ as a function of the leptoquark mass. From the left most panel, it is inferred that only a small region of m_{LQ} around 2 TeV scale is allowed for the current values of R_D and R_{D^*}. As m_{LQ} increases, the value R_D-R_{D^*} decreases and gradually converge to the SM value, and hence, the anomaly can not be explained for higher values of leptoquark mass. In the case of $R_K^{\nu\nu}$ and $R_{K^*}^{\nu\nu}$, the nature is similar to $R_D - R_{D^*}$. As leptoquark mass increases, $R_{K^{(*)}}^{\nu\nu}$ decreases and gradually goes out of the green allowed region for $R_K^{\nu\nu}$. Here, both $R_K^{\nu\nu}$ and $R_{K^{(*)}}^{\nu\nu}$ have the same value because throughout the leptoquark mass range the value of Y_2 is small and $R_{K^{(*)}}^{\nu\nu}$ is dominated by only C_L [cf. Eq. (4.90)].

In Fig. 4.14 rare K meson decay BRs and cLFV decay BRs, $\mu \to e$ conversion rate is plotted as a function of the leptoquark mass. The BRs of cLFV decay are inversely proportional to the leptoquark mass and gradually decrease as m_{LQ} increases as can be seen in the right panel of Fig. 4.14. However, the $\mu \to e$ conversion rate shows a different trend as it is seen to be independent of leptoquark mass for higher values of the leptoquark mass. This can be understood from Eq. (4.24) where is can be seen that for large leptoquark mass and fixed Y_1^L values, all the Wilson coefficients in Eq. (4.29) except the parameter $C_{V_{LR}}^d \sim {Y_2}^2/m_{\text{LQ}}^2$ is independent of m_{LQ} [c.f Eq. (4.10)] making the conversion ratio independent of m_{LQ}.

In Fig. 4.15, variation of lepton $g-2$ anomalies and effective Majorana mass with leptoquark mass is shown. From the right panel of Fig. 4.15, it is observed that m_{ee}^{eff} for NO (IO) decreases as m_{LQ} increases, and for higher values of leptoquark mass, approaches the standard contribution [blue (red) dashed line]. For certain range of m_{LQ}, it is found that $m_{ee}^{\text{eff}} < m_{ee}^{\text{std}}$ which means that in this range the leptoquark contribution is similar to the standard contribution and destructively interferes with the standard contribution for the chosen BP values. Similar behaviour is also seen for the IO case. It is shown in Fig. 4.15 that for $m_{\text{LQ}} = 2$ TeV, the chosen BP values satisfy all the low-energy constraints but m_{ee}^{eff} is higher than the *KamLAND-Zen* limit and hence the given benchmark point is discarded for both orderings of neutrino masses. Therefore, $0\nu\beta\beta$ can be used in conjunction with the other flavour observables mentioned in Section 4.5 to further constrain the leptoquark parameter space. Future ton-scale $0\nu\beta\beta$ experiments like *nEXO* and *LEGEND-1000* will be important in probing the unexplored leptoquark parameter space for both NO and IO.

4.7 Conclusions

Scalar leptoquarks provide an attractive BSM framework for neutrino mass generation radiatively. At the same time, the new leptoquark interactions give rise to new contributions to various lepton number and flavour violating processes. In this chapter the Standard Model augmented with two scalar leptoquarks is considered. While a single leptoquark cannot generate correct neutrino mass, the combination of singlet-doublet leptoquarks ($S_1 - \tilde{R}_2$) can generate the neutrino mass radiatively. Such models have a rich phenomenology since leptoquarks can couple to both quarks and leptons. The main aim of this study was to understand the implications of this combination in context of $0\nu\beta\beta$. To find the allowed values of the Yukawa couplings, constraints from neutrino mass and mixing, as well as demanded compliance with bounds coming from charged lepton flavour violation, lepton flavour universality violation and low-energy rare meson decays is imposed. A comprehensive global parameter scan is performed while satisfying all available experimental data

arising from the above-mentioned constraints, as well as existing anomalies in $R_{D^{(*)}}$ and Δa_ℓ to constrain the allowed parameter space for various Yukawa matrix elements with a TeV-scale leptoquark mass. The combined analysis reveals some interesting interplay and tensions coming from different constraints. For instance, in this two leptoquark scenario, the muon and electron $g-2$ values are in tension with each other. It is found that the most stringent constraints on the allowed Yukawa couplings are obtained from $\mu \to e$ conversion in nuclei. Using the Yukawa coupling values that pass all the above mentioned flavour constraints, prediction for m_{ee}^{eff}, arising from the combined contributions of standard and leptoquark contributions is obtained. It is found that the contribution from leptoquark mediated diagrams to m_{ee}^{eff} can be significant and even greater than the standard contribution for normal ordering of the light neutrinos and the cancellation region is no longer present around $m_{\text{lightest}} \sim$ meV. The total value of m_{ee}^{eff} can lie in the desert region between the standard NO and IO regions and hence can be probed by future experiments like *LEGEND-1000* and *nEXO*. On the other hand, for IO, we find that most of the points otherwise allowed by low-energy flavour constraints are disfavoured by the current $0\nu\beta\beta$ limit from *KamLAND-Zen*.

The leptoquark masses are also varied while fixing some benchmark values of Yukawa couplings and discussed the constraints on this from different observables, as well as from the perturbativity bounds. For the chosen benchmark values, it turns out that stringent constraint on leptoquark mass is $m_{\text{LQ}} > 6.6$ TeV for IO, from the $0\nu\beta\beta$ observable.

5

Neutrino-less double beta decay in a realistic $SU(5)$ model

5.1 Overview

In the previous chapter, we have shown that TeV scale scalar leptoquarks can dominantly contribute to $0\nu\beta\beta$ process. Grand Unified Theories provide an attractive framework where leptoquarks arise naturally [194, 292–296]. GUTs are based on the novel idea of unifying the strong, electromagnetic and weak interactions within a single, larger symmetry group. In these theories, new fields emerge as components of enlarged representations that couple collectively to quark-lepton multiplets. The Yukawa sector proves especially significant in GUT contexts, as the SM Higgs field usually co-exists with additional scalar fields in these extended frameworks. Consequently, the strength of new interactions becomes intimately connected to low-energy observables — particularly the fermion mass spectrum. This characteristic predictive power can distinguish GUTs from other simplified extensions of the SM.

Since the SM gauge group $SU(3)_c \times SU(2)_L \times U(1)_Y$ has rank four (two for $SU(3)_c$ and one each for $SU(2)_L$ and $U(1)_Y$), the minimal choice for unification in a simple group is the rank-four $SU(5)$. However, the original $SU(5)$ model proposed in Ref. [293] suffers from a number of issues, including (i) inability to account for the observed charged fermion mass ratios, (ii) failure to achieve gauge coupling unification, (iii) rapid proton decay , (iv) massless neutrinos,

and (v) doublet-triplet splitting problem. Extensions to the minimal $SU(5)$ model [293] to address these issues typically involve additional scalar/fermion multiplets [297–303]. In this chapter, we discuss the role of the heavy $SU(5)$ scalar multiplets in mediating the L-violating process of $0\nu\beta\beta$, as well as in generating correct neutrino masses and mixing, while being consistent with the observed charged fermion masses.

To this end, we develop a realistic yet minimally extended $SU(5)$ framework in which the leptoquark contribution to $0\nu\beta\beta$ is enhanced relative to the standard light neutrino exchange mechanism. The role of scalar leptoquarks in mediating $0\nu\beta\beta$ has been investigated before; see e.g., Refs. [197, 218–223, 304–308]. Within the context of $SU(5)$ grand unification, the $0\nu\beta\beta$ mechanism has been further examined in Refs. [309–311]. However, there exists no minimal realistic $SU(5)$ GUT framework discussing *both* $0\nu\beta\beta$ and neutrino mass arising from the heavy scalars. Here we propose such a scenario that ensures that the same set of scalar fields is responsible for generating neutrino masses, inducing $0\nu\beta\beta$, and contributing to fermion masses via one-loop corrections—thereby yielding a realistic and predictive $SU(5)$ framework.

In this chapter, we focus our attention on the canonical $SU(5)$ scenario extended by a triplet scalar Δ belonging to the **15**-dimensional representation. This allows generation of neutrino mass at tree level via the type-II seesaw mechanism [81, 83, 84, 312] as well as radiatively at one loop induced by the pair of scalar leptoquarks – S_3 and R_2 [96, 195, 313, 314]. In this model, the scalar leptoquark fields S_3 and $\tilde{R}_2$ (see Tab. 5.1) inducing the L-violating process of $0\nu\beta\beta$ are also the ones inducing the B-violating process of proton decay. The stringent requirement of satisfying the proton decay constraints suppresses the leptoquark induced $0\nu\beta\beta$ rate to extremely small values. In order to evade this, we construct an $SU(5) \times \mathcal{Z}_3$ model which forbids the diquark interactions of S_3 capable of inducing proton decay. Although it yields inconsistent tree-level Yukawa relations in the down-quark and charged lepton sectors at the GUT scale, this inconsistency is resolved by incorporating radiative corrections from the heavy degrees of freedom, achieving realistic

charged and neutral fermion mass spectra and mixing angles [315]. We then compute the $0\nu\beta\beta$ in this model, after taking into account other constraints such as those coming from the charged lepton-flavor-violating (cLFV) process of $\mu \to e$ conversion which restrict the mass of the $\tilde{R}_2$ leptoquark. However, we find that the set of scalars $(\Delta, \tilde{R}_2, S_3)$ inducing the $0\nu\beta\beta$ process, predicts a much suppressed rate as compared to the standard decay rate induced by light neutrinos. This suppression arises because, to achieve viable neutral fermion mass spectra, the scalar mass M_Δ is required to be around 10^{16} GeV, making the scalar-induced contribution negligible. In the allowed parameter space obtained by fitting the fermion mass spectrum, the canonical light neutrino-mediated effective neutrino mass governing $0\nu\beta\beta$ rejects the inverted ordering from the existing*KamLAND-Zen* bound [116].

In order to enhance the scalar-induced $0\nu\beta\beta$ rate, an additional triplet scalar (Δ_2) is then introduced in such a way that it is decoupled from matter multiplet interactions. In this extended scenario, cancellations between standard and non-standard contributions to $0\nu\beta\beta$ allow the inverted mass ordering in certain parameter regions. Furthermore, it is also shown that $0\nu\beta\beta$ can be used as a sensitive probe of the new scalar mass M_{Δ_2} across a broad range, from collider-accessible TeV scale all the way up to $\sim 10^{10}$ GeV. In particular, future ton-scale experiments like *nEXO* [122] and *LEGEND-1000* [120] with half-life sensitivities up to 10^{28} years can probe a wide range of the allowed parameter space in this $SU(5)$ GUT construction.

The rest of the chapter is organised as follows: we review the generic $SU(5)$ framework in Section 5.2 and discuss the contribution of the $SU(5)$ scalars to $0\nu\beta\beta$ decay. In Section 5.3, in order to evade the nucleon decay constraint, an $SU(5) \times \mathcal{Z}_3$ scenario is constructed where some leptoquarks can remain light. This particular framework prohibits the diquark coupling of scalars contributing to $0\nu\beta\beta$. Subsequently, radiative corrections to the Yukawa relations are considered, ensuring a realistic scenario. We also discuss the scalar contributions to the $0\nu\beta\beta$ process in the considered $SU(5) \times \mathcal{Z}_3$ model. Then the parameter fitting procedure is described followed by the prediction of the

scalar contribution to $0\nu\beta\beta$ process. Then in section. 5.4, we provide a scenario where the scalar contribution can be significantly enhanced within the reach of current and future experiments and section 5.5 summarises this study.

5.2 A generic $SU(5)$ Framework

In the $SU(5)$ framework, the SM Weyl fermions are embedded in the $\bar{\mathbf{5}}$ and $\mathbf{10}$ dimensional irreps, as follows [294]:

$$\begin{aligned} \bar{\mathbf{5}}_a &= \varepsilon_{ab} L^b, \quad \bar{\mathbf{5}}_\alpha = d^C_\alpha, \\ \mathbf{10}^{a\alpha} &= \frac{1}{\sqrt{2}} q^{a\,\alpha}, \quad \mathbf{10}^{\alpha\beta} = \frac{\varepsilon^{\alpha\beta\gamma}}{\sqrt{2}} u^C_\gamma, \quad \mathbf{10}^{ab} = \frac{\varepsilon^{ab}}{\sqrt{2}} e^C, \end{aligned} \tag{5.1}$$

where Greek letters $(1 \leq \alpha, \beta, \gamma... \leq 3)$ denote $SU(3)_c$ indices while $SU(2)_L$ labels are depicted by the lowercase Latin alphabets $(4 \leq a, b, c... \leq 5)$. The convention of two-indexed Levi-Civita tensor is as follows: $\varepsilon_{45} = 1 = \varepsilon^{54} = -\varepsilon_{54} = -\varepsilon^{45}$. The three-indexed Levi-Civita follows the convention where $\varepsilon_{123} = 1$ and for other cyclic permutations. The superscript C stands for the charge-conjugated spinor, i.e., $\psi^C = i\sigma_2\psi^*$, where σ_2 is the second Pauli matrix.

The Higgs sector of the $SU(5)$ consists of a $\mathbf{24}_\mathrm{H}$ scalar representation to break $SU(5) \to SU(3)_c \otimes SU(2)_L \otimes U(1)_\mathcal{Y}$. Along with this, it also require $\mathbf{5}_\mathrm{H}$ and $\mathbf{45}_\mathrm{H}$-dimensional irrep to have viable tree-level Yukawa relations in the charged fermion sector [297]. In order to also account for the neutrino masses and mixing, the Yukawa sector can be extended by a $\mathbf{15}_\mathrm{H}$ scalar irrep. This allows generation of neutrino mass at tree level via the type-II seesaw mechanism [81, 83, 84, 312] as well as radiatively at one loop induced by the pair of scalar leptoquarks – S_3 and R_2 [96, 195, 313, 314]. The different scalar multiplets residing in $\mathbf{5}_\mathrm{H}$, $\mathbf{15}_\mathrm{H}$, $\mathbf{24}_\mathrm{H}$ and $\mathbf{45}_\mathrm{H}$ can be inferred from Tab. 5.1. The submultiplets residing in the scalar irreps must be properly normalised so as to have a canonically normalised kinetic term and such decompositions are

Table 5.1: Scalar multiplets residing inside the $\mathbf{5}_{\rm H}$, $\mathbf{15}_{\rm H}$, $\mathbf{24}_{\rm H}$ and $\mathbf{45}_{\rm H}$-dimensional irreps of $SU(5)$ which participate in the Yukawa interactions at renormalisable level. Their charges under the SM gauge group $SU(3)_c \times SU(2)_L \times U(1)_Y$ are also shown.

$SU(5)$ Multiplet	Notation	SM Charge
$\mathbf{5}_{\rm H}$	H_1	$\left(1,2,\frac{1}{2}\right)$
	S_1	$\left(3,1,-\frac{1}{3}\right)$
$\mathbf{15}_{\rm H}$	Δ	$\left(1,3,1\right)$
	$\tilde{R}_2$	$\left(3,2,\frac{1}{6}\right)$
	Σ	$\left(6,1,-\frac{2}{3}\right)$
$\mathbf{24}_{\rm H}$	σ	$\left(1,1,0\right)$
	W	$\left(1,3,0\right)$
	X	$\left(3,2,-5/6\right)$
	$\overline{X}$	$\left(3,2,5/6\right)$
	G	$\left(8,1,0\right)$
$\mathbf{45}_{\rm H}$	H_2	$\left(1,2,\frac{1}{2}\right)$
	S_1'	$\left(3,1,-\frac{1}{3}\right)$
	$\tilde{S}_1$	$\left(\overline{3},1,\frac{4}{3}\right)$
	R_2	$\left(\overline{3},2,-\frac{7}{6}\right)$
	S_3	$\left(3,3,-\frac{1}{3}\right)$
	$\mathbb{S}$	$\left(\overline{6},1,-\frac{1}{3}\right)$
	O	$\left(8,2,\frac{1}{2}\right)$

shown below;

$$
\begin{aligned}
24^{\alpha}_{{\rm H}\,a} &= X^{\alpha}_{a}, & 24^{a}_{{\rm H}\,\alpha} &= \overline{X}^{a}_{\alpha}, \\
24^{\alpha}_{{\rm H}\beta} &= G^{\alpha}_{\beta} + \sqrt{\frac{2}{15}}\delta^{\alpha}_{\beta}\,\sigma, & 24^{a}_{{\rm H}\,b} &= W^{a}_{b} - \frac{3}{2}\sqrt{\frac{2}{15}}\,\delta^{a}_{b}\,\sigma.
\end{aligned} \tag{5.2}
$$

When σ acquires a vev $SU(5)$ symmetry is spontaneously broken into SM symmetry. The heavy gauge bosons residing in $24_{\rm V}$ absorbs the longitudinal modes of X and $\overline{X}$ and becomes massive.

Similarly, the $\mathbf{5}_{\rm H}$, $\mathbf{15}_{\rm H}$ and $\mathbf{45}_{\rm H}$-dimensional scalar irrep can be decomposed as [316],

$$
\mathbf{5}^{a}_{\rm H} = H^{a}_{1}\,, \qquad \mathbf{5}^{\alpha}_{\rm H} = S^{\alpha}_{1} \tag{5.3}
$$

$$
\mathbf{15}^{ab}_{\rm H} = \Delta^{ab}, \qquad \mathbf{15}^{a\alpha}_{\rm H} = \frac{1}{\sqrt{2}}\tilde{R}^{a\alpha}_{2}, \text{ and } \qquad \mathbf{15}^{\alpha\beta}_{\rm H} = \Sigma^{\alpha\beta} \tag{5.4}
$$

$$
\begin{aligned}
\mathbf{45}^{\alpha\beta}_{{\rm H}\,\gamma} &\equiv \mathbb{S}^{\alpha\beta}_{\gamma} + \frac{1}{2\sqrt{2}}\left(\delta^{\alpha}_{\gamma}S_1'^{\,\beta} - \delta^{\beta}_{\gamma}S_1'^{\,\alpha}\right), \quad \mathbf{45}^{\alpha\beta}_{{\rm H}\,a} \equiv R_{2a}{}^{\alpha\beta}\,, \\
\mathbf{45}^{\alpha a}_{{\rm H}\,\beta} &\equiv \frac{1}{\sqrt{2}}O^{\alpha a}_{\beta} + \frac{1}{2\sqrt{6}}\delta^{\alpha}_{\beta}H^{a}_{2}\,, \quad \mathbf{45}^{ab}_{{\rm H}\,\beta} \equiv \frac{1}{\sqrt{2}}\varepsilon^{ab}\tilde{S}_{1\beta}\,,
\end{aligned}
$$

$$\mathbf{45}^{b\alpha}_{\mathrm{H}\,a} \equiv \frac{1}{\sqrt{2}} S_{3\,a}^{\;b\alpha} - \frac{1}{2\sqrt{2}} \delta^b_a S_1'^{\,\alpha}\,, \quad \mathbf{45}^{ab}_{\mathrm{H}\,c} \equiv -\frac{\sqrt{3}}{2\sqrt{2}} \left(\delta^a_c H^b_2 - \delta^b_c H^a_2\right)\,. \tag{5.5}$$

The $SU(5)$-invariant Yukawa Lagrangian with these irreps participating in the Yukawa sector is given as follows:

$$\begin{aligned} -\mathcal{L}_{\mathrm{Y}} &= \frac{1}{4} \left(Y_5\right)_{AB} \mathbf{10}^T_A \, \mathcal{C}^{-1} \, \mathbf{10}_B \, \mathbf{5}_{\mathrm{H}} + \sqrt{2} \left(\widetilde{Y}_5\right)_{AB} \mathbf{10}^T_A \, \mathcal{C}^{-1} \, \bar{\mathbf{5}}_B \, \mathbf{5}^\dagger_{\mathrm{H}} \\ &+ \frac{1}{2} \left(\widetilde{Y}_{45}\right)_{AB} \mathbf{10}^T_A \, \mathcal{C}^{-1} \, \mathbf{10}_B \, \mathbf{45}_{\mathrm{H}} + \sqrt{2} \left(Y_{45}\right)_{AB} \mathbf{10}^T_A \, \mathcal{C}^{-1} \, \bar{\mathbf{5}}_B \, \mathbf{45}^\dagger_{\mathrm{H}} \\ &+ \left(Y_{15}\right)_{AB} \bar{\mathbf{5}}^T_A \, \mathcal{C}^{-1} \, \bar{\mathbf{5}}_B \, \mathbf{15}_{\mathrm{H}} + \mathrm{h.c.} \end{aligned} \tag{5.6}$$

Here $(A, B = 1, 2, 3)$ are the generation labels and $\mathcal{C}$ is the charge conjugation operator. In the above Yukawa Lagrangian, Y_5 ($\tilde{Y}_{45}$) is symmetric (antisymmetric) in flavour indices and Y_{15} is symmetric in generation labels while the remaining matrices can be general complex matrices. Using the embedding of $\mathbf{10}$ and $\bar{\mathbf{5}}$ from Eq. (5.1), it is straightforward to decompose the interaction terms written above in Eq. (5.6) and compute the interactions of different scalars with SM fermions as follows;

$$\begin{aligned} -\mathcal{L} &\supset \varepsilon_{ab} \left(Y_5 \, q^{a\alpha\,T} \, \mathcal{C}^{-1} \, u^C_\alpha \, H^b_1 + \frac{2}{\sqrt{6}} \widetilde{Y}_{45} \, q^{a\alpha\,T} \, \mathcal{C}^{-1} \, u^C_\alpha \, H^b_2 \right) \\ &+ \left(\widetilde{Y}_5 \, q^{a\alpha\,T} \, \mathcal{C}^{-1} \, d_\alpha \, H^\dagger_{1\,a} + \frac{1}{\sqrt{6}} Y_{45} q^{a\alpha\,T} \, \mathcal{C}^{-1} \, d_\alpha \, H^\dagger_{2\,a} \right) \\ &+ \left(\widetilde{Y}_5 \, e^{C\,T} \, \mathcal{C}^{-1} \, L^a \, H^\dagger_{1\,a} - \sqrt{\frac{3}{2}} Y_{45} \, e^{C\,T} \, \mathcal{C}^{-1} \, L^a \, H^\dagger_{2\,a} \right) \\ &+ 2\, Y_{15} \, \epsilon_{ac} \, \epsilon_{bd} \, L^T_c \, \mathcal{C}^{-1} \, L_d \, \Delta^{ab} + \mathrm{h.c.}. \end{aligned} \tag{5.7}$$

From Eq. (5.7), it is easy to identify the tree-level Yukawa relations for charged fermions and neutrinos,

$$\begin{aligned} \left(Y_u\right)_{AB} &= \left(Y_5 + \frac{2}{\sqrt{6}} \widetilde{Y}_{45} \right)_{AB}\,, \\ \left(Y_d\right)_{AB} &= \left(\widetilde{Y}_5 + \frac{1}{\sqrt{6}} Y_{45} \right)_{AB}\,, \\ \left(Y_e\right)_{AB} &= \left(\widetilde{Y}_5 - \sqrt{\frac{3}{2}} Y_{45} \right)_{AB}\,, \\ Y_\nu &= \sqrt{2} \left(Y_{15}\right)_{AB}\,. \end{aligned} \tag{5.8}$$

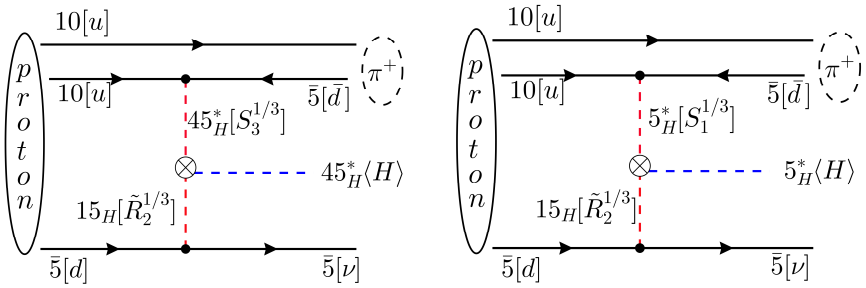

Figure 5.1: Proton decay stemming from $S_3 \in \mathbf{45}_{\mathrm{H}}$ and $S_1 \in \mathbf{5}_{\mathrm{H}}$.

The scalar field $\Delta \in \mathbf{15}_{\mathrm{H}}$ induces tree-level neutrino mass via type-II seesaw [81, 83, 84, 312]. Note that, the above Yukawa couplings contribute to the fermion masses after the EW symmetry breaking. In this scenario, the lightest combination of H_1 and H_2 is identified as SM Higgs. The Yukawa couplings written in Eq. (5.8) has enough free parameters to yield the observed values of charged fermion and neutrino masses and mixings, even at the tree level.

5.2.1 Proton Decay

The phenomenology of different scalars stemming from the $\mathbf{5}_{\mathrm{H}}$, $\mathbf{15}_{\mathrm{H}}$ and $\mathbf{45}_{\mathrm{H}}$, including contributions to neutrino mass, B and L- violating interactions, cLFV and lepton-flavour-universality-violating interactions, has been extensively studied [195]. Particularly, the scalar fields $S_1 \in \mathbf{5}_{\mathrm{H}}$ and $S_{1'}, S_3 \in \mathbf{45}_{\mathrm{H}}$ are known to induce tree-level proton decays while $\tilde{S}_1 \in \mathbf{45}_{\mathrm{H}}$ induces proton decay at one-loop [228, 316]. The tree-level proton decay Feynman diagram stemming from $S_{1'}, S_3$ is given in Fig. 5.1. A distinctive feature of scalar-induced proton decay is that the proton preferentially decays into the $\nu \mathrm{m}^+$, where m^+ is a meson composed of either first or second-generation quarks [316]. The leading proton decay mode induced by the LQs that would be relevant for

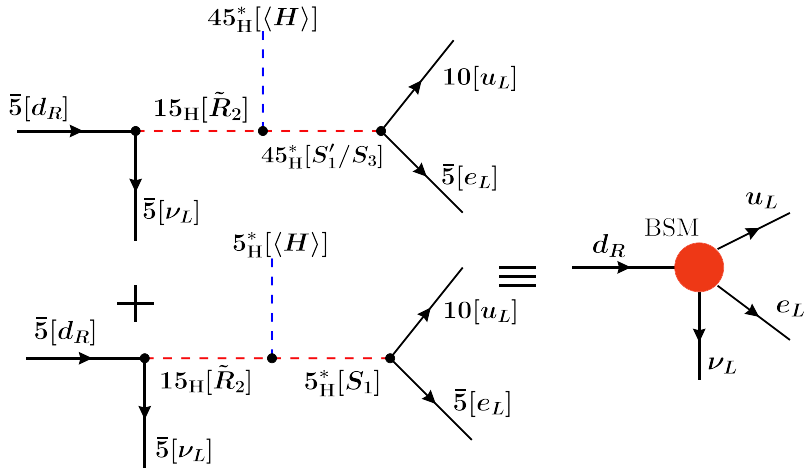

Figure 5.2: $0\nu\beta\beta$ operators stemming from $S_{1',3} \in \mathbf{45}_{\rm H}$ and $S_1 \in \mathbf{5}_{\rm H}$. The left panel shows the operator structure in the $SU(5)$ framework whereas the right panel shows the equivalent LEFT operator.

$0\nu\beta\beta$ is $p \to \nu\,\pi^+$, whose decay width can be computed as follows [317]:[1]

$$\Gamma\left(p \to \nu\,\pi^+\right) \simeq \sum_i \left(\frac{\left(Y_{15}\right)_{1i}\left(Y_{45}\right)_{11}}{M^2_{S_3}\,M^2_{\tilde{R}_2}}\right)^2 \left(\eta\,v\right)^2 \frac{m_p}{32\pi\,f_\pi^2}\,\alpha^2\,A^2\,, \tag{5.9}$$

where η is the strength of the $\mathbf{45}_{\rm H}\mathbf{45}_{\rm H}\mathbf{15}^\dagger_{\rm H}$ vertex with positive mass dimension, v is the vacuum expectation value (vev) of the SM Higgs boson, $\alpha \sim 0.01$ GeV^3 is the hadronic matrix element, $A \sim 1.4$ is the long-distance renormalisation factor, and $f_\pi \simeq 130$ MeV is the pion decay constant. Putting the different factors mentioned above and using the current lower bound of 3.9×10^{32} yr on the lifetime of $p \to \nu\,\pi^+$ [318] gives the following estimate:

$$\frac{\left(Y_{15}\right)_{11}\left(Y_{45}\right)_{11}\eta\,v}{M^2_{S_3}\,M^2_{\tilde{R}_2}} \;\lesssim\; 10^{-28}\,\text{GeV}^{-2}. \tag{5.10}$$

The above relation severely constrains the product of the Yukawa couplings and leptoquark masses from proton decay.

5.2.2 Neutrinoless Double Beta Decay

The inclusion of $\mathbf{15}_{\rm H}$ in $SU(5)$ framework renders neutrinos to be of Majorana type by virtue of Type-II seesaw, which gives rise to the smoking gun signal of $0\nu\beta\beta$ [115] through Fig. 2.11. Apart from this, the pair of scalar leptoquarks $S_{1,1'} - \tilde{R}_2$ and $S_3 - \tilde{R}_2$ can generate lepton number violating operators which can also contribute to the to $0\nu\beta\beta$ decay [307, 308] and are shown in Fig. 5.2. As it can be seen in Fig. 5.1 and Fig. 5.2 that the same pair LQs contribute to both proton decay and $0\nu\beta\beta$. Therefore, one can use the proton decay constraint to calculate the maximum leptoquark contribution to the $0\nu\beta\beta$.

The operator contributing to $0\nu\beta\beta$ generated from Fig. 5.2 is given as,

$$\mathcal{O}_6 = \left(\frac{G_F}{\sqrt{2}}\right)\left[\epsilon^{S+P}_{S+P}\,(\overline{u}P_R d)\left(\overline{e}P_R\nu_e^C\right) + \epsilon^{T+T_5}_{T+T_5}\left(\overline{u}\sigma^{\alpha\beta}P_R d\right)\left(\overline{e}\sigma_{\alpha\beta}P_R\nu_e^C\right)\right] \quad (5.11)$$

with the Wilson co-efficient is identified as,

$$\begin{aligned}\epsilon^{S+P}_{S+P} &= \frac{\eta\left(\sqrt{2}\,Y_{45}\right)_{11}\left(\sqrt{2}\,Y_{15}\right)_{11}v^3}{M^2_{S_3}\,M^2_{\tilde{R}_2}},\\ \epsilon^{T+T_5}_{T+T_5} &= -\frac{1}{4}\epsilon^{S+P}_{S+P}.\end{aligned} \quad (5.12)$$

Following the procedure given in the Appendix. B, the amplitude of the leptoquark mediated diagram is approximated as[2],

$$\mathcal{A}_{\rm LQ} \approx V_{ud}\,M_{PS}\left(\frac{m_N}{m_e}\right)\left(\frac{(Y_{15})_{11}\,(Y_{45})_{11}\,\eta\,v}{M^2_{S_3}\,M^2_{\tilde{R}_2}}\right)v^2 \lesssim 10^{-21}, \quad (5.13)$$

where M_{PS} is the relevant nuclear matrix element (NME), m_N and m_e are the nucleon and electron masses respectively, and V_{ud} is the (1,1) element of the CKM matrix. To arrive at the above estimation, we have used the upper bound given in Eq. (5.10). On the other hand, the canonical light neutrino-mediated

[1]Here, we provide the expression for the $(S_3 - \tilde{R}_2)$-mediated contribution. Similar expression holds for the $(S_{1,1'} - \tilde{R}_2)$ pair for which M_{S_3} is replaced by $M_{S_{1,1'}}$.

[2]Here we have only used the $S+P$-$S+P$ contribution and neglected the tensor contribution as it is smaller than the scalar contribution.

Table 5.2: Assignment of $\mathcal{Z}_3$ charges to different fermion and scalar multiplets in our $SU(5)$ model. The subscript A denotes family labels, with the $\mathcal{Z}_3$ charge being the same for all generations for the given fermionic multiplet. Here ω is the cube-root of unity. The last row shows the $\mathcal{Z}_3$ charge of an additional $\widehat{\mathbf{15}}_{\rm H}$ which could significantly enhance the $0\nu\beta\beta$ rate in the considered framework.

$SU(5)$ Multiplet	$\mathcal{Z}_3$ Charge
$\bar{\mathbf{5}}_A$	ω^2
$\mathbf{10}_A$	ω
$\mathbf{5}_{\rm H}$	ω
$\mathbf{15}_{\rm H}$	ω^2
$\mathbf{24}_{\rm H}$	1
$\mathbf{45}_{\rm H}$	1
$\widehat{\mathbf{15}}_{\rm H}$	1

amplitude,

$$\mathcal{A}_{st} \simeq \frac{m_{ee}^{\rm std}}{m_e} \sim 10^{-8}, \tag{5.14}$$

where $m_{ee}^{\rm std} = \sum_i U_{ei}^2 m_i$, with U being the PMNS mixing matrix and m_i the masses of active neutrinos. Thus, we find that the the leptoquark-mediated $0\nu\beta\beta$ amplitude is more than $\sim$ 13 orders of magnitude smaller than the canonical light neutrino-mediated amplitude, and thus, $0\nu\beta\beta$ cannot place any meaningful constraints on the leptoquarks in this case. It also shows that the B-violating process of proton decay occurring at dimension-7 is more constraining than the L-violating process of $0\nu\beta\beta$ occurring at dimension-9.

5.3 An $SU(5) \times \mathcal{Z}_3$ model

In this section, we explore if the situation mentioned above can be remedied by forbidding the diquark coupling of S_3, thereby removing the constraint on its mass from proton decay and thus allowing a larger contribution to $0\nu\beta\beta$. In order to achieve this, we impose a discrete $\mathcal{Z}_3$ symmetry, in addition to the $SU(5)$ gauge symmetry, which forbids the diquark interactions of S_3. The assignment of $\mathcal{Z}_3$ charges to various (scalar and fermion) multiplets are depicted in Tab. 5.2.

The $\mathbf{24}_{\rm H}$-dimensional scalar irrep transforms as a singlet under the imposed $\mathcal{Z}_3$ symmetry. Consequently, the $\mathcal{Z}_3$ symmetry remains intact even after the breaking of $SU(5)$. Moreover, the assigned $\mathcal{Z}_3$ charges are such that they prohibit any mixing term between $\mathbf{5}_{\rm H}$ and $\mathbf{45}_{\rm H}$. As a result, the scalar fields $H_{1,2}$ and S_1, $S_{1'}$, residing in $\mathbf{5}_{\rm H}$ and $\mathbf{45}_{\rm H}$ respectively, cannot mix as long as $\mathcal{Z}_3$ remains unbroken. One immediate consequence of the non-mixing of $H_{1,2}$ is that the considered model effectively reduces to a Type-II Two Higgs Doublet Model (THDM) [319]. The $\mathcal{Z}_3$ symmetry is broken when any of the SM Higgs fields residing in $\mathbf{5}_{\rm H}$ or $\mathbf{45}_{\rm H}$ acquires a vev, thus mixing $H_{1,2}$ and one of the linear combinations will be identified as the SM Higgs boson. Note that the $\mathcal{Z}_3$-breaking can potentially regenerate the unwanted interactions (e.g. $S_1 - S_3$ mixing) inducing proton decay. However, since $\mathcal{Z}_3$ is broken at a lower scale (electroweak scale), the strength of these undesired couplings is suppressed by $(v/M_{\rm GUT})^2$, which ensures that the proton decay rate remains well below the experimental limit.

Note that spontaneous breaking of a discrete symmetry in the early Universe generates degenerate vacua. These vacua are disconnected in the three-dimensional space, thus leading to the formation of domain walls between them [320]. This can be a problem, because once they form after inflation, they may soon dominate the energy density and overclose the Universe during the Hubble expansion [321, 322]. However, there are various ways to solve this, e.g. by diluting them away during/after inflation for a suitable choice of the reheating temperature [323], by introducing bias terms in the potential [324], perforating them by fast primordial black holes [325], assuming that the discrete symmetry arises as a low-energy remnant symmetry after the spontaneous breaking of some continuous gauge symmetry [326], suppressing the thermal production of domain walls [327], etc.

The assignment of the $\mathcal{Z}_3$ charges in Tab. 5.2 forbids the $\tilde{Y}_{5,45}$ Yukawa couplings in Eq. (5.6) and the only allowed terms in the Yukawa Lagrangian are shown below:

$$-\mathcal{L}_{\rm Y} \;=\; \frac{1}{4}\left(Y_5\right)_{AB} \mathbf{10}_A^T\, \mathcal{C}^{-1}\, \mathbf{10}_B\, \mathbf{5}_{\rm H} \;+\; \sqrt{2}\left(Y_{45}\right)_{AB} \mathbf{10}_A^T\, \mathcal{C}^{-1}\, \bar{\mathbf{5}}_B\, \mathbf{45}_{\rm H}^{\dagger}$$

$$+ \quad (Y_{15})_{AB}\, \overline{\mathbf{5}}_A^T\, \mathcal{C}^{-1}\, \overline{\mathbf{5}}_B\, \mathbf{15}_{\rm H} + \text{h.c.}\,, \tag{5.15}$$

where Y_5 and Y_{15} are symmetric in flavour indices. The tree-level Yukawa relations can be obtained by putting $\widetilde{Y}_5, \widetilde{Y}_{45} \to 0$ in Eq. (5.8):

$$\begin{aligned}
(Y_u)_{AB} &= (Y_5)_{AB}\,, \\
(Y_d)_{AB} &= \frac{1}{\sqrt{6}}\,(Y_{45})_{AB}\,, \\
(Y_e)_{AB} &= -\sqrt{\frac{3}{2}}\,\left(Y_{45}^T\right)_{AB}\,, \\
(Y_\nu)_{AB} &= \sqrt{2}\,(Y_{15})_{AB}\,.
\end{aligned} \tag{5.16}$$

The tree-level Yukawa relations written in Eq. (5.16) have enough freedom to reproduce the correct up-type Yukawa sector. However, in the down quark and charged lepton sectors, it leads to $3\,Y_d = -\,Y_e^T$ which results in $\frac{y_d}{y_e} = \frac{y_c}{y_\mu} = \frac{y_b}{y_\tau} = \frac{1}{3}$. But, at the traditional GUT scale ($M_{\rm GUT} \sim 10^{16}\,\text{GeV}$), the renormalisation group evolution (RGE)-extrapolated SM values predict $\frac{y_d}{y_e} = 2$, $\frac{y_c}{y_\mu} = \frac{1}{5}$, and $\frac{y_b}{y_\tau} = \frac{2}{3}$ [328]. Thus, the tree-level Yukawa relations obtained here are not viable in the down quark and charged lepton sectors, unlike in the $SU(5)$ model without the $\mathcal{Z}_3$ [cf. Eq. (5.6)]. However, this issue is resolved by switching on the one-loop correction imparted by various heavier degrees of freedom (scalar and gauge bosons), which are already present in the model, as discussed in the next section.

5.3.1 Charged Fermion Yukawa Relations at NLO

The inconsistency in the fermion mass relations at the tree-level [c.f. Eq. (5.16)] can be addressed once the heavy scalar and gauge boson-mediated one-loop corrections are included to the Yukawa vertices [329]. To illustrate, we have shown the Feynman diagrams for the one-loop corrections to the $\mathbf{10} - \overline{\mathbf{5}} - \mathbf{45}^*_{\rm H}$ vertex in Fig. 5.3. The one-loop matching condition for the Yukawa couplings at a given renormalisation scale μ, following Refs. [330–335], is derived in

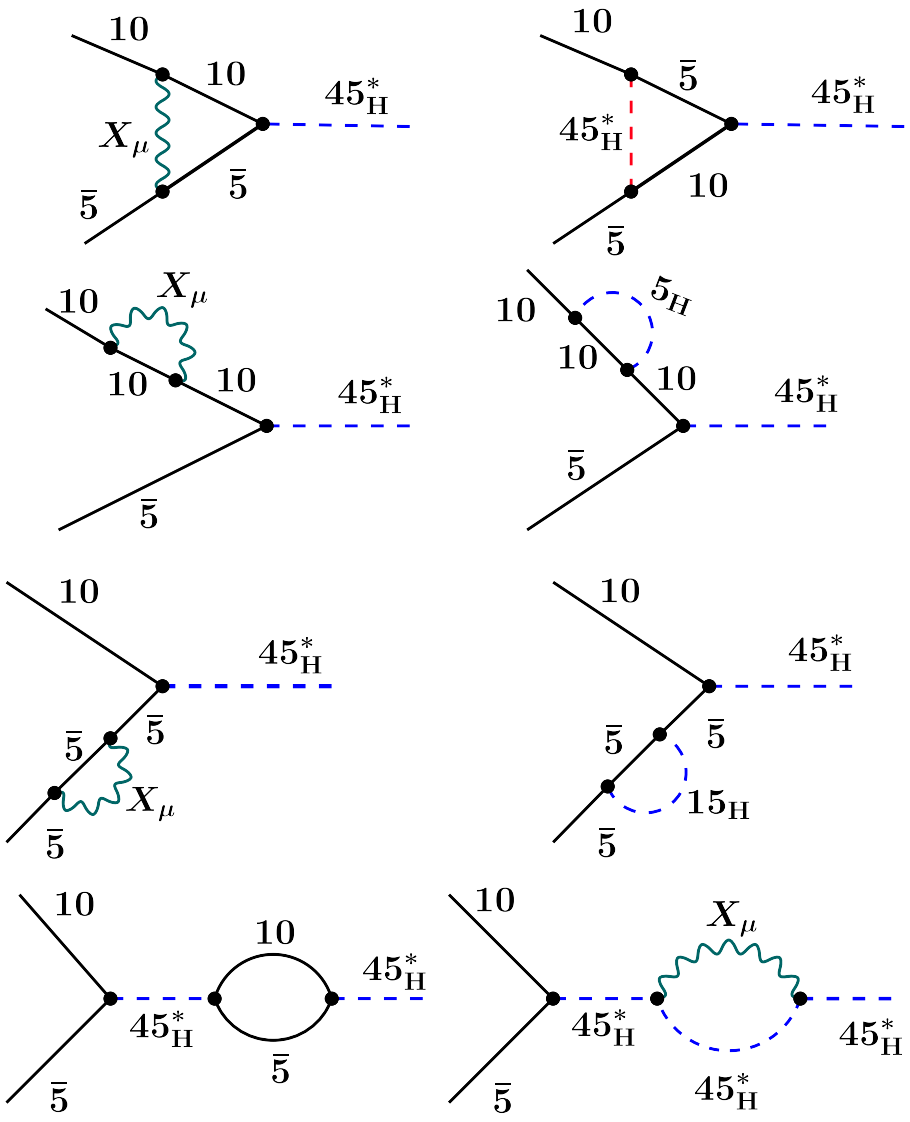

Figure 5.3: Possible Feynman diagrams that contribute to the one loop corrections of $\mathbf{10} - \bar{\mathbf{5}} - \mathbf{45}^*_{\mathrm{H}}$ vertex. The upper row contribute to the vertex corrections whereas the rest contribute to the wave function renormalisation of the external fields.

Refs. [329, 336] and is given as follows:

$$Y_f(\mu) \;=\; Y_f^0\left(1 - \frac{K_H(\mu)}{2}\right) + \delta Y_f(\mu) - \frac{1}{2}\Big(K_f^T(\mu)\, Y_f^0 + Y_f^0\, K_f^C(\mu)\Big), \tag{5.17}$$

where Y_f^0 are the tree-level Yukawa couplings of fermions $f \supset \{q, u^C, d^C, \ell, e^C\}$ with the SM Higgs boson. The one-loop corrected Yukawa

coupling at the scale μ, i.e. $Y_f(\mu)$ is deterministic and calculable in terms of the finite part of the vertex corrections (δY_f) and wave-function renormalisation factors (K_H, K_f). Vertex corrections to various Yukawa couplings and wave function renormalisation for different fields are induced by the heavy fields inherent to this scenario.

To compute the one-loop corrections, the interactions of the heavy degrees of freedom with the SM fermions are required. The interactions between various scalars with SM fermions stemming from $\mathbf{5}_{\rm H}$ and $\mathbf{45}_{\rm H}$ are obtained from the decomposition of Eq. (5.6) using Eqs. (5.1), (5.3), (5.4) and (5.5), as shown below:

$$\begin{aligned}
-\mathcal{L}_{\rm Y} \;\supset\; & -Y_{5\,AB}\left(u^{C\,T}_{\gamma\,A}\,\mathcal{C}^{-1}\,e^{C}_{B} + \frac{1}{2}\,\varepsilon_{\alpha\beta\gamma}\,\varepsilon_{ab}\,q^{a\alpha\,T}_{A}\,\mathcal{C}^{-1}\,q^{b\beta}_{B}\right)S^{\gamma}_{1} \\
& + \frac{Y_{45\,AB}}{\sqrt{2}}\left(\frac{1}{\sqrt{2}}\varepsilon^{\alpha\beta\rho}\,u^{C\,T}_{\rho\,A}\,\mathcal{C}^{-1}\,d^{C}_{\gamma\,B}\,\mathbb{S}^{\dagger\gamma}_{\alpha\beta} + \frac{1}{\sqrt{2}}\,\varepsilon^{\alpha\beta\gamma}\,u^{C\,T}_{\alpha\,A}\,\mathcal{C}^{-1}\,d^{C}_{\beta\,B}\,S^{\prime\dagger}_{1\,\gamma}\right. \\
& - \frac{1}{\sqrt{2}}\,\varepsilon^{\alpha\beta\rho}\,\varepsilon_{ab}\,u^{C\,T}_{\rho\,A}\,\mathcal{C}^{-1}\,\ell^{a}_{B}\,R^{b}_{2\,\alpha\beta} - \sqrt{2}q^{a\alpha\,T}_{A}\,\mathcal{C}^{-1}\,d^{C}_{\beta\,B}\,O^{\dagger\beta}_{\alpha\,a} \\
& \left. - \sqrt{2}\,\varepsilon_{ab}\,q^{p\alpha\,T}_{A}\,\mathcal{C}^{-1}\,\ell^{a}_{B}\,S^{\dagger\,b}_{3\,p\alpha} - \sqrt{2}\,e^{C\,T}_{A}\,\mathcal{C}^{-1}\,d^{C}_{\beta\,B}\,\tilde{S}^{\beta}_{1} - \frac{1}{\sqrt{2}}\,\varepsilon_{ab}\,q^{a\alpha\,T}_{A}\,\mathcal{C}^{-1}\,\ell^{b}_{B}\,S^{\prime\,\dagger}_{1\,\alpha}\right) \\
& + Y_{15\,AB}\left(\varepsilon_{am}\,\varepsilon_{bn}\,\ell^{m\,T}_{A}\,\mathcal{C}^{-1}\,\ell^{n}_{B}\,\Delta^{ab} + \sqrt{2}\,\varepsilon_{ab}\,\ell^{b\,T}_{A}\,\mathcal{C}^{-1}\,d^{C}_{\alpha\,B}\,\tilde{R}^{a\alpha}_{2} + d^{C\,T}_{\alpha\,A}\,\mathcal{C}^{-1}\,d^{C}_{\beta\,B}\,\Sigma^{\alpha\beta}\right) \\
& + \text{h.c.}
\end{aligned} \tag{5.18}$$

It is to be noted that due to the imposed $\mathcal{Z}_3$ symmetry, the diquark coupling of S_3 is forbidden and hence it cannot induce nucleon decay here. The one-loop matching condition also requires the contribution from heavy gauge bosons, whose Lagrangian is shown below:

$$\mathcal{L}_{G} \;=\; \overline{\overline{\mathbf{5}}}\,\overline{\sigma}_{\mu}\,\mathrm{D}^{\mu}\,\overline{\mathbf{5}} + \overline{\mathbf{10}}\,\overline{\sigma}_{\mu}\,\mathrm{D}^{\mu}\,\mathbf{10}\,, \tag{5.19}$$

where D_μ is the covariant derivative and $\overline{\sigma}_\mu = (1, \boldsymbol{\sigma})$, with $\boldsymbol{\sigma}$ being the Pauli matrices. The couplings of heavy gauge boson $X_\mu\left(3, 2, -\frac{5}{6}\right)$ with the SM fermions is shown below:

$$-\mathcal{L}^{(X)}_{\rm G} \;\supset\; \frac{g_5}{\sqrt{2}}\overline{X}_{\mu}\left(\overline{d^{C}}_{i}\overline{\sigma}^{\mu}\ell_{i} - \overline{q}_{i}\overline{\sigma}^{\mu}u^{C}_{i} - \overline{e^{C}}_{i}\overline{\sigma}^{\mu}q_{i}\right) + \text{h.c.}\,, \tag{5.20}$$

where g_5 is the $SU(5)$ gauge coupling.

The vertex corrections to the various Yukawa vertices are induced by heavier scalars and gauge bosons propagating inside the loop. These can be computed from Eqs. (5.18) and (5.20), as shown below:

$$\begin{aligned}
\left(\delta Y_u\right)_{AB} &= 4\, g_5^2 \left(Y_5\right)_{AB} f[M_X^2, 0]\,, \\
\left(\delta Y_d\right)_{AB} &= \frac{2}{\sqrt{6}}\, g_5^2 \left(Y_{45}\right)_{AB} f[M_X^2, 0]\,, \\
\left(\delta Y_e\right)_{AB} &= -6\sqrt{\frac{3}{2}}\, g_5^2 \left(Y_{45}^T\right)_{AB} f[M_X^2, 0]\,,
\end{aligned} \tag{5.21}$$

where (δY_f) represents the finite part of the correction to the Yukawa interaction of fermion f with the SM Higgs. The loop integration factor $f[M_i^2, 0]$ is given as,

$$f[M_1^2, M_2^2] = -\frac{1}{16\pi^2}\left(\frac{M_1^2 \log\frac{M_1^2}{\mu^2} - M_2^2 \log\frac{M_2^2}{\mu^2}}{M_1^2 - M_2^2} - 1\right), \tag{5.22}$$

$$\tag{5.23}$$

where M_i is the mass of the scalar or gauge boson propagating inside the loop. These corrections depend on the renormalisation scale μ and are fully determined in terms of the tree-level Yukawa couplings $Y_{5,45}$, along with a function that involves the masses of heavy particles. While calculating these corrections, all SM fields are considered massless. Due to the assigned $\mathcal{Z}_3$ charges, scalar fields from $\mathbf{5}_\mathrm{H}$ and $\mathbf{45}_\mathrm{H}$ do not mix; consequently, the vertex corrections receive contribution only from the heavy gauge bosons (X_μ), not from the scalar fields. Moreover, the vertex corrections to Y_d and Y_e are unable to break the tree-level inconsistency, $3\,Y_d = Y_e^T$, as δY_d and δY_e also follow the same behaviour. However, the wave-function renormalisation to different fermions will break the generational degeneracy, as shown below.

The finite part of the wave function renormalisation factor of the (scalar or fermion) field f is computed by taking the derivative of the self-energy cor-

rection of the field f with respect to the outgoing momentum and then setting the momentum to zero. The contribution to the wave function renormalisation due to various scalars and gauge bosons to the external leg of SM fermions and Higgs are shown below:

$$
\begin{aligned}
\left(K_q\right)_{AB} &= 3\,g_5^2\,\delta_{AB}\,h[M_X^2,0] - \frac{1}{2}\,\left(Y_5^* Y_5^T\right)_{AB}\,h[M_{S_1}^2,0] \\
&- \left(6\,h[M_O^2,0] + 4\,h[M_{S_3}^2,0] + 0.5\,h[M_{S_1'}^2,0]\right)\left(Y_{45}\,Y_{45}^\dagger\right)_{AB}\,, \\
\left(K_{u^C}\right)_{AB} &= 4\,g_5^2\,\delta_{AB}\,h[M_X^2,0] - h[M_{S_1}^2,0]\left(Y_5^*\,Y_5^T\right) \\
&- \left(3h[M_{\mathbb{S}}^2,0] + 1.5h[M_{S_1'}^2,0] + 2h[M_{R_2}^2,0]\right)\left(Y_{45}\,Y_{45}^\dagger\right)_{AB}\,, \\
\left(K_{d^C}\right)_{AB} &= 2\,g_5^2\,\delta_{AB}\,h[M_X^2,0] \\
&- \left(6h[M_{\mathbb{S}}^2,0] + h[M_{S_1'}^2,0] + 12h[M_O^2,0] + 2\,h[M_{\tilde{S}_1}^2,0]\right)\left(Y_{45}^T\,Y_{45}^*\right)_{AB} \\
&- 4\,h[M_\Sigma^2,0]\left(Y_{15}\,Y_{15}^\dagger\right)_{AB} - 4\,h[M_{R_2}^2,0]\left(Y_{15}^T\,Y_{15}^*\right)_{AB} \\
\left(K_\ell\right)_{AB} &= 3\,g_5^2\,\delta_{AB}\,h[M_X^2,0] - \left(6h[M_{R_2}^2,0] + 6h[M_{S_3}^2,0] + 1.5h[M_{S_1'}^2,0]\right)\left(Y_{45}^T\,Y_{45}^*\right)_{AB}\,, \\
&- 3\,h[M_\Delta^2,0]\left(Y_{15}\,Y_{15}^\dagger\right)_{AB} - 6\,h[M_{\tilde{R}_2}^2,0]\left(Y_{15}\,Y_{15}^\dagger\right)_{AB}\,, \\
\left(K_{e^C}\right)_{AB} &= 6\,g_5^2\,\delta_{AB}\,h[M_X^2,0] - 3\,h[M_{S_1}^2,0]\,Y_5^\dagger\,Y_5 \\
K_{H_1} &= \frac{g_5^2}{2}\Big[2\,\left(f[M_X^2,M_{S_1}^2] + g[M_X^2,M_{S_1}^2]\right), \\
K_{H_2} &= \frac{g_5^2}{2}\Big[2\,\left(f[M_X^2,M_{S_1'}^2] + g[M_X^2,M_{S_1'}^2]\right) \\
&+ 4\,\left(f[M_X^2,M_{S_3}^2] + g[M_X^2,M_{S_3}^2]\right) + 4\,\left(f[M_X^2,M_{\tilde{S}}^2] + g[M_X^2,M_{\tilde{S}}^2]\right)\Big]. \qquad (5.24)
\end{aligned}
$$

Here K_f characterises the finite parts of the wave function renormalisation factor corresponding to the field f. The loop integrating factors $g[M_i^2,0]$ and $h[M_i^2,0]$ are given as,

$$
h[M_1^2,M_2^2] = \frac{1}{16\pi^2}\left(\frac{1}{2}\log\frac{M_1^2}{\mu^2} + \frac{\frac{1}{2}q^2\log q - \frac{3}{4}q^2 + q - \frac{1}{4}}{(1-q)^2}\right), \qquad (5.25)
$$

$$
g[M_1^2,M_2^2] = \frac{1}{16\pi^2}\frac{\frac{q^3}{6} - q^2 + \frac{q}{2} + q\log q + \frac{1}{3}}{(1-q)^3}, \qquad (5.26)
$$

where $q = M_2^2/M_1^2$. In contrast to the vertex corrections, wave function renormalisation factors receive corrections from both heavy scalars and gauge bosons. The interaction of each scalar with SM fermions determines its contri-

bution to different wave-function renormalisation factors. Notably, K_ℓ and K_{d^C} are different because the scalar fields $\mathbb{S}$, O and Σ contribute only to K_{d^C}, while R_2 and Δ contribute to K_ℓ, as the former only have diquark interactions. As a result, these two factors are not the same. Thus, including the wave-function renormalisation effects can help in resolving the inconsistency in the tree-level Yukawa relation in the down quark and charged lepton sectors. Moreover, the SM Higgs residing in $\mathbf{5}_{\rm H}$ and $\mathbf{45}_{\rm H}$ irreps also receives different contributions from scalars, which is due to the imposition of the $\mathcal{Z}_3$ symmetry.

Substituting Eqs. (5.21) and (5.24) into Eq. (5.17), the effective Yukawa relations at one loop valid at a given renormalisation scale μ are as follows:

$$\begin{aligned}
Y_u(\mu) &\simeq Y_5\left(1-\frac{1}{2}K_{H_1}\right)+\delta Y_u-\frac{1}{2}\left(K_q^T\,Y_5+Y_5\,K_{u^C}\right),\\
Y_d(\mu) &\simeq \frac{Y_{45}}{\sqrt{6}}\left(1-\frac{1}{2}K_{H_1}\right)+\delta Y_d-\frac{1}{2\sqrt{6}}\times\left(K_q^T\,Y_{45}+Y_{45}\,K_{d^C}\right),\\
Y_e(\mu) &\simeq -\sqrt{\frac{3}{2}}\,Y_{45}^T\left(1-\frac{1}{2}\,K_{H_2}\right)+\delta Y_e-\frac{1}{2}\left(-\sqrt{\frac{3}{2}}\right)\times\left(K_\ell^T\,Y_{45}^T+Y_{45}^T\,K_{e^C}\right),
\end{aligned} \tag{5.27}$$

where $Y_{5,45}$ are the tree-level Yukawa couplings depicted in Eq. (5.6).

5.3.2 Neutrino Mass

The capability of the considered $SU(5)$ framework to generate neutrino mass is now evaluated. This model includes a $\mathbf{15}_{\rm H}$-dimensional scalar irrep, which is traditionally associated with neutrino mass generation through the Type-II seesaw mechanism [337]. As the charged fermion mass spectrum has been computed up to the one-loop level, consistency requires extending the neutrino mass calculation to the same order. The neutrino mass receives tree level contribution from Δ (c.f. Tab. 5.1) with the Yukawa coupling Y_{15} and also receives contribution from $R_2 - S_3$ at one loop which is shown in Fig. 5.4. The

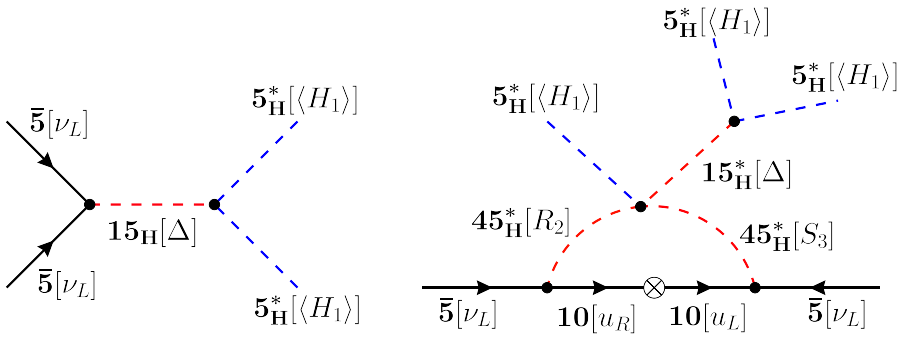

Figure 5.4: Feynman diagrams that contribute to neutrino mass generation up to the one-loop level.

resulting expression is given by

$$\begin{aligned} M_\nu &= -2\,\eta\,\frac{\langle H_1\rangle^2}{M_\Delta^2}\,Y_{15} \\ &+ 6\,\rho\,\eta\,\frac{\langle H_1\rangle^4}{M_\Delta^2}\left[\left(Y_{45}^T\,Y_u^*\,Y_{45}\right)+\left(Y_{45}^T\,Y_u^*\,Y_{45}\right)^T\right] p[M_{S_3}^2, M_{R_2}^2]\,, \end{aligned} \tag{5.28}$$

where the first term is the tree-level Type-II seesaw contribution, and the second term is the one-loop contribution. Here $\langle H_1\rangle$ is the vev of the SM Higgs field residing in the $\mathbf{5_H}$-dimensional Higgs, η is a dimension-full trilinear coupling and is assumed to be close to the GUT scale, while ρ is an $\mathcal{O}(1)$ quartic coupling and has been set to unity. The definition of the loop integration factor $p[M_1^2, M_2^2]$ is given as,

$$p(M_1^2, M_2^2) = \frac{1}{16\pi^2}\,\frac{1}{M_1^2 - M_2^2}\log\left(\frac{M_1^2}{M_2^2}\right). \tag{5.29}$$

It is to be noted that the trilinear vertex $\mathbf{45_H}\,\mathbf{45_H}\,\mathbf{15_H^\dagger}$ is forbidden due to the imposed $\mathcal{Z}_3$ symmetry; as a result, H_2 cannot contribute to the neutrino masses. It is also imperative to note that the neutrino mass receives contributions from the one-loop corrected Yukawa couplings Y_u. Moreover, for a hierarchical neutrino mass spectrum far away from the quasi-degenerate regime, as strongly suggested by the current cosmological limits on the sum of neutrino masses [31, 338], the RGE running of neutrino parameters are known to be small [339–342] and will not be considered here.

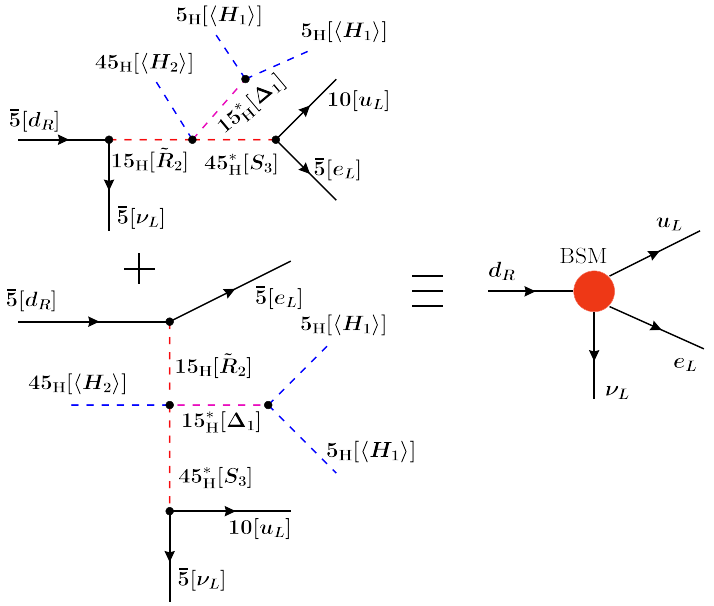

Figure 5.5: Effective operators that contribute to $0\nu\beta\beta$ in the considered $SU(5) \times \mathcal{Z}_3$ model. (**Left Panel:**) Diagrams contributing to $0\nu\beta\beta$ generated by the $SU(5)$ scalars. The number outside the bracket denote the $SU(5)$ representation while the labels in the bracket denote the field under SM charges. (**Right Panel:**) The LEFT operator corresponding to the left diagram after integrating out the heavy scalars.

5.3.3 Contribution to $0\nu\beta\beta$

In this scenario, in addition to the standard long-range contribution mediated by left-handed neutrinos, we have other long-range contributions mediated by the scalars in $SU(5)$ which in given in Fig. 5.5. These contributions are referred to as non-standard contributions are given by

$$\mathcal{O}^{(6)}_{\text{BSM}} = \left(\frac{G_F}{\sqrt{2}}\right) \left[\epsilon^{S+P}_{S+P} \left(\bar{u} P_R d\right) \left(\bar{e} P_R \nu_e^C\right) + \epsilon^{T+T_5}_{T+T_5} \left(\bar{u} \sigma^{\alpha\beta} P_R d\right) \left(\bar{e} \sigma_{\alpha\beta} P_R \nu_e^C\right)\right] \quad (5.30)$$

Both the diagrams given in Fig. 5.5 originate from the same interactions term in the $SU(5)$ Lagrangian. They differ only in the electric charges of the mixing partners: the first diagram involves the mixing of leptoquarks with $Q_{\text{em}} = 1/3$ components of M_{S_3} and $M_{\tilde{R}_2}$, while the second appears when the leptoquarks with $Q_{\text{em}} = 2/3$ mix.

The dimensionless parameters ϵ^{S+P}_{S+P} and $\epsilon^{T+T_5}_{T+T_5}$ appearing in Eq. (5.30) at the

LEFT scale are given by

$$\epsilon^{S+P}_{S+P} \approx \frac{\rho\,\eta\,v^5}{M^2_\Delta}\,\frac{\left(\sqrt{2}\,Y_{\tilde{R}_2}\right)_{11}}{M^2_{\tilde{R}_2}}\,\frac{\left(\sqrt{2}\,Y_{S_3}\right)_{11}}{M^2_{S_3}}\,, \tag{5.31}$$

$$\epsilon^{T+T_5}_{T+T_5} = -\frac{1}{4}\,\epsilon^{S+P}_{S+P}\,, \tag{5.32}$$

corresponding to the $S+P$ and $T+T_5$ contributions, respectively.

Having identified the relevant LEFT operators and their corresponding Wilson coefficients, the half-life can now be computed using the master formula presented in Ref. [244] [see appendix]:

$$\left(T^{0\nu}_{1/2}\right)^{-1}_{\text{total}} = g_A^4 \sum_k G_{0k}\,\left|\mathcal{A}_k\left(\{C_i\}\right)\right|^2, \tag{5.33}$$

where G_{0k} denotes the atomic phase space factors and $\mathcal{A}_k\left(\{C_i\}\right)$ are the sub-amplitudes which depend on the NMEs, low-energy constants (LECs) and the Wilson coefficients of the relevant operators. We use the python package νDoBe [222] to compute the half-life of $0\nu\beta\beta$ process for ^{76}Ge and ^{136}Xe nuclei, incorporating NMEs from the IBM2 model [245].[3] The νDoBe package handles the RG running of the Wilson coefficients—particularly ϵ^{S+P}_{S+P} and $\epsilon^{T+T_5}_{T+T_5}$—from the electroweak scale ($\mu = \mu_{\text{ew}}$) down to $\mu = 2$ GeV. It is to be noted that the decay-rate formula in νDoBe is expressed in terms of the Wilson coefficients evaluated at the chiral symmetry breaking scale ($\mu \sim 2$ GeV) [244].

To have a numerical estimate, the half-life formula in Eq. (5.33) can be simplified as,

$$\begin{aligned}
\left(T^{0\nu}_{1/2}\right)^{-1} &= g_A^4\,G_{01}^2\left|\frac{m^{\text{std}}_{ee}}{m_e}\mathcal{M}^{(3)}_\nu + \frac{m_N}{m_e}\,\mathcal{M}^{(6)}_\nu\right|^2, \\
&= g_A^4 G_{01}\left|\mathcal{M}^{(3)}_\nu\right|^2\left[\frac{m^{\text{std}}_{ee}}{m_e} + \frac{m_N}{m_e}\,\epsilon^{S+P}_{S+P}\,\frac{\mathcal{M}'^{(6)}_\nu}{\mathcal{M}^{(3)}_\nu}\right]^2, \\
&= g_A^4 G_{01}\left|\mathcal{M}^{(3)}_\nu\right|^2\left[\frac{m^{\text{std}}_{ee} + m^{\text{nstd}}_{ee}}{m_e}\right]^2,
\end{aligned}$$

[3] For other nuclei or NME schemes, the results vary by no more than 10%.

$$= g_A^4 G_{01} \left| \mathcal{M}_\nu^{(3)} \right|^2 \left[\frac{m_{ee}^{\rm eff}}{m_e} \right]^2, \tag{5.34}$$

where $\mathcal{M}_\nu^{(3)} = -4.832\ (-8.635)$, $\mathcal{M}_\nu'^{(6)} = -V_{ud} \left(\frac{B}{m_N} M_{PS} + \frac{1}{4} M_{T6} \right) = 0.327\ (0.627)$ for ^{136}Xe (^{76}Ge) nucleus and $m_{ee}^{\rm nstd}$ denotes the non standard contribution and is defined as,

$$m_{ee}^{\rm nstd} = m_N \, \epsilon_{S+P}^{S+P} \left(\frac{\mathcal{M}_\nu'^{(6)}}{\mathcal{M}_\nu^{(3)}} \right). \tag{5.35}$$

The effective Majorana mass is defined as,

$$m_{ee}^{\rm eff} = m_{ee}^{\rm std} + m_{ee}^{\rm nstd}, \tag{5.36}$$

where $m_{ee}^{\rm std} = \sum_i U_{ei}^2 \, m_i$ denotes the canonical light neutrino contribution, and $m_{ee}^{\rm nstd}$ denotes the non-standard contribution.

5.3.4 Parameter Fitting

The viability of the expressions given in Eqs. (5.27) and (5.28) in yielding realistic charged and neutral fermion mass spectra observed at low energies is done via a χ^2 optimisation procedure, similar to that in Ref. [329]. The χ^2 function is defined as

$$\chi^2 = \sum_i \left(\frac{O_{i,\,\rm theo} - O_{i,\,\rm exp}}{\sigma_{i,\,\rm exp}} \right)^2, \tag{5.37}$$

where $O_{i,\rm theo}$ is the theoretical prediction for each observable, and $O_{i,\rm exp}$ is the corresponding experimentally measured value, where index i runs over all observables in the set. The experimental uncertainty for each observable is represented by σ_i. The χ^2 function in Eq. (5.37) includes nine charged fermion Yukawa couplings, four CKM parameters, two neutrino mass-squared differences and three PMNS mixing angles. Since all the $O_{i\,\rm theo}$ values computed in Eqs. (5.27) and (5.28) are at the GUT scale, the corresponding $O_{i\,\rm exp}$ values are also evolved to the GUT scale. The GUT scale values of the experimental

observables are obtained after extrapolating the low energy observables using two-loop THDM RGE equations from $M_t = 173$ GeV (pole mass of the top quark [4]) to $M_{\rm GUT}$, chosen here to be 10^{16} GeV. To compute the observables at the GUT scale, the analysis starts at M_t in a basis where $Y_{u,e} = {\rm Diag}(M_{u,e})/v$, $Y_d = V_{\rm CKM}{\rm Diag}(M_d)/v$, with $M_{u,d,e}$ as diagonal fermion mass matrices at M_t. These serve as inputs for two-loop THDM RG running, with the corresponding β-functions evaluated using the `PyR@TE` package [343]. As there are two Higgs vevs involved in the THDM framework, the ratio of their vevs, i.e. $\tan\beta \equiv \frac{v_1}{v_2}$, is fixed at 1.5 [344] for our numerical purpose. After diagonalisation of the Yukawa matrices, the GUT-scale values of the various observables are obtained (as shown in Tab. 5.3). The low-energy input values of the charged fermion masses and CKM mixing parameters are taken from PDG [4], while the neutrino mass and mixing parameters are taken from a recent `NuFIT` update [345].

Since uncertainties in the experimental observables at the GUT scale are not precisely known, conservative estimates are adopted. A $\pm 10\%$ uncertainty is used for all the observables. Despite knowing the leptonic parameters with high precession at low energies [4], such a large uncertainty is assumed at the GUT scale due to several factors: (i) unknown scalar effects in the RGEs, (ii) uncertainties in scalar masses, (iii) uncertainty in the matching scale, and (iv) higher-order threshold corrections. The limited knowledge of GUT-scale physics justifies the increased uncertainty (see e.g. Refs. [346, 347] for similar fits with different uncertainty assumptions for the leptonic spectrum).

The allowed Yukawa values have been taken to be in the perturbative limit, i.e $\left|Y_{5,15,45}\right| \leq \sqrt{4\pi}$ for obtaining a numerical solution minimising the χ^2 function. This perturbative limit on the magnitude of Yukawa coupling is obtained from $2 \to 2$ tree-level scattering at the high energy limit [348]. The mass of the heavy gauge boson (M_X) appearing in Eq. (5.20) has been set to be equal to the matching scale (μ) which is same as the conventional GUT scale $(\mu = M_{\rm GUT} = M_X = 10^{16}$ GeV) and the gauge coupling g_5 is taken to be 0.524, which is the mean value of the SM gauge couplings at the GUT scale. We do not make an attempt to achieve exact unification of the gauge couplings

in this scenario, which can be done by extending the model by adding more degrees of freedom that do not couple to SM fermions thereby not affecting our analysis. The trilinear coupling η appearing in the expression of neutrino mass [cf. Eq. (5.28)] is also varied around the GUT scale in the range of $(0.1, 10)M_{\rm GUT}$, whereas the quartic coupling ρ appearing in the same expression has been set to unity.

In Eq. (5.27), Y_{45} can be chosen as a real-diagonal matrix, Y_5 a symmetric matrix with complex entries and two cases can be considered for Y_{15}, i.e., **Case-I** where Y_{15} is real symmetric, and **Case-II** where Y_{15} is a complex-symmetric matrix. This yields a total of 21 (27) Yukawa couplings in Case-I (Case-II). Moreover, there are one, three and six BSM scalar fields inside the $\mathbf{5}_{\rm H}$, $\mathbf{15}_{\rm H}$ and $\mathbf{45}_{\rm H}$-dimensional irreps, whose masses can take any value between roughly 1 TeV (to satisfy the LHC constraints) and GUT scale. Additionally, the cubic coupling η can in principle take any value; however, a value much smaller than the GUT scale would bring a fine-tuning problem. Therefore, we vary η near the GUT scale for our analysis. Altogether, there are 32 (38) unknown parameters in Case-I (Case-II) which go into the theoretical predictions for the 18 observables in Eq. (5.37) to be fitted to their corresponding experimental values. Moreover, the neutrino masses can have either NO or IO; and we shall analyse both possibilities. The fitting of low-energy observables require splitting in the masses of scalars residing in a particular irrep $\left(\mathbf{15}_{\rm H}, \mathbf{45}_{\rm H}\right)$. Some of the scalar masses are required to significantly deviate from the matching scale in order to have substantial threshold corrections, which has also been observed in Ref. [315]. This scenario goes beyond the Extended Survival Hypothesis [349–351], which states that all the scalars except the one breaking the symmetry must be heavier than the symmetry-breaking scale. This type of framework calls for a mechanism that generates splitting in the masses of scalars residing in the common multiplet, reminiscent of the doublet-triplet splitting problem generic to all GUTs [352, 353]. This could be addressed, e.g. by invoking higher-dimensional operators [354], the details of which do not really matter for our phenomenological analysis.

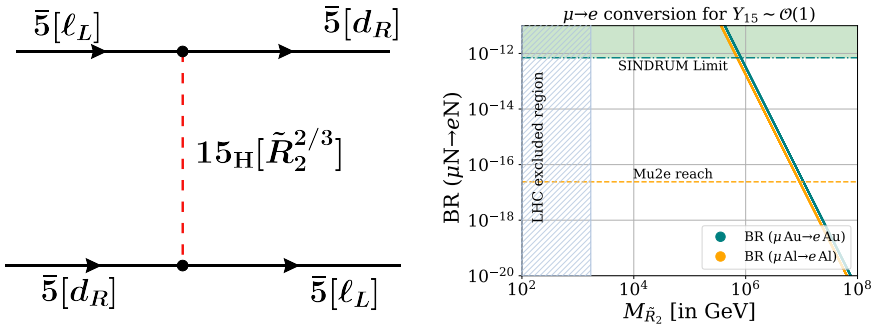

Figure 5.6: **Left panel** shows the Feynman diagram that contribute to $\mu \to e$ conversion in a nuclei at tree level. **Right panel** shows the variation of the branching fraction for $\mu \to e$ conversion in nuclei as a function of the $\widetilde{R}_2$ leptoquark mass for $\mathcal{O}(1)$ Yukawa couplings. The green dashed horizontal line indicates the current upper limit of the μtoe conversion branching fraction set by the SINDRUM experiment while the orange horizontal line shows the future Mu2e reach. The vertical shaded region represents the exclusion bounds on the leptoquark mass from LHC searches.

From Eq. (5.31), it is evident that the $0\nu\beta\beta$ rate, mediated by the $SU(5)$ scalars, depends on two main factors: (i) the Yukawa couplings of the leptoquarks with first-generation fermions, and (ii) the leptoquark masses. This section explores the possibility of obtaining a viable fermion mass fit together with maximising the $0\nu\beta\beta$ rate.

As discussed above, the model with Case-I (II) contains 32 (38) free parameters, including the scalar masses. It is evident from earlier discussions that the pair of scalars $S_3 - R_2$ contribute to neutrino masses at one-loop while $S_3 - \tilde{R}_2$ contribute to $0\nu\beta\beta$. Therefore, to relate these two effects and to maximise the $0\nu\beta\beta$ we fix the leptoquark masses as follows: $M_{S_3} \sim M_{R_2} \sim 2.0\,\text{TeV}$ to satisfy the LHC constraints [231–240][4], while the leptoquark $M_{\tilde{R}_2}$ can induce large contributions to $\mu \to e$ conversion which is shown in the left panel in Fig. 5.6. In the right panel of Fig. 5.6, we have shown the variation of the branching ratio of $\mu \to e$ conversion as a function of the mass of $\tilde{R}_2$. It is found that for $m_{\tilde{R}_2} \sim 10^3$ TeV, we can evade the constraint from $\mu \to e$ conversion. The other scalar masses are varied within one order of magnitude from the GUT scale. Few of the scalars also induce proton decay, and setting their masses close to

[4]Thecurrent LHC constraint on scalar leptoquark masses is 1.58 (1.59) TeV considering its decay to a top quark and electron (muon) with 100% branching ratio with 95% confidence limit (C.L) [240].To safely evade LHC bounds, the leptoquark masses are fixed at approximately 2 TeV. Additionally, since the neutrino mass loop function in Eq. (5.28) diverges for $M_{R_2} = M_{S_3}$, a small mass splitting is introduced to avoid this issue.

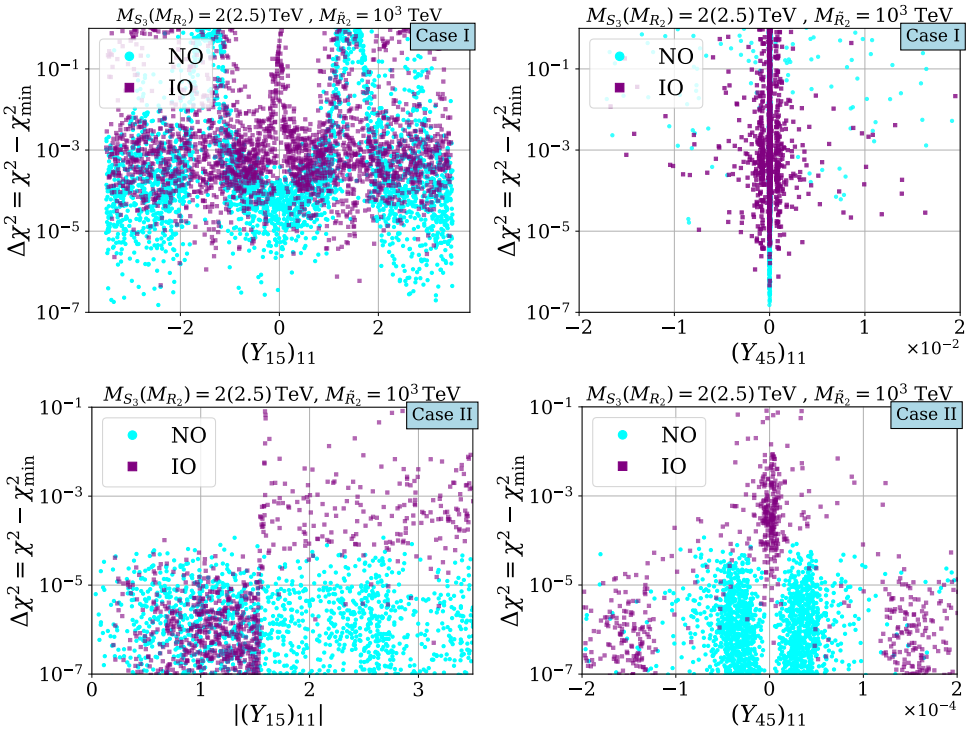

Figure 5.7: The left panel plots show the variation of $\Delta\chi^2$ with $(Y_{15})_{11}$ and $\left|(Y_{15})_{11}\right|$ in the range of $(-3.5, 3.5)$ for the cases I (Y_{15} is real) and II (Y_{15} is complex). The cyan coloured points represent the normal ordering while the purple points represent the inverted ordering. Plots in the second column in both the cases show the distribution of $(Y_{45})_{11}$ for a viable fit.

$M_{\rm GUT}$ automatically satisfies the proton decay constraints. Additionally, the mass of extra scalars Σ and $\mathbb{S}$ are allowed to vary between 1 TeV and the GUT scale, which is necessary for a split between the charged lepton and down quark sector. These particular choices reduce the number of free parameters contributing to the different observables and maximise the $0\nu\beta\beta$ contribution.

Having fixed the masses of scalar leptoquarks contributing to $0\nu\beta\beta$, the allowed range of Yukawa couplings contributing $0\nu\beta\beta$ need to be explored. As the aim is to maximise the leptoquark contribution to $0\nu\beta\beta$ together with the viable fermion mass fit, the Yukawa coupling $(Y_{15})_{11}$ for the cases I and II are varied in steps between $(-3.5, 3.5)$ under the aforementioned constraints. With this choice, the algorithm is configured to fit the theoretical observables. The variation of $\Delta\chi^2 \equiv \chi^2 - \chi^2_{\rm min}$ as a function of $(Y_{15})_{11}$ and $\left|(Y_{15})_{11}\right|$ is shown in Fig. 5.7. The adjacent plot shows the range of predicted/preferred

Table 5.3: The best-fit values of the predicted theoretical observables corresponding to BP1 and BP2 points and the minimum χ^2 is also given. The definition of χ^2 includes charged and neutral fermion sector observables. The extrapolated values of the experimental observables at the scale of $\mu = 10^{16}$ GeV are provided along with the values reproduced through χ^2 minimisation. The fitted value of mass of the various scalars and cubic coupling η are also given, where the masses of R_2 and S_3 is fixed close to 2 TeV and $\tilde{R}_2$ is 10^6 GeV.

Observable	$O_{\rm exp}$	**BP-I** $O_{\rm th}$	**BP-II** $O_{\rm th}$
$y_u/10^{-6}$	4.087	4.086	4.083
$y_c/10^{-3}$	2.060	2.060	2.061
y_t	0.6580	0.6845	0.6826
$y_d/10^{-6}$	8.777	8.776	8.789
$y_s/10^{-4}$	1.792	1.791	1.800
$y_b/10^{-3}$	9.992	9.9921	9.513
$y_e/10^{-6}$	3.921	3.921	3.9179
$y_\mu/10^{-4}$	8.172	8.174	8.0957
$y_\tau/10^{-3}$	13.82	13.78	14.535
$\lvert V_{us}\rvert$	0.2286	0.2286	0.2289
$\lvert V_{cb}\rvert$	0.03794	0.03791	0.03798
$\lvert V_{ub}\rvert$	0.003518	0.003518	0.003516
$\sin\delta_{\rm CKM}$	0.78	0.78	0.78
$\Delta m^2_{\rm sol}$ [eV^2]$/10^{-5}$	7.49	7.49	7.49
$\Delta m^2_{\rm atm}$ [eV^2]$/10^{-3}$	2.534	2.532	2.532
$\sin^2\theta_{12}$	0.307	0.307	0.2940
$\sin^2\theta_{23}$	0.561	0.5602	0.5685
$\sin^2\theta_{13}$	0.02195	0.02194	0.0229
$\chi^2_{\rm min}$		10^{-3}	0.7
M_{S_1} [GeV]		5.45405×10^{15}	4.39036×10^{16}
$M_{S_1'}$ [GeV]		8.55261×10^{15}	9.30636×10^{16}
$M_{\tilde{S}}$ [GeV]		1.75281×10^{15}	2.28598×10^{15}
$M_{\mathbb{S}}$ [GeV]		2.64956×10^{13}	10^3
M_O [GeV]		5.98515×10^{15}	10^{15}
M_Σ [GeV]		6.62310×10^{10}	3.12650×10^{10}
M_Δ [GeV]		2.70915×10^{16}	2.69230×10^{16}
η [GeV]		9.54343×10^{16}	9.68322×10^{16}
M_{R_2} [GeV]		2500	2500
M_{S_3} [GeV]		2004	2004
$M_{\tilde{R}_2}$ [GeV]		10^6	10^6

value of $(Y_{45})_{11}$. The cyan colour (purple colour) dots in Fig. 5.7 represent normal (inverted) ordering for the neutrino spectrum.

It is clear from Fig. 5.7 that the entire fermion mass spectra and mixing angles can be fitted considering the above mentioned choices. As evident from

the plot, the first element of the Yukawa matrix $\left(Y_{15}\right)_{11}$ can take any value between $(-3.5, 3.5)$ for the case I and the same is also true for its magnitude in case-II, yielding a desirable numerical fit. The preferred value of the first element satisfies $\left|\left(Y_{45}\right)_{11}\right| \lesssim 2 \times 10^{-2}$ in case-I and $\lesssim 2 \times 10^{-4}$ in case-II, for both normal and inverted orderings.

To illustrate the numerical estimates in the subsequent sections, we have provided two benchmark points (BP1 and BP2) from the solution space. The Yukawa couplings for the benchmark points are given as follows[5]:

BP1:

$$
\begin{aligned}
Y_5 &= \begin{pmatrix} (8.09002 + i\ 3.26336) \times 10^{-5} & (-1.9705 + i\ 0.667620) \times 10^{-4} & (-3.80612 - i\ 1.91173) \times 10^{-3} \\ (-1.9705 + i\ 0.667620) \times 10^{-4} & (3.05963 + i\ -0.02150) \times 10^{-3} & (-2.83391 - i\ 0.84882) \times 10^{-2} \\ (-3.80612 - i\ 1.91173) \times 10^{-3} & (-2.83391 - i\ 0.84882) \times 10^{-2} & (7.22552 + i\ 1.89986) \times 10^{-1} \end{pmatrix}, \\
Y_{45} &= \begin{pmatrix} 1.64251 \times 10^{-2} & 0 & 0 \\ 0 & -9.38426 \times 10^{-5} & 0 \\ 0 & 0 & -3.78806 \times 10^{-1} \end{pmatrix}, \text{and} \\
Y_{15} &= \begin{pmatrix} -1.41343 & 0.00564 & 0.46266 \\ 0.00564 & 3.49915 & -0.00987 \\ 0.46266 & -0.00987 & 1.30712 \end{pmatrix}, \qquad (5.38)
\end{aligned}
$$

BP2:

$$
\begin{aligned}
Y_5 &= \begin{pmatrix} (-0.160022 + i\ 1.78568) \times 10^{-4} & (2.37783 - i\ 2.28594) \times 10^{-4} & (1.07006 - i\ 6.42993) \times 10^{-3} \\ (2.37783 - i\ 2.28594) \times 10^{-4} & (-1.7098 + i\ 1.34955) \times 10^{-3} & (-1.35222 - i\ 2.13648) \times 10^{-2} \\ (1.07006 - i\ 6.42993) \times 10^{-3} & (-1.35222 - i\ 2.13648) \times 10^{-2} & (0.28407 + i\ 7.72693) \times 10^{-1} \end{pmatrix}, \\
Y_{45} &= \begin{pmatrix} -1.34103 \times 10^{-2} & 0 & 0 \\ 0 & 1.08804 \times 10^{-4} & 0 \\ 0 & 0 & 3.87003 \times 10^{-1} \end{pmatrix}, \text{and} \\
Y_{15} &= \begin{pmatrix} -1.39680 & 0.001433 & -0.51452 \\ 0.001433 & 3.42342 & 0.00113 \\ -0.51452 & 0.00113 & 1.29648 \end{pmatrix}. \qquad (5.39)
\end{aligned}
$$

The fitted value of different observables corresponding to the above Yukawa

[5]The Yukawa entries have been specified with very high precision. Any deviation in these Yukawa values or masses given in Tab. 5.3 would significantly alter the χ^2.

matrices are relegated to Tab. 5.3. The obtained value of the optimised χ^2 for the given benchmark points are 10^{-3} and 0.7 respectively, indicating that the considered $SU(5)$ model appropriately reproduces the observed charged and neutral fermion mass spectra. In addition to the fitted Yukawa coupling, the absolute values of obtained neutrino masses and $m_{ee}^{\rm std}$ are also provided in the following ;

$$\begin{aligned}
\text{BP1: Diag}(M_\nu) &= \begin{pmatrix} 0.0021666 & 0 & 0 \\ 0 & 0.0023311 & 0 \\ 0 & 0 & 0.0547934 \end{pmatrix} \text{eV}\,, \quad m_{ee}^{\rm std} = 0.0229\,\text{eV}, \\
\text{BP2: Diag}\,(M_\nu) &= \begin{pmatrix} 0.0022384 & 0 & 0 \\ 0 & 0.002400 & 0 \\ 0 & 0 & 0.0547934 \end{pmatrix} \text{eV}\,, \quad m_{ee}^{\rm std} = 0.0236\,\text{eV}.
\end{aligned} \tag{5.40}$$

5.3.5 Model Predictions for $0\nu\beta\beta$

Now we compute the model predictions for $0\nu\beta\beta$. Any solution with acceptable χ^2 must respect the current experimental upper bound on $m_{ee}^{\rm eff}$. We use the result from *KamLAND-Zen* experiment using ^{136}Xe which is quoted as $m_{ee}^{\rm eff} < (0.018 - 0.024)$ eV [116], where the range is due to NME uncertainties. Note that the experimental limits for $m_{ee}^{\rm eff}$ were obtained using νDoBE [222], which includes short-range effects. This makes these constraints slightly different from direct experimental quoted results.

Fig. 5.8 shows the variation of $m_{ee}^{\rm eff}$ as a function of the lightest neutrino mass for Case-I (left panel) and Case-II (right panel). The cyan (purple) points are the solutions reproducing the correct fermion mass spectra for NO (IO). The gray (pink) shaded regions denote the standard NO (IO) region, whereas the black and orange bands show the current *KamLAND-Zen* limit [116] and future *LEGEND-1000* sensitivity [120] calculated using νDoBE [222]. The vertical dashed lines (from right to left) indicate the direct limit on the absolute neutrino mass $m_\nu < 0.45$ eV (at 90% CL) from KATRIN [355], and the indirect

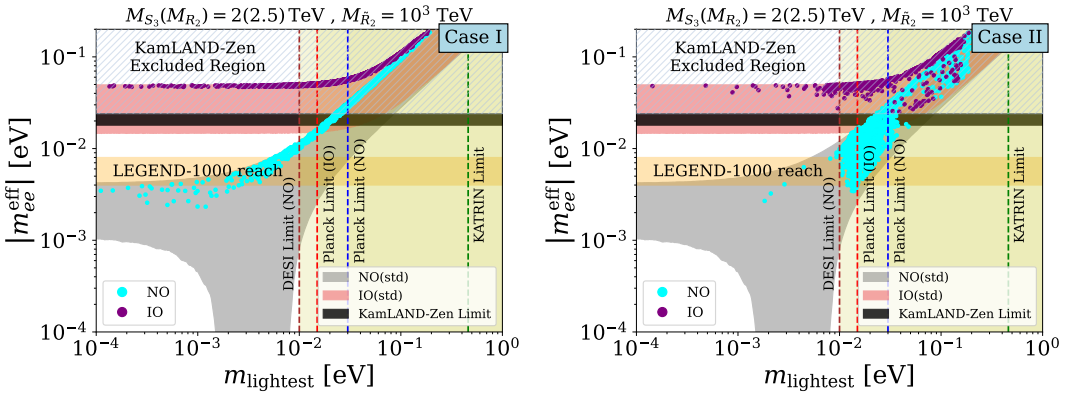

Figure 5.8: Variation of $m_{ee}^{\rm eff}$ as a function of lightest neutrino mass obtained from the fitted solutions. The grey and pink regions show the allowed ranges for NO and IO in the standard $0\nu\beta\beta$ mechanism. The teal and orange bands show the current *KamLAND-Zen* limit and future *LEGEND-1000* sensitivity, respectively.

limits derived from the sum of neutrino mass constraint of $\sum_i m_i < 0.12$ eV from Planck [31] and $\sum m_\nu < 0.064$ eV from DESI [338]. Note that the DESI limit disfavours the IO; therefore, there is no DESI line corresponding to the IO case. From Fig. 5.8, it is evident that the values of $m_{ee}^{\rm eff}$ obtained here are all within the allowed range of standard m_{ee} values, implying that the non-standard scalar contributions are small. This can also be seen from Eq. (5.35):

$$m_{ee}^{\rm nstd} \simeq 2\, m_N \times \frac{\rho\, \eta\, v^5}{M_\Delta^2} \frac{\left(Y_{\tilde{R}_2}\right)_{11}}{M_{\tilde{R}_2}^2} \frac{\left(Y_{S_3}\right)_{11}}{M_{S_3}^2} \lesssim 3.5 \times 10^{-17}\ \text{eV} \tag{5.41}$$

In the above equation, the considered values for the scalar masses and the trilinear scalar coupling contributing to $0\nu\beta\beta$ are obtained from the χ^2 analysis, which are $\eta \sim 10^{16}$ GeV, $M_\Delta \sim 10^{16}$ GeV, and $M_{S_3} = 2 \times 10^3$ GeV, $M_{R_2} = 2.5 \times 10^3$ GeV and $M_{\tilde{R}_2} = 10^6$ GeV. The Yukawa couplings are taken as $\left(Y_{\tilde{R}_2}\right)_{11} \approx (Y_{15})_{11} = 3.5$ and $\left(Y_{S_3}\right)_{11} \approx (Y_{45})_{11} = 2 \times 10^{-2}$ which are the maximum allowed Yukawa couplings, required for the fermion mass fitting, as evident from Fig. 5.7. Additionally, in Eq. (5.41), a factor of two is multiplied for the two contributions yielding the same LEFT operator, as shown in Fig. 5.5. With these assumptions, the value of maximum possible $m_{ee}^{\rm nstd}$ is negligible compared to the standard contribution, $m_{ee}^{\rm std} \sim 10^{-2}$ eV. The suppression of $m_{ee}^{\rm nstd}$ is due to the high mass scale of the triplet scalar (M_Δ), which is required to generate the observed small neutrino masses [cf. Eq. (5.28)]. Con-

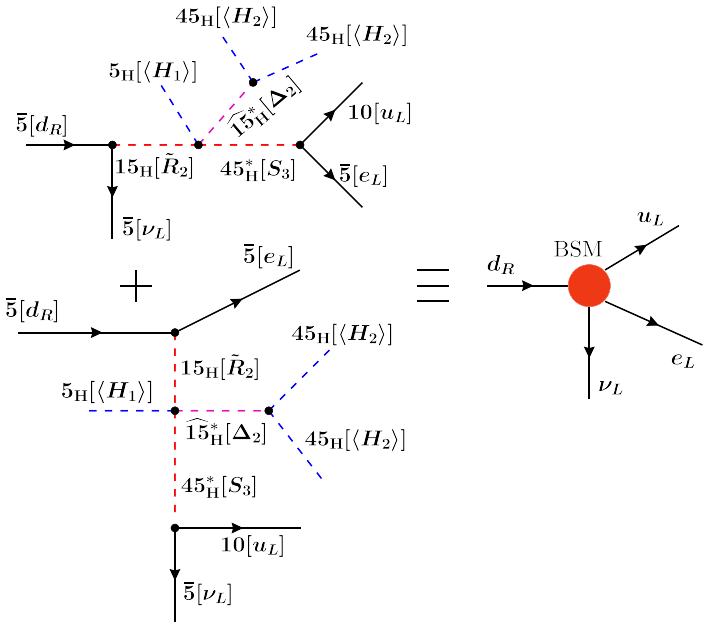

Figure 5.9: Effective operator diagrams that contribute to $0\nu\beta\beta$ in the $SU(5) \times \mathcal{Z}_3$ model in the presence of $\widehat{\mathbf{15}}_H$. The diagram in the left panel shows the scalar-induced $0\nu\beta\beta$ in the considered scenario, where the irreps outside the parenthesis depict the parent multiplets. The right panel shows the equivalent LEFT operator.

sequently, within the considered settings of the $SU(5)$ framework, the effective Majorana mass is dominated by the standard light-neutrino exchange contribution, yielding $m_{ee}^{\text{eff}} \approx m_{ee}^{\text{std.}}$. It is also clear from Fig. 5.8 that in both cases, for the considered choice of parameters, IO is ruled out as the prediction for m_{ee}^{eff} is larger than the *KamLAND-Zen* limit.

In the left panel of Fig. 5.8, since Y_{15} is real (Case-I), the Majorana phases are zero, and m_{ee}^{eff} values stay close to the upper limit of the standard contribution for NO. On the other hand, in the right panel, the Majorana phases are non-zero due to complex Y_{15}. However, it is evident from the right panel that the fermion mass fits prefer the higher values of m_1 (through higher values of Y_{15}) and the cancellation regime of the standard m_{ee}^{eff} is not reached.

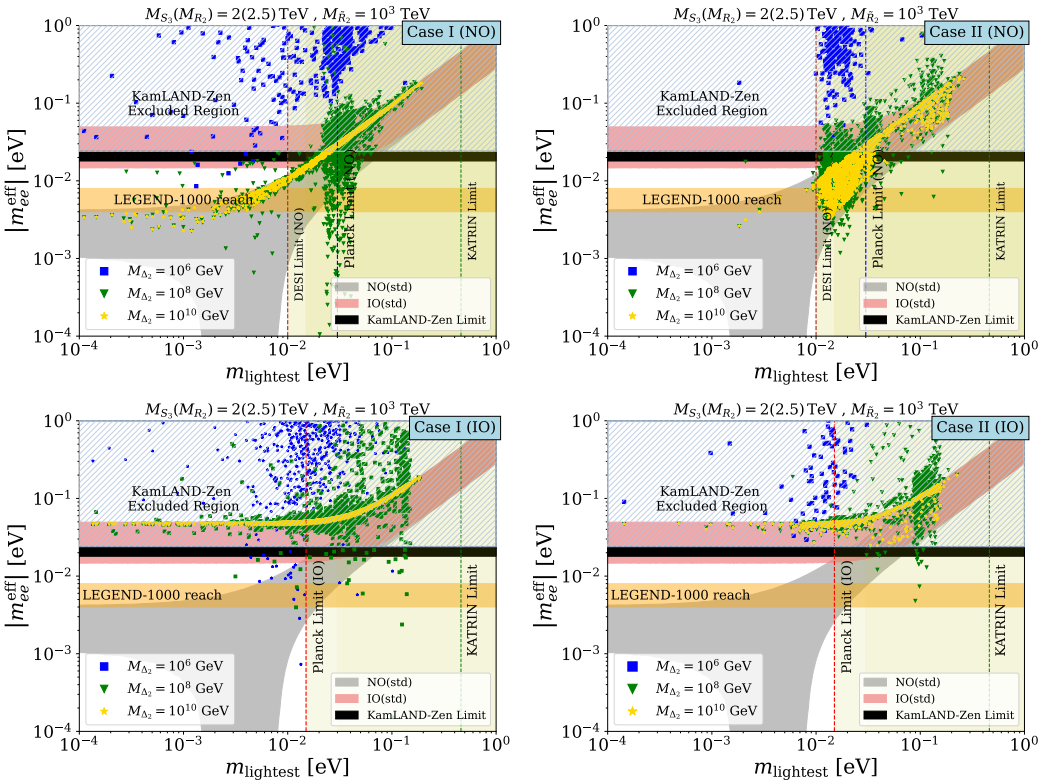

Figure 5.10: Same as in Fig. 5.8 but with an additional scalar contribution from Δ_2 arising from an extra $\mathbf{15}_{\rm H}$. The results are shown for different benchmark values of M_{Δ_2}. For clarity of presentation, we have separated the NO and IO results for Cases-I and II.

5.4 Enhancing the $0\nu\beta\beta$ contribution

As concluded in the previous section, the $0\nu\beta\beta$ contribution arising from leptoquarks in the considered $SU(5)$ framework is suppressed due to the high mass scale of Δ, which is required to accommodate the observed smallness of neutrino masses. In this section, we consider an alternative scenario by extending the scalar sector with a new $\mathbf{15}_{\rm H}$ irrep, where the scalar-induced contributions to the $0\nu\beta\beta$ can be enhanced. This additional $\mathbf{15}_{\rm H}$ is denoted as $\widehat{\mathbf{15}}_{\rm H}$ in Tab. 5.2. In terms of the scalar content, $\widehat{\mathbf{15}}_{\rm H}$ resembles with the $\mathbf{15}_{\rm H}$ irrep shown in Tab. 5.1 and the new scalar stemming from this extra $\mathbf{15}_{\rm H}$ which contributes to $0\nu\beta\beta$ is denoted as $\Delta_2\,(1,3,1)$. Here, $\widehat{\mathbf{15}}_{\rm H}$ irrep is assigned a $\mathcal{Z}_3 = 1$ charge that forbids its coupling to the $SU(5)$ fermionic multiplets i.e. $\bar{\mathbf{5}}$ and $\mathbf{10}$. As a result, the scalars in $\widehat{\mathbf{15}}_{\rm H}$ do not contribute to the fermion mass fitting discussed earlier. Since it does not contribute to neutrino masses,

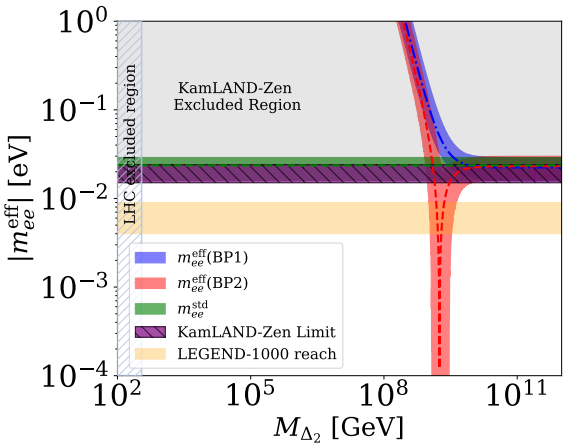

Figure 5.11: Variation of $m_{ee}^{\rm eff}$ for BP1 (blue band) and BP2 (red band) as function of M_{Δ_2}. Green band shows the standard contributions for the two BPs are calculated as 0.0229 eV and 0.0236 eV. The purple-shaded region corresponds to the current *KamLAND-Zen* limit, while the orange band shows the *LEGEND-1000* sensitivity. The vertical hatched region is disfavored by LHC data.

the triplet scalar (Δ_2) residing in $\widehat{\mathbf{15}}_{\rm H}$ can be as light as possible, enabling it to generate substantial contributions to the $0\nu\beta\beta$ amplitude. The corresponding diagrams are shown in Fig. 5.9. The current non-observation of $0\nu\beta\beta$ can therefore be utilised to establish a lower bound on the mass of this triplet scalar. The role of Δ_2 in enhancing the $0\nu\beta\beta$ rate is illustrated in Fig. 5.10, by considering different values of $M_{\Delta_2} \supset \{10^6, 10^8, 10^{10}\}$ GeV. The value of $m_{ee}^{\rm std}$ as a function of the lightest neutrino mass is obtained from the solution set shown in Fig. 5.8, whereas the non-standard $0\nu\beta\beta$ contribution for M_{Δ_2} is given below in Eq. (5.42). It is found that for $M_{\Delta_2} \sim 10^8$ GeV the interplay between the standard and non-standard contributions can lead to the cancellation among these contributions depending upon the sign of the first matrix elements of $Y_{15,45}$, which will be discussed subsequently by choosing two suitable benchmark values (BP1, BP2) from Case-I (given in Eqs. (5.38) and (5.39)). The destructive interference between the standard and non-standard contributions reduces the effective Majorana mass to levels compatible with current experimental bounds, thereby allowing the IO scenario in Case-I, as can be seen from the lower left panel of Fig. 5.10.

The expression relating $T_{1/2}^{0\nu}$ and $m_{ee}^{\rm eff}$ is given in Eq. (5.34). The standard and non-standard contributions can interfere either constructively or destruc-

tively depending on the sign of ϵ_{S+P}^{S+P}. For BP1, as $(Y_{15})_{11} \times (Y_{45})_{11} < 0$, it implies $\epsilon_{S+P}^{S+P} < 0$ [cf. Eq. (5.31)] and $\mathcal{M}_\nu'^{(6)}/\mathcal{M}_\nu^{(3)} < 0$. Consequently, the non-standard term in Eq. (5.35) is positive and it constructively interferes with $m_{ee}^{\rm std}$. On the other hand, the converse happens for the BP2, where the non-standard term is negative and it destructively interferes with $m_{ee}^{\rm std}$. This constructive or destructive interference effect between the standard and non-standard contributions is shown in Fig. 5.11 as a function of M_{Δ_2}, where the cancellation is evident for BP2 (red points). The figure also shows that for BP1, M_{Δ_2} values below 4.7×10^9 GeV are ruled out by *KamLAND-Zen* whereas for BP2, this bound gets relaxed to 1.2×10^9 GeV due to the cancellation effect. Both Figs. 5.10 and 5.11 indicate that the non-standard contribution becomes subdominant for $M_{\Delta_2} \gtrsim 10^{10}$ GeV. It implies that $0\nu\beta\beta$ can provide more stringent limits on M_{Δ_2} well beyond the reach of colliders. For comparison, the current LHC bound on M_{Δ_2} is around 350 GeV from the diboson decay channel [356], as shown by the vertical hatched region in Fig. 5.11. Note that since Δ_2 does not couple to SM fermions, the more stringent limits on triplet scalars from (di)leptonic decay modes do not apply in our case.

We can derive a lower bound on M_{Δ_2} from $0\nu\beta\beta$ using the expression

$$m_{ee}^{\rm nstd} \;\simeq\; 2\, m_N \times \frac{\rho\,\eta\, v^5}{M_{\Delta_2}^2} \frac{\left(\sqrt{2}\, Y_{15}\right)_{11}}{M_{\tilde{R}_2}^2} \frac{\left(\sqrt{2}\, Y_{45}\right)_{11}}{M_{S_3}^2}\,. \tag{5.42}$$

By applying the current *KamLAND-Zen* upper limit of $m_{ee} < 0.02$ eV, a conservative upper bound on M_{Δ_2} can be derived as:

$$M_{\Delta_2} \;\gtrsim\; 10^{10}\text{GeV} \left[\frac{m_N}{1\,\text{GeV}} \frac{10^{-2}\,\text{eV}}{m_{ee}} \frac{\rho}{\mathcal{O}(1)} \frac{\eta}{10^{16}\,\text{GeV}} \frac{(Y_{15})_{11}}{\mathcal{O}(1)} \frac{(Y_{45})_{11}}{10^{-2}} \right.$$
$$\left. \left(\frac{v}{10^2\,\text{GeV}}\right)^5 \left(\frac{10^6\,\text{GeV}}{M_{\tilde{R}_2}}\right)^2 \left(\frac{2\times 10^3\,\text{GeV}}{M_{S_3}}\right)^2 \right]^{-1/2} \tag{5.43}$$

The bound mentioned in Eq. (5.43) is subjected to the minimum masses of the leptoquarks and maximum values of the Yukawa couplings yielding a viable fermion mass spectrum and evading the cLFVs. For larger leptoquark mass and smaller Yukawa couplings, the bound on M_{Δ_2} can be relaxed down to the

LHC exclusion limit. The point is that the $0\nu\beta\beta$ bound on M_{Δ_2} can be much stronger than the collider bounds, depending on the leptoquark masses and Yukawa couplings.

5.5 Summary

Processes violating the Baryon and Lepton number are significant yardstick to constrain/detect the unobserved (potentially new) physics. Grand unified models provide a viable setup in which such violations can be studied. This work investigated a particular optimal and realistic $SU(5)$ scenario where the scalar contributions to neutrinoless double beta decay are analysed. Unified models are known to strongly constrain Yukawa parameters by unifying quarks and leptons in the same multiplet. This study intended to analyse the contribution to $0\nu\beta\beta$, arising from leptoquarks embedded in a UV complete scenario. It is found that some set of scalars can induce proton decay as well as $0\nu\beta\beta$. As those leptoquarks have to comply with proton decay bounds, the effect of scalars inducing the $0\nu\beta\beta$ is suppressed.

To avoid this, a discrete symmetry $(\mathcal{Z}_3)$ has been imposed to restrict the diquark coupling of specific scalar (S_3). Imposing the discrete symmetry makes the Yukawa unrealistic at the tree level. However, as shown in this work, switching on radiative corrections can make the scenario from the heavy degrees of freedom made the scenario realistic and predictive. The considered model reproduces the observed fermion mass spectra (within the assumed uncertainty). In order to yield the observed tiny neutrino masses, the desired value of the mass of scalar field Δ is close to the GUT scale. Such high value of mass of Δ suppresses the $0\nu\beta\beta$ amplitude. Consequently, the scalar-mediated $0\nu\beta\beta$ amplitude becomes nineteen orders of magnitude weaker than the standard light-neutrino exchange mechanism.

A significant enhancement in the $0\nu\beta\beta$ rate can be achieved by introducing

an additional scalar irrep ($\widehat{\mathbf{15}}_{\mathrm{H}}$) consisting of Δ_2, with $\mathcal{Z}_3 = 1$. This charge assignment disable it from having fermion interactions at the GUT scale. This ensures that Δ_2 does not contribute to neutrino masses (or any other fermion mass), allowing its mass to remain independent from seesaw constraints. By optimising Yukawa couplings and minimising leptoquark masses within experimental limits, conservative constraints on M_{Δ_2} is derived, $M_{\Delta_2} \geq 10^{10}$ GeV. This scenario demonstrates that while minimal $SU(5)$ frameworks face severe phenomenological constraints, extended symmetry structures with carefully chosen scalar sectors can enhance $0\nu\beta\beta$ process without conflicting with the stability of the proton and satisfying the neutrino mass bounds.

This page is intentionally left blank.

6

Monopole-dipole potential and tests of gravity

6.1 Overview

Axions were first proposed to solve the strong CP problem in the SM [52–55, 58, 357], but the concept has evolved over the time, leading to a more generalised notion of axion-like-particles (ALPs), arsing from either string compactifications or spontaneous breaking of a global $U(1)$ symmetry [358]. Unlike the QCD axions, the mass of ALPs and the symmetry breaking scale is independent of each other. The mass spectrum of the ALPs spans a wide range of scale, from 10^{-22} eV to TeV scale. This broad range highlights the versatility of ALPs in addressing various BSM phenomena. Typically these ultralight bosons couple very weakly with the SM particles and hence, it is extremely challenging to search for these particles in direct detection experiments. Several laboratory, astrophysical, and cosmological constraints on the mass and decay constant (related to the $U(1)$ symmetry breaking scale) of QCD axions and ALPs are discussed in [357, 359–381].

Ultralight ALPs can also be a promising candidate for Dark Matter (DM) [382–384]. For instance, ALPs with mass 10^{-22} eV have a de Broglie wavelength comparable to the order of a dwarf galaxy $(1-2$ kpc$)$ [385, 386]. Therefore, these ultralight DM particles behave as waves and such wave nature of the DM can solve the longstanding core-cusp problem [387–389], evading

the direct detection constraints [390–392]. These ultralight ALPs can also mediate a long range macroscopic force between two objects if the mass of the ALP is smaller than the inverse distance between the two bodies [393]. Therefore, there is significant phenomenological importance in the search for these particles and in obtaining constraints on ALP parameters.

In this chapter, we mainly focus on constraining the monopole-dipole interaction strength from astrophysical observation since, there is no single astrophysical phenomenon that can directly constrain the monopole-dipole interaction, so far. The most stringent bound on monopole-dipole interaction is claimed by combining the best experimental bound on scalar interaction multiplied by the best astrophysical bound from stellar energy loss on the pseudoscalar interaction. It is also highlighted by the authors of Ref. [394] that in several scenarios these hybrid bounds could be overly stringent leading to a premature abandoning of the ALPs as an attractive theoretical prospect. There is lack of a complete astrophysical probe of monopole-dipole potential as most of the astrophysical objects are considered to be unpolarised. Even if a polarised astrophysical object is considered, its degree of polarisation is not known precisely.

We consider the Earth as a polarised source and there are about 10^{39} number of polarised electrons in Earth due to the presence of Earth's geomagnetic field [395]. Here, the Earth is treated as a polarised source and the Sun is treated as an unpolarised object. The ALP has a pseudoscalar coupling with the electrons in the Earth and scalar coupling with the nucleons in the Sun. This can give rise to an ALP mediated monopole-dipole potential for the Earth-Sun system. This ALP mediated monopole-dipole potential can affect the geodesic of light and the Earth. We obtain constraints on monopole-dipole interaction strength in this pure astrophysical scenario from perihelion precession of Earth, gravitational light bending and Shapiro time delay. The bounds on the monopole-dipole coupling obtained from these gravity tests are strictly valid for the range of the force greater than the Earth-Sun distance which corresponds to the mass of the ALP $(m_a) \lesssim 10^{-18}$ eV.

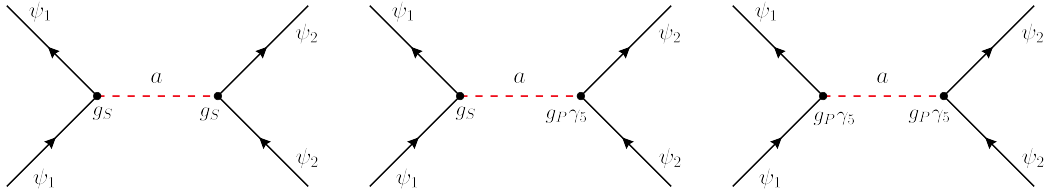

Figure 6.1: Feynman diagrams of different types of interactions between fermions and ALP.

The organisation of this chapter is as follows: The next section presents detailed derivations of the monopole–monopole, monopole–dipole, and dipole–dipole interactions and reviews the current experimental limits on the monopole–dipole potential. In Section 6.3, we discuss how the Earth can be treated as a polarised source. Section 6.4 focuses on the impact of the monopole–dipole potential on key gravitational phenomena which include: the perihelion precession of Earth, gravitational light bending, and the Shapiro time delay. We have derived bounds on the monopole–dipole coupling strength based on individual astrophysical observations mentioned above and showed the results in section 6.5. Section 6.6 extends this analysis by obtaining combined constraints on the monopole–dipole interaction strength using two independent astrophysical measurements. Finally, Section 6.7 provides a summary and discussion of our findings.

6.2 Long range interactions of ALPs

The mediation of ALP between two fermion currents can give rise to long range macroscopic forces. ALP can interact with fermions through either a spin-dependent pseudoscalar coupling $(\overline{\psi}\gamma_5\psi a)$ or a spin-independent scalar coupling $(\overline{\psi}\psi a)$, where ψ represents the fermion field and a denotes the ALP field. The most general interaction Lagrangian can be written as,

$$-\mathcal{L} \;=\; g_S\,\overline{\psi}\psi a + i\,g_P\,\overline{\psi}\gamma_5\psi a + \text{h.c.}, \tag{6.1}$$

In general, there are three different ways in which the fermions interact among each other via the mediation of ALPs, as illustrated in Fig. 6.1. The left panel

shows the possibility where the ALP (a) couples as scalar at both the interaction vertices. The right panel depicts the scenario where the ALP couples as pseudo-scalar at both vertices. The middle panel represents the mixed case, where the ALP couples as a scalar at one vertex and as a pseudoscalar at the other. Each of these interaction structures leads to different physical potentials, with varying parity and spin dependence.

The amplitude of the left panel diagram becomes,

$$\begin{aligned} i\mathcal{M} &= \overline{u}_{s_1'}(p_1')(-ig_S)u_{s_1}(p_1)\frac{i}{q^2-m_a^2}\overline{u}_{s_2'}(p_2')(-ig_S)u_{s_2}(p_2) \\ &= -i\frac{g_S^2}{q^2-m_a^2}\left[\overline{u}_{s_1'}(p_1')u_{s_1}(p_1)\right]\left[\overline{u}_{s_2'}(p_2')u_{s_2}(p_2)\right], \end{aligned} \tag{6.2}$$

where $q = p_1 - p_1' = p_2' - p_2$. In the Non Relativistic (NR) limit, all three momentum components are much smaller than the mass of the particle (m) and hence, the energy of the particle is $E \approx m$. The normalisation condition is chosen as

$$u_{s'}^{\dagger}(p)u_s(p) = \delta_{ss'}, \tag{6.3}$$

and the positive energy spinor in the NR limit is written as [396],

$$u_s(p) = \left(1 - \frac{\gamma_i p_i}{2m}\right)\chi_s + \mathcal{O}(p^2), \tag{6.4}$$

where χ_s is a normalised eigenvector satisfying $\chi_s^{\dagger}\gamma^0 = \chi_s^{\dagger}$ and $\gamma_0\chi_s = \chi_s$. Here, γ_i denotes the Dirac gamma matrices and i runs from 1 to 3. Hence, in the NR limit, we can calculate the following bilinear terms using Eq. (6.4) as,

$$\overline{u}_{s_2'}(p_2')u_{s_2}(p_2) = 1, \quad \overline{u}_{s_1'}(p_1')\gamma_5 u_{s_1}(p_1) = \frac{1}{2m_\psi}\chi_{s_1'}^{\dagger}\,\boldsymbol{\sigma}.\mathbf{q}\,\chi_{s_1}, \tag{6.5}$$

where $\boldsymbol{\sigma}$ denotes the Pauli spin vector and m_ψ denotes the mass of the particle to which the ALP couples as a pseudoscalar. In this approximation, Eq. (6.2) can be written as,

$$\mathcal{M} = \frac{g_S^2}{|\mathbf{q}|^2 + m_a^2}\left[\overline{u}_{s_1'}(p_1')\,u_{s_1}(p_1)\right]\left[\overline{u}_{s_2'}(p_2')u_{s_2}(p_2)\right], \tag{6.6}$$

where we can write $q^2 = q^{0^2} - |\mathbf{q}|^2$, and $|q^0| \ll |\mathbf{q}|$ in the NR limit. Using, Eq. (6.5) we can write the monopole-monopole potential as,

$$\begin{aligned} V_{\text{m-m}}(r) &= -\int \frac{d^3q}{(2\pi)^3} e^{i\mathbf{q}.\mathbf{r}} \left(\frac{g_S^2}{|\mathbf{q}|^2 + m_a^2} \right) \\ &= -\frac{e^{-m_a r}}{4\pi r}. \end{aligned} \tag{6.7}$$

Similarly, the diagram in the middle panel of Fig. 6.1 shows that the ALP couples as scalar in one vertex and as a pseudoscalar in the other vertex. The amplitude of the diagram is written as,

$$i\mathcal{M} = \frac{g_P g_S}{q^2 - m_a^2} \overline{u}_{s_1'}(p_1') \gamma_5 u_{s_1}(p_1) \overline{u}_{s_2'}(p_2') u_{s_2}(p_2), \tag{6.8}$$

Following the similar procedure as above and using Eq. (6.5), we can write the monopole dipole potential as,

$$V_{\text{m-d}}(r) = -\int \frac{d^3q}{(2\pi)^3} e^{i\mathbf{q}.\mathbf{r}} \left(\frac{i g_P g_S}{|\mathbf{q}|^2 + m_a^2} \right) \frac{\mathbf{s}.\mathbf{q}}{m_{\psi_2}}, \tag{6.9}$$

where $\mathbf{s} = \frac{\boldsymbol{\sigma}}{2}$ is the spin vector and m_{ψ_2} is the mass of ψ_2 to which the ALP couples as a pseudo-scalar. Therefore, the potential becomes

$$\begin{aligned} V_{\text{m-d}}(r) &= -\frac{g_P g_S}{m_{\psi_2}} (\mathbf{s}.\boldsymbol{\nabla}) \int \frac{d^3q}{(2\pi)^3} \frac{1}{|\mathbf{q}|^2 + m_a^2} e^{i\mathbf{q}.\mathbf{r}} \\ &= -\frac{g_P g_S}{m_{\psi_2}} (\mathbf{s}.\boldsymbol{\nabla}) \frac{1}{4\pi r} e^{-m_a r} \\ &= \frac{g_P g_S}{4\pi m_{\psi_2}} (\mathbf{s}.\hat{\boldsymbol{r}}) \left(\frac{m_a}{r} + \frac{1}{r^2} \right) e^{-m_a r}. \end{aligned} \tag{6.10}$$

This is the expression for monopole-dipole potential which can act between polarised and an unpolarised objects.

The dipole-dipole force which acts between two polarised objects by the mediation of ALP is given as,

$$V_{\text{d-d}}(r) = \frac{g_P^2}{m_{\psi_1} m_{\psi_2}} (\mathbf{s_1}.\boldsymbol{\nabla}) (\mathbf{s_2}.\boldsymbol{\nabla}) \left(\frac{e^{-m_a r}}{4\pi r} \right), \tag{6.11}$$

The monopole-monopole, and dipole-dipole forces are parity (P) and time

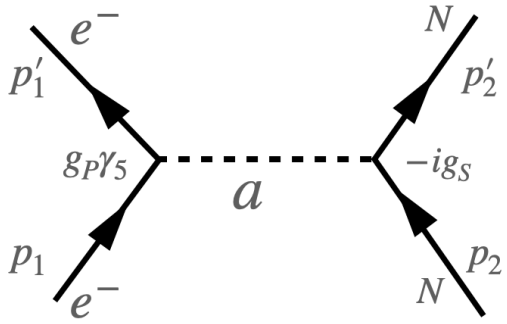

Figure 6.2: Feynman diagram of e^-N scattering mediated by a pseudoscalar ALP. Here, the electrons are spin polarised and the nucleons are unpolarised.

reversal (T) conserving. However, the search for monopole-dipole force is interesting as it can violate P and T.

In the following discussion, we assume that ALPs couple with electrons as pseudoscalars and couple with nucleons as scalars. The Lagrangian is written as [394],

$$-\mathcal{L}_{\text{int.}} \supset g_s\,\overline{N}Na + ig_P\,\bar{e}\gamma_5 ea + \text{h.c.}\,. \tag{6.12}$$

These interaction terms enable the mediation of a long range monopole-dipole force between electrons and nucleons. The Feynman diagram for an ALP mediated monopole-dipole potential between polarised electron current and unpolarised nucleonic current is shown in Fig. 6.2. The expression of the monopole-dipole potential mediated by ultralight ALP between two fermion currents is given by [393, 397]

$$V(r) = \frac{g_P g_S}{4\pi m_e}(\mathbf{s_e}.\hat{r})\left(\frac{m_a}{r} + \frac{1}{r^2}\right)e^{-m_a r}, \tag{6.13}$$

where we consider that ALP with mass m_a is coupled with the polarised electron by a pseudoscalar coupling with strength g_P and the ALP is also coupled with unpolarised nucleon by a scalar coupling with strength g_S. Here, m_e is the mass of the electron, and $\mathbf{s_e}$ is the electron's spin vector. The term $\mathbf{s_e}.\hat{r}$ violates P and T symmetries.

There exist several experiments dedicated to the search for parity and

time reversal violating monopole-dipole potentials [394, 398–401]. Such potential can be constrained from the torsion balance method using polarised electrons in the torsion pendulum and unpolarised nucleons in the Earth or in the Sun [402]. The bound on $g_S g_P$ obtained from this laboratory experiment is most sensitive for the ALPs of mass $m_a \lesssim 10^{-14}$ eV. The *QUAX*-$g_S g_P$ [398, 403] experiment obtains lab-lab bound on $g_S g_P$ for the mass of the ALP 5×10^{-7} eV $\lesssim m_a \lesssim 10^{-5}$ eV. An experiment like *ARIADNE* is made to search for monopole-dipole potential using a laser polarised ^{3}He and a rotating tungsten source mass [404]. This lab-lab $g_S g_P$ bound is valid for the ALPs of mass 1 μeV $\lesssim m_a \lesssim 6$ meV. In [405], polarised ultracold neutron spins and unpolarised nucleons are used to constrain such potential. This lab-lab experiment can probe ALPs of mass 1 meV $\lesssim m_a \lesssim 0.1$ eV. There are other laboratory experiments like *SMILE* ($m_a \lesssim 10^{-10}$ eV) [406], *NIST* ($m_a \lesssim 10^{-14}$ eV) [407], J-PARC muon $g-2$ ($m_a \lesssim 3 \times 10^{-14}$ eV) [408] , *Washington* (10 μeV $\lesssim m_a \lesssim 10$ meV) [409, 410], *Magnon* based axion dark matter search ($m_a \lesssim 10^{-5}$ eV) [411, 412] which obtain bounds on monopole-dipole interaction. The cooling of red giants and white dwarfs put constraint on $g_P \lesssim 1.6 \times 10^{-13}$ [103] and the constraint on g_S obtained from the energy loss of globular cluster stars is $g_S \lesssim 1.1 \times 10^{-12}$ [413]. Multiplying these two numbers, one can obtain a hybrid bound on monopole-dipole coupling as $g_S g_P \lesssim 10^{-25}$ for $m_a \lesssim 10$ keV. The lab-astro bound on $g_S g_P$ is obtained from two independent experimental bounds and the bound is sensitive for $m_a \lesssim 10^{-18}$ eV. The astro-astro $g_S g_P$ bound also considers two separate observations. So far there is no single astrophysical phenomenon that can directly constrain the monopole-dipole interaction as most of the astrophysical objects are considered to be unpolarised. However, in the next section we have discussed how the Earth can be used as a good source of polarised electrons and can be used to constrain the monopole-dipole interaction strength.

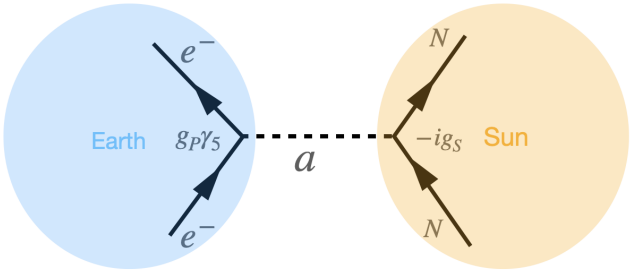

Figure 6.3: Feynman diagram of $e^- N$ scattering mediated by ultralight ALP in the Earth-Sun system.

6.3 Earth as a polarised source

Recently, a long range dipole-dipole interaction arising between two spin polarised bodies is studied in Ref. [395] where the authors have considered the Earth as a source of spin polarised electrons. In the presence of the geomagnetic field, some of the electrons in paramagnetic minerals within the Earth acquire a small spin polarisation oriented antiparallel to their local magnetic field. The magnitude and direction of the induced geoelectron spins depend on the Earth's material composition, geomagnetic field and temperature profile [414]. The core of the Earth is mostly made of Fe-Ni alloy which does not contain any unpaired electron spins due to high pressure and temperature [415, 416]. Hence, the Earth's core does not make any contribution to its polarisation. The dominant contribution to the polarisation comes from Fe, the most abundant transition metal in various oxides and silicates in the Earth's mantle and crust. Other major rock forming elements like Mg, Si, Al, and O have a negligible contribution to the Earth's polarisation due to their closed electron shells. In Ref. [395], the electron spin density as a function of depth and all the mineral proportions in Earth's crust and mantle are mentioned very accurately. It is found that the unpaired electron density around 10^4 km depth is about 10^{22} /cm^3. Hence, the total unpaired electron spins inside the Earth will be $N_e \sim 10^{22} \times 10^{27} = 10^{49}$. Most of the unpaired electrons exist in the Fe^{2+} state with a total spin $s = 2$, the so called HS state. When the spin-$\frac{1}{2}$ electron in HS Fe^{2+} interacts with the external geomagnetic field, the spins become polarised and the polarisation fraction becomes $\alpha = \frac{2\mu_B B}{kT}$,

where the electron Bohr magneton is $\mu_B = \frac{e}{2m_e} = 2.94 \times 10^{-7}$ eV^{-1}, k is the Boltzmann constant, $B \sim 1$ G is the Earth's magnetic field in the mantle, and $T \sim 2000$ K is the temperature. Hence, we can obtain the polarisation fraction as $\alpha \sim 10^{-7}$. Therefore, the total polarised electron spins in Earth is $N_e \times \alpha \sim 10^{49} \times 10^{-7} = 10^{42}$. However, when integrated over any spherically symmetric Earth model, is is found that that the vector sum of these spins is zero [417]. But, to our rescue, it is also known that the Earth is not strictly an sphere because of the following reason:

1. The most evident deviation from the assumption of spherical symmetry arises from the fact that the Earth is an oblate spheroid, with its polar radius approximately 21 km (or about 0.3%) shorter than its equatorial radius [418]. This flattening results in a net $\sim 3.2 \times 10^{38}$ electrons spin polarised along the $-z$-axis.

2. As it is described earlier that majority of the polarisation arises from the iron isotopes. Therefore, using a global crustal model and estimating the iron content within each layer, it has been calculated that the crustal heterogeneities produce approximately $(2.2 \pm 1.5) \times 10^{38}$ electrons whose spins are polarised along the $-\hat{z}$ direction [417, 419].

3. Non-spherical heterogeneities also arise due to the two Large Low Shear Velocity Provinces (LLSVPs) [420]. It was shown that these LLVPs contribute $\sim 1.6 \times 10^{38}$ electrons spin polarised along the $-\hat{z}$ direction.

In conclusion, due to the Earth's non-spherical structure, it is conservatively estimated that there are at least $\sim 10^{39}$ spin-polarised electrons aligned antiparallel to the Earth's rotation axis.

6.4 Constraining Monopole-dipole potential from single observation

The spin polarised geoelectrons can interact with the unpolarised nucleons in the Sun and generate an ALP mediated monopole-dipole potential for the Earth-Sun system. Consequently, presence of such new interaction can induce an extra gravitational potential between the Earth-Sun system which can be examined from tests of gravity. The tests of gravity include the perihelion precession of the Earth, gravitational light bending, and Shapiro time delay. However, the contribution of monopole-dipole potential for these observations is limited by the measurement uncertainties of the mentioned observables. In Fig. 6.3 we have shown the Feynman diagram for $e^- N$ scattering mediated by ultralight ALP for the Earth-Sun system. The ALP is coupled with the electrons in the Earth by a pseudoscalar coupling. The ALP is also coupled with unpolarised nucleons in the Sun by a scalar coupling. In the following sections, we obtain the contribution of monopole-dipole potential from the measurements of perihelion precession of the Earth, gravitational light bending, and Shapiro time delay.

6.4.1 Perihelion precession in presence of a monopole-dipole potential

The success of General Relativity (GR) theory has been consolidated by the observation of the perihelion precession of the Mercury planet. While orbiting around the Sun, the perihelion position of the Mercury planet shifts by a very small angle in each revolution around the Sun. The dominant contribution to the perihelion shift comes from the gravitational effect of other solar bodies. There is also a subdominant contribution on perihelion shift due to the oblateness of the Sun and Lens-Thirring precession. These non relativistic contributions are calculated based on Newtonian mechanics which follows $\frac{1}{r^2}$ force law. However, there is about 42.9799 arcsecond/century [421, 422] mismatch from the observation after including all the non-relativistic effects in the measurement of perihelion precession of Mercury. In 1915, Einstein's

GR calculation provided a complete explanation of the anomalous perihelion precession of the Mercury. All the other planets also experience this perihelion shifts. For example, the Earth has a perihelion shift of 3.84 arcsecond/century due to GR correction. Since, the Earth is taken as a polarised source, there can be an ALP mediated monopole-dipole potential for the Earth-Sun system. This ALP mediated long range potential can affect the geodesic of the Earth and contribute to its perihelion precession measurements. However, the contribution of monopole-dipole interaction should be limited to be no larger than the measurement uncertainty which is 10^{-4} arcsecond/century [423, 424] for the Earth-Sun system.

For a timelike particle, we can write

$$g_{\mu\nu}\dot{x}^{\mu}\dot{x}^{\nu} = -1, \tag{6.14}$$

where $g_{\mu\nu}$ is the metric tensor for the Schwarzschild background spacetime and denoted as,

$$g_{\mu\nu} = \text{Diag}\left\{\left(1-\frac{2GM}{r}\right), \left(1-\frac{2GM}{r}\right)^{-1}, r^2, r^2\sin^2\theta\right\}. \tag{6.15}$$

In presence of a long range monopole-dipole potential, the trajectory of unit mass can be described as [425],

$$\frac{\dot{r}^2}{2} + \frac{L^2}{2r^2} - \frac{GML^2}{r^3} - \frac{GM}{r} - \frac{\beta E m_a}{M_P r}e^{-m_a r} - \frac{\beta E}{M_P r^2}e^{-m_a r} = \frac{E^2-1}{2} \tag{6.16}$$

where $\dot{r} = \frac{L}{r^2}\frac{dr}{d\phi}$, M and M_P are the masses of the Sun and the Earth respectively, G is the Newton's Gravitational constant and $\beta = \frac{g_S g_P N_1 N_2}{4\pi m_e}$. N_1 and N_2 are the numbers of polarised electrons in the Earth and unpolarised nucleons in the Sun respectively. We have also neglected the $\mathcal{O}(\beta^2)$ term because the coupling for the monopole-dipole potential is small. E is a constant of motion which is termed as the total energy per unit mass for a timelike geodesic relative to an observer in rest frame at infinity. The total energy of the system per unit mass for a very small eccentric orbit in presence of a monopole-dipole

potential is

$$E \approx 1 - \frac{GM}{2D} - \frac{g_S g_P N_1 N_2}{4\pi m_e} e^{-m_a D}\Big(\frac{m_a}{M_P D} + \frac{m_a^2}{2M_P} + \frac{1}{M_P D^2}\Big), \tag{6.17}$$

and L is another constant of motion which is the angular momentum per unit mass of the system and D denotes the semi major axis of the orbit. In Eq. (6.16), the first term on the right hand side denotes the kinetic energy part, the second term denotes the centrifugal potential part, the third term arises due to the contribution of GR, the fourth term denotes the Newtonian potential, and the last two terms appear due to the contribution of monopole-dipole potential. We can write Eq. (6.16) in terms of reciprocal coordinate $u = \frac{1}{r}$ as

$$\Big(\frac{du}{d\phi}\Big)^2 + u^2 = \frac{E^2 - 1}{L^2} + 2GMu^3 + \frac{2GMu}{L^2} + \frac{2\beta E m_a u}{L^2 M_P} e^{-\frac{m_a}{u}} + \frac{2\beta E u^2}{L^2 M_P} e^{-\frac{m_a}{u}}, \tag{6.18}$$

where ϕ denotes the azimuthal coordinate and we have used $r^2 \frac{d\phi}{dt} = L$ which is another equation of motion. Expanding the exponential term in Eq. (6.18) and take derivative with respect to ϕ, we obtain

$$\frac{d^2u}{d\phi^2} + u = \frac{GM}{L^2} + 3GMu^2 + \frac{2\beta E u}{L^2 M_P} - \frac{\beta E m_a^3}{3L^2 M_P u^2}. \tag{6.19}$$

To solve this second order differential equation we consider $u = u_0(\phi) + \Delta u(\phi)$, where $u_0(\phi)$ is the solution for Newton's theory and $\Delta u(\phi)$ is the solution due to the contribution of GR and monopole-dipole potential. Hence, we can write

$$\frac{d^2u_0}{d\phi^2} + u_0 = \frac{GM}{L^2}. \tag{6.20}$$

The solution of Eq. (6.20) becomes

$$u_0(\phi) = \frac{GM}{L^2}(1 + \epsilon \cos\phi), \tag{6.21}$$

where ϵ is the eccentricity of the Earth-Sun elliptic orbit. The differential equation for Δu is

$$\frac{d^2\Delta u}{d\phi^2} + \Delta u = \frac{3G^3M^3}{L^4}(1 + \epsilon^2\cos^2\phi + 2\epsilon\cos\phi) + \frac{2\beta GME}{L^4 M_P}(1 + \epsilon\cos\phi)$$

$$-\frac{\beta E m_a^3 L^2}{3M_P G^2 M^2(1+\epsilon^2\cos\phi+2\epsilon\cos\phi)}. \tag{6.22}$$

The solution of Eq. (6.22) becomes

$$\Delta u\,(\phi) = \frac{3G^3M^3}{L^4}\epsilon\phi\sin\phi + \frac{\beta GME}{L^4M_P}\epsilon\phi\sin\phi + \frac{\beta E m_a^3L^2}{3M_PG^2M^2}\frac{\epsilon\phi\sin\phi}{(1-\epsilon^2)^{\frac{3}{2}}}\times\frac{\sqrt{1-\epsilon^2}}{(1+\epsilon)}, \tag{6.23}$$

where we keep terms which are linear in ϕ and hence contribute to the perihelion precession of Earth. Hence, the total solution of Eq. (6.19) becomes

$$\begin{aligned} u\,(\phi) &= u_0(\phi)+\Delta u(\phi) = \frac{GM}{L^2}(1+\epsilon\cos\phi) + \frac{3G^3M^3}{L^4}\epsilon\phi\sin\phi + \frac{\beta GME}{L^4M_P}\epsilon\phi\sin\phi \\ &\quad + \frac{\beta E m_a^3L^2}{3M_PG^2M^2}\frac{\epsilon\phi\sin\phi}{(1+\epsilon)(1-\epsilon^2)}. \end{aligned} \tag{6.24}$$

We can also rewrite Eq. (6.24) as,

$$u = \frac{GM}{L^2}[1+\epsilon\cos\phi(1-\gamma)], \tag{6.25}$$

where

$$\gamma = \frac{3G^2M^2}{L^2} + \frac{\beta}{L^2M_P} + \frac{\beta L^4 m_a^3}{3M_PG^3M^3}\frac{1}{(1+\epsilon)(1-\epsilon^2)}, \tag{6.26}$$

Here, we take $E\approx 1$ as other terms in Eq. (6.17) are very small compared to 1. As $\phi\to\phi+2\pi$, $u(\phi)$ and $u(\phi+2\pi)$ are not the same. Therefore, Earth does not follow its previous orbit. Hence, the change in the azimuthal angle or the perihelion shift becomes,

$$\Delta\phi = \frac{2\pi}{1-\gamma} - 2\pi = 2\pi\gamma = \frac{6\pi G^2M^2}{L^2} + \frac{2\pi\beta}{L^2M_P} + \frac{2\pi\beta L^4m_a^3}{3M_PG^3M^3}\frac{1}{(1+\epsilon)(1-\epsilon^2)}. \tag{6.27}$$

Substituting $L^2 = GMD(1-\epsilon^2)$, and $\beta = \frac{g_Sg_PN_1N_2}{4\pi m_e}$, we obtain

$$\Delta\phi = \frac{6\pi GM}{D(1-\epsilon^2)} + \frac{g_Sg_PN_1N_2}{2GMD(1-\epsilon^2)M_Pm_e} + \frac{g_Sg_PN_1N_2D^2m_a^3(1+\epsilon)}{6M_PGMm_e}, \tag{6.28}$$

Eq. (6.28) is the general expression for the perihelion shift due to monopole-dipole potential between a polarised object and an unpolarised object. The first term on the right hand side arises due to the GR contribution in perihelion shift

and its value for Earth is 3.84 arcsecond/century. The last two terms arise due to the contribution of monopole-dipole potential. In $g_S g_P \to 0$ limit, we get back the standard GR correction. Hence, the contribution of monopole-dipole potential in perihelion shift is

$$\Delta\phi_{\text{monopole}-\text{dipole}} \simeq \frac{g_S g_P N_1 N_2}{2GMD(1-\epsilon^2)M_P m_e} + \frac{g_S g_P N_1 N_2 D^2 m_a^3 (1+\epsilon)}{6M_P GMm_e} + \mathcal{O}\Big((g_S g_P)^2, m_a^4\Big). \tag{6.29}$$

Note that, Eq. (6.29) denotes that change in the perihelion precession of Earth in radian per revolution around the Sun. Using the values of the solar mass $M = 1.11 \times 10^{57}$ GeV, Newton's Gravitational constant, $G \simeq \frac{1}{M_{\rm Pl}^2} \sim 10^{-38}$ GeV^{-2}, the Sun-Earth distance $D = 0.98$ AU $= 7.37 \times 10^{26}$ GeV^{-1}, the eccentrcity of the Earth-Sun orbit $\epsilon = 0.017$, the mass of the electron $m_e = 5.1 \times 10^{-4}$ GeV, the mass of the planet Earth $M_P = 3.35 \times 10^{51}$ GeV, the number of polarised electrons in Earth $N_1 = 10^{39}$, the number of unpolarised nucleons in the Sun $N_2 = 10^{57}$, we obtain the upper bound on monopole-dipole coupling as $g_S g_P \lesssim 1.75 \times 10^{-13}$ for mass of the ALP $m_a \lesssim 1.35 \times 10^{-18}$ eV. We obtain this bound by considering that the contribution of monopole-dipole potential is $\leq 10^{-4}$ arcsecond/century which is the perihelion precession measurement uncertainty.

6.4.2 Gravitational light bending

Besides, the perihelion precession of planets, gravitational light bending is another test of Einstein's GR theory [426, 427]. It demonstrates that when a light rays from a distant pulsar comes to Earth, then the presence of a massive object like the Sun can distort the spacetime between the light source and the Earth. The increased gravitational potential due to the presence of the Sun decreases the speed of light and the light bends. The amount of bending depends on the mass of the gravitating object (Sun) and the impact parameter. In 1915, Einstein first calculated the amount of light bending due to the presence of the Sun based on the Equivalence principle. The calculated value of light bending is 1.75 arcsecond which matches well with the experiment to an uncertainty

of 10^{-4} arcsecond [428]. The presence of monopole dipole potential between the Earth-Sun system can affect the geodesic of light as it modifies the effective gravitational potential and contribute to the measurement of gravitational light bending. The strength of this monopole-dipole potential should be limited by the experimental uncertainty.

To calculate the light bending, we consider the null geodesic which is followed by massless photons in a Schwarzschild background,

$$g_{\mu\nu}V^{\mu}V^{\nu} = 0, \tag{6.30}$$

where $V^{\mu} = \frac{dx^{\mu}}{d\lambda}$ is the tangent vector along the path parametrised by $x^{\mu}(\lambda)$, where λ is the affine parameter. For a Schwarzschild background and planar motion ($\theta = \pi/2$), the conserved quantities are,

$$E = (1 - \frac{2GM}{r})\dot{t}, \qquad \text{and} \qquad L = r^2\dot{\phi}. \tag{6.31}$$

Here, E and L denote the total energy and angular momentum per unit mass of the system respectively. The null geodesic in terms of these conserved quantities can be expressed as,

$$\frac{E^2}{2} = \frac{L^2}{2}\Big(\frac{du}{d\phi}\Big)^2 + \frac{L^2u^2}{2}(1 - 2GMu), \tag{6.32}$$

where $\dot{r} = \frac{dr}{d\lambda} = \frac{L}{r^2}\frac{dr}{d\phi}$ and the reciprocal coordinate $u = \frac{1}{r}$. First term in the RHS of Eq. (6.32) represents the kinetic term, the second term denotes the classical potential term and the third term shows the GR correction. The presence of long range monopole-dipole potential changes the effective potential of the Sun-Earth system as

$$V_{\text{eff}} = \frac{L^2u^2}{2}(1 - 2GMu) - \frac{\beta m_a u}{M_P}e^{-\frac{m_a}{u}} - \frac{\beta u^2}{M_P}e^{-\frac{m_a}{u}}, \tag{6.33}$$

where the last two terms arise due to the presence of long range monopole-

dipole potential. Hence, Eq. (6.32) becomes

$$\frac{E^2}{2} = \frac{L^2}{2}\Big(\frac{du}{d\phi}\Big)^2 + \frac{L^2u^2}{2}(1-2GMu) - \frac{\beta m_a u}{M_P}e^{-\frac{m_a}{u}} - \frac{\beta u^2}{M_P}e^{-\frac{m_a}{u}}. \tag{6.34}$$

Differentiating Eq. (6.34) w.r.t ϕ and expanding the exponential term upto $\mathcal{O}\left(m_a^3\right)$ we obtain,

$$\frac{d^2u}{d\phi^2} + u = 3GMu^2 + \frac{2\beta u}{M_P L^2} - \frac{\beta m_a^3}{3u^2 M_P L^2}. \tag{6.35}$$

To solve this second order differential equation, we consider $u(\phi) = u_0(\phi) + \Delta u(\phi)$, where $u_0(\phi)$ is the complementary function and $\Delta u(\phi)$ is the particular integral. Hence, the differential equation for the complementary function is,

$$\frac{d^2u_0}{d\phi^2} + u_0 = 0, \tag{6.36}$$

and the solution of Eq. (6.36) is $u_0 = \frac{\sin\phi}{b}$, where b is the impact parameter. To find the solution to a particular integral, we can write

$$\frac{d^2\Delta u}{d\phi^2} + \Delta u = \frac{3GM\sin^2\phi}{b^2} + \frac{2\beta\sin\phi}{M_P L^2 b} - \frac{\beta m_a^3 b^2}{3M_P L^2\sin\phi}. \tag{6.37}$$

The solution of Eq. (6.37) turns out to be,

$$\Delta u(\phi) = \frac{3GM}{2b^2}\Big(1+\frac{1}{3}\cos 2\phi\Big) + \frac{2\beta}{M_P L^2 b}\Big(-\frac{\phi\cos\phi}{2}\Big) - \frac{\beta m_a^3 b^2}{3M_P L^2}[\cos\phi\ln|\csc\phi+\cot\phi| - 1]. \tag{6.38}$$

Hence, the total solution of Eq. (6.35) becomes

$$u(\phi) = \frac{\sin\phi}{b} + \frac{3GM}{2b^2}\Big(1+\frac{1}{3}\cos 2\phi\Big) - \frac{\beta\phi\cos\phi}{M_P L^2 b} - \frac{\beta m_a^3 b^2}{3M_P L^2}[\cos\phi\ln|\csc\phi+\cot\phi| - 1]. \tag{6.39}$$

At a far distance from the Sun, $u \to 0$ as $\phi \to 0$. Hence, in the presence of the Sun the angle slightly changes from zero. We can expand Eq. (6.39) around zero and the change in the angular coordinate can be denoted as,

$$\delta\phi = \frac{-\frac{2GM}{b^2} + \frac{\beta m_a^3 b^2}{3M_P L^2}\ln 2}{\frac{1}{b} - \frac{\beta}{M_P L^2 b} + \frac{\beta m_a^3 b^2}{3M_P L^2}}. \tag{6.40}$$

From the symmetry argument, we can claim that the contribution to $\delta\phi$ before and after the turning points are the same. Therefore, the total light bending is

$$\Delta\phi = -2\delta\phi = \frac{\frac{4GM}{b^2} - \frac{2\beta m_a^3 b^2}{3M_P L^2}\ln 2}{\frac{1}{b} - \frac{\beta}{M_P L^2 b} + \frac{\beta m_a^3 b^2}{3M_P L^2}}. \tag{6.41}$$

It can be checked that in the $\beta \to 0$ limit, standard GR result for gravitational light bending $\Delta\phi = \frac{4GM}{b}$ is obtained. Hence, we can write the contribution of monopole-dipole potential in gravitational light bending as,

$$\begin{aligned}
\Delta\phi_{\text{monopole}-\text{dipole}} &= \frac{\frac{4GM}{b^2} - \frac{2m_a^3 b^2 \ln 2}{3M_P L^2}\frac{g_S g_P N_1 N_2}{4\pi m_e}}{\frac{1}{b} - \frac{1}{M_P L^2 b}\frac{g_S g_P N_1 N_2}{4\pi m_e} + \frac{m_a^3 b^2}{3M_P L^2}\frac{g_S g_P N_1 N_2}{4\pi m_e}} - \frac{4GM}{b} + \mathcal{O}\Big((g_S g_P)^2, m_a^4\Big), \\
&\simeq -\frac{2m_a^3 b^3 g_S g_P N_1 N_2 \ln 2}{3M_P L^2 \times 4\pi m_e} + \frac{g_S g_P N_1 N_2}{M_P L^2 \times 4\pi m_e} \times \frac{4GM}{b} \\
&\quad -\frac{m_a^3 b^3 g_S g_P N_1 N_2}{3M_P L^2 \times 4\pi m_e} \times \frac{4GM}{b} + \mathcal{O}\Big((g_S g_P)^2, m_a^4\Big).
\end{aligned} \tag{6.42}$$

We use $L^2 = GMD(1-\epsilon^2)$, and the value of the impact parameter b as the solar radius $b \sim R_\odot = 6.96 \times 10^8$ m $= 3.51 \times 10^{24}$ GeV^{-1}. The contribution of monopole-dipole potential in the measurement of gravitational light bending should be smaller than 10^{-5} arcsecond which is the measurement uncertainty in the gravitational light bending and we obtain the bound on coupling as $g_S g_P \lesssim 4.25 \times 10^{-6}$ for $m_a \lesssim 1.35 \times 10^{-18}$ eV.

6.4.3 Shapiro time delay

When a radar signal is sent from Earth to Venus and it reflects from Venus to Earth, then in this round trip, there is a time delay in getting the signal compared to the expectation. In 1964, Irwin Shapiro calculated the amount of time delay as 2×10^{-4} s [429, 430] which agrees well with the experiment to an uncertainty of 10^{-5} s [431]. The presence of long range monopole-dipole potential can modify the strong gravitational potential near the Sun and thereby contributing to the Shapiro time delay. However, its contribution should be within the measurement uncertainty.

We can write the trajectory of light in presence of monopole-dipole potential as,[cf. Eq. (6.34)]

$$\frac{E^2}{2} = \frac{\dot{r}^2}{2} + \frac{L^2}{2r^2}\left(1 - \frac{2GM}{r}\right) - \frac{\beta m_a}{M_P r} e^{-m_a r} - \frac{\beta}{r^2 M_P} e^{-m_a r}, \tag{6.43}$$

where we have used $\dot{r} = \frac{dr}{d\lambda}$, $r^2\frac{d\phi}{d\lambda} = L$ and λ is affine parameter. Now, using Eq. (6.31) and defining $\frac{dr}{d\lambda} = \frac{dr}{dt}\frac{dt}{d\lambda} = \frac{E}{\left(1-\frac{2GM}{r}\right)}\frac{dr}{dt}$, we can write Eq. (6.43) as,

$$\frac{E^2}{2} = \frac{E^2}{2\left(1-\frac{2GM}{r}\right)^2}\left(\frac{dr}{dt}\right)^2 + \frac{L^2}{2r^2}\left(1 - \frac{2GM}{r}\right) - \frac{\beta m_a}{M_P r} e^{-m_a r} - \frac{\beta}{r^2 M_P} e^{-m_a r}. \tag{6.44}$$

Let, $r = r_0$ is the closest approach of light where $\frac{dr}{dt} = 0$. Put, $r = r_0$ and $\frac{dr}{dt} = 0$ in Eq. (6.44) we obtain

$$\frac{L^2}{E^2} = \frac{r_0^2}{\left(1 - \frac{2GM}{r_0}\right)}\left[1 + \frac{2\beta}{M_P r_0 E^2}\left(m_a + \frac{1}{r_0}\right)e^{-m_a r_0}\right]. \tag{6.45}$$

In absence of monopole-dipole potential, Eq. (6.45) becomes $\frac{L^2}{E^2} = \frac{r_0^2}{\left(1-\frac{2GM}{r_0}\right)}$. Using Eq. (6.44) and Eq. (6.45), we can write the time taken by the light to reach from r_0 to r as

$$t = \int_{r_0}^{r}\frac{dt}{dr}dr = \int_{r_0}^{r} dr \frac{1}{\left(1 - \frac{2GM}{r}\right)}\left[1 - \frac{r_0^2}{r^2}\frac{\left(1 - \frac{2GM}{r}\right)}{\left(1 - \frac{2GM}{r_0}\right)}(1+\eta) + \frac{2\beta}{M_P r E^2}\left(m_a + \frac{1}{r}\right)e^{-m_a r}\right]^{-\frac{1}{2}}, \tag{6.46}$$

where $\eta = \frac{2\beta}{M_P r_0 E^2}\left(m_a + \frac{1}{r_0}\right)e^{-m_a r_0}$. The solution of Eq. (6.46) in $r \gg r_0$ limit is

$$t_1 = \sqrt{r^2 - r_0^2} + 2GM\ln\left(\frac{2r}{r_0}\right) + GM - \frac{\beta}{M_P E^2}\left(\frac{GM}{r_0^2} + \frac{1}{r_0}\right) + \frac{\eta r_0}{2}\left(1 + \frac{2GM}{r_0}\right). \tag{6.47}$$

If r_e denotes the distance between the Sun and the Earth and r_v denotes the distance between the Sun and the Venus then the total time required for the

signal to go from the Earth to the Venus and returns to the Earth is

$$T_1 = 2t_1 = 2\Big[\sqrt{r_e^2 - r_0^2} + \sqrt{r_v^2 - r_0^2} + 2GM\ln\Big(\frac{2r_e}{r_0}\Big) + 2GM\ln\Big(\frac{2r_v}{r_0}\Big) + 2GM - \frac{2\beta M}{M_P E^2 r_0^2} - \frac{2\beta}{M_P E^2 r_0} + \eta r_0\Big(1 + \frac{2GM}{r_0}\Big)\Big]. \tag{6.48}$$

If there is no massive gravitating object between Earth and Venus, then the total time required for the pulse to go from Earth to Venus and returns to Earth is

$$T_2 = 2\Big[\sqrt{r_e^2 - r_0^2} + \sqrt{r_v^2 - r_0^2} - \frac{2\beta}{M_P E^2 r_0} + \eta r_0\Big]. \tag{6.49}$$

Hence, the excess time due to GR correction and monopole-dipole potential is $\Delta T = T_1 - T_2$ and we can write

$$\Delta T = 4GM\Big[1 + \ln\Big(\frac{4r_e r_v}{r_0^2}\Big)\Big] - \frac{4GM}{M_P E^2 r_0^2}\Big(\frac{g_S g_P N_1 N_2}{4\pi m_e}\Big) + \frac{8GM}{M_P r_0 E^2}\Big(m_a + \frac{1}{r_0}\Big)e^{-m_a r_0}\Big(\frac{g_S g_P N_1 N_2}{4\pi m_e}\Big),$$

where we have put back the expressions of β and η. In the absence of monopole-dipole potential ($g_S g_P \to 0$), the standard GR contribution in Shapiro time delay is obtained as,

$$\Delta T_{\rm GR} = 4GM\Big[1 + \ln\Big(\frac{4r_e r_v}{r_0^2}\Big)\Big]. \tag{6.50}$$

Using the Earth-Sun distance $r_e = D = 1.46 \times 10^{11}$ m $= 7.37 \times 10^{26}$ GeV^{-1}, the Venus-Earth distance $r_v = 1.08 \times 10^{11}$ m $= 5.47 \times 10^{26}$ GeV^{-1}, and the solar radius $r_0 = R_\odot = 6.96 \times 10^8$ m $= 3.51 \times 10^{24}$ GeV^{-1}, we obtain the GR contribution in Shapiro time delay as 2×10^{-4} s. Thus the contribution of monopole-dipole potential in Shapiro time delay is,

$$\Delta T_{\rm monopole-dipole} = \frac{8GM}{M_P r_0 E^2}\Big(m_a + \frac{1}{r_0}\Big)e^{-m_a r_0}\Big(\frac{g_S g_P N_1 N_2}{4\pi m_e}\Big) - \frac{4GM}{M_P E^2 r_0^2}\Big(\frac{g_S g_P N_1 N_2}{4\pi m_e}\Big) + \mathcal{O}\Big((g_S g_P)^2, m_a^2, M^2\Big). \tag{6.51}$$

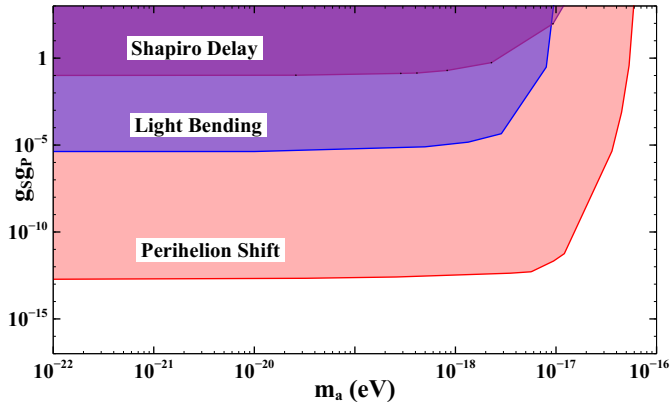

Figure 6.4: Bounds on the monopole-dipole interaction strength from single astrophysical observation

Using the Earth-Sun distance $r_e = D = 1.46 \times 10^{11}$ m $= 7.37 \times 10^{26}$ GeV^{-1}, the Venus-Earth distance $r_v = 1.08 \times 10^{11}$ m $= 5.47 \times 10^{26}$ GeV^{-1}, the solar radius $r_0 = R_\odot = 6.96 \times 10^8$ m $= 3.51 \times 10^{24}$ GeV^{-1}, and $E^2 \simeq \frac{L^2}{r_0^2}\left(1 - \frac{2GM}{r_0}\right)$ we obtain the upper bound on coupling as $g_S g_P \lesssim 1.08 \times 10^{-1}$ for $m_a \lesssim 1.35 \times 10^{-18}$ eV.

6.5 Results

In Fig. 6.4 we obtain numerically the bounds on monopole-dipole coupling from perihelion precession of the Earth (red region), gravitational light bending (blue region), and Shapiro time delay (purple region). The shaded regions are excluded. In obtaining these bounds, we have used an extra multiplicative factor of $\exp\left[-\frac{m_a L^2}{GM}\right]$ in Eq. (6.29), Eq. (6.42), and Eq. (6.51) to incorporate the exponential suppression due to the large value of ALP mass. We obtain a stronger bound on $g_S g_P$ from perihelion precession of the Earth as $g_S g_P \lesssim 1.75 \times 10^{-13}$ for the ALPs of mass $m_a \lesssim 1.35 \times 10^{-18}$ eV. This is the first bound on $g_S g_P$ that we obtain from a single astrophysical observation and for ALPs of mass $m_a \lesssim \mathcal{O}(10^{-18})$ eV.

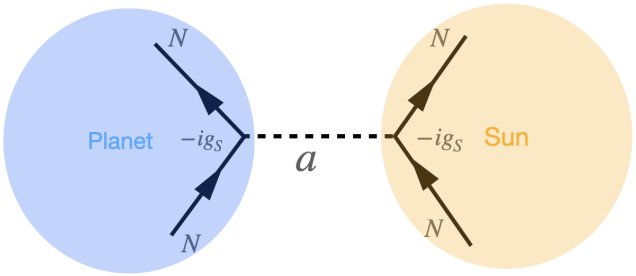

Figure 6.5: Monopole-Monopole interaction between the nucleons in Sun-planet system.

6.6 Constraints on the monopole-dipole coupling using two different observations

As discussed in section 6.2 also pointed out in Ref. [394, 432] that the most stringent limit on the monopole-dipole strength ($g_S g_P$) is obtained by multiplying the best experimental limit on scalar interaction strength (g_S) and best astrophysical limit on pseudo-scalar interaction strength (g_P). In this section, we obtain constraints on monopole-dipole coupling from two different astrophysical observations. We obtained the limit on g_S considering the monopole-monopole interaction between the unpolarised nucleons in the planet and the Sun that can change the perihelion precession of planets, gravitational light bending and Shapiro time delay within the measurement uncertainty. In Fig. 6.5, we have shown the monopole-monopole interaction between the Sun and the Planet system. The monopole-monopole potential due to ALP mediated nucleon-nucleon scattering in the Earth-Planet system is

$$V_{\text{m-m}} = \frac{g_S^2 N_1 N_2}{4\pi r} e^{-m_a r}, \tag{6.52}$$

where N_1 and N_2 are the numbers of nucleons in the Sun and the planet respectively. Now following the similar procedure as above, we calculate the change in perihelion precession of planet, bending of light and delay in light propagation from Earth to Venus considering the monopole-monopole potential. The perihelion shift due to the ALP mediated monopole-monopole potential

between the Sun and the planet is [425]

$$\Delta\phi_{\text{monopole}-\text{monopole}} \simeq \frac{g_S^2 N_1 N_2 m_a^2 D^2(1-\epsilon^2)}{4M_P(GM+\frac{g_S^2 N_1 N_2}{4\pi M_P})(1+\epsilon)} + \mathcal{O}(g_S^3, m_a^3), \tag{6.53}$$

where M_P is the mass of the planet, M is the mass of the Sun, and D is the semi-major axis of the planetary orbit with eccentricity ϵ. The contribution of ALP mediated monopole-monopole potential should be limited to be no larger than the perihelion precession measurement uncertainty. We obtain the stronger bound on g_S for the planet Mars [425] and its value is $g_S \lesssim 3.51 \times 10^{-25}$ for the mass of the ALP $m_a \lesssim 1.35 \times 10^{-18}$ eV.

The bending of light due to the ALP mediated monopole-monopole potential is [380]

$$\Delta\phi_{\text{monopole}-\text{monopole}} \simeq \frac{g_S^2 N_1 N_2 b}{2\pi M_P L^2}(1-0.347 m_a^2 b^2) - \frac{g_S^2 N_1 N_2 G M m_a^2 b^2}{2\pi M_P L^2} + \mathcal{O}(g_S^3, m_a^3). \tag{6.54}$$

We obtain the constraint on ALP monopole coupling from the gravitational light bending as $g_S \lesssim 5.82 \times 10^{-23}$ for the ALPs of mass $m_a \lesssim 1.35 \times 10^{-18}$ eV.

Similarly, the contribution of ALP mediated monopole potential in Shapiro time delay is [380]

$$\Delta T_{\text{monopole}-\text{monopole}} \simeq 2b_0 c_0(-1+c_0 GM)(r_e+r_v) + \frac{b_0 c_0^2}{2}(r_e^2+r_v^2) + 2b_0 - 4c_0 GM b_0 + 2a_0(r_e+r_v) + \frac{b_0}{24}(48 + 36 c_0^2 r_0^2[E_i(-c_0 r_e) + E_i(-c_0 r_v)]) + \mathcal{O}(g_S^3, m_a^3), \tag{6.55}$$

where $a_0 = \frac{g_S^2 N_1 N_2 e^{-m_a r_0}}{4\pi G M_P E^2 r_0}$, $b_0 = \frac{g_S^2 N_1 N_2}{4\pi M_P E^2}$, and $c_0 = m_a$.

We obtain the constraint on ALP monopole coupling from the Shapiro time delay as $g_S \lesssim 3.59 \times 10^{-22}$ for the ALP mass $m_a \lesssim 1.35 \times 10^{-18}$ eV. In Eq. (6.53), Eq. (6.54) and Eq. (6.55) an extra multiplicative factor of $\exp\left[-\frac{m_a L^2}{GM}\right]$ is added to incorporate the exponential suppression due to large values of ALP mass.

The bound on the ALP-electron pseudoscalar coupling can be obtained

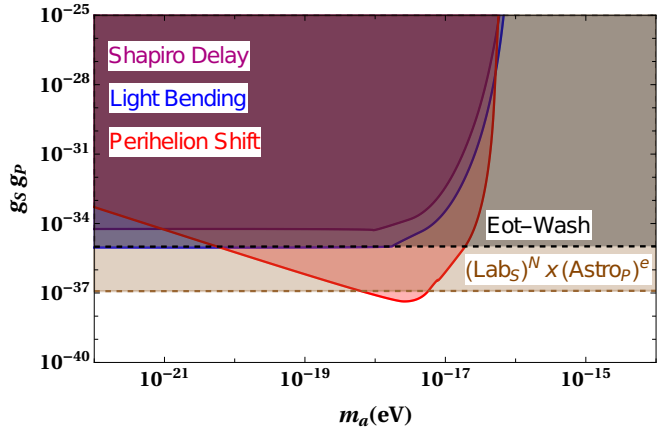

Figure 6.6: Bounds on monopole-dipole interaction strength from two different astrophysical observations

from the cooling of red giant stars and white dwarfs. The ALP-electron coupling allows the stellar energy loss by the bremsstrahlung $(e + Ze \rightarrow e + Ze + a)$ and Compton process $(\gamma + e \rightarrow e + a)$ [433, 434]. The excessive energy loss due to these processes will delay the Helium ignition in the red giant stars. Therefore the tip of the red giant branch becomes brighter. The measurement of the tip of the red giant branch in the ω Centaury from Gaia DR2 data put bound on the ALP-electron coupling as $g_P \lesssim 1.6 \times 10^{-13}$ for the mass of the ALPs $m_a \lesssim 10$ keV [103].

To obtain the bound on monopole-dipole coupling $(g_S g_P)$, we take the product of the bounds on g_S obtained from the tests of gravity (perihelion precession of planet, gravitational light bending and Shapiro time delay) and g_P obtained from the energy loss from the red giant branch. In Fig. 6.6 we obtain the bounds on $g_S g_P$ from two different astrophysical observations. The perihelion precession of the planet Mars and red giant branch give the bound on monopole-dipole coupling as $g_S g_P \lesssim 5.61 \times 10^{-38}$. We also obtain the bound on $g_S g_P$ from gravitational light bending and red giant branch as $g_S g_P \lesssim 9.31 \times 10^{-36}$. Lastly, the bound on $g_S g_P$ obtained from Shapiro time delay and red giant branch is $g_S g_P \lesssim 5.74 \times 10^{-35}$. These bounds are only valid for the mass of the ALP $m_a \lesssim 1.35 \times 10^{-18}$ eV. We obtain the stronger bound on $g_S g_P$ from the perihelion precession of the planet Mars and energy loss of the red giant branch. The shaded regions in Fig. 6.6 are excluded.

The bound $g_S g_P \lesssim 5.61 \times 10^{-38}$ is three orders of magnitude stronger than the Eöt-Wash experiment [435] and one order of magnitude stronger than the $(\text{Lab})^{\text{N}}_{\text{S}} \times (\text{Astro})^{\text{e}}_{\text{P}}$ limit [394].

The behaviour of the curves in Fig. 6.4 and Fig. 6.6 can be effectively explained by considering Eqs. (6.29), (6.42), (6.51), (6.53), (6.54) and Eq. (6.55). The expression of $(\Delta\phi)_{\text{monopole}-\text{dipole}}$ in Eq. (6.29) depends on two terms. The first term is independent of the ALP mass, while the second term depends on ALP mass. For ALP masses at the lower end of the spectrum, we can disregard the mass-dependent term, resulting in flat curves within this range. This same scenario applies to all the curves depicted in Fig. 6.4 and Fig. 6.6, except for the curve representing the perihelion precession of the planet in Fig. 6.6. In this case, at the lower mass range, the curve does not remain flat; instead, it exhibits an apparent slope. This is attributed to the fact that in Eq. (6.53), $(\Delta\phi)_{\text{monopole}-\text{monopole}}$ solely comprises a term dependent on the ALP mass. The monopole-monopole coupling is approximately inversely proportional to the ALP mass. Hence, in the lower mass region the curve shows a negative slope. In the high ALP mass region, the exponential suppression term $\exp\left[-\frac{m_a L^2}{GM}\right]$ dominates as usual.

6.7 Summary

In this chapter, we discuss constraints on monopole-dipole coupling strength from single astrophysical observations such as the perihelion precession of Earth, gravitational light bending, and Shapiro time delay. These bounds are strictly valid for the ALP mass $m_a \lesssim 1.35 \times 10^{-18}$ eV. Due to the presence of a geomagnetic field and non-spherical shape of the Earth, 10^{39} number of electrons can be polarised in Earth and ALP mediated monopole-dipole force can act between the Earth and the Sun. We obtain a stronger bound on monopole-dipole coupling strength from perihelion precession of the Earth as $g_S g_P \lesssim 1.75 \times 10^{-13}$ from single astrophysical observation.

The previous lab-astro bounds on $g_S g_P$ obtained in the literature are de-

rived from two different observations. In these studies, the monopole coupling g_S and the dipole coupling g_P are measured independently from two different observations and they are simply multiplied to get bound on $g_S g_P$. To get the bound in this way is overly stringent and may not be completely reliable if the ALP changes its behaviour in different environments. The bounds on $g_S g_P$ obtained from lab-lab experiments are only valid for the ALPs of mass $\mu\text{eV} \lesssim m_a \lesssim \text{meV}$. We have obtained the first bounds on $g_S g_P$ from single astrophysical observations. In all of these observations, the massless limit gives the stronger bound on monopole-dipole coupling strength. In the massless limit, the perihelion shift is inversely proportional to the Sun-planet distance. This means planets which are closer to the Sun will put the best bound on $g_S g_P$. However, the bounds on the monopole-dipole couplings, obtained from perihelion precession, gravitational light bending, and Shapiro time delay are the order of magnitude calculations. They strongly depend on the number of polarised electrons in the Earth which is not a fixed quantity at all its layers. In fact, this number depends on the magnetic field and temperature at each layer of the Earth which varies with its depth. Hence, at the massless limit, the monopole-dipole coupling strength will not be a fixed quantity and it should have different values at different depths. Therefore, the bounds can be improved by accurate incorporation of the number of polarised spins at each layer of Earth from geochemical and geological surveys. Such analyses will be important to probe these long range spin dependent interactions.

We also obtain constraints on monopole-dipole coupling strength from two different astrophysical observations. We consider monopole coupling of ALPs with unpolarised nucleons in the Earth and the Sun to obtain bounds on monopole coupling from perihelion precession of the planet Mars, gravitational light bending and Shapiro time delay. Multiplying these monopole couplings with the dipole coupling obtained from excessive energy loss of the red giant branch, we derive the monopole-dipole coupling strength. For $m_a \lesssim 1.35 \times 10^{-18}$ eV, we obtain $g_S g_P \lesssim 5.61 \times 10^{-38}$ from perihelion precession and red giant branch. This bound is three orders of magnitude stronger than the Eöt-Wash experiment and one order of magnitude stronger than the

current $(\text{Lab})^{\text{N}}_{\text{S}} \times (\text{Astro})^{\text{e}}_{\text{P}}$ limit. In comparison to the pseudoscalar coupling of electrons in the Earth, the scalar coupling of nucleons in the Earth does not get stronger in the massless limit for the perihelion precession measurements. In fact, in this case the scalar coupling gets stronger for the planets which are further away from the Sun.

We can also constrain the ALP mediated monopole-dipole coupling between nucleonic currents. The cooling of hot neutron star HESS J1731-347 puts bound on ALP nucleon pseudoscalar coupling as $g_P^N \lesssim 2.8 \times 10^{-10}$. We also obtain ALP nucleon scalar coupling as $g_S^N \lesssim 3.51 \times 10^{-25}$. Combining these two couplings, we obtain the bound on the monopole-dipole coupling strength for only nucleonic currents as $g_S^N g_P^N \lesssim 9.83 \times 10^{-35}$ for the mass of the ALPs $m_a \lesssim 1.35 \times 10^{-18}$ eV. This bound is better than the projected *ARIADNE* experiment [436] and $(\text{Lab})^{\text{N}}_{\text{S}} \times (\text{Astro})^{\text{N}}_{\text{P}}$ by a factor of 2 [394]. Future space missions with better precision can significantly improve the bounds of monopole-dipole couplings.

7

Summary and Outlook

The Standard Model of particle physics has been consolidated by numerous precision experiments. However, the observation of neutrino oscillation phenomena which requires neutrinos to have masses, provides evidence for beyond-the SM physics. Additional observational evidences such as matter-antimatter asymmetry and dark also remain unexplained within the context of the SM. Additionally, there are also anomalous results in precision experiments such as rare meson decays which do not coincide with the prediction of the SM. To address these shortcomings, the SM needs to be extended either by new particles or by embedding the SM in a large gauge group. This thesis mainly focuses on constraining selected BSM scenarios through a multi-pronged approach combining different terrestrial experiments with cosmological observations. We have also considered astrophysical observations to provide stringent limits on the BSM parameter spaces. In some cases, combined constraint from different experiments provides a powerful avenue to put complementary constraints on new physics parameter spaces.

The results of various solar, atmospheric, reactor and accelerator neutrino oscillation experiments have established that the neutrinos change their flavours as they propagate. Oscillation experiments have measured the mass-squared differences and mixing angles quite precisely, but they do not provide information about the absolute scale of neutrino masses or their nature i.e. whether neutrinos are Dirac or Majorana particles. Mass related observables such as the sum of neutrino masses ($\sum m_\nu$) from cosmology, effective elec-

tron mass (m_β) from nuclear β decay and effective Majorana mass (m_{ee}) from $0\nu\beta\beta$ are sensitive to the absolute mass scale of neutrinos. Moreover, the observation of $0\nu\beta\beta$ will provide unambiguous evidence for the Majorana nature of neutrinos as the process violates the lepton number by two units. Current upper limits on the mass observables indicate that the neutrinos should have tiny masses $(m_\nu \sim 0.01\,\text{eV})$. The most elegant way to generate such small masses is provided by the dimension 5 Weinberg operator which also implies lepton number violation and leads to Majorana masses for neutrinos. In chapter 2, we review various mechanisms for generating neutrino masses. These include seesaw models which realise the Weinberg operator at tree level and radiative models which realise Weinberg operator at the one-loop level. We also explore approaches to generate neutrino masses involving higher-dimensional operators beyond dimension five. The implications of neutrino mass for the lepton number violation, neutrino electromagnetic properties and $0\nu\beta\beta$ are subsequently discussed. We have also briefly described the mass observables in this chapter.

In chapter 3, we have studied a minimal extension of SM with a light sterile neutrino with $\Delta m_s^2 = 10^{-4}$ eV^2, 10^{-2} eV^2 and 1.3 eV^2. Such scenarios are well motivated for explaining certain inconsistencies in experimental observations. The presence of an additional neutrino state introduces four distinct mass orderings : (i) SNO-NO ($\Delta m_s^2 > 0\,, \Delta m^2_{\text{atm}} > 0$), (ii) SNO-IO ($\Delta m_s^2 > 0\,, \Delta m^2_{\text{atm}} < 0$), (iii) SIO-NO ($\Delta m_s^2 < 0\,, \Delta m^2_{\text{atm}} > 0$), and (iv) SIO-IO ($\Delta m_s^2 < 0\,, \Delta m^2_{\text{atm}} < 0$) and we have studied the implications of these mass orderings on the mass related observables: (1) sum of neutrino masses from cosmology, $\Sigma m_\nu = \sum_i m_i$, (2) effective electron neutrino mass from nuclear β decay, $m_\beta = \sqrt{\sum_i |U_{ei}|^2\, m_i^2}$, and effective majorana mass from $0\nu\beta\beta$, given as $m_{ee} = \sum U_{ei}^2\, m_i$.

It is found that the SIO-NO and SIO-IO scenarios for $\Delta m_s^2 = 1.3\,\text{eV}^2$are in conflict with the cosmological bound on the sum of neutrino masses. Moreover, such scenarios are also disfavoured from the current limit on m_β by *KATRIN* experiment and also from the upper limit on m_{ee} by *KamLAND-Zen* ex-

periment. For $\Delta m_s^2 = 0.01\,\text{eV}^2$, SIO-NO and SIO-IO is disfavoured from the cosmological model whereas SNO-NO and SNO-IO scenarios remain valid up to $m_{\text{lightest}} \sim 0.03\,\text{eV}$. It is also noted that the future sensitivity of *Project 8* experiments will be able to probe SNO-IO, SIO-NO, and SIO-IO scenarios. From the result of *KamLAND-Zen* experiment, most of the parameter space is ruled out for SIO-NO and SIO-IO scenario for $\Delta m_s^2 = 0.01\,\text{eV}^2$ and next generation experiment like *nEXO* will be able to probe the parameter space completely. Sterile neutrino with $\Delta m_s^2 = 10^{-4}\,\text{eV}^2$ is allowed from standard cosmology. In case of direct mass measurement, *KATRIN*'s projected limit can probe the mass spectra up to $m_{\text{lightest}} \approx 0.2\,\text{eV}$ whereas *Project 8* will be able to probe SNO-IO, SIO-IO scenarios completely and SNO-NO, SIO-NO scenarios up to $m_{\text{lightest}} \approx 0.04\,\text{eV}$. It is found that neither *KamLAND-Zen* nor *nEXO* can completely probe the mass spectra, but they rule out some parameter space for SNO-IO, SIO-NO and SIO-IO scenarios.

In chapter 4, we considered a scenario where the SM is extended with two LQs such as $S_1 : (3, 3, 1/3)$ and $\tilde{R}_2 : (3, 2, 1/6)$. In this extension, Majorana type of neutrino mass is generated via radiative corrections. Apart from neutrino mass, the LQs induce new long-range mechanisms that dominantly contribute to $0\nu\beta\beta$ decay process. We perform a comprehensive analysis of $0\nu\beta\beta$ and its interplay with low-energy flavor observables in this two LQ framework and found a parameter space allowed by all flavor constraint. The combined analysis reveals that the muon and electron $g-2$ values are in tension with each other implying that the considered model can not simultaneously satisfy both the lepton magnetic moment anomalies. We have also shown in Fig. 4.10 that the prediction for m_{ee}^{eff}, arising from the combined contributions of standard and leptoquark contributions can be significant and even greater than the standard contribution and the cancellation region is no longer present around $m_{\text{lightest}} \sim$ meV. The total value of m_{ee}^{eff} can lie in the desert region between the standard NO and IO regions and hence can be probed by future experiments like *LEGEND-1000* and *nEXO*. We find that for IO ordering of neutrinos, most of the parameter space otherwise allowed by low-energy flavor constraints are disfavoured by the current $0\nu\beta\beta$ limit from *KamLAND-Zen*. To conclude, the

considered model provides a simple and effective framework for addressing the observed flavor anomalies. The main drawback of the framework lies in the considerable freedom available in choosing the Yukawa couplings values to satisfy the flavor anomalies. This issue can be mitigated by embedding the model within a larger gauge structure, such as a grand unified theory. In such scenarios, leptoquarks arise naturally and the Yukawa couplings are subject to more stringent constraints, thereby enhancing the model's predictive power and reducing arbitrariness in the parameter choices.

In chapter 5, we investigated a realistic $SU(5)$ scenario where the scalar leptoquark contributions to $0\nu\beta\beta$ are analysed. It was found that the set of scalar leptoquarks (LQs) responsible for mediating proton decay also induce $0\nu\beta\beta$. As a result, the $0\nu\beta\beta$ rate mediated by scalar LQs are suppressed to comply with proton decay constraints, making their contribution to $0\nu\beta\beta$ subdominant compared to standard canonical contribution within the $SU(5)$ framework. It is also shown that this limitation from the proton decay can be circumvented by imposing a discrete $(\mathcal{Z}_3)$ symmetry in this framework. This imposition forbids the diquark coupling of specific LQ (S_3) which contributes to $0\nu\beta\beta$. However, the imposed symmetry spoils the fermion mass relations. Thereafter, quantum corrections from the heavy degrees of freedom are considered to reproduce the observed fermion mass spectra (within the assumed uncertainty). Although the considered framework produces the observed fermion masses correctly, but the $0\nu\beta\beta$ is still dominated by the canonical contribution and the scalar contribution remains subdominant. However, $0\nu\beta\beta$ rate can be enhanced by the extending the scalar sector with an additional 15_H scalar representation which is singlet under the $\mathcal{Z}_3$ symmetry. Using the current experimental limit of the $0\nu\beta\beta$, conservative limits on the scalars are provided.

In chapter 6, we adopted a different strategy to constrain a BSM scenario where the SM is extended with ultra-light ALPs. In this chapter, we have demonstrated that these ultra light ALPs can mediated a long range monopole dipole force between macroscopic astrophysical bodies, such as the Sun and the Earth. The central idea is, the new long range force introduces an addi-

tional potential in the Sun–Earth system, which can lead to observable modifications in both the Earth's orbital dynamics and the propagation of light in the vicinity of these bodies. Two scenarios are investigated for constraining the monopole-dipole coupling strength. In the first scenario, a constraint is established on the monopole-dipole strength, treating the Earth as a source of polarised electrons. The perihelion precession of Earth sets an upper limit on the monopole-dipole coupling strength as $g_S g_P \lesssim 1.75 \times 10^{-13}$ for the ALP of mass $m_a \lesssim 1.35 \times 10^{-18}$ eV. This bound surpasses the limits obtained from gravitational light bending and Shapiro time delay.

In the second scenario, the constraints on monopole-monopole coupling strength g_S is obtained from the perihelion precession of the planet, gravitational light bending and Shapiro time delay. It is found that the stringent limit on g_S $\left(\lesssim 3.51 \times 10^{-25}\right)$ is obtained from the perihelion precession of the planet Mars, while the limit on dipole-dipole coupling strength g_P $\left(\lesssim 1.6 \times 10^{-13}\right)$ is taken from the measurement of the tip of the red giant branch in ω Centauri using Gaia DR2 data. Together, they yield a hybrid constraint on the monopole-dipole coupling strength as $g_S g_P \lesssim 5.61 \times 10^{-38}$. Our obtained bound is three orders of magnitude more stringent than the Eöt-Wash experiment and one order of magnitude stronger than the current hybrid $(\text{Lab})^{\text{N}}_{\text{S}} \times (\text{Astro})^{\text{e}}_{\text{P}}$ limit.

In this thesis, we have studied various BSM scenarios and their implications. Some of the predictions of these scenarios can be tested in future experiments and can either favour or disfavour the considered models. In future, we have planed to study the collider implications of the leptoquark models and finding complementary constraints on the parameter space. We also plan to study the leptogenesis in some BSM models and check their viability in generating the observed matter-antimatter asymmetry of the universe.

This page is intentionally left blank.

A

Fierz Transformation

Calculations of low-energy weak interactions with fermions often involve superposition of quartic products of Dirac spinors, where the order of the spinors varies among the terms. A common technique to standardise their ordering is known as the Fierz transformation. This transformations are used to express the product of two bilinears as a linear combination of other product of bilinears with the Dirac spinors placed in a different order. The usual Fierz relation can be written as [437, 438]

$$e_\Gamma(1234) \;=\; \sum_{\Gamma'} F_{\Gamma\,\Gamma'}\, e_{\Gamma'}(1432). \tag{A.1}$$

Here $\Gamma, \Gamma' \in \{S, V, T, A, P\}$, and they stand for scalar, vector, tensor, axial vector, and pseudoscalar, respectively. $e_\Gamma(1234) \equiv (\overline{w}_1 \Gamma w_2)\,(\overline{w}_3 \Gamma w_4)$, where w_i are the Dirac spinors. $F_{\Gamma\,\Gamma'}$ are numerical coefficients and given as [437],

$$F_{\Gamma\Gamma'} \;=\; \frac{1}{4}\begin{pmatrix} 1 & 1 & \frac{1}{2} & -1 & 1 \\ 4 & -2 & 0 & -2 & -4 \\ 12 & 0 & -2 & 0 & 12 \\ -4 & -2 & 0 & -2 & 4 \\ 1 & -1 & \frac{1}{2} & 1 & 1 \end{pmatrix} \tag{A.2}$$

In case of leptoquark interactions, we use the following Fierz relation

$$e_S(1234) = \frac{1}{4}\left[e_S(1432) + e_V(1432) + \frac{1}{2}e_T(1432) - e_A(1432) + e_P(1432)\right]. \tag{A.3}$$

Then the Fierz transformation list is as follows:

$$\left(\overline{d}^C P_L \nu\right)\left(\bar{e} P_R u^C\right) = -\frac{1}{2}\left(\overline{u}\gamma^\mu P_L d\right)\left(\bar{e}\gamma_\mu P_L \nu_L\right), \tag{A.4}$$

$$\begin{aligned}\left(\overline{d}^C P_L \nu\right)\left(\bar{e} P_L u^C\right) &= \frac{1}{2}\left(\overline{d}^C P_L u^C\right)\left(\bar{e} P_L \nu\right) + \frac{1}{8}\left(\overline{d}^C \sigma^{\mu\nu} P_L u^C\right)\left(\bar{e}\sigma_{\mu\nu} P_L \nu\right) \\ &= \frac{1}{2}\left(\overline{u} P_L d\right)\left(\bar{e} P_L \nu\right) - \frac{1}{8}\left(\overline{u}\sigma^{\mu\nu} P_L d\right)\left(\bar{e}\sigma_{\mu\nu} P_L \nu\right),\end{aligned} \tag{A.5}$$

$$\begin{aligned}\left(\overline{d}^C P_R \nu^C\right)\left(\bar{e} P_R u^C\right) &= \frac{1}{2}\left(\overline{d}^C P_R u^C\right)\left(\bar{e} P_R \nu^C\right) + \frac{1}{8}\left(\overline{d}^C \sigma^{\mu\nu} P_R u^C\right)\left(\bar{e}\sigma_{\mu\nu} P_R \nu^C\right) \\ &= \frac{1}{2}\left(\overline{u} P_R d\right)\left(\bar{e} P_R \nu^C\right) - \frac{1}{8}\left(\overline{u}\sigma^{\mu\nu} P_R d\right)\left(\bar{e}\sigma_{\mu\nu} P_R \nu^C\right),\end{aligned} \tag{A.6}$$

$$\left(\overline{d}^C P_R \nu^C\right)\left(\bar{e} P_L u^C\right) = \frac{1}{2}\left(\overline{d}^C \gamma^\mu P_L u^C\right)\left(\bar{e}\gamma_\mu P_R \nu^C\right) = -\frac{1}{2}\left(\overline{u}\gamma^\mu P_R d\right)\left(\bar{e}\gamma_\mu P_R \nu^C\right). \tag{A.7}$$

B

Neutrinoless double beta decay in EFT Framework

In this section, we present the derivation of the master formula for calculating the half-life of $0\nu\beta\beta$ using the EFT approach [244, 439]. The $0\nu\beta\beta$ process involves the transmutation of two neutrons within an atomic nucleus into two protons and two electrons, with no neutrinos emitted. The observation of this rare process would indicate that lepton number (L) is not conserved in nature and the neutrinos possess Majorana mass implying that the neutrinos are their own antiparticles. In general, the results of the $0\nu\beta\beta$ experiments are interpreted under the assumption that lepton number violation (LNV) arises from the exchange of light Majorana neutrinos. However in various BSM scenarios other sources of LNV exist that can induce $0\nu\beta\beta$ and we have referred them as non-standard contributions. For instance, in Chapter 4 and Chapter 5, the mixing of two LQ states induce LNV in the theory and it enables contributions other than the standard neutrino exchange contribution.

Since $0\nu\beta\beta$ is a low energy process, they can be described by low-energy Effective Field Theory (LEFT) [243, 440].

The most general LEFT Lagrangian for long range mechanisms can be written as [241–243]

$$-\mathcal{L}_{\text{eff}} \supset \frac{G_F}{\sqrt{2}} \left[j^{\mu}_{V-A} J_{V-A,\mu} + \sum_{\dot{\alpha},\dot{\beta}} \epsilon^{\dot{\beta}}_{\dot{\alpha}} \, j_{\dot{\beta}} \, J_{\dot{\alpha}} + \text{h.c.} \right], \tag{B.1}$$

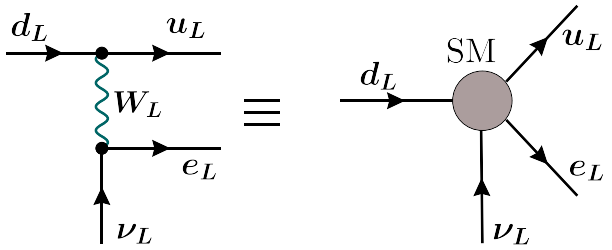

Figure B.1: The canonical effective operator that contributes to $0\nu\beta\beta$ decay. **(Left Panel:)** SM interactions. **(Right Panel:)** LEFT operator after integrating out the W_L boson.

where the first term contributes to the standard canonical long-range mechanism and shown in Fig. B.1. The leptonic and hadronic currents are defined as,

$$j^{\mu}_{V-A} \;=\; \bar{e}\gamma^{\mu}\,P_L\,\nu_e\,, \quad J_{V-A,\mu} = \bar{u}\gamma_{\mu}\,P_L\,d, \tag{B.2}$$

where $P_L = \frac{1}{2}\,(1-\gamma_5)$.

Other leptonic and hadronic currents that can be generated in BSM theories are defined as

$$j_{\dot{\beta}} \;=\; \bar{e}\mathcal{O}_{\dot{\beta}}\nu_e^C\,, \quad J_{\dot{\alpha}} = \bar{u}\mathcal{O}_{\dot{\alpha}}d. \tag{B.3}$$

The Greek indices $\dot{\beta}$ can be $V+A$, $S+P$, $T+T_5$, and $\dot{\alpha}$ can be $V\mp A$, $S\mp P$, $T\mp T_5$ where V, A, S, P, T, T_5 correspond to vector, axial-vector, scalar, pseudo-scalar, tensor, and axial-tensor respectively. In Eq. (B.1), the standard canonical long range mechanism (first term) has been separated from the non-standard contributions, with $\epsilon^{\dot{\beta}}_{\dot{\alpha}}$ being the corresponding Wilson coefficients of the non-standard operators.

For the $0\nu\beta\beta$ process, one has to take two terms from the effective Lagrangian in Eq. (B.1) which can be written as

$$(\mathcal{L}_1\mathcal{L}_2) \;=\; \frac{G_F^2}{2}\left[j^{\mu}_{V-A}J_{V-A,\mu}\,j^{\nu}_{V-A}J_{V-A,\nu} + \sum_{\dot{\alpha},\dot{\beta}}\epsilon^{\dot{\beta}}_{\dot{\alpha}}\,j^{\mu}_{V-A}\,J_{V-A,\mu}\;j_{\dot{\beta}}\,J_{\dot{\alpha}} + \mathcal{O}(\epsilon^2)\right]. \tag{B.4}$$

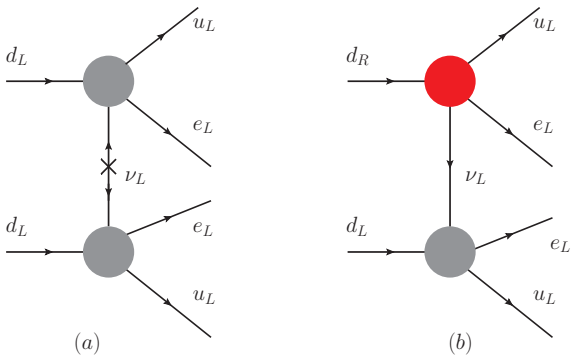

Figure B.2: **(Left Panel:)** $0\nu\beta\beta$ process where both vertices contain SM interaction terms $\left(j^{\mu}_{V-A}\, J_{V-A\,\mu}\right)$. **(Right Panel:)** $0\nu\beta\beta$ process where one of the SM interaction vertex is replaced by a higher dimensional non-standard operator $(j_i\, J^i)$.

The standard long-range W_L-W_L contribution to $0\nu\beta\beta$ decay is represented by the first term in Eq. (B.4), while the second term corresponds to the product of the standard and non-standard contribution, suppressed by a factor of ϵ. The third term, proportional to $\mathcal{O}(\epsilon^2)$, arises purely from non-standard contributions. In Fig. B.2, $0\nu\beta\beta$ contributions are shown up to $\mathcal{O}(\epsilon)$, as the $\mathcal{O}(\epsilon^2)$ terms are typically negligible. The cross mark in the left panel diagrams indicates that standard majorana mass insertion in the standard mechanism.

In a BSM theory, having specified the Wilson coefficients of the operators, one can calculate the amplitude of the $0\nu\beta\beta$ as[1] [244],

$$\begin{aligned}\mathcal{A} &= \frac{g_A^2 G_F^2 m_e}{\pi R_A}\left[\mathcal{A}_\nu \overline{u}(k_1) P_R \mathcal{C}\overline{u}^T(k_2) + \mathcal{A}_E\, \overline{u}(k_1)\gamma_0\, \mathcal{C}\overline{u}^T(k_2)\frac{E_1 - E_2}{m_e}\right.\\ &+ \left.\mathcal{A}_{m_e}\, \overline{u}(k_1)\mathcal{C}\overline{u}^T(k_2) + \mathcal{A}_M\, \overline{u}(k_1)\gamma_0\gamma_5\mathcal{C}\overline{u}^T(k_2)\right], \end{aligned} \tag{B.5}$$

where $k_{1,2}$ $(E_{1,2})$ are the momentum (energies) of the final state electrons, m_e is the mass of the electron and $R_A = 1.2\, A^{1/3}$ is atomic radius of the daughter nucleus. The sub-amplitudes, $\mathcal{A}_i$'s depend on the Wilson coefficients and nuclear matrix elements (NMEs) and they are defined as,

$$\mathcal{A}_\nu = \frac{m_{ee}^{std}}{m_e}\mathcal{M}_\nu^{(3)} + \frac{m_N}{m_e}\mathcal{M}_\nu^{(6)}, \tag{B.6}$$

[1]The BSM scenarios considered in this thesis, contribute to the LEFT operators up to dimension 6. Therefore, in Eq. (B.5), we have ignored the contributions from dimension 9 operators.

$$\mathcal{A}_E = \mathcal{M}^{(6)}_{E,L} + \mathcal{M}^{(6)}_{E,R}, \tag{B.7}$$

$$\mathcal{A}_{m_e} = \mathcal{M}^{(6)}_{m_e,L} + \mathcal{M}^{(6)}_{m_e,R}\,. \tag{B.8}$$

$$\mathcal{A}_M = \frac{m_N}{m_e}\,\mathcal{M}^{(6)}_{M}. \tag{B.9}$$

Here, m_N is the nucleon mass ($\sim$ 1 GeV), $\mathcal{M}^{(3)}_{\nu}$ denotes the contribution induced by the light Majorana neutrinos and $\mathcal{M}^{(6)}_{i}$ encapsulate the contributions from dimension-6 LNV operators which can be expressed in terms of Wilson coefficients and NMEs,

$$\mathcal{M}^{(3)}_{\nu} = -V^2_{ud}\left(-\frac{M_F}{g^2_A} + M_{GT} + M_T + \frac{2m^2_\pi g^{NN}_\nu}{g^2_A}\,M_{F,sd}\right), \tag{B.10}$$

$$\mathcal{M}^{(6)}_{\nu} = V_{ud}\left(\frac{B}{m_N}\left(\epsilon^{S+P}_{S-P} - \epsilon^{S+P}_{S+P}\right)M_{PS} + \epsilon^{T+T_5}_{T+T_5}\,M_{T6}\right), \tag{B.11}$$

$$\mathcal{M}^{(6)}_{E,L} = V_{ud}\,\epsilon^{V+A}_{V-A}\,M_{E,L}\,, \tag{B.12}$$

$$\mathcal{M}^{(6)}_{E,R} = V_{ud}\,\epsilon^{V+A}_{V+A}\,M_{E,R}\,, \tag{B.13}$$

$$\mathcal{M}^{(6)}_{m_e,L} = V_{ud}\,\epsilon^{V+A}_{V-A}\,M_{m_e,L} \tag{B.14}$$

$$\mathcal{M}^{(6)}_{m_e,R} = V_{ud}\,\epsilon^{V+A}_{V+A}\,M_{m_e,R}\,, \tag{B.15}$$

$$\mathcal{M}^{(6)}_{M} = V_{ud}\,\epsilon^{V+A}_{V-A}\,M_M \tag{B.16}$$

where $g^{NN}_\nu \sim \mathcal{O}(f_\pi^{-2}) = -92.9\,\text{GeV}^{-2} \pm 50\%$ [222, 244] and $B = 2.7$ GeV at $\mu = 2$ GeV in the $\overline{\text{MS}}$ scheme [244]. The NMEs can be calculated via [244]

$$M_{GT} = M^{AA}_{GT} + M^{AP}_{GT} + M^{PP}_{GT} + M^{MM}_{GT}\,, \tag{B.17}$$

$$M_T = M^{AP}_T + M^{PP}_T + M^{MM}_T\,, \tag{B.18}$$

$$M_{PS} = \frac{1}{2}M^{AP}_{GT} + M^{PP}_{GT} + \frac{1}{2}M^{AP}_T + M^{PP}_T\,, \tag{B.19}$$

$$\begin{aligned} M_{T6} &= 2\frac{g'_T - g^{NN}_T}{g^2_A}\frac{m^2_\pi}{m^2_N}M_{F,sd} - 8\frac{g_T}{g_M}(M^{MM}_{GT} + M^{MM}_T) \\ &\quad + g^{\pi N}_T\frac{m^2_\pi}{4m^2_N}(M^{AP}_{GT,sd} + M^{AP}_{T,sd}) + g^{\pi\pi}_T\frac{m^2_\pi}{4m^2_N}(M^{PP}_{GT,sd} + M^{PP}_{T,sd}), \end{aligned} \tag{B.20}$$

$$M_{E,L} = -\frac{1}{3}\left(\frac{g^2_V}{g^2_A}M_F + \frac{1}{3}(2M^{AA}_{GT} + M^{AA}_T) + 6\frac{g^E_{VR}}{g^2_A}M_{F,sd}\right) \tag{B.21}$$

$$M_{E,R} = -\frac{1}{3}\left(\frac{g^2_V}{g^2_A}M_F - \frac{1}{3}(2M^{AA}_{GT} + M^{AA}_T) + 6\frac{g^E_{VR}}{g^2_A}M_{F,sd}\right) \tag{B.22}$$

Table B.1: NMEs of ^{136}Xe and ^{76}Ge obtained using IBM2 [222].

Nucleus	M_F	M_{GT}^{AA}	M_{GT}^{AP}	M_{GT}^{PP}	M_{GT}^{MM}	M_T^{AA}	M_T^{AP}	M_T^{PP}
^{136}Xe	−0.52	3.203	−0.45	0.09	0.10	0.00	0.12	−0.03
^{76}Ge	−0.78	6.062	−0.86	0.17	0.20	0.00	0.24	−0.06
Nucleus	M_T^{MM}	$M_{F,sd}$	$M_{GT,sd}^{AA}$	$M_{GT,sd}^{PP}$	$M_{T,sd}^{AP}$	$M_{T,sd}^{AP}$	$M_{T,sd}^{PP}$	
^{136}Xe	0.02	−0.76	2.40	−0.71	0.17	−0.38	0.12	
^{76}Ge	0.04	−1.25	4.34	−1.28	0.30	−0.795	0.24	

Table B.2: Phase space factors of ^{136}Xe and ^{76}Ge given in units of $10^{-14}\,\mathrm{yr}^{-1}$ [244].

Nucleus	G_{01}	G_{02}	G_{03}	G_{04}	G_{06}	G_{09}
^{136}Xe	1.5	3.2	0.86	1.2	1.8	2.8
^{76}Ge	0.22	0.35	0.12	0.19	0.33	0.48

$$
\begin{aligned}
M_{m_e,L} &= \frac{1}{6}\left(\frac{g_V^2}{g_A^2}M_F - \frac{1}{3}\left(M_{GT}^{AA} - 4M_T^{AA}\right) - 3\left(M_{GT}^{AP} + M_{GT}^{PP} + M_T^{AP} + M_T^{PP}\right)\right. \\
&\quad \left. -12\,\frac{g_{VR}^{m_e}}{g_A^2}M_{F,sd}\right), \qquad \text{(B.23)} \\
M_{m_e,R} &= \frac{1}{6}\left(\frac{g_V^2}{g_A^2}M_F + \frac{1}{3}\left(M_{GT}^{AA} - 4M_T^{AA}\right) + 3\left(M_{GT}^{AP} + M_{GT}^{PP} + M_T^{AP} + M_T^{PP}\right)\right. \\
&\quad \left. -12\,\frac{g_{VR}^{m_e}}{g_A^2}M_{F,sd}\right), \qquad \text{(B.24)} \\
M_M &= 2\frac{g_A}{g_M}\left(M_{GT}^{MM} + M_T^{MM}\right) \\
&\quad + \frac{m_\pi^2}{m_N^2}\left(-\frac{2}{g_A^2}\,g_{VL}^{NN}M_{F,sd} + \frac{1}{2}g_{VL}^{\pi N}\left(M_{GT,sd}^{AP} + M_{T,sd}^{AP}\right)\right). \qquad \text{(B.25)}
\end{aligned}
$$

Here the values of the low-energy constants (LECs) are given in Tab. 1 in Ref. [244] and we have also used the same values. In this thesis, we have used the NMEs of ^{136}Xe nucleus obtained using IBM2 and given in [222]. These values are tabulated in Tab. B.1.

After identifying the sub-amplitudes Eq. (B.5), the expression for the half-

life becomes [244, 441, 442],

$$\left(T^{0\nu}_{1/2}\right)^{-1} = g_A^4 \sum_k G_{0k} \left|\mathcal{A}_k\left(\{C_i\}\right)\right|^2, \tag{B.26}$$

$$= g_A^4 \Big[G_{01} \left|\mathcal{A}_\nu\right|^2 + 4\, G_{02} \left|\mathcal{A}_E\right|^2 + 2\, G_{04} \left(\left|\mathcal{A}_{m_e}\right|^2 + \mathrm{Re}\left[\mathcal{A}^*_{m_e}\, \mathcal{A}_\nu\right]\right) - 2\, G_{03}\, \mathrm{Re}\left[\mathcal{A}_\nu\, \mathcal{A}^*_E + 2\, \mathcal{A}_{m_e}\, \mathcal{A}^*_E\right] + G_{09} \left|\mathcal{A}_M\right|^2 + G_{06}\, \mathrm{Re}\left[\mathcal{A}_\nu\, \mathcal{A}^*_M\right]\Big]. \tag{B.27}$$

Here G_{0i} denote the phase space factors (PSFs) and their numerical values are tabulated in Tab. B.2.

Eq. (B.27) describes the master formula for calculating the half-life for . It includes the standard long-range contribution and non-standard contribution generated by dimension 6 LEFT operators.

In absence of the non-standard contributions, $\epsilon \to 0$ limit, only mediated by standard mechanism and the half-life becomes,

$$\left(T^{0\nu}_{1/2}\right)^{-1} = g_A^4 G_{01} \left|\mathcal{M}^{(3)}_\nu\right|^2 \frac{\left|m^{std}_{ee}\right|^2}{m_e^2}. \tag{B.28}$$

However, in presence of the non-standard contribution, the half-life becomes complicated but we can always parametrise the half-life as,

$$\left(T^{0\nu}_{1/2}\right)^{-1}_{\text{total}} = g_A^4 G_{01} \left|\mathcal{M}^{(3)}_\nu\right|^2 \frac{\left|m^{std}_{ee} + m^{\text{nstd}}_{ee}\right|^2}{m_e^2},$$

$$= g_A^4 G_{01} \left|\mathcal{M}^{(3)}_\nu\right|^2 \frac{\left|m^{\text{eff}}_{ee}\right|^2}{m_e^2}, \tag{B.29}$$

where we have defined $m^{\text{eff}}_{ee} = m^{\text{std}}_{ee} + m^{\text{nstd}}_{ee}$. The advantage of writing it this way is that when the non-standard contributions become sub-dominant i.e., $m^{\text{eff}}_{ee} \to m^{\text{std}}_{ee}$, we would recover the canonical result. In other words, the deviation of m^{eff}_{ee} from m^{std}_{ee} gives a measure of the non-standard contributions, including interference with the SM contribution.

References

[1] Steven Weinberg. "A Model of Leptons". In: *Phys. Rev. Lett.* 19 (1967), pp. 1264–1266. DOI: 10.1103/PhysRevLett.19.1264.

[2] S. L. Glashow. "Partial Symmetries of Weak Interactions". In: *Nucl. Phys.* 22 (1961), pp. 579–588. DOI: 10.1016/0029-5582(61)90469-2.

[3] Abdus Salam. "Weak and Electromagnetic Interactions". In: *Conf. Proc. C* 680519 (1968), pp. 367–377. DOI: 10.1142/9789812795915_0034.

[4] S. Navas et al. "Review of particle physics". In: *Phys. Rev. D* 110.3 (2024), p. 030001. DOI: 10.1103/PhysRevD.110.030001.

[5] F. Englert and R. Brout. "Broken Symmetry and the Mass of Gauge Vector Mesons". In: *Phys. Rev. Lett.* 13 (1964). Ed. by J. C. Taylor, pp. 321–323. DOI: 10.1103/PhysRevLett.13.321.

[6] Peter W. Higgs. "Broken symmetries, massless particles and gauge fields". In: *Phys. Lett.* 12 (1964), pp. 132–133. DOI: 10.1016/0031-9163(64)91136-9.

[7] Peter W. Higgs. "Broken Symmetries and the Masses of Gauge Bosons". In: *Phys. Rev. Lett.* 13 (1964). Ed. by J. C. Taylor, pp. 508–509. DOI: 10.1103/PhysRevLett.13.508.

[8] Makoto Kobayashi and Toshihide Maskawa. "CP Violation in the Renormalizable Theory of Weak Interaction". In: *Prog. Theor. Phys.* 49 (1973), pp. 652–657. DOI: 10.1143/PTP.49.652.

[9] S. L. Glashow, J. Iliopoulos, and L. Maiani. "Weak Interactions with Lepton-Hadron Symmetry". In: *Phys. Rev. D* 2 (1970), pp. 1285–1292. DOI: 10.1103/PhysRevD.2.1285.

[10] B. T. Cleveland et al. "Measurement of the solar electron neutrino flux with the Homestake chlorine detector". In: *Astrophys. J.* 496 (1998), pp. 505–526. DOI: 10.1086/305343.

[11] John N. Bahcall and Roger K. Ulrich. "Solar Models, Neutrino Experiments and Helioseismology". In: *Rev. Mod. Phys.* 60 (1988), pp. 297–372. DOI: 10.1103/RevModPhys.60.297.

[12] F. Kaether et al. "Reanalysis of the GALLEX solar neutrino flux and source experiments". In: *Phys. Lett. B* 685 (2010), pp. 47–54. DOI: 10.1016/j.physletb.2010.01.030. arXiv: 1001.2731 [hep-ex].

[13] J. N. Abdurashitov et al. "Measurement of the solar neutrino capture rate with gallium metal. III: Results for the 2002–2007 data-taking period". In: *Phys. Rev. C* 80 (2009), p. 015807. DOI: 10.1103/PhysRevC.80.015807. arXiv: 0901.2200 [nucl-ex].

[14] K. Abe et al. "Solar neutrino results in Super-Kamiokande-III". In: *Phys. Rev. D* 83 (2011), p. 052010. DOI: 10.1103/PhysRevD.83.052010. arXiv: 1010.0118 [hep-ex].

[15] B. Aharmim et al. "Combined Analysis of all Three Phases of Solar Neutrino Data from the Sudbury Neutrino Observatory". In: *Phys. Rev. C* 88 (2013), p. 025501. DOI: 10.1103/PhysRevC.88.025501. arXiv: 1109.0763 [nucl-ex].

[16] G. Bellini et al. "Precision measurement of the 7Be solar neutrino interaction rate in Borexino". In: *Phys. Rev. Lett.* 107 (2011), p. 141302. DOI: 10.1103/PhysRevLett.107.141302. arXiv: 1104.1816 [hep-ex].

[17] G. Bellini et al. "Neutrinos from the primary proton–proton fusion process in the Sun". In: *Nature* 512.7515 (2014), pp. 383–386. DOI: 10.1038/nature13702.

[18] B. Pontecorvo. "Inverse beta processes and nonconservation of lepton charge". In: *Zh. Eksp. Teor. Fiz.* 34 (1957), p. 247.

[19] B. Pontecorvo. "Mesonium and anti-mesonium". In: *Sov. Phys. JETP* 6 (1957), p. 429.

[20] Ziro Maki, Masami Nakagawa, and Shoichi Sakata. "Remarks on the unified model of elementary particles". In: *Prog. Theor. Phys.* 28 (1962), pp. 870–880. DOI: 10.1143/PTP.28.870.

[21] Ivan Esteban et al. "The fate of hints: updated global analysis of three-flavor neutrino oscillations". In: *JHEP* 09 (2020), p. 178. DOI: 10.1007/JHEP09(2020)178. arXiv: 2007.14792 [hep-ph].

[22] Sacha Davidson, Enrico Nardi, and Yosef Nir. "Leptogenesis". In: *Phys. Rept.* 466 (2008), pp. 105–177. DOI: 10.1016/j.physrep.2008.06.002. arXiv: 0802.2962 [hep-ph].

[23] Chee Sheng Fong, Enrico Nardi, and Antonio Riotto. "Leptogenesis in the Universe". In: *Adv. High Energy Phys.* 2012 (2012), p. 158303. DOI: 10.1155/2012/158303. arXiv: 1301.3062 [hep-ph].

[24] A. D. Sakharov. "Violation of CP Invariance, C asymmetry, and baryon asymmetry of the universe". In: *Pisma Zh. Eksp. Teor. Fiz.* 5 (1967), pp. 32–35. DOI: 10.1070/PU1991v034n05ABEH002497.

[25] V. A. Kuzmin, V. A. Rubakov, and M. E. Shaposhnikov. "On the Anomalous Electroweak Baryon Number Nonconservation in the Early Universe". In: *Phys. Lett. B* 155 (1985), p. 36. DOI: 10.1016/0370-2693(85)91028-7.

[26] Z. Fodor. "Electroweak phase transition, perturbative and lattice studies". In: *31st Rencontres de Moriond: Electroweak Interactions and Unified Theories*. 1996, pp. 471–478.

[27] Z. Fodor. "Electroweak phase transitions". In: *Nucl. Phys. B Proc. Suppl.* 83 (2000). Ed. by M. Campostrini et al., pp. 121–125. DOI: 10.1016/S0920-5632(00)91603-7. arXiv: hep-lat/9909162.

[28] M. Fukugita and T. Yanagida. "Baryogenesis Without Grand Unification". In: *Phys. Lett. B* 174 (1986), pp. 45–47. DOI: 10.1016/0370-2693(86)91126-3.

[29] F. Zwicky. "On the Masses of Nebulae and of Clusters of Nebulae". In: *Astrophys. J.* 86 (1937), pp. 217–246. DOI: 10.1086/143864.

[30] Douglas Clowe et al. "A direct empirical proof of the existence of dark matter". In: *Astrophys. J. Lett.* 648 (2006), pp. L109–L113. DOI: 10.1086/508162. arXiv: astro-ph/0608407.

[31] N. Aghanim et al. "Planck 2018 results. VI. Cosmological parameters". In: *Astron. Astrophys.* 641 (2020). [Erratum: Astron.Astrophys. 652, C4 (2021)], A6. DOI: 10.1051/0004-6361/201833910. arXiv: 1807.06209 [astro-ph.CO].

[32] Julian S. Schwinger. "On Quantum electrodynamics and the magnetic moment of the electron". In: *Phys. Rev.* 73 (1948), pp. 416–417. DOI: 10.1103/PhysRev.73.416.

[33] G. W. Bennett et al. "Final Report of the Muon E821 Anomalous Magnetic Moment Measurement at BNL". In: *Phys. Rev. D* 73 (2006), p. 072003. DOI: 10.1103/PhysRevD.73.072003. arXiv: hep-ex/0602035.

[34] D. P. Aguillard et al. "Measurement of the Positive Muon Anomalous Magnetic Moment to 0.20 ppm". In: *Phys. Rev. Lett.* 131.16 (2023), p. 161802. DOI: 10.1103/PhysRevLett.131.161802. arXiv: 2308.06230 [hep-ex].

[35] T. Aoyama et al. "The anomalous magnetic moment of the muon in the Standard Model". In: *Phys. Rept.* 887 (2020), pp. 1–166. DOI: 10.1016/j.physrep.2020.07.006. arXiv: 2006.04822 [hep-ph].

[36] Sz. Borsanyi et al. "Leading hadronic contribution to the muon magnetic moment from lattice QCD". In: *Nature* 593.7857 (2021), pp. 51–55. DOI: 10.1038/s41586-021-03418-1. arXiv: 2002.12347 [hep-lat].

[37] *The Status of Muon $g-2$ Theory in the Standard Model*. URL: https://muon-gm2-theory.illinois.edu.

[38] Hartmut Wittig. "Progress on $(g-2)_\mu$ from Lattice QCD". In: *57th Rencontres de Moriond on Electroweak Interactions and Unified Theories*. June 2023. arXiv: 2306.04165 [hep-ph].

[39] R. Aliberti et al. "The anomalous magnetic moment of the muon in the Standard Model: an update". In: (May 2025). arXiv: 2505.21476 [hep-ph].

[40] X. Fan et al. "Measurement of the Electron Magnetic Moment". In: *Phys. Rev. Lett.* 130.7 (2023), p. 071801. DOI: 10.1103/PhysRevLett.130.071801. arXiv: 2209.13084 [physics.atom-ph].

[41] Tatsumi Aoyama, Toichiro Kinoshita, and Makiko Nio. "Theory of the Anomalous Magnetic Moment of the Electron". In: *Atoms* 7.1 (2019), p. 28. DOI: 10.3390/atoms7010028.

[42] Léo Morel et al. "Determination of the fine-structure constant with an accuracy of 81 parts per trillion". In: *Nature* 588.7836 (2020), pp. 61–65. DOI: 10.1038/s41586-020-2964-7.

[43] Richard H. Parker et al. "Measurement of the fine-structure constant as a test of the Standard Model". In: *Science* 360 (2018), p. 191. DOI: 10.1126/science.aap7706. arXiv: 1812.04130 [physics.atom-ph].

[44] J. P. Lees et al. "Measurement of an Excess of $\overline{B} \to D^{(*)}\tau^-\overline{\nu}_\tau$ Decays and Implications for Charged Higgs Bosons". In: *Phys. Rev. D* 88.7 (2013), p. 072012. DOI: 10.1103/PhysRevD.88.072012. arXiv: 1303.0571 [hep-ex].

[45] G. Caria et al. "Measurement of $\mathcal{R}(D)$ and $\mathcal{R}(D^*)$ with a semileptonic tagging method". In: *Phys. Rev. Lett.* 124.16 (2020), p. 161803. DOI: 10.1103/PhysRevLett.124.161803. arXiv: 1910.05864 [hep-ex].

[46] I. Adachi et al. "A test of lepton flavor universality with a measurement of $R(D^*)$ using hadronic B tagging at the Belle II experiment". In: (Jan. 2024). arXiv: 2401.02840 [hep-ex].

[47] Roel Aaij et al. "Measurement of the ratios of branching fractions $\mathcal{R}(D^*)$ and $\mathcal{R}(D^0)$". In: *Phys. Rev. Lett.* 131 (2023), p. 111802. DOI: 10.1103/PhysRevLett.131.111802. arXiv: 2302.02886 [hep-ex].

[48] Syuhei Iguro, Teppei Kitahara, and Ryoutaro Watanabe. "Global fit to $b \to c\tau\nu$ anomaly 2024 Spring breeze". In: (Apr. 2024). arXiv: 2405.06062 [hep-ph].

[49] Andrzej J. Buras, Julia Harz, and Martin A. Mojahed. "Disentangling new physics in $K \to \pi\bar{\nu}\nu$ and $B \to K(K^*)\bar{\nu}\nu$ observables". In: (May 2024). arXiv: 2405.06742 [hep-ph].

[50] I. Adachi et al. "Evidence for $B^+ \to K^+\nu\bar{\nu}$ Decays". In: (Nov. 2023). arXiv: 2311.14647 [hep-ex].

[51] Gerard 't Hooft. "Naturalness, chiral symmetry, and spontaneous chiral symmetry breaking". In: *NATO Sci. Ser. B* 59 (1980). Ed. by Gerard 't Hooft et al., pp. 135–157. DOI: 10.1007/978-1-4684-7571-5_9.

[52] R. D. Peccei and Helen R. Quinn. "CP Conservation in the Presence of Instantons". In: *Phys. Rev. Lett.* 38 (1977), pp. 1440–1443. DOI: 10.1103/PhysRevLett.38.1440.

[53] R. D. Peccei and Helen R. Quinn. "Constraints Imposed by CP Conservation in the Presence of Instantons". In: *Phys. Rev. D* 16 (1977), pp. 1791–1797. DOI: 10.1103/PhysRevD.16.1791.

[54] Frank Wilczek. "Problem of Strong P and T Invariance in the Presence of Instantons". In: *Phys. Rev. Lett.* 40 (1978), pp. 279–282. DOI: 10.1103/PhysRevLett.40.279.

[55] Steven Weinberg. "A New Light Boson?" In: *Phys. Rev. Lett.* 40 (1978), pp. 223–226. DOI: 10.1103/PhysRevLett.40.223.

[56] Jihn E. Kim. "Weak Interaction Singlet and Strong CP Invariance". In: *Phys. Rev. Lett.* 43 (1979), p. 103. DOI: 10.1103/PhysRevLett.43.103.

[57] Mikhail A. Shifman, A. I. Vainshtein, and Valentin I. Zakharov. "Can Confinement Ensure Natural CP Invariance of Strong Interactions?" In: *Nucl. Phys. B* 166 (1980), pp. 493–506. DOI: 10.1016/0550-3213(80)90209-6.

[58] Michael Dine, Willy Fischler, and Mark Srednicki. "A Simple Solution to the Strong CP Problem with a Harmless Axion". In: *Phys. Lett. B* 104 (1981), pp. 199–202. DOI: 10.1016/0370-2693(81)90590-6.

[59] Nathaniel Craig. "Naturalness: past, present, and future". In: *Eur. Phys. J. C* 83.9 (2023), p. 825. DOI: 10.1140/epjc/s10052-023-11928-7. arXiv: 2205.05708 [hep-ph].

[60] Michael E. Peskin. "What is the Hierarchy Problem?" In: *Nucl. Phys. B* 1018 (2025), p. 116971. DOI: 10.1016/j.nuclphysb.2025.116971. arXiv: 2505.00694 [hep-ph].

[61] Jonathan Kriewald. "Indirect searches for New Physics via flavour observables". PhD thesis. Clermont-Ferrand U., 2021. arXiv: 2202.14015 [hep-ph].

[62] Gurucharan Mohanta and Ketan M. Patel. "Radiatively generated fermion mass hierarchy from flavor nonuniversal gauge symmetries". In: *Phys. Rev. D* 106.7 (2022), p. 075020. DOI: 10.1103/PhysRevD.106.075020. arXiv: 2207.10407 [hep-ph].

[63] Gurucharan Mohanta and Ketan M. Patel. "Gauged $SU(3)_F$ and loop induced quark and lepton masses". In: *JHEP* 10 (2023), p. 128. DOI: 10.1007/JHEP10(2023)128. arXiv: 2308.05642 [hep-ph].

[64] Gurucharan Mohanta and Ketan M. Patel. "Loop-induced masses for the first two generations with optimum flavour violation". In: *JHEP* 12 (2024), p. 158. DOI: 10.1007/JHEP12(2024)158. arXiv: 2406.19179 [hep-ph].

[65] Gurucharan Mohanta. "Radiative mass mechanism: addressing the flavour hierarchy and strong CP puzzle". In: *JHEP* 04 (2025), p. 170. DOI: 10.1007/JHEP04(2025)170. arXiv: 2411.13385 [hep-ph].

[66] Elizabeth E. Jenkins, Aneesh V. Manohar, and Peter Stoffer. "Low-Energy Effective Field Theory below the Electroweak Scale: Anomalous Dimensions". In: *JHEP* 01 (2018). [Erratum: JHEP 12, 042 (2023)], p. 084. DOI: 10.1007/JHEP01(2018)084. arXiv: 1711.05270 [hep-ph].

[67] Elizabeth E. Jenkins, Aneesh V. Manohar, and Michael Trott. "Renormalization Group Evolution of the Standard Model Dimension Six Operators I: Formalism and lambda Dependence". In: *JHEP* 10 (2013), p. 087. DOI: 10.1007/JHEP10(2013)087. arXiv: 1308.2627 [hep-ph].

[68] Elizabeth E. Jenkins, Aneesh V. Manohar, and Michael Trott. "Renormalization Group Evolution of the Standard Model Dimension Six Operators II: Yukawa Dependence". In: *JHEP* 01 (2014), p. 035. DOI: 10.1007/JHEP01(2014)035. arXiv: 1310.4838 [hep-ph].

[69] Rodrigo Alonso et al. "Renormalization Group Evolution of the Standard Model Dimension Six Operators III: Gauge Coupling Dependence and Phenomenology". In: *JHEP* 04 (2014), p. 159. DOI: 10.1007/JHEP04(2014)159. arXiv: 1312.2014 [hep-ph].

[70] Elizabeth E. Jenkins, Aneesh V. Manohar, and Peter Stoffer. "Low-Energy Effective Field Theory below the Electroweak Scale: Operators and Matching". In: *JHEP* 03 (2018). [Erratum: JHEP 12, 043 (2023)], p. 016. DOI: 10.1007/JHEP03(2018)016. arXiv: 1709.04486 [hep-ph].

[71] Jason Aebischer et al. "B physics Beyond the Standard Model at One Loop: Complete Renormalization Group Evolution below the Electroweak Scale". In: *JHEP* 09 (2017), p. 158. DOI: 10.1007/JHEP09(2017)158. arXiv: 1704.06639 [hep-ph].

[72] Steven Weinberg. "Baryon and Lepton Nonconserving Processes". In: *Phys. Rev. Lett.* 43 (1979), pp. 1566–1570. DOI: 10.1103/PhysRevLett.43.1566.

[73] M. Hirsch et al. "Neutrino masses and mixings from supersymmetry with bilinear R parity violation: A Theory for solar and atmospheric neutrino oscillations". In: *Phys. Rev. D* 62 (2000). [Erratum: Phys.Rev.D 65, 119901 (2002)], p. 113008. DOI: 10.1103/PhysRevD.62.113008. arXiv: hep-ph/0004115.

[74] R. N. Mohapatra and J. W. F. Valle. "Neutrino Mass and Baryon Number Nonconservation in Superstring Models". In: *Phys. Rev. D* 34 (1986), p. 1642. DOI: 10.1103/PhysRevD.34.1642.

[75] Evgeny K. Akhmedov et al. "Left-right symmetry breaking in NJL approach". In: *Phys. Lett. B* 368 (1996), pp. 270–280. DOI: 10.1016/0370-2693(95)01504-3. arXiv: hep-ph/9507275.

[76] Evgeny K. Akhmedov et al. "Dynamical left-right symmetry breaking". In: *Phys. Rev. D* 53 (1996), pp. 2752–2780. DOI: 10.1103/PhysRevD.53.2752. arXiv: hep-ph/9509255.

[77] Peter Minkowski. "$\mu \to e\gamma$ at a Rate of One Out of 10^9 Muon Decays?" In: *Phys. Lett. B* 67 (1977), pp. 421–428. DOI: 10.1016/0370-2693(77)90435-X.

[78] Murray Gell-Mann, Pierre Ramond, and Richard Slansky. "Complex Spinors and Unified Theories". In: *Conf. Proc. C* 790927 (1979), pp. 315–321. arXiv: 1306.4669 [hep-th].

[79] Tsutomu Yanagida. "Horizontal gauge symmetry and masses of neutrinos". In: *Conf. Proc. C* 7902131 (1979). Ed. by Osamu Sawada and Akio Sugamoto, pp. 95–99.

[80] Rabindra N. Mohapatra and Goran Senjanovic. "Neutrino Mass and Spontaneous Parity Nonconservation". In: *Phys. Rev. Lett.* 44 (1980), p. 912. DOI: 10.1103/PhysRevLett.44.912.

[81] J. Schechter and J. W. F. Valle. "Neutrino Masses in SU(2) x U(1) Theories". In: *Phys. Rev. D* 22 (1980), p. 2227. DOI: 10.1103/PhysRevD.22.2227.

[82] J. Schechter and J. W. F. Valle. "Neutrino Decay and Spontaneous Violation of Lepton Number". In: *Phys. Rev. D* 25 (1982), p. 774. DOI: 10.1103/PhysRevD.25.774.

[83] George Lazarides, Q. Shafi, and C. Wetterich. "Proton Lifetime and Fermion Masses in an SO(10) Model". In: *Nucl. Phys. B* 181 (1981), pp. 287–300. DOI: 10.1016/0550-3213(81)90354-0.

[84] Rabindra N. Mohapatra and Goran Senjanovic. "Neutrino Masses and Mixings in Gauge Models with Spontaneous Parity Violation". In: *Phys. Rev. D* 23 (1981), p. 165. DOI: 10.1103/PhysRevD.23.165.

[85] Robert Foot et al. "Seesaw Neutrino Masses Induced by a Triplet of Leptons". In: *Z. Phys. C* 44 (1989), p. 441. DOI: 10.1007/BF01415558.

[86] W. Grimus and L. Lavoura. "The Seesaw mechanism at arbitrary order: Disentangling the small scale from the large scale". In: *JHEP* 11 (2000), p. 042. DOI: 10.1088/1126-6708/2000/11/042. arXiv: hep-ph/0008179.

[87] F. F. Freitas, C. A. de S. Pires, and P. S. Rodrigues da Silva. "Inverse type II seesaw mechanism and its signature at the LHC and ILC". In: *Phys. Lett. B* 769 (2017), pp. 48–56. DOI: 10.1016/j.physletb.2017.03.016. arXiv: 1408.5878 [hep-ph].

[88] A. Zee. "A Theory of Lepton Number Violation, Neutrino Majorana Mass, and Oscillation". In: *Phys. Lett. B* 93 (1980). [Erratum: Phys.Lett.B 95, 461 (1980)], p. 389. DOI: 10.1016/0370-2693(80)90349-4.

[89] K. S. Babu, S. Nandi, and Zurab Tavartkiladze. "New Mechanism for Neutrino Mass Generation and Triply Charged Higgs Bosons at the LHC". In: *Phys. Rev. D* 80 (2009), p. 071702. DOI: 10.1103/PhysRevD.80.071702. arXiv: 0905.2710 [hep-ph].

[90] Gulab Bambhaniya et al. "Generation of neutrino mass from new physics at TeV scale and multilepton signatures at the LHC". In: *Phys. Rev. D* 88.7 (2013), p. 075006. DOI: 10.1103/PhysRevD.88.075006. arXiv: 1305.2795 [hep-ph].

[91] Tathagata Ghosh, Sudip Jana, and S. Nandi. "Neutrino mass from Higgs quadruplet and multicharged Higgs searches at the LHC". In: *Phys. Rev. D* 97.11 (2018), p. 115037. DOI: 10.1103/PhysRevD.97.115037. arXiv: 1802.09251 [hep-ph].

[92] Di Zhang. "Radiative neutrino masses, lepton flavor mixing and muon g − 2 in a leptoquark model". In: *JHEP* 07 (2021), p. 069. DOI: 10.1007/JHEP07(2021)069. arXiv: 2105.08670 [hep-ph].

[93] Snehashis Parashar et al. "Phenomenology of scalar leptoquarks at the LHC in explaining the radiative neutrino masses, muon g-2, and lepton flavor violating observables". In: *Phys. Rev. D* 106.9 (2022), p. 095040. DOI: 10.1103/PhysRevD.106.095040. arXiv: 2209.05890 [hep-ph].

[94] D. Aristizabal Sierra, M. Hirsch, and S. G. Kovalenko. "Leptoquarks: Neutrino masses and accelerator phenomenology". In: *Phys. Rev. D* 77 (2008), p. 055011. DOI: 10.1103/PhysRevD.77.055011. arXiv: 0710.5699 [hep-ph].

[95] Yi Cai et al. "Testing Radiative Neutrino Mass Models at the LHC". In: *JHEP* 02 (2015), p. 161. DOI: 10.1007/JHEP02(2015)161. arXiv: 1410.0689 [hep-ph].

[96] Ilja Doršner, Svjetlana Fajfer, and Nejc Košnik. "Leptoquark mechanism of neutrino masses within the grand unification framework". In: *Eur. Phys. J. C* 77.6 (2017), p. 417. DOI: 10.1140/epjc/s10052-017-4987-2. arXiv: 1701.08322 [hep-ph].

[97] R. N. Mohapatra and P. B. Pal. *Massive neutrinos in physics and astrophysics*. Vol. 41. 1991.

[98] Wilhelm H. Bertl et al. "A Search for muon to electron conversion in muonic gold". In: *Eur. Phys. J. C* 47 (2006), pp. 337–346. DOI: 10.1140/epjc/s2006-02582-x.

[99] K. Afanaciev et al. "A search for $\mu^+ \to e^+\gamma$ with the first dataset of the MEG II experiment". In: *Eur. Phys. J. C* 84.3 (2024), p. 216. DOI: 10.1140/epjc/s10052-024-12416-2. arXiv: 2310.12614 [hep-ex].

[100] U. Bellgardt et al. "Search for the Decay $\mu^+ \to e^+e^+e^-$". In: *Nucl. Phys. B* 299 (1988), pp. 1–6. DOI: 10.1016/0550-3213(88)90462-2.

[101] Kazuo Fujikawa and Robert Shrock. "On a neutrino electroweak radius". In: *Phys. Rev. D* 69 (2004), p. 013007. DOI: 10.1103/PhysRevD.69.013007. arXiv: hep-ph/0309329.

[102] A. Bolaños-Carrera, M. Guiot-Lomelí, and G. Tavares-Velasco. "Neutrino charge radius and electromagnetic dipole moments via scalar and vector leptoquarks". In: *Eur. Phys. J. C* 84.3 (2024), p. 217. DOI: 10.1140/epjc/s10052-024-12495-1. arXiv: 2308.07493 [hep-ph].

[103] Francesco Capozzi and Georg Raffelt. "Axion and neutrino bounds improved with new calibrations of the tip of the red-giant branch using geometric distance determinations". In: *Phys. Rev. D* 102.8 (2020), p. 083007. DOI: 10.1103/PhysRevD.102.083007. arXiv: 2007.03694 [astro-ph.SR].

[104] F. del Aguila and Marc Sher. "The Electric dipole moment of the tau". In: *Phys. Lett. B* 252 (1990), pp. 116–118. DOI: 10.1016/0370-2693(90)91091-O.

[105] Keiichi Akama, Takashi Hattori, and Kazuo Katsuura. "Naturalness bounds on dipole moments from new physics". In: *Phys. Rev. Lett.* 88 (2002), p. 201601. DOI: 10.1103/PhysRevLett.88.201601. arXiv: hep-ph/0111238.

[106] Steen Hannestad. "Primordial neutrinos". In: *Ann. Rev. Nucl. Part. Sci.* 56 (2006), pp. 137–161. DOI: 10.1146/annurev.nucl.56.080805.140548. arXiv: hep-ph/0602058.

[107] Eleonora Di Valentino, Stefano Gariazzo, and Olga Mena. "Neutrinos in Cosmology". In: (Apr. 2024). arXiv: 2404.19322 [astro-ph.CO].

[108] Julien Froustey, Cyril Pitrou, and Maria Cristina Volpe. "Neutrino decoupling including flavour oscillations and primordial nucleosynthesis". In: *JCAP* 12 (2020), p. 015. DOI: 10.1088/1475-7516/2020/12/015. arXiv: 2008.01074 [hep-ph].

[109] Jack J. Bennett et al. "Towards a precision calculation of $N_{\rm eff}$ in the Standard Model II: Neutrino decoupling in the presence of flavour oscillations and finite-temperature QED". In: *JCAP* 04 (2021), p. 073. DOI: 10.1088/1475-7516/2021/04/073. arXiv: 2012.02726 [hep-ph].

[110] Cyril Pitrou et al. "Precision big bang nucleosynthesis with improved Helium-4 predictions". In: *Phys. Rept.* 754 (2018), pp. 1–66. DOI: 10.1016/j.physrep.2018.04.005. arXiv: 1801.08023 [astro-ph.CO].

[111] Shouvik Roy Choudhury. "Neutrino mass bounds from cosmology". PhD thesis. HBNI, Mumbai, 2020.

[112] A. Ashtari Esfahani et al. "The Project 8 Neutrino Mass Experiment". In: *Snowmass 2021*. Mar. 2022. arXiv: 2203.07349 [nucl-ex].

[113] Joseph A. Formaggio, André Luiz C. de Gouvêa, and R. G. Hamish Robertson. "Direct Measurements of Neutrino Mass". In: *Phys. Rept.* 914 (2021), pp. 1–54. DOI: 10.1016/j.physrep.2021.02.002. arXiv: 2102.00594 [nucl-ex].

[114] P. J. Doe et al. "Project 8: Determining neutrino mass from tritium beta decay using a frequency-based method". In: *Snowmass 2013: Snowmass on the Mississippi*. Sept. 2013. arXiv: 1309.7093 [nucl-ex].

[115] J. Schechter and J. W. F. Valle. "Neutrinoless Double beta Decay in SU(2) x U(1) Theories". In: *Phys. Rev. D* 25 (1982), p. 2951. DOI: 10.1103/PhysRevD.25.2951.

[116] S. Abe et al. "Search for Majorana Neutrinos with the Complete KamLAND-Zen Dataset". In: (June 2024). arXiv: 2406.11438 [hep-ex].

[117] M. Agostini et al. "Final Results of GERDA on the Search for Neutrinoless Double-β Decay". In: *Phys. Rev. Lett.* 125.25 (2020), p. 252502. DOI: 10.1103/PhysRevLett.125.252502. arXiv: 2009.06079 [nucl-ex].

[118] O. Azzolini et al. "Final Result on the Neutrinoless Double Beta Decay of ^{82}Se with CUPID-0". In: *Phys. Rev. Lett.* 129.11 (2022), p. 111801. DOI: 10.1103/PhysRevLett.129.111801. arXiv: 2206.05130 [hep-ex].

[119] D. Q. Adams et al. "New Direct Limit on Neutrinoless Double Beta Decay Half-Life of Te128 with CUORE". In: *Phys. Rev. Lett.* 129.22 (2022), p. 222501. DOI: 10.1103/PhysRevLett.129.222501. arXiv: 2205.03132 [nucl-ex].

[120] N. Abgrall et al. "The Large Enriched Germanium Experiment for Neutrinoless $\beta\beta$ Decay: LEGEND-1000 Preconceptual Design Report". In: (July 2021). arXiv: 2107.11462 [physics.ins-det].

[121] G. Anton et al. "Search for Neutrinoless Double-β Decay with the Complete EXO-200 Dataset". In: *Phys. Rev. Lett.* 123.16 (2019), p. 161802. DOI: 10.1103/PhysRevLett.123.161802. arXiv: 1906.02723 [hep-ex].

[122] G. Adhikari et al. "nEXO: neutrinoless double beta decay search beyond 10^{28} year half-life sensitivity". In: *J. Phys. G* 49.1 (2022), p. 015104. DOI: 10.1088/1361-6471/ac3631. arXiv: 2106.16243 [nucl-ex].

[123] A. Aguilar et al. "Evidence for neutrino oscillations from the observation of $\overline{\nu}_e$ appearance in a $\overline{\nu}_\mu$ beam". In: *Phys. Rev. D* 64 (2001), p. 112007. DOI: 10.1103/PhysRevD.64.112007. arXiv: hep-ex/0104049.

[124] A. A. Aguilar-Arevalo et al. "Updated MiniBooNE neutrino oscillation results with increased data and new background studies". In: *Phys. Rev. D* 103.5 (2021), p. 052002. DOI: 10.1103/PhysRevD.103.052002. arXiv: 2006.16883 [hep-ex].

[125] Srubabati Goswami. "Accelerator, reactor, solar and atmospheric neutrino oscillation: Beyond three generations". In: *Phys. Rev. D* 55 (1997), pp. 2931–2949. DOI: 10.1103/PhysRevD.55.2931. arXiv: hep-ph/9507212.

[126] B. Armbruster et al. "Upper limits for neutrino oscillations muon-anti-neutrino —> electron-anti-neutrino from muon decay at rest". In: *Phys. Rev. D* 65 (2002), p. 112001. DOI: 10.1103/PhysRevD.65.112001. arXiv: hep-ex/0203021.

[127] P Astier et al. "Final NOMAD results on muon-neutrino —> tau-neutrino and electron-neutrino —> tau-neutrino oscillations including a new search for tau-neutrino appearance using hadronic tau decays". In: *Nucl. Phys. B* 611 (2001), pp. 3–39. DOI: 10.1016/S0550-3213(01)00339-X. arXiv: hep-ex/0106102.

[128] M Antonello et al. "Experimental search for the "LSND anomaly" with the ICARUS detector in the CNGS neutrino beam". In: *Eur. Phys. J. C* 73.3 (2013), p. 2345. DOI: 10.1140/epjc/s10052-013-2345-6. arXiv: 1209.0122 [hep-ex].

[129] A. A. Aguilar-Arevalo et al. "Improved Search for $\overline{\nu}_\mu \to \overline{\nu}_e$ Oscillations in the MiniBooNE Experiment". In: *Phys. Rev. Lett.* 110 (2013), p. 161801. DOI: 10.1103/PhysRevLett.110.161801. arXiv: 1303.2588 [hep-ex].

[130] A. A. Aguilar-Arevalo et al. "Significant Excess of ElectronLike Events in the MiniBooNE Short-Baseline Neutrino Experiment". In: *Phys. Rev. Lett.* 121.22 (2018), p. 221801. DOI: 10.1103/PhysRevLett.121.221801. arXiv: 1805.12028 [hep-ex].

[131] Mona Dentler et al. "Updated Global Analysis of Neutrino Oscillations in the Presence of eV-Scale Sterile Neutrinos". In: *JHEP* 08 (2018), p. 010. DOI: 10.1007/JHEP08(2018)010. arXiv: 1803.10661 [hep-ph].

[132] K. N. Abazajian et al. "Light Sterile Neutrinos: A White Paper". In: (Apr. 2012). arXiv: 1204.5379 [hep-ph].

[133] P. Adamson et al. "Search for sterile neutrinos in MINOS and MINOS+ using a two-detector fit". In: *Phys. Rev. Lett.* 122.9 (2019), p. 091803. DOI: 10.1103/PhysRevLett.122.091803. arXiv: 1710.06488 [hep-ex].

[134] K. Abe et al. "Search for light sterile neutrinos with the T2K far detector Super-Kamiokande at a baseline of 295 km". In: *Phys. Rev. D* 99.7 (2019), p. 071103. DOI: 10.1103/PhysRevD.99.071103. arXiv: 1902.06529 [hep-ex].

[135] C. A. Argüelles et al. "MicroBooNE and the νe Interpretation of the MiniBooNE Low-Energy Excess". In: *Phys. Rev. Lett.* 128.24 (2022), p. 241802. DOI: 10.1103/PhysRevLett.128.241802. arXiv: 2111.10359 [hep-ph].

[136] Harry R. Hausner. "Sterile neutrino search with the NOvA detectors". PhD thesis. U. Wisconsin, Madison (main), Wisconsin U., Madison, SAL, 2022.

[137] David Vannerom et al. "Search for sterile neutrinos in low-energy double-cascade events with the IceCube Neutrino Observatory: a first expected sensitivity". In: *PoS* PANIC2021 (2022), p. 299. DOI: 10.22323/1.380.0299.

[138] Zhuojun Hu. "Improved Limits on Sterile Neutrino Mixing from a Joint Search of the MINOS, MINOS+, Daya Bay, and Bugey-3 Experiments". In: *PoS* ICHEP2020 (2021), p. 201. DOI: 10.22323/1.390.0201.

[139] P. Adamson et al. "Improved Constraints on Sterile Neutrino Mixing from Disappearance Searches in the MINOS, MINOS+, Daya Bay, and Bugey-3 Experiments". In: *Phys. Rev. Lett.* 125.7 (2020), p. 071801. DOI: 10.1103/PhysRevLett.125.071801. arXiv: 2002.00301 [hep-ex].

[140] P. Abratenko et al. "Search for an Excess of Electron Neutrino Interactions in MicroBooNE Using Multiple Final-State Topologies". In: *Phys. Rev. Lett.* 128.24 (2022), p. 241801. DOI: 10.1103/PhysRevLett.128.241801. arXiv: 2110.14054 [hep-ex].

[141] P. Abratenko et al. "Search for an anomalous excess of charged-current quasielastic νe interactions with the MicroBooNE experiment using Deep-Learning-based reconstruction". In: *Phys. Rev. D* 105.11 (2022), p. 112003. DOI: 10.1103/PhysRevD.105.112003. arXiv: 2110.14080 [hep-ex].

[142] P. Abratenko et al. "Search for an anomalous excess of charged-current νe interactions without pions in the final state with the MicroBooNE experiment". In: *Phys. Rev. D* 105.11 (2022), p. 112004. DOI: 10.1103/PhysRevD.105.112004. arXiv: 2110.14065 [hep-ex].

[143] P. Abratenko et al. "First Constraints on Light Sterile Neutrino Oscillations from Combined Appearance and Disappearance Searches with the MicroBooNE Detector". In: *Phys. Rev. Lett.* 130.1 (2023), p. 011801. DOI: 10.1103/PhysRevLett.130.011801. arXiv: 2210.10216 [hep-ex].

[144] Peter B. Denton. "Sterile Neutrino Search with MicroBooNE's Electron Neutrino Disappearance Data". In: *Phys. Rev. Lett.* 129.6 (2022), p. 061801. DOI: 10.1103/PhysRevLett.129.061801. arXiv: 2111.05793 [hep-ph].

[145] A. A. Aguilar-Arevalo et al. "MiniBooNE and MicroBooNE Combined Fit to a 3+1 Sterile Neutrino Scenario". In: *Phys. Rev. Lett.* 129.20 (2022), p. 201801. DOI: 10.1103/PhysRevLett.129.201801. arXiv: 2201.01724 [hep-ex].

[146] M. Aker et al. "Search for keV-scale sterile neutrinos with the first KATRIN data". In: *Eur. Phys. J. C* 83.8 (2023), p. 763. DOI: 10.1140/epjc/s10052-023-11818-y. arXiv: 2207.06337 [nucl-ex].

[147] R. Acciarri et al. "A Proposal for a Three Detector Short-Baseline Neutrino Oscillation Program in the Fermilab Booster Neutrino Beam". In: (Mar. 2015). arXiv: 1503.01520 [physics.ins-det].

[148] S. Ajimura et al. "The JSNS2 detector". In: *Nucl. Instrum. Meth. A* 1014 (2021), p. 165742. DOI: 10.1016/j.nima.2021.165742. arXiv: 2104.13169 [physics.ins-det].

[149] W. Hampel et al. "Final results of the Cr-51 neutrino source experiments in GALLEX". In: *Phys. Lett. B* 420 (1998), pp. 114–126. DOI: 10.1016/S0370-2693(97)01562-1.

[150] Dzh. N. Abdurashitov et al. "The Russian-American gallium experiment (SAGE) Cr neutrino source measurement". In: *Phys. Rev. Lett.* 77 (1996), pp. 4708–4711. DOI: 10.1103/PhysRevLett.77.4708.

[151] V. V. Barinov et al. "Results from the Baksan Experiment on Sterile Transitions (BEST)". In: *Phys. Rev. Lett.* 128.23 (2022), p. 232501. DOI: 10.1103/PhysRevLett.128.232501. arXiv: 2109.11482 [nucl-ex].

[152] G. Bellini et al. "Measurement of the solar 8B neutrino rate with a liquid scintillator target and 3 MeV energy threshold in the Borexino detector". In: *Phys. Rev. D* 82 (2010), p. 033006. DOI: 10.1103/PhysRevD.82.033006. arXiv: 0808.2868 [astro-ph].

[153] P. C. de Holanda and A. Yu. Smirnov. "Solar neutrino spectrum, sterile neutrinos and additional radiation in the Universe". In: *Phys. Rev. D* 83 (2011), p. 113011. DOI: 10.1103/PhysRevD.83.113011. arXiv: 1012.5627 [hep-ph].

[154] K. Abe et al. "The T2K Experiment". In: *Nucl. Instrum. Meth. A* 659 (2011), pp. 106–135. DOI: 10.1016/j.nima.2011.06.067. arXiv: 1106.1238 [physics.ins-det].

[155] K. Abe et al. "Measurements of neutrino oscillation in appearance and disappearance channels by the T2K experiment with 6.6×10^{20} protons on target". In: *Phys. Rev. D* 91.7 (2015), p. 072010. DOI: 10.1103/PhysRevD.91.072010. arXiv: 1502.01550 [hep-ex].

[156] K. Abe et al. "Measurement of neutrino and antineutrino oscillations by the T2K experiment including a new additional sample of ν_e interactions at the far detector". In: *Phys. Rev. D* 96.9 (2017). [Erratum: Phys.Rev.D 98, 019902 (2018)], p. 092006. DOI: 10.1103/PhysRevD.96.092006. arXiv: 1707.01048 [hep-ex].

[157] K. Abe et al. "Combined Analysis of Neutrino and Antineutrino Oscillations at T2K". In: *Phys. Rev. Lett.* 118.15 (2017), p. 151801. DOI: 10.1103/PhysRevLett.118.151801. arXiv: 1701.00432 [hep-ex].

[158] P. Adamson et al. "First measurement of electron neutrino appearance in NOvA". In: *Phys. Rev. Lett.* 116.15 (2016), p. 151806. DOI: 10.1103/PhysRevLett.116.151806. arXiv: 1601.05022 [hep-ex].

[159] M. A. Acero et al. "New constraints on oscillation parameters from ν_e appearance and ν_μ disappearance in the NOvA experiment". In: *Phys. Rev. D* 98 (2018), p. 032012. DOI: 10.1103/PhysRevD.98.032012. arXiv: 1806.00096 [hep-ex].

[160] M. A. Acero et al. "First Measurement of Neutrino Oscillation Parameters using Neutrinos and Antineutrinos by NOvA". In: *Phys. Rev. Lett.* 123.15 (2019), p. 151803. DOI: 10.1103/PhysRevLett.123.151803. arXiv: 1906.04907 [hep-ex].

[161] André de Gouvêa, Giancarlo Jusino Sánchez, and Kevin J. Kelly. "Very light sterile neutrinos at NOvA and T2K". In: *Phys. Rev. D* 106.5 (2022), p. 055025. DOI: 10.1103/PhysRevD.106.055025. arXiv: 2204.09130 [hep-ph].

[162] Sanjib Kumar Agarwalla, Sabya Sachi Chatterjee, and Antonio Palazzo. "Physics potential of ESSνSB in the presence of a light sterile neutrino". In: *JHEP* 12 (2019), p. 174. DOI: 10.1007/JHEP12(2019)174. arXiv: 1909.13746 [hep-ph].

[163] Sanjib Kumar Agarwalla, Sabya Sachi Chatterjee, and Antonio Palazzo. "Signatures of a Light Sterile Neutrino in T2HK". In: *JHEP* 04 (2018), p. 091. DOI: 10.1007/JHEP04(2018)091. arXiv: 1801.04855 [hep-ph].

[164] Animesh Chatterjee, Srubabati Goswami, and Supriya Pan. "Probing mass orderings in presence of a very light sterile neutrino in a liquid argon detector". In: *Nucl. Phys. B* 996 (2023), p. 116370. DOI: 10.1016/j.nuclphysb.2023.116370. arXiv: 2307.12885 [hep-ph].

[165] Animesh Chatterjee, Srubabati Goswami, and Supriya Pan. "Matter effect in presence of a sterile neutrino and resolution of the octant degeneracy using a liquid argon detector". In: *Phys. Rev. D* 108.9 (2023), p. 095050. DOI: 10.1103/PhysRevD.108.095050. arXiv: 2212.02949 [hep-ph].

[166] Srubabati Goswami and Werner Rodejohann. "Constraining mass spectra with sterile neutrinos from neutrinoless double beta decay, tritium beta decay and cosmology". In: *Phys. Rev. D* 73 (2006), p. 113003. DOI: 10.1103/PhysRevD.73.113003. arXiv: hep-ph/0512234.

[167] Kensuke Akita and Masahide Yamaguchi. "A precision calculation of relic neutrino decoupling". In: *JCAP* 08 (2020), p. 012. DOI: 10.1088/1475-7516/2020/08/012. arXiv: 2005.07047 [hep-ph].

[168] Carlos E. Yaguna. "Sterile neutrino production in models with low reheating temperatures". In: *JHEP* 06 (2007), p. 002. DOI: 10.1088/1126-6708/2007/06/002. arXiv: 0706.0178 [hep-ph].

[169] Kevork N. Abazajian. "Sterile neutrinos in cosmology". In: *Phys. Rept.* 711-712 (2017), pp. 1–28. DOI: 10.1016/j.physrep.2017.10.003. arXiv: 1705.01837 [hep-ph].

[170] Basudeb Dasgupta and Joachim Kopp. "Cosmologically Safe eV-Scale Sterile Neutrinos and Improved Dark Matter Structure". In: *Phys. Rev. Lett.* 112.3 (2014), p. 031803. DOI: 10.1103/PhysRevLett.112.031803. arXiv: 1310.6337 [hep-ph].

[171] Xiaoyong Chu, Basudeb Dasgupta, and Joachim Kopp. "Sterile neutrinos with secret interactions—lasting friendship with cosmology". In: *JCAP* 10 (2015), p. 011. DOI: 10.1088/1475-7516/2015/10/011. arXiv: 1505.02795 [hep-ph].

[172] Mario A. Acero and Julien Lesgourgues. "Cosmological constraints on a light non-thermal sterile neutrino". In: *Phys. Rev. D* 79 (2009), p. 045026. DOI: 10.1103/PhysRevD.79.045026. arXiv: 0812.2249 [astro-ph].

[173] Scott Dodelson and Lawrence M. Widrow. "Sterile-neutrinos as dark matter". In: *Phys. Rev. Lett.* 72 (1994), pp. 17–20. DOI: 10.1103/PhysRevLett.72.17. arXiv: hep-ph/9303287.

[174] Adam G. Riess et al. "New Parallaxes of Galactic Cepheids from Spatially Scanning the Hubble Space Telescope: Implications for the Hubble Constant". In: *Astrophys. J.* 855.2 (2018), p. 136. DOI: 10.3847/1538-4357/aaadb7. arXiv: 1801.01120 [astro-ph.SR].

[175] D. M. Scolnic et al. "The Complete Light-curve Sample of Spectroscopically Confirmed SNe Ia from Pan-STARRS1 and Cosmological Constraints from the Combined Pantheon Sample". In: *Astrophys. J.* 859.2 (2018), p. 101. DOI: 10.3847/1538-4357/aab9bb. arXiv: 1710.00845 [astro-ph.CO].

[176] M. A. Acero et al. "White Paper on Light Sterile Neutrino Searches and Related Phenomenology". In: (Mar. 2022). arXiv: 2203.07323 [hep-ex].

[177] Steffen Hagstotz et al. "Bounds on light sterile neutrino mass and mixing from cosmology and laboratory searches". In: *Phys. Rev. D* 104.12 (2021), p. 123524. DOI: 10.1103/PhysRevD.104.123524. arXiv: 2003.02289 [astro-ph.CO].

[178] Graciela Gelmini, Sergio Palomares-Ruiz, and Silvia Pascoli. "Low reheating temperature and the visible sterile neutrino". In: *Phys. Rev. Lett.* 93 (2004), p. 081302. DOI: 10.1103/PhysRevLett.93.081302. arXiv: astro-ph/0403323.

[179] Graciela B. Gelmini, Philip Lu, and Volodymyr Takhistov. "Visible Sterile Neutrinos as the Earliest Relic Probes of Cosmology". In: *Phys. Lett. B* 800 (2020), p. 135113. DOI: 10.1016/j.physletb.2019.135113. arXiv: 1909.04168 [hep-ph].

[180] Takuya Hasegawa et al. "MeV-scale reheating temperature and cosmological production of light sterile neutrinos". In: *JCAP* 08 (2020), p. 015. DOI: 10.1088/1475-7516/2020/08/015. arXiv: 2003.13302 [hep-ph].

[181] Ninetta Saviano et al. "Unveiling secret interactions among sterile neutrinos with big-bang nucleosynthesis". In: *Phys. Rev. D* 90.11 (2014), p. 113009. DOI: 10.1103/PhysRevD.90.113009. arXiv: 1409.1680 [astro-ph.CO].

[182] Maria Archidiacono et al. "Cosmology with self-interacting sterile neutrinos and dark matter - A pseudoscalar model". In: *Phys. Rev. D* 91.6 (2015), p. 065021. DOI: 10.1103/PhysRevD.91.065021. arXiv: 1404.5915 [astro-ph.CO].

[183] Maria Archidiacono et al. "Pseudoscalar—sterile neutrino interactions: reconciling the cosmos with neutrino oscillations". In: *JCAP* 08 (2016), p. 067. DOI: 10.1088/1475-7516/2016/08/067. arXiv: 1606.07673 [astro-ph.CO].

[184] Francesco Forastieri et al. "Cosmic microwave background constraints on secret interactions among sterile neutrinos". In: *JCAP* 07 (2017), p. 038. DOI: 10.1088/1475-7516/2017/07/038. arXiv: 1704.00626 [astro-ph.CO].

[185] Xiaoyong Chu et al. "Sterile neutrinos with secret interactions—cosmological discord?" In: *JCAP* 11 (2018), p. 049. DOI: 10.1088/1475-7516/2018/11/049. arXiv: 1806.10629 [hep-ph].

[186] Jeffrey M. Berryman and Patrick Huber. "Reevaluating Reactor Antineutrino Anomalies with Updated Flux Predictions". In: *Phys. Rev. D* 101.1 (2020), p. 015008. DOI: 10.1103/PhysRevD.101.015008. arXiv: 1909.09267 [hep-ph].

[187] Christina D. Kreisch, Francis-Yan Cyr-Racine, and Olivier Doré. "Neutrino puzzle: Anomalies, interactions, and cosmological tensions". In: *Phys. Rev. D* 101.12 (2020), p. 123505. DOI: 10.1103/PhysRevD.101.123505. arXiv: 1902.00534 [astro-ph.CO].

[188] P. Adamson et al. "Constraints on Large Extra Dimensions from the MINOS Experiment". In: *Phys. Rev. D* 94.11 (2016), p. 111101. DOI: 10.1103/PhysRevD.94.111101. arXiv: 1608.06964 [hep-ex].

[189] G. L. Fogli et al. "Observables sensitive to absolute neutrino masses: Constraints and correlations from world neutrino data". In: *Phys. Rev. D* 70 (2004), p. 113003. DOI: 10.1103/PhysRevD.70.113003. arXiv: hep-ph/0408045.

[190] K. S. Babu. "Model of 'Calculable' Majorana Neutrino Masses". In: *Phys. Lett. B* 203 (1988), pp. 132–136. DOI: 10.1016/0370-2693(88)91584-5.

[191] Yi Cai et al. "From the trees to the forest: a review of radiative neutrino mass models". In: *Front. in Phys.* 5 (2017), p. 63. DOI: 10.3389/fphy.2017.00063. arXiv: 1706.08524 [hep-ph].

[192] Savas Dimopoulos and Leonard Susskind. "Mass Without Scalars". In: *Nucl. Phys. B* 155 (1979). Ed. by A. Zichichi, pp. 237–252. DOI: 10.1016/0550-3213(79)90364-X.

[193] Jogesh C. Pati and Abdus Salam. "Unified Lepton-Hadron Symmetry and a Gauge Theory of the Basic Interactions". In: *Phys. Rev. D* 8 (1973), pp. 1240–1251. DOI: 10.1103/PhysRevD.8.1240.

[194] Harald Fritzsch and Peter Minkowski. "Unified Interactions of Leptons and Hadrons". In: *Annals Phys.* 93 (1975), pp. 193–266. DOI: 10.1016/0003-4916(75)90211-0.

[195] I. Doršner et al. "Physics of leptoquarks in precision experiments and at particle colliders". In: *Phys. Rept.* 641 (2016), pp. 1–68. DOI: 10.1016/j.physrep.2016.06.001. arXiv: 1603.04993 [hep-ph].

[196] Lawrence J. Hall and Mahiko Suzuki. "Explicit R-Parity Breaking in Supersymmetric Models". In: *Nucl. Phys. B* 231 (1984), pp. 419–444. DOI: 10.1016/0550-3213(84)90513-3.

[197] M. Hirsch, H. V. Klapdor-Kleingrothaus, and S. G. Kovalenko. "New leptoquark mechanism of neutrinoless double beta decay". In: *Phys. Rev. D* 54 (1996), R4207–R4210. DOI: 10.1103/PhysRevD.54.R4207. arXiv: hep-ph/9603213.

[198] L. Lavoura. "General formulae for f(1) —> f(2) gamma". In: *Eur. Phys. J. C* 29 (2003), pp. 191–195. DOI: 10.1140/epjc/s2003-01212-7. arXiv: hep-ph/0302221.

[199] Rachid Benbrik and Chun-Khiang Chua. "Lepton Flavor Violating $l \to l'\gamma$ and $Z \to l\bar{l}\prime$ Decays Induced by Scalar Leptoquarks". In: *Phys. Rev. D* 78 (2008), p. 075025. DOI: 10.1103/PhysRevD.78.075025. arXiv: 0807.4240 [hep-ph].

[200] Bibhabasu De. "Leptoquark-induced CLFV decays with a light SM-singlet scalar". In: *Phys. Lett. B* 855 (2024), p. 138784. DOI: 10.1016/j.physletb.2024.138784. arXiv: 2405.06970 [hep-ph].

[201] S. Fajfer, N. Košnik, and L. Vale Silva. "Footprints of leptoquarks: from $R_{K^{(*)}}$ to $K \to \pi\nu\bar{\nu}$". In: *Eur. Phys. J. C* 78.4 (2018), p. 275. DOI: 10.1140/epjc/s10052-018-5757-5. arXiv: 1802.00786 [hep-ph].

[202] Sébastien Descotes-Genon et al. "Implications of $b \to s\mu\mu$ anomalies for future measurements of $B \to K^{(*)}\nu\bar{\nu}$ and $K \to \pi\nu\bar{\nu}$". In: *Phys. Lett. B* 809 (2020). [Addendum: Phys.Lett.B 840, 137830 (2023)], p. 135769. DOI: 10.1016/j.physletb.2020.135769. arXiv: 2005.03734 [hep-ph].

[203] Frank F. Deppisch, Kåre Fridell, and Julia Harz. "Constraining lepton number violating interactions in rare kaon decays". In: *JHEP* 12 (2020), p. 186. DOI: 10.1007/JHEP12(2020)186. arXiv: 2009.04494 [hep-ph].

[204] Andreas Crivellin, Dario Müller, and Francesco Saturnino. "Flavor Phenomenology of the Leptoquark Singlet-Triplet Model". In: *JHEP* 06 (2020), p. 020. DOI: 10.1007/JHEP06(2020)020. arXiv: 1912.04224 [hep-ph].

[205] Andreas Crivellin, Dario Müller, and Toshihiko Ota. "Simultaneous explanation of R($D^{(*)}$) and b$\to s\mu^+\mu^-$: the last scalar leptoquarks standing". In: *JHEP* 09 (2017), p. 040. DOI: 10.1007/JHEP09(2017)040. arXiv: 1703.09226 [hep-ph].

[206] Andreas Crivellin, Benjamin Fuks, and Luc Schnell. "Explaining the hints for lepton flavour universality violation with three S_2 leptoquark generations". In: *JHEP* 06 (2022), p. 169. DOI: 10.1007/JHEP06(2022)169. arXiv: 2203.10111 [hep-ph].

[207] Andreas Crivellin et al. "Scalar Leptoquarks in Leptonic Processes". In: *JHEP* 02 (2021), p. 182. DOI: 10.1007/JHEP02(2021)182. arXiv: 2010.06593 [hep-ph].

[208] Estefania Coluccio Leskow et al. "$(g-2)\mu$, lepton flavor violation, and Z decays with leptoquarks: Correlations and future prospects". In: *Phys. Rev. D* 95.5 (2017), p. 055018. DOI: 10.1103/PhysRevD.95.055018. arXiv: 1612.06858 [hep-ph].

[209] Andreas Crivellin, Dario Mueller, and Francesco Saturnino. "Correlating h→μ+μ- to the Anomalous Magnetic Moment of the Muon via Leptoquarks". In: *Phys. Rev. Lett.* 127.2 (2021), p. 021801. DOI: 10.1103/PhysRevLett.127.021801. arXiv: 2008.02643 [hep-ph].

[210] Yasuhito Sakaki et al. "Testing leptoquark models in $\overline{B} \to D^{(*)}\tau\overline{\nu}$". In: *Phys. Rev. D* 88.9 (2013), p. 094012. DOI: 10.1103/PhysRevD.88.094012. arXiv: 1309.0301 [hep-ph].

[211] Martin Bauer and Matthias Neubert. "Minimal Leptoquark Explanation for the $R_{D^{(*)}}$, R_K , and $(g-2)_\mu$ Anomalies". In: *Phys. Rev. Lett.* 116.14 (2016), p. 141802. DOI: 10.1103/PhysRevLett.116.141802. arXiv: 1511.01900 [hep-ph].

[212] Oleg Popov and Graham A White. "One Leptoquark to unify them? Neutrino masses and unification in the light of $(g-2)_\mu$, $R_{D^{(*)}}$ and R_K anomalies". In: *Nucl. Phys. B* 923 (2017), pp. 324–338. DOI: 10.1016/j.nuclphysb.2017.08.007. arXiv: 1611.04566 [hep-ph].

[213] Yi Cai et al. "Reconsidering the One Leptoquark solution: flavor anomalies and neutrino mass". In: *JHEP* 10 (2017), p. 047. DOI: 10.1007/JHEP10(2017)047. arXiv: 1704.05849 [hep-ph].

[214] Wolfgang Altmannshofer, P. S. Bhupal Dev, and Amarjit Soni. "$R_{D^{(*)}}$ anomaly: A possible hint for natural supersymmetry with R-parity violation". In: *Phys. Rev. D* 96.9 (2017), p. 095010. DOI: 10.1103/PhysRevD.96.095010. arXiv: 1704.06659 [hep-ph].

[215] Andrei Angelescu et al. "Single leptoquark solutions to the B-physics anomalies". In: *Phys. Rev. D* 104.5 (2021), p. 055017. DOI: 10.1103/PhysRevD.104.055017. arXiv: 2103.12504 [hep-ph].

[216] Bernat Capdevila, Andreas Crivellin, and Joaquim Matias. "Review of Semileptonic B Anomalies". In: *Eur. Phys. J. ST* 1 (2023), p. 20. DOI: 10.1140/epjs/s11734-023-01012-2. arXiv: 2309.01311 [hep-ph].

[217] A. Angelescu et al. "Closing the window on single leptoquark solutions to the B-physics anomalies". In: *JHEP* 10 (2018), p. 183. DOI: 10.1007/JHEP10(2018)183. arXiv: 1808.08179 [hep-ph].

[218] J. C. Helo et al. "Short-range mechanisms of neutrinoless double beta decay at the LHC". In: *Phys. Rev. D* 88 (2013), p. 073011. DOI: 10.1103/PhysRevD.88.073011. arXiv: 1307.4849 [hep-ph].

[219] Heinrich Päs and Erik Schumacher. "Common origin of R_K and neutrino masses". In: *Phys. Rev. D* 92.11 (2015), p. 114025. DOI: 10.1103/PhysRevD.92.114025. arXiv: 1510.08757 [hep-ph].

[220] Michael L. Graesser et al. "Uncovering a chirally suppressed mechanism of $0\nu\beta\beta$ decay with LHC searches". In: *JHEP* 10 (2022), p. 034. DOI: 10.1007/JHEP10(2022)034. arXiv: 2202.01237 [hep-ph].

[221] Lukáš Gráf, Manfred Lindner, and Oliver Scholer. "Unraveling the $0\nu\beta\beta$ decay mechanisms". In: *Phys. Rev. D* 106.3 (2022), p. 035022. DOI: 10.1103/PhysRevD.106.035022. arXiv: 2204.10845 [hep-ph].

[222] Oliver Scholer, Jordy de Vries, and Lukáš Gráf. "νDoBe — A Python tool for neutrinoless double beta decay". In: *JHEP* 08 (2023), p. 043. DOI: 10.1007/JHEP08(2023)043. arXiv: 2304.05415 [hep-ph].

[223] Gang Li, Jiang-Hao Yu, and Xiang Zhao. "Complementary LHC searches for UV resonances of the $0\nu\beta\beta$ decay operators". In: *Phys. Rev. D* 109.5 (2024), p. 055012. DOI: 10.1103/PhysRevD.109.055012. arXiv: 2311.10079 [hep-ph].

[224] R. Aaij et al. "Test of lepton universality in $b \to s\ell^+\ell^-$ decays". In: *Phys. Rev. Lett.* 131.5 (2023), p. 051803. DOI: 10.1103/PhysRevLett.131.051803. arXiv: 2212.09152 [hep-ex].

[225] R. Aaij et al. "Measurement of lepton universality parameters in $B^+ \to K^+\ell^+\ell^-$ and $B^0 \to K^{*0}\ell^+\ell^-$ decays". In: *Phys. Rev. D* 108.3 (2023), p. 032002. DOI: 10.1103/PhysRevD.108.032002. arXiv: 2212.09153 [hep-ex].

[226] Wolfgang Altmannshofer et al. "Addressing $R_{D^{(*)}}$, $R_{K^{(*)}}$, muon $g-2$ and ANITA anomalies in a minimal R-parity violating supersymmetric framework". In: *Phys. Rev. D* 102.1 (2020), p. 015031. DOI: 10.1103/PhysRevD.102.015031. arXiv: 2002.12910 [hep-ph].

[227] P. S. Bhupal Dev, Amarjit Soni, and Fang Xu. "Hints of natural supersymmetry in flavor anomalies?" In: *Phys. Rev. D* 106.1 (2022), p. 015014. DOI: 10.1103/PhysRevD.106.015014. arXiv: 2106.15647 [hep-ph].

[228] Ilja Dorsner, Svjetlana Fajfer, and Nejc Kosnik. "Heavy and light scalar leptoquarks in proton decay". In: *Phys. Rev. D* 86 (2012), p. 015013. DOI: 10.1103/PhysRevD.86.015013. arXiv: 1204.0674 [hep-ph].

[229] Chun-Khiang Chua, Xiao-Gang He, and W-Y. P. Hwang. "Neutrino mass induced radiatively by supersymmetric leptoquarks". In: *Phys. Lett. B* 479 (2000), pp. 224–229. DOI: 10.1016/S0370-2693(00)00325-7. arXiv: hep-ph/9905340.

[230] Uma Mahanta. "Neutrino masses and mixing angles from leptoquark interactions". In: *Phys. Rev. D* 62 (2000), p. 073009. DOI: 10.1103/PhysRevD.62.073009. arXiv: hep-ph/9909518.

[231] Georges Aad et al. "Search for leptoquarks decaying into the bτ final state in pp collisions at $\sqrt{s}$ = 13 TeV with the ATLAS detector". In: *JHEP* 10 (2023), p. 001. DOI: 10.1007/JHEP10(2023)001. arXiv: 2305.15962 [hep-ex].

[232] Albert M Sirunyan et al. "Search for pair production of second-generation leptoquarks at $\sqrt{s} = 13$ TeV". In: *Phys. Rev. D* 99.3 (2019), p. 032014. DOI: 10.1103/PhysRevD.99.032014. arXiv: 1808.05082 [hep-ex].

[233] Albert M Sirunyan et al. "Search for heavy neutrinos and third-generation leptoquarks in hadronic states of two τ leptons and two jets in proton-proton collisions at $\sqrt{s} = 13$ TeV". In: *JHEP* 03 (2019), p. 170. DOI: 10.1007/JHEP03(2019)170. arXiv: 1811.00806 [hep-ex].

[234] Albert M Sirunyan et al. "Search for pair production of first-generation scalar leptoquarks at $\sqrt{s} = 13$ TeV". In: *Phys. Rev. D* 99.5 (2019), p. 052002. DOI: 10.1103/PhysRevD.99.052002. arXiv: 1811.01197 [hep-ex].

[235] Morad Aaboud et al. "Searches for scalar leptoquarks and differential cross-section measurements in dilepton-dijet events in proton-proton collisions at a centre-of-mass energy of $\sqrt{s}$ = 13 TeV with the ATLAS experiment". In: *Eur. Phys. J. C* 79.9 (2019), p. 733. DOI: 10.1140/epjc/s10052-019-7181-x. arXiv: 1902.00377 [hep-ex].

[236] Georges Aad et al. "Search for pairs of scalar leptoquarks decaying into quarks and electrons or muons in $\sqrt{s}$ = 13 TeV pp collisions with the ATLAS detector". In: *JHEP* 10 (2020), p. 112. DOI: 10.1007/JHEP10(2020)112. arXiv: 2006.05872 [hep-ex].

[237] Albert M Sirunyan et al. "Search for singly and pair-produced leptoquarks coupling to third-generation fermions in proton-proton collisions at s=13 TeV". In: *Phys. Lett. B* 819 (2021), p. 136446. DOI: 10.1016/j.physletb.2021.136446. arXiv: 2012.04178 [hep-ex].

[238] Georges Aad et al. "Search for pair production of third-generation scalar leptoquarks decaying into a top quark and a τ-lepton in pp collisions at $\sqrt{s}$ = 13 TeV with the ATLAS detector". In: *JHEP* 06 (2021), p. 179. DOI: 10.1007/JHEP06(2021)179. arXiv: 2101.11582 [hep-ex].

[239] Armen Tumasyan et al. "Inclusive nonresonant multilepton probes of new phenomena at $\sqrt{s}$=13 TeV". In: *Phys. Rev. D* 105.11 (2022), p. 112007. DOI: 10.1103/PhysRevD.105.112007. arXiv: 2202.08676 [hep-ex].

[240] Georges Aad et al. "Search for leptoquark pair production decaying into $te^-\bar{t}e^+$ or $t\mu^-\bar{t}\mu^+$ in multi-lepton final states in pp collisions at 13 TeV with the ATLAS detector". In: (June 2023). arXiv: 2306.17642 [hep-ex].

[241] H. Pas et al. "Towards a superformula for neutrinoless double beta decay". In: *Workshop on Physics Beyond the Standard Model: Beyond the Desert: Accelerator and Nonaccelerator Approaches*. June 1997, pp. 884–890. arXiv: hep-ph/9804374.

[242] A. Ali, A. V. Borisov, and D. V. Zhuridov. "Probing new physics in the neutrinoless double beta decay using electron angular correlation". In: *Phys. Rev. D* 76 (2007). [Erratum: Phys.Rev.D 105, 099902 (2022)], p. 093009. DOI: 10.1103/PhysRevD.76.093009. arXiv: 0706.4165 [hep-ph].

[243] Jenni Kotila, Jacopo Ferretti, and Francesco Iachello. "Long-range neutrinoless double beta decay mechanisms". In: (Oct. 2021). arXiv: 2110.09141 [hep-ph].

[244] V. Cirigliano et al. "A neutrinoless double beta decay master formula from effective field theory". In: *JHEP* 12 (2018), p. 097. DOI: 10.1007/JHEP12(2018)097. arXiv: 1806.02780 [hep-ph].

[245] Frank F. Deppisch et al. "Analysis of light neutrino exchange and short-range mechanisms in $0\nu\beta\beta$ decay". In: *Phys. Rev. D* 102.9 (2020), p. 095016. DOI: 10.1103/PhysRevD.102.095016. arXiv: 2009.10119 [hep-ph].

[246] Benjamin W. Lee, C. Quigg, and H. B. Thacker. "Weak Interactions at Very High-Energies: The Role of the Higgs Boson Mass". In: *Phys. Rev. D* 16 (1977), p. 1519. DOI: 10.1103/PhysRevD.16.1519.

[247] Michael E. Peskin and Tatsu Takeuchi. "Estimation of oblique electroweak corrections". In: *Phys. Rev. D* 46 (1992), pp. 381–409. DOI: 10.1103/PhysRevD.46.381.

[248] Ryuichiro Kitano, Masafumi Koike, and Yasuhiro Okada. "Detailed calculation of lepton flavor violating muon electron conversion rate for various nuclei". In: *Phys. Rev. D* 66 (2002). [Erratum: Phys.Rev.D 76, 059902 (2007)], p. 096002. DOI: 10.1103/PhysRevD.76.059902. arXiv: hep-ph/0203110.

[249] I. Plakias and O. Sumensari. "Lepton Flavor Violation in Semileptonic Observables". In: (Dec. 2023). arXiv: 2312.14070 [hep-ph].

[250] L. Bartoszek et al. "Mu2e Technical Design Report". In: (Oct. 2014). DOI: 10.2172/1172555. arXiv: 1501.05241 [physics.ins-det].

[251] R. Abramishvili et al. "COMET Phase-I Technical Design Report". In: *PTEP* 2020.3 (2020), p. 033C01. DOI: 10.1093/ptep/ptz125. arXiv: 1812.09018 [physics.ins-det].

[252] T. Suzuki, David F. Measday, and J. P. Roalsvig. "Total Nuclear Capture Rates for Negative Muons". In: *Phys. Rev. C* 35 (1987), p. 2212. DOI: 10.1103/PhysRevC.35.2212.

[253] Ilja Doršner, Svjetlana Fajfer, and Olcyr Sumensari. "Muon $g-2$ and scalar leptoquark mixing". In: *JHEP* 06 (2020), p. 089. DOI: 10.1007/JHEP06(2020)089. arXiv: 1910.03877 [hep-ph].

[254] A. Abdesselam et al. "Search for lepton-flavor-violating tau-lepton decays to $\ell\gamma$ at Belle". In: *JHEP* 10 (2021), p. 19. DOI: 10.1007/JHEP10(2021)019. arXiv: 2103.12994 [hep-ex].

[255] Bernard Aubert et al. "Searches for Lepton Flavor Violation in the Decays tau+- —> e+- gamma and tau+- —> mu+- gamma". In: *Phys. Rev. Lett.* 104 (2010), p. 021802. DOI: 10.1103/PhysRevLett.104.021802. arXiv: 0908.2381 [hep-ex].

[256] Latika Aggarwal et al. "Snowmass White Paper: Belle II physics reach and plans for the next decade and beyond". In: (July 2022). arXiv: 2207.06307 [hep-ex].

[257] Rachid Benbrik, Mohamed Chabab, and Gaber Faisel. "Lepton Flavour Violating τ and μ decays induced by scalar leptoquark". In: (Sept. 2010). arXiv: 1009.3886 [hep-ph].

[258] Uladzimir Khasianevich et al. "Constraint on scalar leptoquark from low-energy leptonic observables". In: *Phys. Rev. D* 108.9 (2023), p. 095027. DOI: 10.1103/PhysRevD.108.095027. arXiv: 2305.05016 [hep-ph].

[259] K. Hayasaka et al. "Search for Lepton Flavor Violating Tau Decays into Three Leptons with 719 Million Produced Tau+Tau- Pairs". In: *Phys. Lett. B* 687 (2010), pp. 139–143. DOI: 10.1016/j.physletb.2010.03.037. arXiv: 1001.3221 [hep-ex].

[260] Chun-Khiang Chua and W. -Y. P. Hwang. "The Neutrino magnetic moment induced by leptoquarks". In: *Phys. Rev. D* 60 (1999), p. 073002. DOI: 10.1103/PhysRevD.60.073002. arXiv: hep-ph/9811232.

[261] Vedran Brdar et al. "The Neutrino Magnetic Moment Portal: Cosmology, Astrophysics, and Direct Detection". In: *JCAP* 01 (2021), p. 039. DOI: 10.1088/1475-7516/2021/01/039. arXiv: 2007.15563 [hep-ph].

[262] R. Sánchez-Vélez. "Neutrino electromagnetic properties in a Leptoquark model". In: (Apr. 2022). arXiv: 2204.01167 [hep-ph].

[263] Jonathan M. Arnold, Bartosz Fornal, and Mark B. Wise. "Phenomenology of scalar leptoquarks". In: *Phys. Rev. D* 88 (2013), p. 035009. DOI: 10.1103/PhysRevD.88.035009. arXiv: 1304.6119 [hep-ph].

[264] W. Dekens et al. "The phenomenology of electric dipole moments in models of scalar leptoquarks". In: *JHEP* 01 (2019), p. 069. DOI: 10.1007/JHEP01(2019)069. arXiv: 1809.09114 [hep-ph].

[265] Felipe F. Freitas et al. "Interplay between flavor anomalies and neutrino properties". In: *Phys. Rev. D* 108.11 (2023), p. 115002. DOI: 10.1103/PhysRevD.108.115002. arXiv: 2206.01674 [hep-ph].

[266] T. Hurth, F. Mahmoudi, and S. Neshatpour. "B anomalies in the post $R_{K^{(*)}}$ era". In: *Phys. Rev. D* 108.11 (2023), p. 115037. DOI: 10.1103/PhysRevD.108.115037. arXiv: 2310.05585 [hep-ph].

[267] Damir Bečirević et al. "RD(*) and survival of the fittest scalar leptoquark". In: *Phys. Rev. D* 110.5 (2024), p. 055023. DOI: 10.1103/PhysRevD.110.055023. arXiv: 2404.16772 [hep-ph].

[268] K. G. Chetyrkin. "Quark mass anomalous dimension to O (alpha-s**4)". In: *Phys. Lett. B* 404 (1997), pp. 161–165. DOI: 10.1016/S0370-2693(97)00535-2. arXiv: hep-ph/9703278.

[269] J. A. Gracey. "Three loop $\overline{\text{MS}}$ tensor current anomalous dimension in QCD". In: *Phys. Lett. B* 488 (2000), pp. 175–181. DOI: 10.1016/S0370-2693(00)00859-5. arXiv: hep-ph/0007171.

[270] Ilja Doršner et al. "Minimally flavored colored scalar in $\overline{B} \to D^{(*)}\tau\overline{\nu}$ and the mass matrices constraints". In: *JHEP* 11 (2013), p. 084. DOI: 10.1007/JHEP11(2013)084. arXiv: 1306.6493 [hep-ph].

[271] Gudrun Hiller, Dennis Loose, and Kay Schönwald. "Leptoquark Flavor Patterns & B Decay Anomalies". In: *JHEP* 12 (2016), p. 027. DOI: 10.1007/JHEP12(2016)027. arXiv: 1609.08895 [hep-ph].

[272] Andrzej J. Buras and Elena Venturini. "The exclusive vision of rare K and B decays and of the quark mixing in the standard model". In: *Eur. Phys. J. C* 82.7 (2022), p. 615. DOI: 10.1140/epjc/s10052-022-10583-8. arXiv: 2203.11960 [hep-ph].

[273] J. Grygier et al. "Search for $\boldsymbol{B \to h\nu\overline{\nu}}$ decays with semileptonic tagging at Belle". In: *Phys. Rev. D* 96.9 (2017). [Addendum: Phys.Rev.D 97, 099902 (2018)], p. 091101. DOI: 10.1103/PhysRevD.96.091101. arXiv: 1702.03224 [hep-ex].

[274] Thomas E. Browder et al. "Impact of $B \to K\nu\overline{\nu}$ measurements on beyond the Standard Model theories". In: *Phys. Rev. D* 104.5 (2021), p. 053007. DOI: 10.1103/PhysRevD.104.053007. arXiv: 2107.01080 [hep-ph].

[275] Xiao-Gang He, Xiao-Dong Ma, and German Valencia. "Revisiting models that enhance $B^+ \to K^+\nu\overline{\nu}$ in light of the new Belle II measurement". In: *Phys. Rev. D* 109.7 (2024), p. 075019. DOI: 10.1103/PhysRevD.109.075019. arXiv: 2309.12741 [hep-ph].

[276] Nico Gubernari, Ahmet Kokulu, and Danny van Dyk. "$B \to P$ and $B \to V$ Form Factors from B-Meson Light-Cone Sum Rules beyond Leading Twist". In: *JHEP* 01 (2019), p. 150. DOI: 10.1007/JHEP01(2019)150. arXiv: 1811.00983 [hep-ph].

[277] Christoph Bobeth and Andrzej J. Buras. "Leptoquarks meet ε'/ε and rare Kaon processes". In: *JHEP* 02 (2018), p. 101. DOI: 10.1007/JHEP02(2018)101. arXiv: 1712.01295 [hep-ph].

[278] Rusa Mandal and Antonio Pich. "Constraints on scalar leptoquarks from lepton and kaon physics". In: *JHEP* 12 (2019), p. 089. DOI: 10.1007/JHEP12(2019)089. arXiv: 1908.11155 [hep-ph].

[279] Eduardo Cortina Gil et al. "Measurement of the very rare $K^+ \to \pi^+ \nu\bar{\nu}$ decay". In: *JHEP* 06 (2021), p. 093. DOI: 10.1007/JHEP06(2021)093. arXiv: 2103.15389 [hep-ex].

[280] Joachim Brod, Martin Gorbahn, and Emmanuel Stamou. "Updated Standard Model Prediction for $K \to \pi\nu\bar{\nu}$ and ϵ_K". In: *PoS* BEAUTY2020 (2021), p. 056. DOI: 10.22323/1.391.0056. arXiv: 2105.02868 [hep-ph].

[281] Christoph Bobeth et al. "Patterns of Flavour Violation in Models with Vector-Like Quarks". In: *JHEP* 04 (2017), p. 079. DOI: 10.1007/JHEP04(2017)079. arXiv: 1609.04783 [hep-ph].

[282] J. K. Ahn et al. "Study of the $K_L \to \pi^0 \nu\bar{\nu}$ Decay at the J-PARC KOTO Experiment". In: *Phys. Rev. Lett.* 126.12 (2021), p. 121801. DOI: 10.1103/PhysRevLett.126.121801. arXiv: 2012.07571 [hep-ex].

[283] Andrzej J. Buras and Elena Venturini. "Searching for New Physics in Rare K and B Decays without $|V_{cb}|$ and $|V_{ub}|$ Uncertainties". In: *Acta Phys. Polon. B* 53.6 (Sept. 2021), 6–A1. DOI: 10.5506/APhysPolB.53.6-A1. arXiv: 2109.11032 [hep-ph].

[284] D. Ambrose et al. "New limit on muon and electron lepton number violation from $K^0_L \to \mu^\pm e^\mp$ decay". In: *Phys. Rev. Lett.* 81 (1998), pp. 5734–5737. DOI: 10.1103/PhysRevLett.81.5734. arXiv: hep-ex/9811038.

[285] Aleksey Sher et al. "An Improved upper limit on the decay $K^+ \to \pi^+ \mu^+ e^-$". In: *Phys. Rev. D* 72 (2005), p. 012005. DOI: 10.1103/PhysRevD.72.012005. arXiv: hep-ex/0502020.

[286] J. A. Casas and A. Ibarra. "Oscillating neutrinos and $\mu \to e, \gamma$". In: *Nucl. Phys. B* 618 (2001), pp. 171–204. DOI: 10.1016/S0550-3213(01)00475-8. arXiv: hep-ph/0103065.

[287] Matthew J. Dolan, Tomasz P. Dutka, and Raymond R. Volkas. "Dirac-Phase Thermal Leptogenesis in the extended Type-I Seesaw Model". In: *JCAP* 06 (2018), p. 012. DOI: 10.1088/1475-7516/2018/06/012. arXiv: 1802.08373 [hep-ph].

[288] Lukas Allwicher et al. "HighPT: A tool for high-p_T Drell-Yan tails beyond the standard model". In: *Comput. Phys. Commun.* 289 (2023), p. 108749. DOI: 10.1016/j.cpc.2023.108749. arXiv: 2207.10756 [hep-ph].

[289] Marco Fedele et al. "Impact of $\Lambda_b \to \Lambda_c \tau\nu$ measurement on new physics in $b \to c\ell\nu$ transitions". In: *Phys. Rev. D* 107.5 (2023), p. 055005. DOI: 10.1103/PhysRevD.107.055005. arXiv: 2211.14172 [hep-ph].

[290] *Three-neutrino fit based on data available in March 2024*. URL: www.nu-fit.org.

[291] R. L. Workman et al. "Review of Particle Physics". In: *PTEP* 2022 (2022), p. 083C01. DOI: 10.1093/ptep/ptac097.

[292] Jogesh C. Pati and Abdus Salam. "Lepton Number as the Fourth Color". In: *Phys. Rev. D* 10 (1974). [Erratum: Phys.Rev.D 11, 703–703 (1975)], pp. 275–289. DOI: 10.1103/PhysRevD.10.275.

[293] H. Georgi and S. L. Glashow. "Unity of All Elementary Particle Forces". In: *Phys. Rev. Lett.* 32 (1974), pp. 438–441. DOI: 10.1103/PhysRevLett.32.438.

[294] Paul Langacker. "Grand Unified Theories and Proton Decay". In: *Phys. Rept.* 72 (1981), p. 185. DOI: 10.1016/0370-1573(81)90059-4.

[295] R. N. Mohapatra. *Unification and Supersymmetry: The Frontiers of Quark-Lepton Physics*. Berlin: Springer, 1986. ISBN: 978-1-4757-1930-7, 978-1-4757-1928-4. DOI: 10.1007/978-1-4757-1928-4.

[296] Djuna Croon et al. "GUT Physics in the era of the LHC". In: *Front. in Phys.* 7 (2019), p. 76. DOI: 10.3389/fphy.2019.00076. arXiv: 1903.04977 [hep-ph].

[297] Howard Georgi and C. Jarlskog. "A New Lepton - Quark Mass Relation in a Unified Theory". In: *Phys. Lett. B* 86 (1979), pp. 297–300. DOI: 10.1016/0370-2693(79)90842-6.

[298] John R. Ellis and Mary K. Gaillard. "Fermion Masses and Higgs Representations in SU(5)". In: *Phys. Lett. B* 88 (1979), pp. 315–319. DOI: 10.1016/0370-2693(79)90476-3.

[299] Ilja Dorsner and Pavel Fileviez Perez. "Unification without supersymmetry: Neutrino mass, proton decay and light leptoquarks". In: *Nucl. Phys. B* 723 (2005), pp. 53–76. DOI: 10.1016/j.nuclphysb.2005.06.016. arXiv: hep-ph/0504276.

[300] Borut Bajc and Goran Senjanovic. "Seesaw at LHC". In: *JHEP* 08 (2007), p. 014. DOI: 10.1088/1126-6708/2007/08/014. arXiv: hep-ph/0612029.

[301] Shaikh Saad. "Origin of a two-loop neutrino mass from SU(5) grand unification". In: *Phys. Rev. D* 99.11 (2019), p. 115016. DOI: 10.1103/PhysRevD.99.115016. arXiv: 1902.11254 [hep-ph].

[302] Christiane Klein, Manfred Lindner, and Stefan Vogl. "Radiative neutrino masses and successful $SU(5)$ unification". In: *Phys. Rev. D* 100.7 (2019), p. 075024. DOI: 10.1103/PhysRevD.100.075024. arXiv: 1907.05328 [hep-ph].

[303] Ilja Doršner and Shaikh Saad. "Towards Minimal $SU(5)$". In: *Phys. Rev. D* 101.1 (2020), p. 015009. DOI: 10.1103/PhysRevD.101.015009. arXiv: 1910.09008 [hep-ph].

[304] Florian Bonnet et al. "Systematic decomposition of the neutrinoless double beta decay operator". In: *JHEP* 03 (2013). [Erratum: JHEP 04, 090 (2014)], p. 055. DOI: 10.1007/JHEP03(2013)055. arXiv: 1212.3045 [hep-ph].

[305] J. C. Helo and M. Hirsch. "LHC dijet constraints on double beta decay". In: *Phys. Rev. D* 92.7 (2015), p. 073017. DOI: 10.1103/PhysRevD.92.073017. arXiv: 1509.00423 [hep-ph].

[306] L. Gonzalez et al. "Scalar-mediated double beta decay and LHC". In: *JHEP* 12 (2016), p. 130. DOI: 10.1007/JHEP12(2016)130. arXiv: 1606.09555 [hep-ph].

[307] S. Fajfer et al. "Correlating $0\nu\beta\beta$ decays and flavor observables in leptoquark models". In: (June 2024). arXiv: 2406.20050 [hep-ph].

[308] P. S. Bhupal Dev et al. "Neutrinoless double beta decay from scalar leptoquarks: interplay with neutrino mass and flavor physics". In: *JHEP* 01 (2025), p. 004. DOI: 10.1007/JHEP01(2025)004. arXiv: 2407.04670 [hep-ph].

[309] Renato M. Fonseca and Martin Hirsch. "SU(5)-inspired double beta decay". In: *Phys. Rev. D* 92.1 (2015), p. 015014. DOI: 10.1103/PhysRevD.92.015014. arXiv: 1505.06121 [hep-ph].

[310] M. K. Parida and Rajesh Satpathy. "High Scale Type-II Seesaw, Dominant Double Beta Decay within Cosmological Bound and LFV Decays in SU(5)". In: *Adv. High Energy Phys.* 2019 (2019), p. 3572862. DOI: 10.1155/2019/3572862. arXiv: 1809.06612 [hep-ph].

[311] Ilja Doršner, Mijo Matković, and Shaikh Saad. "Nonrenormalizable SU(5) GUTs: Leptoquark-induced neutrino masses". In: *Phys. Rev. D* 111.11 (2025), p. 115039. DOI: 10.1103/3plx-vwrb. arXiv: 2504.16022 [hep-ph].

[312] M. Magg and C. Wetterich. "Neutrino Mass Problem and Gauge Hierarchy". In: *Phys. Lett. B* 94 (1980), pp. 61–64. DOI: 10.1016/0370-2693(80)90825-4.

[313] K. S. Babu et al. "Non-Standard Interactions in Radiative Neutrino Mass Models". In: *JHEP* 03 (2020), p. 006. DOI: 10.1007/JHEP03(2020)006. arXiv: 1907.09498 [hep-ph].

[314] K. S. Babu et al. "Unified framework for B-anomalies, muon $g-2$ and neutrino masses". In: *JHEP* 03 (2021), p. 179. DOI: 10.1007/JHEP03(2021)179. arXiv: 2009.01771 [hep-ph].

[315] Saurabh K. Shukla. "Revisiting $SU(5)$ Yukawa Sectors Through Quantum Corrections". In: (Nov. 2024). arXiv: 2411.06906 [hep-ph].

[316] Ketan M. Patel and Saurabh K. Shukla. "Anatomy of scalar mediated proton decays in SO(10) models". In: *JHEP* 08 (2022), p. 042. DOI: 10.1007/JHEP08(2022)042. arXiv: 2203.07748 [hep-ph].

[317] Pran Nath and Pavel Fileviez Perez. "Proton stability in grand unified theories, in strings and in branes". In: *Phys. Rept.* 441 (2007), pp. 191–317. DOI: 10.1016/j.physrep.2007.02.010. arXiv: hep-ph/0601023.

[318] K. Abe et al. "Search for Nucleon Decay via $n \to \bar{\nu}\pi^0$ and $p \to \bar{\nu}\pi^+$ in Super-Kamiokande". In: *Phys. Rev. Lett.* 113.12 (2014), p. 121802. DOI: 10.1103/PhysRevLett.113.121802. arXiv: 1305.4391 [hep-ex].

[319] G. C. Branco et al. "Theory and phenomenology of two-Higgs-doublet models". In: *Phys. Rept.* 516 (2012), pp. 1–102. DOI: 10.1016/j.physrep.2012.02.002. arXiv: 1106.0034 [hep-ph].

[320] T. W. B. Kibble. "Topology of Cosmic Domains and Strings". In: *J. Phys. A* 9 (1976), pp. 1387–1398. DOI: 10.1088/0305-4470/9/8/029.

[321] Ya. B. Zeldovich, I. Yu. Kobzarev, and L. B. Okun. "Cosmological Consequences of the Spontaneous Breakdown of Discrete Symmetry". In: *Zh. Eksp. Teor. Fiz.* 67 (1974), pp. 3–11.

[322] Alexander Vilenkin. "Cosmic Strings and Domain Walls". In: *Phys. Rept.* 121 (1985), pp. 263–315. DOI: 10.1016/0370-1573(85)90033-X.

[323] Edward W. Kolb and Michael S. Turner. *The Early Universe*. Vol. 69. Taylor and Francis, May 2019. ISBN: 978-0-429-49286-0, 978-0-201-62674-2. DOI: 10.1201/9780429492860.

[324] Sebastian E. Larsson, Subir Sarkar, and Peter L. White. "Evading the cosmological domain wall problem". In: *Phys. Rev. D* 55 (1997), pp. 5129–5135. DOI: 10.1103/PhysRevD.55.5129. arXiv: hep-ph/9608319.

[325] Dejan Stojkovic, Katherine Freese, and Glenn D. Starkman. "Holes in the walls: Primordial black holes as a solution to the cosmological domain wall problem". In: *Phys. Rev. D* 72 (2005), p. 045012. DOI: 10.1103/PhysRevD.72.045012. arXiv: hep-ph/0505026.

[326] Stephen F. King and Ye-Ling Zhou. "Spontaneous breaking of $SO(3)$ to finite family symmetries with supersymmetry - an A_4 model". In: *JHEP* 11 (2018), p. 173. DOI: 10.1007/JHEP11(2018)173. arXiv: 1809.10292 [hep-ph].

[327] G. R. Dvali and Goran Senjanovic. "Is there a domain wall problem?" In: *Phys. Rev. Lett.* 74 (1995), pp. 5178–5181. DOI: 10.1103/PhysRevLett.74.5178. arXiv: hep-ph/9501387.

[328] C. R. Das and M. K. Parida. "New formulas and predictions for running fermion masses at higher scales in SM, 2 HDM, and MSSM". In: *Eur. Phys. J. C* 20 (2001), pp. 121–137. DOI: 10.1007/s100520100628. arXiv: hep-ph/0010004.

[329] Ketan M. Patel and Saurabh K. Shukla. "Quantum corrections and the minimal Yukawa sector of SU(5)". In: *Phys. Rev. D* 109.1 (2024), p. 015007. DOI: 10.1103/PhysRevD.109.015007. arXiv: 2310.16563 [hep-ph].

[330] Steven Weinberg. "Effective Gauge Theories". In: *Phys. Lett. B* 91 (1980), pp. 51–55. DOI: 10.1016/0370-2693(80)90660-7.

[331] Lawrence J. Hall. "Grand Unification of Effective Gauge Theories". In: *Nucl. Phys. B* 178 (1981), pp. 75–124. DOI: 10.1016/0550-3213(81)90498-3.

[332] J. Oliensis and M. Fischler. "Two Loop Calculations of M_b/M_τ and Heavy Fermion Masses in the SU(5) Model". In: *Phys. Rev. D* 28 (1983), p. 194. DOI: 10.1103/PhysRevD.28.194.

[333] Gordon L. Kane et al. "Study of constrained minimal supersymmetry". In: *Phys. Rev. D* 49 (1994), pp. 6173–6210. DOI: 10.1103/PhysRevD.49.6173. arXiv: hep-ph/9312272.

[334] Ralf Hempfling. "Yukawa coupling unification with supersymmetric threshold corrections". In: *Phys. Rev. D* 49 (1994), pp. 6168–6172. DOI: 10.1103/PhysRevD.49.6168.

[335] Brian D. Wright. "Yukawa coupling thresholds: Application to the MSSM and the minimal supersymmetric SU(5) GUT". In: (Mar. 1994). arXiv: hep-ph/9404217.

[336] Saurabh K. Shukla. "Unravelling the Scalar Sector of Grand Unification: Phenomenology & Implications". Other thesis. July 2025. arXiv: 2507.16605 [hep-ph].

[337] Ilja Dorsner and Irina Mocioiu. "Predictions from type II see-saw mechanism in SU(5)". In: *Nucl. Phys. B* 796 (2008), pp. 123–136. DOI: 10.1016/j.nuclphysb.2007.12.004. arXiv: 0708.3332 [hep-ph].

[338] M. Abdul Karim et al. "DESI DR2 Results II: Measurements of Baryon Acoustic Oscillations and Cosmological Constraints". In: (Mar. 2025). arXiv: 2503.14738 [astro-ph.CO].

[339] Piotr H. Chankowski and Zbigniew Pluciennik. "Renormalization group equations for seesaw neutrino masses". In: *Phys. Lett. B* 316 (1993), pp. 312–317. DOI: 10.1016/0370-2693(93)90330-K. arXiv: hep-ph/9306333.

[340] K. S. Babu, Chung Ngoc Leung, and James T. Pantaleone. "Renormalization of the neutrino mass operator". In: *Phys. Lett. B* 319 (1993), pp. 191–198. DOI: 10.1016/0370-2693(93)90801-N. arXiv: hep-ph/9309223.

[341] Stefan Antusch et al. "Running neutrino mass parameters in see-saw scenarios". In: *JHEP* 03 (2005), p. 024. DOI: 10.1088/1126-6708/2005/03/024. arXiv: hep-ph/0501272.

[342] Jian-wei Mei. "Running neutrino masses, leptonic mixing angles and CP-violating phases: From M(Z) to Lambda(GUT)". In: *Phys. Rev. D* 71 (2005), p. 073012. DOI: 10.1103/PhysRevD.71.073012. arXiv: hep-ph/0502015.

[343] Lohan Sartore and Ingo Schienbein. "PyR@TE 3". In: *Comput. Phys. Commun.* 261 (2021), p. 107819. DOI: 10.1016/j.cpc.2020.107819. arXiv: 2007.12700 [hep-ph].

[344] V. Suryanarayana Mummidi and Ketan M. Patel. "Pseudo-Dirac Higgsino dark matter in GUT scale supersymmetry". In: *JHEP* 01 (2019), p. 224. DOI: 10.1007/JHEP01(2019)224. arXiv: 1811.06297 [hep-ph].

[345] Ivan Esteban et al. "NuFit-6.0: updated global analysis of three-flavor neutrino oscillations". In: *JHEP* 12 (2024), p. 216. DOI: 10.1007/JHEP12(2024)216. arXiv: 2410.05380 [hep-ph].

[346] Alexander Dueck and Werner Rodejohann. "Fits to SO(10) Grand Unified Models". In: *JHEP* 09 (2013), p. 024. DOI: 10.1007/JHEP09(2013)024. arXiv: 1306.4468 [hep-ph].

[347] K. S. Babu, Borut Bajc, and Shaikh Saad. "Yukawa Sector of Minimal SO(10) Unification". In: *JHEP* 02 (2017), p. 136. DOI: 10.1007/JHEP02(2017)136. arXiv: 1612.04329 [hep-ph].

[348] Lukas Allwicher et al. "Perturbative unitarity constraints on generic Yukawa interactions". In: *JHEP* 10 (2021), p. 129. DOI: 10.1007/JHEP10(2021)129. arXiv: 2108.00013 [hep-ph].

[349] F. del Aguila and Luis E. Ibanez. "Higgs Bosons in SO(10) and Partial Unification". In: *Nucl. Phys. B* 177 (1981), pp. 60–86. DOI: 10.1016/0550-3213(81)90266-2.

[350] Rabindra N. Mohapatra and Goran Senjanovic. "Higgs Boson Effects in Grand Unified Theories". In: *Phys. Rev. D* 27 (1983), p. 1601. DOI: 10.1103/PhysRevD.27.1601.

[351] S. Dimopoulos and H. M. Georgi. "Extended Survival Hypothesis and Fermion Masses". In: *Phys. Lett. B* 140 (1984), pp. 67–70. DOI: 10.1016/0370-2693(84)91049-9.

[352] Savas Dimopoulos and Howard Georgi. "Softly Broken Supersymmetry and SU(5)". In: *Nucl. Phys. B* 193 (1981), pp. 150–162. DOI: 10.1016/0550-3213(81)90522-8.

[353] N. Sakai. "Naturalness in Supersymmetric Guts". In: *Z. Phys. C* 11 (1981), p. 153. DOI: 10.1007/BF01573998.

[354] Ilja Doršner and Shaikh Saad. "Is doublet-triplet splitting necessary?" In: *Phys. Rev. D* 110.7 (2024), p. 075025. DOI: 10.1103/PhysRevD.110.075025. arXiv: 2404.09021 [hep-ph].

[355] Max Aker et al. "Direct neutrino-mass measurement based on 259 days of KATRIN data". In: *Science* 388.6743 (2025), adq9592. DOI: 10.1126/science.adq9592. arXiv: 2406.13516 [nucl-ex].

[356] Georges Aad et al. "Search for doubly and singly charged Higgs bosons decaying into vector bosons in multi-lepton final states with the ATLAS detector using proton-proton collisions at $\sqrt{s}$ = 13 TeV". In: *JHEP* 06 (2021), p. 146. DOI: 10.1007/JHEP06(2021)146. arXiv: 2101.11961 [hep-ex].

[357] Jihn E. Kim. "Light Pseudoscalars, Particle Physics and Cosmology". In: *Phys. Rept.* 150 (1987), pp. 1–177. DOI: 10.1016/0370-1573(87)90017-2.

[358] Peter Svrcek and Edward Witten. "Axions In String Theory". In: *JHEP* 06 (2006), p. 051. DOI: 10.1088/1126-6708/2006/06/051. arXiv: hep-th/0605206.

[359] Y. Inoue et al. "Search for solar axions with mass around 1 eV using coherent conversion of axions into photons". In: *Phys. Lett. B* 668 (2008), pp. 93–97. DOI: 10.1016/j.physletb.2008.08.020. arXiv: 0806.2230 [astro-ph].

[360] E. Arik et al. "Probing eV-scale axions with CAST". In: *JCAP* 02 (2009), p. 008. DOI: 10.1088/1475-7516/2009/02/008. arXiv: 0810.4482 [hep-ex].

[361] Steen Hannestad, Alessandro Mirizzi, and Georg Raffelt. "New cosmological mass limit on thermal relic axions". In: *JCAP* 07 (2005), p. 002. DOI: 10.1088/1475-7516/2005/07/002. arXiv: hep-ph/0504059.

[362] Alessandro Melchiorri, Olga Mena, and Anze Slosar. "An improved cosmological bound on the thermal axion mass". In: *Phys. Rev. D* 76 (2007), p. 041303. DOI: 10.1103/PhysRevD.76.041303. arXiv: 0705.2695 [astro-ph].

[363] Steen Hannestad et al. "Cosmological constraints on neutrino plus axion hot dark matter: Update after WMAP-5". In: *JCAP* 04 (2008), p. 019. DOI: 10.1088/1475-7516/2008/04/019. arXiv: 0803.1585 [astro-ph].

[364] Jan Hamann et al. "Isocurvature forecast in the anthropic axion window". In: *JCAP* 06 (2009), p. 022. DOI: 10.1088/1475-7516/2009/06/022. arXiv: 0904.0647 [hep-ph].

[365] Y. Semertzidis et al. "Limits on the Production of Light Scalar and Pseudoscalar Particles". In: *Phys. Rev. Lett.* 64 (1990), pp. 2988–2991. DOI: 10.1103/PhysRevLett.64.2988.

[366] R. Cameron et al. "Search for nearly massless, weakly coupled particles by optical techniques". In: *Phys. Rev. D* 47 (1993), pp. 3707–3725. DOI: 10.1103/PhysRevD.47.3707.

[367] Cecile Robilliard et al. "No light shining through a wall". In: *Phys. Rev. Lett.* 99 (2007), p. 190403. DOI: 10.1103/PhysRevLett.99.190403. arXiv: 0707.1296 [hep-ex].

[368] Aaron S. Chou et al. "Search for axion-like particles using a variable baseline photon regeneration technique". In: *Phys. Rev. Lett.* 100 (2008), p. 080402. DOI: 10.1103/PhysRevLett.100.080402. arXiv: 0710.3783 [hep-ex].

[369] P. Sikivie, D. B. Tanner, and Karl van Bibber. "Resonantly enhanced axion-photon regeneration". In: *Phys. Rev. Lett.* 98 (2007), p. 172002. DOI: 10.1103/PhysRevLett.98.172002. arXiv: hep-ph/0701198.

[370] Hai-Yang Cheng. "The Strong CP Problem Revisited". In: *Phys. Rept.* 158 (1988), p. 1. DOI: 10.1016/0370-1573(88)90135-4.

[371] L. J. Rosenberg and K. A. van Bibber. "Searches for invisible axions". In: *Phys. Rept.* 325 (2000), pp. 1–39. DOI: 10.1016/S0370-1573(99)00045-9.

[372] Mark P Hertzberg, Max Tegmark, and Frank Wilczek. "Axion Cosmology and the Energy Scale of Inflation". In: *Phys. Rev. D* 78 (2008), p. 083507. DOI: 10.1103/PhysRevD.78.083507. arXiv: 0807.1726 [astro-ph].

[373] Luca Visinelli and Paolo Gondolo. "Dark Matter Axions Revisited". In: *Phys. Rev. D* 80 (2009), p. 035024. DOI: 10.1103/PhysRevD.80.035024. arXiv: 0903.4377 [astro-ph.CO].

[374] R. A. Battye and E. P. S. Shellard. "Axion string constraints". In: *Phys. Rev. Lett.* 73 (1994). [Erratum: Phys.Rev.Lett. 76, 2203–2204 (1996)], pp. 2954–2957. DOI: 10.1103/PhysRevLett.73.2954. arXiv: astro-ph/9403018.

[375] Masahide Yamaguchi, M. Kawasaki, and Jun'ichi Yokoyama. "Evolution of axionic strings and spectrum of axions radiated from them". In: *Phys. Rev. Lett.* 82 (1999), pp. 4578–4581. DOI: 10.1103/PhysRevLett.82.4578. arXiv: hep-ph/9811311.

[376] C. Hagmann, Sanghyeon Chang, and P. Sikivie. "Axion radiation from strings". In: *Phys. Rev. D* 63 (2001), p. 125018. DOI: 10.1103/PhysRevD.63.125018. arXiv: hep-ph/0012361.

[377] Tanmay Kumar Poddar, Subhendra Mohanty, and Soumya Jana. "Constraints on ultralight axions from compact binary systems". In: *Phys. Rev. D* 101.8 (2020), p. 083007. DOI: 10.1103/PhysRevD.101.083007. arXiv: 1906.00666 [hep-ph].

[378] Tanmay Kumar Poddar, Subhendra Mohanty, and Soumya Jana. "Vector gauge boson radiation from compact binary systems in a gauged $L_\mu - L_\tau$ scenario". In: *Phys. Rev. D* 100.12 (2019), p. 123023. DOI: 10.1103/PhysRevD.100.123023. arXiv: 1908.09732 [hep-ph].

[379] Tanmay Kumar Poddar and Subhendra Mohanty. "Probing the angle of birefringence due to long range axion hair from pulsars". In: *Phys. Rev. D* 102.8 (2020), p. 083029. DOI: 10.1103/PhysRevD.102.083029. arXiv: 2003.11015 [hep-ph].

[380] Tanmay Kumar Poddar. "Constraints on axionic fuzzy dark matter from light bending and Shapiro time delay". In: *JCAP* 09 (2021), p. 041. DOI: 10.1088/1475-7516/2021/09/041. arXiv: 2104.09772 [hep-ph].

[381] Tanmay Kumar Poddar. "Constraints on ultralight axions, vector gauge bosons, and unparticles from geodetic and frame-dragging measurements". In: *Eur. Phys. J. C* 82.11 (2022), p. 982. DOI: 10.1140/epjc/s10052-022-10956-z. arXiv: 2111.05632 [hep-ph].

[382] John Preskill, Mark B. Wise, and Frank Wilczek. "Cosmology of the Invisible Axion". In: *Phys. Lett. B* 120 (1983). Ed. by M. A. Srednicki, pp. 127–132. DOI: 10.1016/0370-2693(83)90637-8.

[383] L. F. Abbott and P. Sikivie. "A Cosmological Bound on the Invisible Axion". In: *Phys. Lett. B* 120 (1983). Ed. by M. A. Srednicki, pp. 133–136. DOI: 10.1016/0370-2693(83)90638-X.

[384] Michael Dine and Willy Fischler. "The Not So Harmless Axion". In: *Phys. Lett. B* 120 (1983). Ed. by M. A. Srednicki, pp. 137–141. DOI: 10.1016/0370-2693(83)90639-1.

[385] Wayne Hu, Rennan Barkana, and Andrei Gruzinov. "Cold and fuzzy dark matter". In: *Phys. Rev. Lett.* 85 (2000), pp. 1158–1161. DOI: 10.1103/PhysRevLett.85.1158. arXiv: astro-ph/0003365.

[386] Lam Hui et al. "Ultralight scalars as cosmological dark matter". In: *Phys. Rev. D* 95.4 (2017), p. 043541. DOI: 10.1103/PhysRevD.95.043541. arXiv: 1610.08297 [astro-ph.CO].

[387] Se-Heon Oh et al. "Dark and luminous matter in THINGS dwarf galaxies". In: *Astron. J.* 141 (2011), p. 193. DOI: 10.1088/0004-6256/141/6/193. arXiv: 1011.0899 [astro-ph.CO].

[388] Renée Hlozek et al. "A search for ultralight axions using precision cosmological data". In: *Phys. Rev. D* 91.10 (2015), p. 103512. DOI: 10.1103/PhysRevD.91.103512. arXiv: 1410.2896 [astro-ph.CO].

[389] Philip Mocz et al. "Schrödinger-Poisson–Vlasov-Poisson correspondence". In: *Phys. Rev. D* 97.8 (2018), p. 083519. DOI: 10.1103/PhysRevD.97.083519. arXiv: 1801.03507 [astro-ph.CO].

[390] E. Aprile et al. "Dark Matter Search Results from a One Ton-Year Exposure of XENON1T". In: *Phys. Rev. Lett.* 121.11 (2018), p. 111302. DOI: 10.1103/PhysRevLett.121.111302. arXiv: 1805.12562 [astro-ph.CO].

[391] D. S. Akerib et al. "First results from the LUX dark matter experiment at the Sanford Underground Research Facility". In: *Phys. Rev. Lett.* 112 (2014), p. 091303. DOI: 10.1103/PhysRevLett.112.091303. arXiv: 1310.8214 [astro-ph.CO].

[392] Xiangyi Cui et al. "Dark Matter Results From 54-Ton-Day Exposure of PandaX-II Experiment". In: *Phys. Rev. Lett.* 119.18 (2017), p. 181302. DOI: 10.1103/PhysRevLett.119.181302. arXiv: 1708.06917 [astro-ph.CO].

[393] J. E. Moody and Frank Wilczek. "NEW MACROSCOPIC FORCES?" In: *Phys. Rev. D* 30 (1984), p. 130. DOI: 10.1103/PhysRevD.30.130.

[394] Ciaran A. J. O'Hare and Edoardo Vitagliano. "Cornering the axion with *CP*-violating interactions". In: *Phys. Rev. D* 102.11 (2020), p. 115026. DOI: 10.1103/PhysRevD.102.115026. arXiv: 2010.03889 [hep-ph].

[395] L. Hunter et al. "Using the Earth as a Polarized Electron Source to Search for Long-Range Spin-Spin Interactions". In: *Science* 339.6122 (2013), pp. 928–932. DOI: 10.1126/science.1227460.

[396] Palash B. Pal. *An Introductory Course of Particle Physics*. CRC Press, July 2014. ISBN: 978-0-429-06851-5. DOI: 10.1201/b17199.

[397] Ryuji Daido and Fuminobu Takahashi. "The sign of the dipole–dipole potential by axion exchange". In: *Phys. Lett. B* 772 (2017), pp. 127–129. DOI: 10.1016/j.physletb.2017.06.027. arXiv: 1704.00155 [hep-ph].

[398] N. Crescini et al. "Improved constraints on monopole-dipole interaction mediated by pseudo-scalar bosons". In: *Phys. Lett. B* 773 (2017), pp. 677–680. DOI: 10.1016/j.physletb.2017.09.019. arXiv: 1705.06044 [hep-ex].

[399] Prateek Agrawal et al. "Searching for axion forces with precision precession in storage rings". In: (Oct. 2022). arXiv: 2210.17547 [hep-ph].

[400] Hooman Davoudiasl and Robert Szafron. "Muon g-2 and a Geocentric New Field". In: (Oct. 2022). arXiv: 2210.14959 [hep-ph].

[401] Y. V. Stadnik, V. A. Dzuba, and V. V. Flambaum. "Improved Limits on Axionlike-Particle-Mediated P , T -Violating Interactions between Electrons and Nucleons from Electric Dipole Moments of Atoms and Molecules". In: *Phys. Rev. Lett.* 120.1 (2018), p. 013202. DOI: 10.1103/PhysRevLett.120.013202. arXiv: 1708.00486 [physics.atom-ph].

[402] Blayne R. Heckel et al. "Preferred-Frame and CP-Violation Tests with Polarized Electrons". In: *Phys. Rev. D* 78 (2008), p. 092006. DOI: 10.1103/PhysRevD.78.092006. arXiv: 0808.2673 [hep-ex].

[403] Nicolò Crescini et al. "The QUAX-g_p g_s experiment to search for monopole-dipole Axion interaction". In: *Nucl. Instrum. Meth. A* 842 (2017), pp. 109–113. DOI: 10.1016/j.nima.2016.10.050. arXiv: 1606.04751 [physics.ins-det].

[404] A. A. Geraci et al. "Progress on the ARIADNE axion experiment". In: *Springer Proc. Phys.* 211 (2018). Ed. by Gianpaolo Carosi, Gray Rybka, and Karl van Bibber, pp. 151–161. DOI: 10.1007/978-3-319-92726-8_18. arXiv: 1710.05413 [astro-ph.IM].

[405] S. Afach et al. "Constraining interactions mediated by axion-like particles with ultracold neutrons". In: *Phys. Lett. B* 745 (2015), pp. 58–63. DOI: 10.1016/j.physletb.2015.04.024. arXiv: 1412.3679 [hep-ex].

[406] Junyi Lee, Attaallah Almasi, and Michael Romalis. "Improved Limits on Spin-Mass Interactions". In: *Phys. Rev. Lett.* 120.16 (2018), p. 161801. DOI: 10.1103/PhysRevLett.120.161801. arXiv: 1801.02757 [hep-ex].

[407] D. J. Wineland et al. "Search for anomalous spin-dependent forces using stored-ion spectroscopy". In: *Phys. Rev. Lett.* 67 (1991), pp. 1735–1738. DOI: 10.1103/PhysRevLett.67.1735.

[408] Davoudiasl, Hooman and Szafron, Robert. "Muon $g-2$ and a Geocentric New Field". In: *Phys. Rev. Lett.* 130 (18 May 2023), p. 181802. DOI: 10.1103/PhysRevLett.130.181802. URL: https://link.aps.org/doi/10.1103/PhysRevLett.130.181802.

[409] S. A. Hoedl et al. "Improved Constraints on an Axion-Mediated Force". In: *Phys. Rev. Lett.* 106 (2011), p. 041801. DOI: 10.1103/PhysRevLett.106.041801.

[410] W. A. Terrano et al. "Short-range spin-dependent interactions of electrons: a probe for exotic pseudo-Goldstone bosons". In: *Phys. Rev. Lett.* 115.20 (2015), p. 201801. DOI: 10.1103/PhysRevLett.115.201801. arXiv: 1508.02463 [hep-ex].

[411] So Chigusa, Takeo Moroi, and Kazunori Nakayama. "Detecting light boson dark matter through conversion into a magnon". In: *Phys. Rev. D* 101.9 (2020), p. 096013. DOI: 10.1103/PhysRevD.101.096013. arXiv: 2001.10666 [hep-ph].

[412] Andrea Mitridate et al. "Detectability of Axion Dark Matter with Phonon Polaritons and Magnons". In: *Phys. Rev. D* 102.9 (2020), p. 095005. DOI: 10.1103/PhysRevD.102.095005. arXiv: 2005.10256 [hep-ph].

[413] Edward Hardy and Robert Lasenby. "Stellar cooling bounds on new light particles: plasma mixing effects". In: *JHEP* 02 (2017), p. 033. DOI: 10.1007/JHEP02(2017)033. arXiv: 1611.05852 [hep-ph].

[414] Stefan Maus et al. "The US/UK world magnetic model for 2010-2015". In: (2010).

[415] Dario Alfe and Michael J Gillan. "First-principles simulations of liquid Fe-S under Earth's core conditions". In: *Physical Review B* 58.13 (1998), p. 8248.

[416] Dario Alfe and Michael J Gillan. "First-principles calculation of transport coefficients". In: *Physical review letters* 81.23 (1998), p. 5161.

[417] Nathan B. Clayburn et al. "Spherically symmetric Earth models yield no net electron spin". In: *Phys. Rev. D* 111.1 (2025), p. 015015. DOI: 10.1103/PhysRevD.111.015015. arXiv: 2411.08050 [hep-ph].

[418] John P. Snyder. "Map projections: A working manual". In: *Professional Paper* (1987). ISSN: 2330-7102. DOI: 10.3133/pp1395. URL: http://dx.doi.org/10.3133/pp1395.

[419] James E Huheey, Ellen A Keiter, and Richard L Keiter. *Inorganic Chemistry: Principles of Structure and Reactivity*. 4th ed. HarperCollins College Publishers, 1993, p. 949.

[420] Edward J. Garnero, Allen K. McNamara, and Sang-Heon Shim. "Continent-sized anomalous zones with low seismic velocity at the base of Earth's mantle". In: *Nature Geoscience* 9.7 (June 2016), pp. 481–489. ISSN: 1752-0908. DOI: 10.1038/ngeo2733. URL: http://dx.doi.org/10.1038/ngeo2733.

[421] I. I. Shapiro. *Solar system tests of general relativity: recent results and present plans*. United Kingdom: Cambridge University Press, 1990. ISBN: 0 521 38428 1. URL: http://inis.iaea.org/search/search.aspx?orig_q=RN:22036209.

[422] Ryan S. Park et al. "Precession of Mercury's Perihelion from Ranging to the MESSENGER Spacecraft". In: *The Astronomical Journal* 153.3 (Feb. 2017), p. 121. DOI: 10.3847/1538-3881/aa5be2. URL: https://dx.doi.org/10.3847/1538-3881/aa5be2.

[423] E. V. Pitjeva. "Relativistic effects and solar oblateness from radar observations of planets and spacecraft". In: *Astronomy Letters* 31.5 (May 2005), pp. 340–349. ISSN: 1562-6873. DOI: 10.1134/1.1922533. URL: https://doi.org/10.1134/1.1922533.

[424] Abhijit Biswas and Krishnan R. S. Mani. "Relativistic Perihelion Precession of Orbits of Venus and the Earth". In: *Central Eur. J. Phys.* 6 (2008), p. 754. DOI: 10.2478/s11534-008-0081-6. arXiv: 0802.0176 [gr-qc].

[425] Tanmay Kumar Poddar, Subhendra Mohanty, and Soumya Jana. "Constraints on long range force from perihelion precession of planets in a gauged $L_e - L_{\mu,\tau}$ scenario". In: *Eur. Phys. J. C* 81.4 (2021), p. 286. DOI: 10.1140/epjc/s10052-021-09078-9. arXiv: 2002.02935 [hep-ph].

[426] Clifford M. Will. "The Confrontation between General Relativity and Experiment". In: *Living Rev. Rel.* 17 (2014), p. 4. DOI: 10.12942/lrr-2014-4. arXiv: 1403.7377 [gr-qc].

[427] Clifford M. Will. "The 1919 measurement of the deflection of light". In: *Class. Quant. Grav.* 32.12 (2015), p. 124001. DOI: 10.1088/0264-9381/32/12/124001. arXiv: 1409.7812 [physics.hist-ph].

[428] E. Fomalont et al. "Progress in Measurements of the Gravitational Bending of Radio Waves Using the VLBA". In: *Astrophys. J.* 699 (2009), pp. 1395–1402. DOI: 10.1088/0004-637X/699/2/1395. arXiv: 0904.3992 [astro-ph.CO].

[429] Irwin I. Shapiro. "Fourth Test of General Relativity". In: *Phys. Rev. Lett.* 13 (1964), pp. 789–791. DOI: 10.1103/PhysRevLett.13.789.

[430] Irwin I. Shapiro et al. "Fourth Test of General Relativity: Preliminary Results". In: *Phys. Rev. Lett.* 20 (1968), pp. 1265–1269. DOI: 10.1103/PhysRevLett.20.1265.

[431] B. Bertotti, L. Iess, and P. Tortora. "A test of general relativity using radio links with the Cassini spacecraft". In: *Nature* 425 (2003), pp. 374–376. DOI: 10.1038/nature01997.

[432] Georg Raffelt. "Limits on a CP-violating scalar axion-nucleon interaction". In: *Phys. Rev. D* 86 (2012), p. 015001. DOI: 10.1103/PhysRevD.86.015001. arXiv: 1205.1776 [hep-ph].

[433] Georg G. Raffelt. "Particle physics from stars". In: *Ann. Rev. Nucl. Part. Sci.* 49 (1999), pp. 163–216. DOI: 10.1146/annurev.nucl.49.1.163. arXiv: hep-ph/9903472.

[434] Georg G. Raffelt. "Astrophysical axion bounds". In: *Lect. Notes Phys.* 741 (2008). Ed. by Markus Kuster, Georg Raffelt, and Berta Beltran, pp. 51–71. DOI: 10.1007/978-3-540-73518-2_3. arXiv: hep-ph/0611350.

[435] Joel Bergé et al. "MICROSCOPE Mission: First Constraints on the Violation of the Weak Equivalence Principle by a Light Scalar Dilaton". In: *Phys. Rev. Lett.* 120.14 (2018), p. 141101. DOI: 10.1103/PhysRevLett.120.141101. arXiv: 1712.00483 [gr-qc].

[436] Asimina Arvanitaki and Andrew A. Geraci. "Resonantly Detecting Axion-Mediated Forces with Nuclear Magnetic Resonance". In: *Phys. Rev. Lett.* 113.16 (2014), p. 161801. DOI: 10.1103/PhysRevLett.113.161801. arXiv: 1403.1290 [hep-ph].

[437] Jose F. Nieves and Palash B. Pal. "Generalized Fierz identities". In: *Am. J. Phys.* 72 (2004), pp. 1100–1108. DOI: 10.1119/1.1757445. arXiv: hep-ph/0306087.

[438] C. C. Nishi. "Simple derivation of general Fierz-like identities". In: *Am. J. Phys.* 73 (2005), pp. 1160–1163. DOI: 10.1119/1.2074087. arXiv: hep-ph/0412245.

[439] V. Cirigliano et al. "Neutrinoless double beta decay in chiral effective field theory: lepton number violation at dimension seven". In: *JHEP* 12 (2017), p. 082. DOI: 10.1007/JHEP12(2017)082. arXiv: 1708.09390 [hep-ph].

[440] Lukas Graf et al. "Short-Range Neutrinoless Double Beta Decay Mechanisms". In: *Phys. Rev. D* 98.9 (2018), p. 095023. DOI: 10.1103/PhysRevD.98.095023. arXiv: 1806.06058 [hep-ph].

[441] M. Doi, T. Kotani, and E. Takasugi. "Double beta Decay and Majorana Neutrino". In: *Prog. Theor. Phys. Suppl.* 83 (1985), p. 1. DOI: 10.1143/PTPS.83.1.

[442] S. M. Bilenky and C. Giunti. "Neutrinoless Double-Beta Decay: a Probe of Physics Beyond the Standard Model". In: *Int. J. Mod. Phys. A* 30.04n05 (2015), p. 1530001. DOI: 10.1142/S0217751X1530001X. arXiv: 1411.4791 [hep-ph].